Galaxy clusters : a probe to galaxy evolution and cosmology

Nicolas Martinet

Université Pierre et Marie Curie

ED 127 - Astronomie et astrophysique

Institut d'Astrophysique de Paris

Galaxy clusters: a probe to galaxy evolution and cosmology

Par Nicolas Martinet

Thèse de doctorat d'Astrophysique et Cosmologie

Dirigée par Florence Durret & Douglas Clowe

Présentée et soutenue publiquement le lundi 31 août 2015
devant un jury composé de :

Benoît Semelin	Professeur d'université – LERMA	Président du jury
Joe Mohr	Professor – LMU	Rapporteur
Peter Schneider	Professor – AIfA	Rapporteur
Christophe Adami	Astronome Adjoint – LAM	Invité
James Bartlett	Professeur d'université – APC	Examinateur
Sophie Maurogordato	Directeur de recherche CNRS – OCA	Examinateur

Abstract

This thesis presents some recent results concerning galaxy evolution and cosmology, based on the observation of galaxy clusters at optical wavelengths. We first introduce the main properties of galaxy clusters (Sect. 1.1) and how they can be used for cosmology within the standard cosmological model (Sect. 1.2). A large fraction of the presented results comes from the study of the DAFT/FADA galaxy cluster survey at redshifts $0.4 < z < 0.9$ (Sect. 1.3). We divide our study in two parts according to the observable that is considered: galaxy luminosity or galaxy shape.

The distribution of galaxy luminosities is called the galaxy luminosity function (GLF), which can be used to probe the evolution of cluster galaxies (Sect. 2.1). Computing the GLFs for a sub sample of 25 DAFT/FADA clusters, we find that faint blue star forming galaxies are quenched into red quiescent galaxies from high redshift until today. Comparing to the field shows that this transformation is more efficient in high density environments.

We also study the fraction of baryons in galaxy groups and clusters (Sect. 2.2). We find that in groups, the stars contained in galaxies can reach masses of the same order as those of the intra-cluster gas, while in clusters they are usually negligible relatively to the gas. Taking both stars and gas into account we constrain the matter density parameter Ω_M.

Galaxy shapes are distorted by foreground objects that bend light in their vicinity. This lensing signal can be exploited to measure the mass distribution of a foreground cluster. We review the basic theory of weak lensing and shear measurement (Sect. 3.1), and then apply it to a subsample of 16 DAFT/FADA clusters, with Subaru/SuprimeCam or CFHT/MegaCam imaging (Sect. 3.2). We estimate the masses of these clusters, and take advantage of the large fields of view of our images to detect filaments and structures in the cluster vicinity, observationally supporting the hierarchical scenario of cluster growth.

Finally, we detect shear peaks in *Euclid*-like simulations, and use their statistics as a cosmological probe, similarly to cluster counts (Sect. 3.3). We forecast the cosmological constraints that this technique will achieve when applied to the *Euclid* space mission, and develop a tomographic analysis that adds information from redshifts.

We conclude with a discussion of our perspectives on future studies in all the fields investigated in the present thesis.

Résumé

Cette thèse présente un certain nombre de résultats récents à propos de l'évolution des galaxies et la cosmologie, à partir de l'observation d'amas de galaxies en lumière visible. Nous introduisons d'abord les principales propriétés des amas de galaxies (Chapitre 1.1) et la façon dont ces objets permettent de contraindre le modèle cosmologique standard (Chapitre 1.2). Une grande partie des résultats présentés ici ont été obtenus à partir de l'étude du relevé d'amas DAFT/FADA, qui regroupe des amas dans la gamme de décalages spectraux $0.4 < z < 0.9$ (Chapitre 1.3). Cette thèse est séparée en deux parties, chacune traitant d'une observable particulière : la luminosité des galaxies, puis la forme des galaxies.

La fonction de luminosité des galaxies, c'est-à-dire la distribution de leur luminosité, permet d'étudier l'évolution des galaxies dans les amas (Chapitre 2.1). Nous avons calculé les fonctions de luminosité pour un sous-échantillon de 25 amas DAFT/FADA, et avons montré que les galaxies faibles bleues, à fort taux de formation stellaire, évoluent en des galaxies rouges passives des hauts décalages spectraux à aujourd'hui. En comparant les fonctions de luminosité des amas à celles du champ, on observe que cette transformation est plus efficace dans les environnements denses.

Nous avons également étudié la fraction de baryons dans les groupes et amas de galaxies (Chapitre 2.2). Nous avons remarqué que dans les groupes la fraction massique d'étoiles peut atteindre des valeurs du même ordre de grandeur que celles de la fraction de gaz intra-amas, alors que dans les amas, la fraction stellaire est généralement négligeable devant celle du gaz. En prenant en compte à la fois les étoiles et le gaz, nous avons posé des contraintes sur le paramètre de densité de matière Ω_M.

Les galaxies apparaissent déformées par la présence d'objets d'avant-plan qui courbent les trajectoires lumineuses à leur voisinage. Ce signal de lentille gravitationnelle peut être exploité afin de mesurer la distribution de masse des amas d'avant-plan. Les bases du phénomène de lentille gravitationnelle faible et de la mesure du cisaillement sont introduites au Chapitre 3.1. Ces techniques sont ensuite appliquées à un sous-échantillon de 16 amas DAFT/FADA présentant des images Subaru/SuprimeCam ou CFHT/MegaCam (Chapitre 3.2). Nous avons estimé la masse de ces amas, et profité de la large dimension angulaire de ces images pour détecter des filaments et des structures autour de ces amas. Cette étude valide observationnellement le scénario de croissance hiérarchique des amas.

Finalement, nous avons détecté les pics de cisaillement dans des simulations de type *Euclid*, et avons utilisé leur statistique en tant que sonde cosmologique, de façon similaire aux comptages d'amas (Chapitre 3.3). Nous avons calculé les contraintes cosmologiques que cette technique pourra apporter avec les données de la mission spatiale *Euclid*, et avons développé une approche tomographique qui ajoute l'information des décalages spectraux.

Une discussion sur les développements envisagés dans les différents domaines traités conclut cette thèse.

Acknowledgement

I am very grateful to Florence Durret for all the time she spent teaching and helping me. Besides, it was a really pleasant collaboration, with some very nice souvenirs, such as the ski sessions in Italy! Then I would like to thank the jury members for reviewing my work and attending the defense. Finally, I also thank all my colleagues who either helped me or entertained me during the past few years, and all my friends and relatives who do not already belong to the aforementioned categories for supporting me.

I dedicate this thesis to myself, when I was 10.

Contents

Acronyms

ACS ..... Advanced Camera for Surveys
AGN ..... Active Galactic Nucleus
ARCLETS ..... Analysis of Realistic Cluster Lensing through Extensive Training Simulations
BAO ..... Baryon Acoustic Oscillation
BCG ..... Brightest Cluster Galaxy
CDM ..... Cold Dark Matter
CFHT ..... Canada-France-Hawai Telescope
CFHTLenS ..... Canada-France-Hawaii Lensing Survey
CFHTLS ..... Canada-France-Hawai Telescope Legacy Survey
COSMOS ..... COSMOlogical evolution Survey
CMB ..... Cosmic Microwave Background
DAFT/FADA ..... Dark energy American French Team (in french FADA)
DE ..... Dark Energy
DM ..... Dark Matter
EDisCS ..... ESO Distant Clusters Survey
ESA ..... European Space Agency
ESO ..... European Space Observatory
FLRW ..... Friedmann Lemaître Robertson Walker
GLF ..... Galaxy Luminosity Function
GREAT ..... GRavitational lEnsing Accuracy Testing
HST ..... Hubble Space Telescope
IAP ..... Institut d'Astrophysique de Paris
ICL ..... Intra Cluster Light
ICM ..... Intra Cluster Medium
KiDS ..... Kilo Degree Survey
KSB ..... Kaiser, Squires, and Broadhurst
ΛCDM ..... Lambda Cold Dark Matter
LCDCS ..... Las Campanas Distant Cluster Survey
LePHARE ..... PHotometric Analysis for Redshift Estimate
LSB ..... Low Surface Brightness
LSST ..... Large Synoptic Survey Telescope
MOND ..... MOdified Newtonian Dynamics
NASA ..... National Aeronautics and Space Administration
NGC ..... New General Catalog
photo-z ..... photometric redshift
PSF ..... Point Spread Function
PSFEx ..... PSF Extractor
RASS ..... ROSAT All Sky Survey
RCSLenS ..... Red Cluster Sequence Lensing Survey
RS ..... Red Sequence
SED ..... Spectral Energy Distribution
SExtractor ..... Source Extractor

SDSS ..... Sloan Digital Sky Survey
SL ..... Strong Lensing
SMF ..... Stellar Mass Function
SN ..... SuperNova
STEP ..... Shear TEsting Programme
SUNGLASS Simulated UNiverses for Gravitational Lensing Analysis and Shear Surveys
S/N ..... Signal-to-Noise
WFIRST ..... Wide-Field Infrared Survey Telescope
WL ..... Weak Lensing
WLTC ..... Weak Lensing Tomography with Clusters
WMAP ..... Wilkinson Microwave Anisotropy Probe
XMM ..... X-ray Multi-Mirror

Chapter 1

Introduction

1.1 Galaxy clusters

Galaxy clusters are the most massive structures in our Universe. They are originally defined as a large ensemble of galaxies gravitationally bound together and were first observed in the mid-twentieth century (e.g. Abell 1958). However, with the evolution of instrumentation, it became clear that galaxies are only the visible part of these giant icebergs.

1.1.1 Cluster composition

Indeed, galaxy clusters are mainly made of a dark matter halo. DM has first been invoked by Zwicky (Zwicky 1933) to explain the difference between the luminous mass, obtained from adding each galaxy stellar mass, and the dynamical mass, derived from the dispersion of galaxy velocities in the Coma cluster. Note also that several researchers consider a modification of general relativity laws, referred as modified gravity, a pioneer of which was the MOND theory (Milgrom 1983). This debate on DM versus modified gravity arises from the need to modify the gravitational potential of very massive objects, from galaxy to cosmological sizes. Modifying gravity or mass can equally solve this issue. However, DM led to a wide range of observational successes and is now the current framework. Throughout this thesis, we will assume general relativity with DM. We know very little about DM properties, except that it is non luminous. Comparing the observed number of baryons to that expected from primordial nucleosynthesis revealed that DM is mainly non-baryonic (e.g. Dodelson et al. 1996). In addition, Clowe et al. (2006) found an offset between the gas and the total mass positions in the merging Bullet cluster, observationally proving that DM is very weakly interacting, and perhaps collisionless.

Another important component of the galaxy clusters is the intra cluster medium which is probed with X-ray observations. This medium is made of ionized hydrogen that does not lie inside galaxies. This gas is heated by gravitational energy to $10^7 - 10^8$ K at the epoch of cluster formation. Electrons are therefore not linked to nuclei and emit photons through Bremsstrahlung process, to satisfy the conservation of energy when they are deflected by a nucleus. This ICM is well understood and one can convert X-ray observations into an ICM mass. Note that when the system is virialized, we can also constrain the total mass of the cluster. The determination of ICM and total mass from

Figure 1.1: Galaxy cluster components for Abell 1689. Superposed to the HST galaxy observation (*left*) are the ICM component measured with Chandra (*middle*) and the DM component measured through strong lensing (*right*). Adapted from the following images: Optical: NASA/STScI; X-ray: NASA/CXC/MIT/E.-H Peng et al; Dark Matter: NASA, ESA, E. Jullo (JPL/LAM), P. Natarajan (Yale) and J-P. Kneib (LAM).

X-ray observations is described in part 2.2 where we compute the fraction of baryons in galaxy clusters.

The third component is the luminous galaxies. Fig. 1.1 shows the three main components of galaxy clusters on the example of Abell 1689. We usually consider that DM counts for about 90% of the total cluster mass, ICM for about 8-9%, and galaxies for about 1-2%. These fractions are only indicative and we know that they vary from one cluster to another. In particular, they are correlated with the total cluster mass as can be seen in Fig.1.2, from Laganá et al. (2013). We see that baryons in massive clusters are dominated by the hot X-ray gas, while the gas fraction for smaller systems is closer to the galaxy component.

Despite their low contribution to the cluster mass budget, galaxies are a tremendous tool to understand galaxy clusters. In this thesis, we will see that considering two of the galaxy observables: shape and luminosity, we can infer various results on e.g. cluster formation and evolution, cluster luminous and total masses, and cosmology.

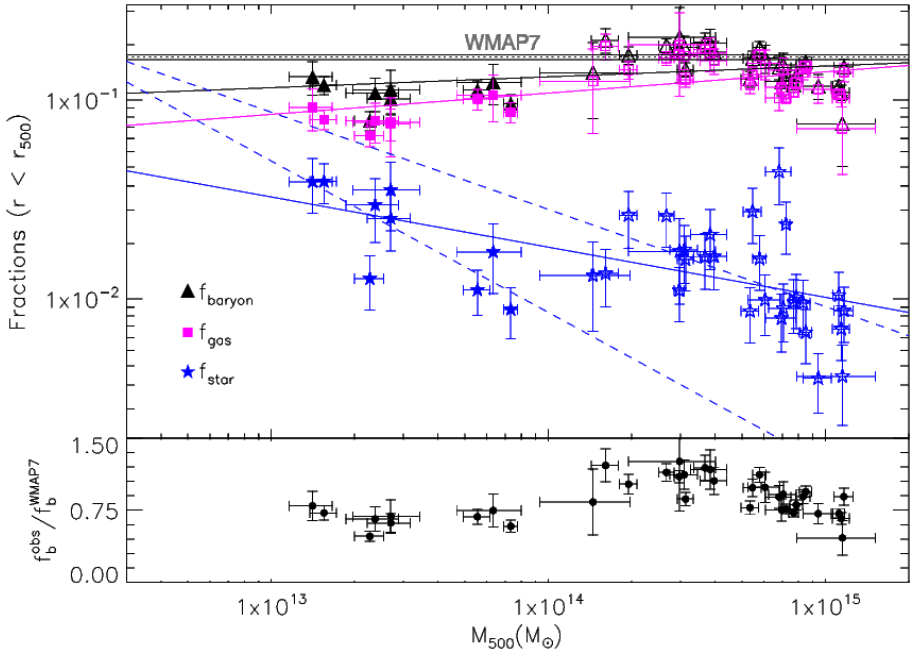

Figure 1.2: Stellar (blue stars), gas (magenta squares), and total baryon (black triangles) mass fractions as a function of total mass in r_{500}. The solid lines correspond to the best linear fit for each relation. The two blue dashed lines correspond to the fits for the groups and clusters separately. On the bottom of the panel, we show the ratio between the total baryon fraction determined by the sum of $f_{\rm star}$ and $f_{\rm gas}$ and the WMAP-7 value as a function of total mass. See part 2.2 for details.

1.1.2 Cluster formation

Cluster formation is dominated by its main component: DM. In our current understanding, halos of DM form from the density fluctuations after the reionization era. Galaxies form later from the baryonic matter, and fall into the gravitational potential of these DM halos, that then grow through this accretion and the merging with other halos, giving birth to galaxy clusters. This scenario, known as the hierarchical scenario, is mainly assessed by cold DM simulations and still lacks observational support at high redshifts. Fig. 1.3 shows the same field of the Millennium simulation (Springel et al. 2005) at different redshifts. The small density variations in the early Universe ($z = 18.3$) are amplified to create a cluster around $z = 1.4$. In this formation scheme, the matter spread into filamentary structures, and clusters lie at the node of those filaments. This filamentary structure is well observed, in particular through spectroscopic (e.g. SDSS: Tegmark et al. 2004) and weak lensing surveys (COSMOS: Massey et al. 2007b). A less obvious point is the detection of filaments around clusters, which is mandatory to confirm that clusters are formed following this scenario and not through a different process. The detection of such objects are studied in detail in part 3.2 of this thesis.

In the same scenario, clusters are formed from smaller galaxy groups that merge together at higher redshifts (Adami et al. 2013). The redshift at which clusters form is still in debate. Most clusters seem to form around $z = 1.4$. The farthest clusters are detected around $z \sim 1.5 - 2$ (Fassbender et al. 2011; Gobat et al. 2011). Groups of

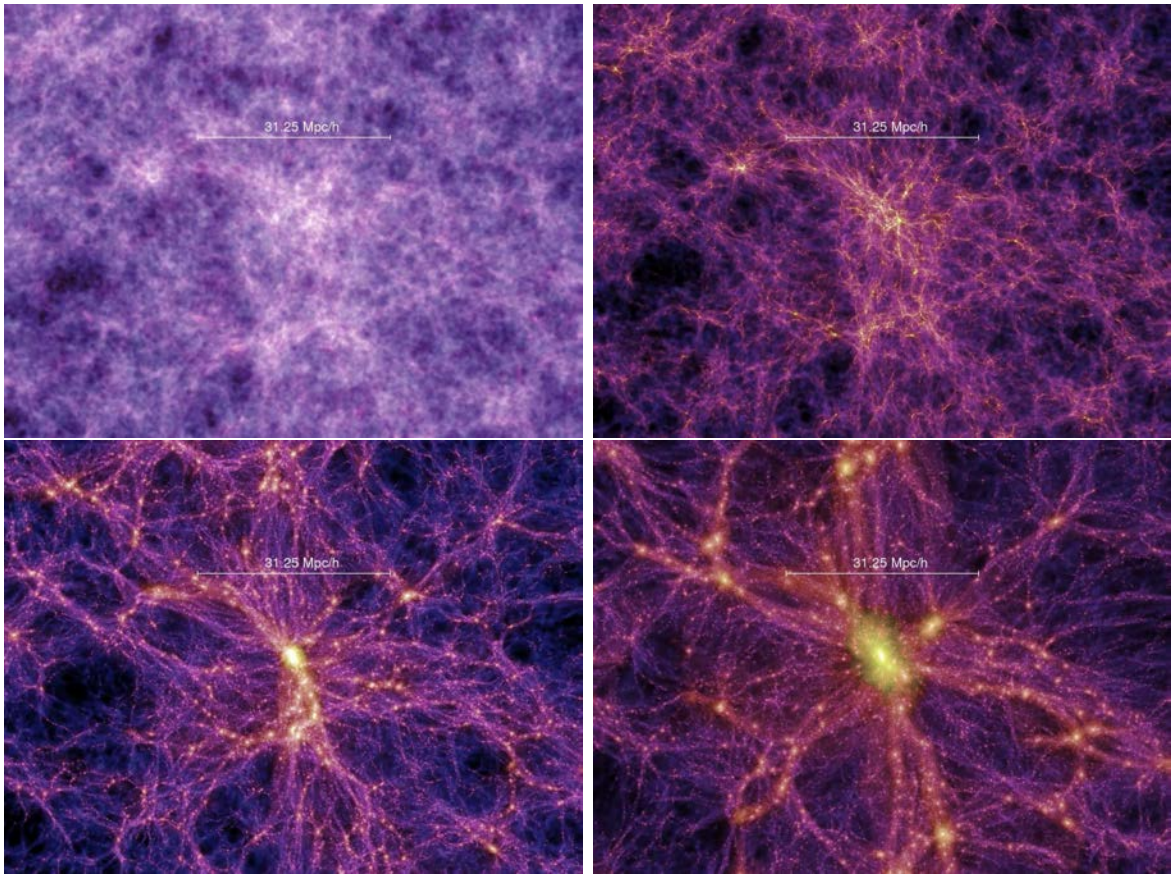

Figure 1.3: Formation of a cluster in the Millennium simulation (Springel et al. 2005). The same projected density field is shown at different redshifts for a 15 Mpc.h^{-1} thick slice: upper left is $z = 18.3$, upper right $z = 5.7$, lower left $z = 1.4$, and lower right $z = 0$.

galaxies only contain a few to a few tens of galaxies and are therefore difficult to detect at high redshift. Hence, we propose to study local groups of galaxies, and compare them to clusters in part 2.2.

1.1.3 Cluster evolution

As seen in simulations, the formation and the evolution of galaxy clusters are dominated by the evolution of the DM halo that grows through accretion of nearby material. However, the remaining 10 to 20% (i.e. the baryons), undergo several changes along the cluster life. The various interactions happening within clusters will often modify the properties of the gas and the galaxies. We can classify these interactions into two categories: (1) those between galaxies, and (2) those between galaxies and the Intra Cluster Medium (ICM).

The first category of interactions includes *galaxy merging* and *galaxy harassment*. In both cases two galaxies hit one another. In the case of mergers, galaxy relative speeds are small enough that the galaxies will collapse together, usually creating a burst of star formation, followed by an evolution into a larger elliptical galaxy (e.g. Negroponte & White 1983; Barnes & Hernquist 1992, 1996; Mihos & Hernquist 1996). In the second

case, the velocity of galaxies is higher, and the galaxies will pass one through (or next to) each other. Depending on the trajectory of galaxies, this will result in high tidal forces, and often also in a burst of star formation (e.g. Spitzer & Baade 1951; Moore et al. 1996, 1998). However, the galaxies will not merge and each one will continue with its own material. Finally, once a galaxy reaches a large size compared to the others, the merging with other galaxies does not strongly change its properties but increases its mass, a process referred as *cannibalism*, and which could explain the formation of the Brightest Cluster Galaxies (BCGs) (e.g. Ostriker & Tremaine 1975).

The second category consists of interactions between galaxies and ICM, such as *ram pressure stripping* and *AGN feedback* (Active Galactic Nucleus). Ram pressure stripping is the removal of the galaxy gas due to the dynamical friction with the ICM when the galaxy moves within it. The main effect of the gas stripping is to suppress star formation, as the galaxy gets poorer in gas, that would normally be used to form stars (e.g. Gunn & Gott 1972; Cowie & Songaila 1977; Quilis et al. 2000). AGNs are active objects made of a super massive black hole surrounded by an accretion disk, lying at the center of very massive galaxies, and have the property to re-emit infalling matter into collimated jets. When the ICM gas cools, it falls onto the massive black hole, that, when having accreted a sufficient quantity of gas, ejects it to re-enrich the ICM. The process also referred as AGN heating, explains why the ICM remains at a very high temperature, in particular in the central regions of clusters (e.g. Churazov et al. 2002; Brüggen & Kaiser 2002; Sijacki & Springel 2006).

A third category of interplays could be invoked to explain the quenching of star formation: the interaction between the DM potential and the galaxy. Galaxies falling into the DM halo for the first time, undergo tidal forces that allow the gas to escape from the galaxy, a phenomenon refered as *galaxy strangulation*. This effect also results in a gas depletion, and then in the suppression of star formation, but happens on time scale that might be longer than gas stripping (e.g. Larson et al. 1980; Balogh et al. 2000).

All these interactions help to better understand galaxy evolution within clusters, and in particular, why and how spiral star forming galaxies become elliptical quiescent galaxies in denser environment, an effect named the morphology-density relation. While it has been studied in detail at low redshifts (e.g. Hubble 1926; Dressler 1980), another interesting question is the evolution of the galaxy population with redshift (e.g. Smith et al. 2005). Peng et al. (2010) recently proposed a scenario in which star forming galaxies are first quenched due to environment effects while falling onto the cluster DM potential, and at lower redshifts ($0 < z < 1$), are quenched proportionally to their star formation rate, until they have used all their available gas.

In part 2.1, we shed light on the evolution of galaxies within clusters in the redshift range $0.4 < z < 0.9$, studying the galaxy luminosity functions of medium-high redshift clusters.

1.2 Galaxy clusters in cosmology

Being the most massive collapsed structures in the Universe, galaxy clusters have a particular place among observational cosmology. Their distribution with mass is linked to the evolution of the entire Universe as shown in part 1.1.2. In addition, their inner part

traces the fraction of baryons in the highest existing density environments.

To understand which constraints can be calculated from clusters, we first have to define the standard cosmological model.

1.2.1 Standard cosmology

In general relativity, gravity is defined as the response of space-time to matter and is governed by the Einstein equation (Einstein 1916):

$$G_{\mu\nu} + \Lambda g_{\mu\nu} = \frac{8\pi G}{c^4} T_{\mu\nu}, \tag{1.1}$$

where $G_{\mu\nu}$ is the Einstein tensor, $g_{\mu\nu}$ the metric tensor, $T_{\mu\nu}$ the mass-energy tensor, Λ is the cosmological constant, G the gravitational constant, and c the speed of light. The left-hand term of eq. 1.1 corresponds to the curvature of space-time given the metric $g_{\mu\nu}$, and the right-hand term to the matter-energy content of the space-time. Solving this equation in the Friedmann Lemaître Robertson Walker (FLRW) metric leads to the Friedmann equations that describe the evolution of the Universe (Friedmann 1922). The FLRW metric (eq. 1.2) assumes a spatially homogeneous and isotropic Universe, a strong hypothesis called the cosmological principal, in either expansion or contraction and is defined as:

$$ds^2 = dt^2 - a^2(t) \left[\frac{dr^2}{1 - Kr^2} + r^2(d\theta^2 + (\sin\theta)^2 d\phi^2) \right], \tag{1.2}$$

where t is the time, $(r,\, \theta,\, \phi)$ the space coordinates, K the space curvature, and $a(t)$ the scale factor that describes the expansion with time. K equals 0 for a flat infinite Universe, is negative for an infinite hyperbolic Universe, and positive for a spherical finite Universe. Note that the expansion factor $a(t)$ is the same in every direction and depends only on time in eq. 1.2, a choice made to respect the cosmological principle. Assuming a fluid with a pressure P, a density ρ, and a null velocity leads to a very simple matter-energy tensor $T_{\mu\nu}$ for the Universe content, allowing a simple resolution of Einstein's equation. It results in the Friedmann equations (eq. 1.3 & 1.4):

$$\left(\frac{\dot{a}}{a}\right)^2 = \frac{8\pi G}{3}\rho - \frac{K}{a^2} + \frac{\Lambda}{3}, \tag{1.3}$$

$$\frac{\ddot{a}}{a} = -\frac{4\pi G}{3}(\rho + 3P) + \frac{\Lambda}{3}. \tag{1.4}$$

These equations describe the evolution of the expansion of the Universe, represented by the scale factor $a(t)$. Note that this factor only depends on time and on the content of the Universe. We define the Hubble parameter as $H = \dot{a}/a$, which represents the expansion rate of the Universe.

An additional equation is mandatory to solve Friedmann's equation, which is the equation of state of the content of the Universe. We usually assume a perfect fluid equation for the content of the Universe:

$$P = w\rho c^2, \tag{1.5}$$

where w depends on the type of energy considered. For cold matter, $w = 0$ and the resolution of Friedmann's equations gives a matter density proportional to the scale factor at the power of minus three: $\rho = \rho_0 a^{-3}$. For radiating energy, $w = 1/3$ and $\rho = \rho_0 a^{-4}$. Finally, for vacuum, $w = -1$ and the density is constant: $\rho = \rho_0$. We can now rewrite Friedmann's equation as:

$$H^2 = H_0^2 \left[\Omega_R (1+z)^4 + \Omega_M (1+z)^3 + \Omega_K (1+z)^2 + \Omega_\Lambda\right] = H_0^2 E^2(z), \tag{1.6}$$

where we have linked the scale factor to the redshift observable z as follows:

$$a(t) = \frac{a_0}{1+z}, \tag{1.7}$$

and where we have introduced the density parameters for each energy source:

$$\Omega_R = \frac{8\pi G \rho_{R,0}}{3H_0^2}, \qquad \Omega_M = \frac{8\pi G \rho_{M,0}}{3H_0^2}, \qquad \Omega_K = -\frac{K}{H_0^2 a_0^2}, \qquad \Omega_\Lambda = \frac{\Lambda}{3H_0^2}. \tag{1.8}$$

In eq. 1.6 to 1.8, index $_0$ means that the quantity is evaluated at the present time. In particular, H_0 corresponds to the present expansion rate and is called the Hubble constant. We sometimes use h which is equal to H_0 divided by 100 km.s^{-1}.Mpc^{-1}. The different density parameters represent the normalized contribution of one specific energy source to the present Universe content. Hence, we have $\sum \Omega_i = 1$. All studies conducted so far have revealed that $K = 0$ and thus $\Omega_K = 0$, meaning that we are living in a flat Universe. Under this assumption, the resolution of Friedmann's equations shows that radiation was dominating in the early Universe, followed by an era of matter domination. Today, we are dominated by the vacuum energy as Ω_Λ is about 0.7, and then by matter with Ω_M about 0.3. The matter density parameter can be separated under its DM content Ω_c, and baryonic content Ω_b, with $\Omega_M = \Omega_c + \Omega_b$. The matter repartition in the present Universe is often represented as the so-called cosmological pie (Fig 1.4).

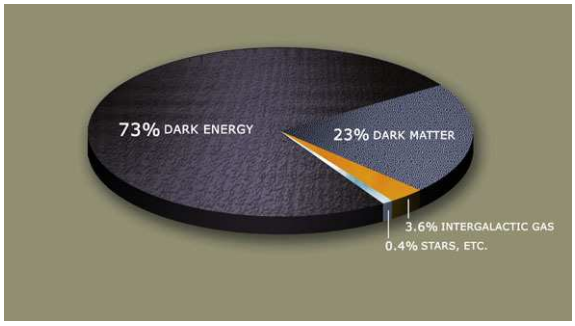

Figure 1.4: Universe density parameter repartition. Image taken from the NASA website.

In this figure, we introduce the notion of Dark Energy which is the energy of the vacuum and drives the Universe expansion. There is a strong debate about the nature of this energy. It could either be a fundamental constant of our Universe or an invisible fluid. In the first case, it naturally arises from the Einstein equation but in the second case it needs an equation of state. We use the same equation of state than for normal

matter (eq. 1.5). The case where $w = -1$ corresponds to the cosmological constant case. Measuring a significant deviation from this value would confirm the DE paradigm, explaining why great efforts are made to accurately measure the actual value of w for DE (e.g. the *Euclid* mission Laureijs et al. 2011).

The density parameters, together with the Hubble constant, are sufficient to describe the present Universe. However, to make predictions on the history of our Universe, we need to introduce some other parameters. In part 1.1.2, we said that galaxy clusters form from the amplification of initial density fluctuations. This deviation from homogeneity is often described by the power spectrum of the curvature perturbation Δ^2_R, which is a power law at the power $n_s - 1$, where n_s is referred as the spectral index, and is close to 1. Finally, we need a measure of the ionization state of the Universe. This is quantified by the re-ionization optical depth τ which is the probability of a photon to scatter once.

The actual Lambda Cold Dark Matter cosmological model assumes that DE is a cosmological constant. This hypothesis leads to a Universe which can be fully described with 6 parameters. These parameters are the DE density Ω_Λ, the DM density Ω_c, the baryon density Ω_b, the curvature fluctuation amplitude Δ^2_R, the scalar spectral index n_s, and the re-ionization optical depth τ[1]. All other parameters can be computed from these ones. However, depending on the data we want to fit, some parameters are more convenient. In particular, the density perturbation amplitude is often studied through the more convenient σ_8: the present linear mass dispersion on a scale of 8 h^{-1}.Mpc. The six cosmological parameters can then be rewritten as $(\Omega_\Lambda, \Omega_c, \Omega_b, \sigma_8, n_s, \tau)$.

In addition to these parameters, one can add some which are not yet necessary, but might one day become. Among those, we just mention the DE equation of state w which, if it is rigorously equal to -1 corresponds to a cosmological constant. We usually decompose the DE equation of state between a constant term w_0 and a term that depends on the expansion $w_a(1-a)$, such that $w = w_0 + w_a(1-a)$, where a is the scale factor. The case of a cosmological constant corresponds to $(w_0, w_a) = (-1, 0)$.

Many efforts have been deployed in the past few decades to estimate these parameters. The most famous are: Cosmic Microwave Background experiments, type Ia supernovae, galaxy clustering (including Baryon Acoustic Oscillation), shear power spectrum, cluster counts... In this thesis, we will only review the techniques relevant to galaxy clusters. We show the present value for the six minimum cosmological parameters, along with H_0, σ_8, Ω_M and the age of the Universe, as measured from CMB experiments combined with BAO in Table 1.1. We give two different values depending on the use of the WMAP-9 (Hinshaw et al. 2013) or Planck (Planck Collaboration et al. 2014) experiments. Presently, one should refer to the more accurate Planck values. However, as the Planck results were issued during the completion of this thesis, we use WMAP values therein.

An important remark is that due to the expansion, the measurable distances in the Universe depend on cosmological parameters. In the framework described above, we can write the distance between two objects, the co-moving distance χ, as a function of the density parameters and the Hubble constant:

[1]Note that the observables for the DM and baryon density parameters are in facts $\Omega_c h^2$ and $\Omega_b h^2$, such that the Hubble constant $H_0 = h \times 100$ km.s^{-1}.Mpc^{-1} can be derived from it.

Table 1.1: Cosmological parameters from WMAP-9 and Planck (CMB and BAO combined). The six first parameters are the minimum parameters for the ΛCDM model, the following four can be calculated from the first but are sometimes more convenient, and the last one supposes an equation of state for the DE. Uncertainties are given with a 68% confidence level. See text for details.

Parameter	Planck	WMAP
Ω_Λ	0.692±0.010	0.703±0.012
$\Omega_c h^2$	0.1187±0.0017	0.1160±0.0025
$\Omega_b h^2$	0.02212±0.00025	0.02249±0.00044
$\ln(10^{10}\Delta_R^2)$	3.090±0.025	3.093±0.030
n_s	0.9629±0.0057	0.969±0.010
τ	0.091±0.013	0.086±0.014
H_0 (km.s^{-1}.Mpc^{-1})	67.79±0.78	68.45±0.96
σ_8	0.826±0.012	0.816±0.018
Ω_M	0.308±0.010	0.297±0.012
Age (Gyr)	13.800±0.038	13.807±0.090
w	-1.13±0.13	-1.073±0.090

$$\chi(z) = \int \frac{cdz}{H(z)} = \frac{c}{H_0} \int \frac{dz}{\sqrt{\Omega_R (1+z)^4 + \Omega_M (1+z)^3 + \Omega_K (1+z)^2 + \Omega_\Lambda}}. \tag{1.9}$$

In practical, the co-moving distance is not directly measurable but only the angular and the luminous distances, which are linked to the first one in a very simple way: $D_{\text{ang}} = a\chi$ and $D_{\text{lum}} = (1+z)^2 a\chi$. Thus, a measure of these distances is sensitive to the matter and energy content of the Universe.

1.2.2 Cluster cosmological probes

The two main cosmological probes based on clusters are cluster counts and baryon fractions. Here, we briefly describe these two techniques. See Allen et al. (2011) for a full review of cosmology with galaxy clusters. Results concerning cluster counts can be found in parts 3.2 and 3.3, and concerning baryon fractions in part 2.2 of this thesis. We also describe one promising future probe: Weak Lensing Tomography with Clusters (WLTC). In part 1.3, we introduce the DAFT/FADA survey which is built to serve as a test study for this new probe.

Cluster counts

We saw in parts 1.1.2 & 1.2.1 that the formation of clusters depends on the initial density fluctuations, and the density parameters of the Universe. The idea here is to link the cluster abundance to the cosmology, assuming the standard scenario for the evolution of clusters. The expected number of clusters for a survey of area $\Delta\Omega$ can be expressed as:

$$\frac{dN}{dz} = \Delta\Omega \frac{dV}{dz d\Omega}(z) \int_0^\infty f(M,z) \frac{dn(M,z)}{dM} dM, \tag{1.10}$$

where $\frac{dV}{dzd\Omega}(z)$ is the co-moving volume element at redshift z, $f(M,z)$ the selection function, and $\frac{dn(M,z)}{dM}$ the halo mass function. The dependence on cosmology is contained in the co-moving volume (see eq. 1.9 for distance cosmology dependence) and the halo mass function. The halo mass function represents the distribution of galaxy clusters with mass in the Universe, and thus depends on the matter density parameter and on the CDM primordial fluctuations. The evolution of cluster abundance with redshift also allows to probe the DE equation of state w (e.g. Wang & Steinhardt 1998; Haiman et al. 2001). The choice of the halo mass function is a delicate question which is well debated in the literature. The halo mass function can be calculated, either theoretically: e.g. Press & Schechter (1974), or from simulations: e.g. Tinker et al. (2008). While most studies now resort to simulations, we must note that the classical choice of neglecting the baryons in these simulations can have important effects on the cosmological constraint estimates (Bocquet et al. 2015). Once this function is chosen, one can compute the expected cluster distribution and compare it with the observed distribution, usually in a Fisher formalism. This formalism is described in section 3.3, where we apply it to *Euclid*-like simulations.

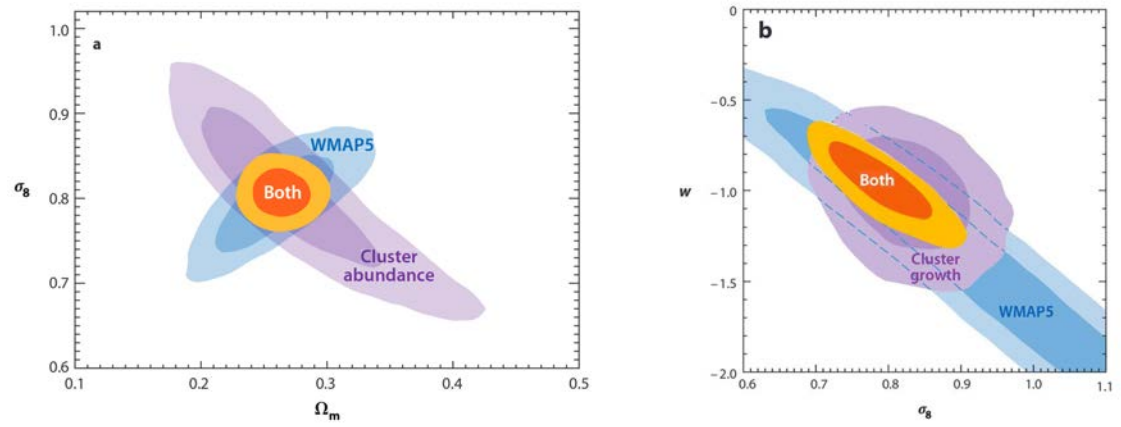

Figure 1.5: Joint 68.3% and 95.4% confidence regions for σ_8, Ω_M and w from cluster abundances, compared with those from WMAP-5 data (Dunkley et al. 2009) for spatially flat ΛCDM models. In *(a)*, cluster abundance is measured in the MaxBCG sample ($z < 0.3$) from Rozo et al. (2010). In *(b)* cluster abundance is measured in the ROSAT All-Sky Survey (RASS) clusters at $z < 0.5$ (Mantz et al. 2010). The gold region is the combination of both constraints. Adapted from Allen et al. (2011).

In Fig. 1.5, we present some of the latest results on cosmological constraints from cluster abundance studies, and compare it with CMB experiments. We see that cluster counts are less sensitive to the density parameters than CMB experiments but that they are more sensitive to the equation of state of the DE. On a more general point of view, cluster counts are more sensitive to the parameters that are linked to the growth of structures, as the CMB is emitted before those structures have the time to evolve. In any case, the constraints are oriented in a different way, allowing an important gain when combining both probes. Furthermore, the systematics are not the same, and the fact that constraints overlap for all methods is a good sanity check.

We showed that cluster abundance is an accurate cosmological probe, but there are some biases in its application that need to be checked. From eq. 1.10, we identify three

observational challenges: the measurement of accurate redshifts, of accurate masses, and the control of the detection systematics, in other terms the selection function.

The best way to measure redshifts is spectroscopy. However, this technique requires too much observational time, explaining why most studies rely on photometric redshifts.

The selection function quantifies the biases of the cluster detection algorithm. In particular, we want to know how many clusters we miss (i.e. the completeness) and how many of our identified clusters correspond to wrong detections (i.e. the purity). Assessing the cluster detection quality is a hot topic which is being investigated for the next generation wide surveys (e.g. the *Euclid* Cluster Detection Challenge).

The hardest problem is the mass measurement. Indeed, in most cases, we do not measure the true mass of clusters but only a proxy to this quantity derived through observation. Hence we need to calibrate the mass observable relation with a sample of fully known cluster masses. So far, the best way to determine this relation is to use weak lensing as it takes into account the full mass distribution of the cluster. Other observables are the X-ray emission, the dispersion of velocities, the strong lensing, and the Sunyev Zeldovich effect. Those techniques all enable to determine cluster masses but they rely on some physical assumptions that cannot be verified for every cluster. In particular, most of them require that systems are virialized, i.e. that kinetic and potential energies equilibrate, which is true only for relaxed clusters, that do not undergo any specific effect such as merging. The strong lensing observable does not require such a hypothesis, but it can only probe masses in the inner part of clusters, i.e. at scales lower than the Einstein radius. In part 3.2, we determine cluster masses through WL at the required accuracy, extending the number of clusters that can be used to constrain the observable mass relation.

In part 3.3, we propose to overpass the problems of the observable mass relation and of the cluster selection function by studying not clusters but directly projected mass peaks, using many simulations.

Fraction of baryons

The fraction of baryons can be used to probe the evolution of matter from the early Universe. This fraction is a direct constraint of the baryon to matter parameters (e.g. Briel et al. 1992; White et al. 1993; Evrard 1997; Mohr et al. 1999) and can be compared to the same ratio measured in the early Universe through CMB analysis:

$$f_{\rm gas} = \Gamma(z)\frac{\Omega_b}{\Omega_M}, \tag{1.11}$$

where $\Gamma(z)$ is the gas depletion parameter and characterizes the cluster halo at redshift z, and within the radius in which masses are computed. Using priors on Ω_b and H_0 from other cosmological probes then allows to estimate the matter parameter Ω_M for a sufficiently large number of clusters.

A more precise measurement of cosmological parameters can be performed by exploiting the angular distance dependence of the gas fraction measurement (e.g Allen et al. 2004, 2008):

$$f_{\rm gas} \propto D_{\rm ang}(z)^{3/2}. \tag{1.12}$$

As already shown in eq. 1.9, distance depends on cosmology, and thus the fraction of gas in clusters can constrain cosmological models. Such measurements are shown in Fig. 1.6. We see that $f_{\rm gas}$ achieves only low constraints compared to CMB experiments. However, the degeneracy between parameters being oriented in a complete different way, this additional information leads to much tighter constraints when combined with other probes.

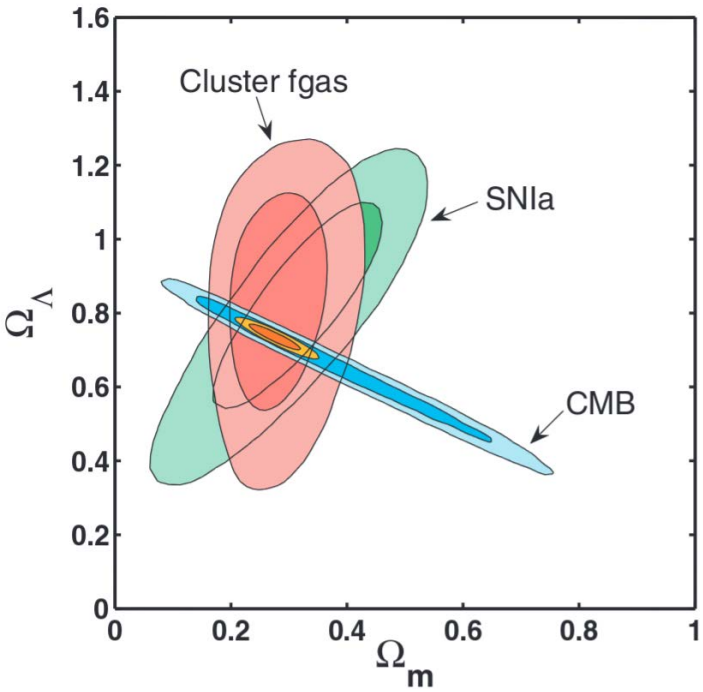

Figure 1.6: Joint 68.3% and 95.4% confidence regions in the (Ω_Λ, Ω_M) plane for the Chandra $f_{\rm gas}$ data at $z < 1.1$ (Allen et al. 2008), compared to those from WMAP-3 CMB data (Spergel et al. 2007) and SNIa (Davis et al. 2007). The inner gold contours show results from the combination of these data.

An important limitation of this method is the high scatter in the gas and total mass estimates. As for cluster counts, it is preferable to estimate the total mass from lensing analysis (e.g. Allen et al. 2013; Mantz et al. 2014), as lensing does not depend on the cluster hydrodynamical equilibrium. Accurate redshifts of galaxy clusters are also required. Finally, one needs to consider a very large number of clusters, due to the large scatter of the gas fraction, to have a statistical estimate of it at every redshift.

Even if our study of the fraction of baryons is more oriented towards a comparison between groups and clusters, we draw such constraints and present them in part 2.2.

Weak lensing tomography with clusters

Weak Lensing Tomography with Clusters (WLTC) has first been introduced by Jain & Taylor (2003). The main idea is that the shear ratio of background populations at the same angular distance from the cluster center only depends on the distances of the different elements of the system. Refer to Sect. 3.1 for insights in the weak lensing theory. In the case of galaxy clusters, the galaxies of which lie at the same redshift, the average

tangential shear induced on background galaxies, noted γ, can be written as the product of a function of angular distance θ and a function of comoving distances (eq. 1.13):

$$\gamma(\theta, z) = \gamma(\theta, \infty) g(z), \tag{1.13}$$

where $g(z)$ is the ratio of the distance of the lens to the sources ($D_{\rm ls}$) over the distance to the sources ($D_{\rm s}$):

$$g(z) = \frac{D_{\rm ls}}{D_{\rm s}} = \frac{\chi_{\rm s} - \chi_{\rm l}}{\chi_{\rm s}}, \tag{1.14}$$

where χ denotes the comoving distance, which depends on cosmology through eq. 1.9. $\gamma(\theta, \infty)$ vanishes for a ratio of galaxy populations at the same angular distance from the lens position, but at different redshift. The shear ratio at the same angular distance thus only depends on comoving distances as shown in eq. 1.15:

$$\frac{\gamma(\theta, z_1)}{\gamma(\theta, z_2)} = \frac{(\chi_{\rm s1} - \chi_{\rm l})/\chi_{\rm s1}}{(\chi_{\rm s2} - \chi_{\rm l})/\chi_{\rm s2}} \tag{1.15}$$

Weak lensing tomography with clusters thus provides a geometrical measure of distance ratios, and then of cosmology. This dependence only on a geometrical measurement (the shear of background galaxies) makes it a very clean cosmological probe. However, one needs to measure the shape and redshift of background galaxies with a sufficient accuracy to be able to constrain our cosmological model. Systematic biases in these measurements are discussed in Sect. 1.3.1, as the DAFT/FADA survey has been carried out with the aim of applying WLTC to observational data.

1.3 The DAFT/FADA survey

1.3.1 Goals and data

The DAFT/FADA survey (Dark energy American French Team, in French FADA) is a galaxy cluster survey encompassing $\sim$ 90 high-redshift ($0.4 \leq z \leq 0.9$) massive ($M \geq 2 \times 10^{14}$ $M_\odot$) clusters of galaxies with Hubble Space Telescope (HST) imaging available. The project has been granted about 70 nights of telescope time since 2009, mainly for deep optical and infrared imaging, on various 4m class telescopes, to build a ground based follow up in BVRIZ optical and J near-infrared bands. The status of the survey can be found at: http://cencosw.oamp.fr/DAFT/project.php, and we now have complete data for a large number of clusters. DAFT/FADA has been built with the main goal of applying WLTC, a technique described in Sect. 1.2.2, and to serve as a test study for this new probe. The HST images are used for the shear analysis while photometric redshifts are computed from the ground based multi-band data. We also gathered spectroscopic measurements of at least 15 galaxies per field to train the photometric redshift software. Finally, about half of the sample is covered by X-ray observations, in majority *XMM*–Newton, but also *Chandra*.

However, the systematics in the shear and photometric measurements in the DAFT/FADA survey do not allow to constrain the DE equation of state to an interesting accuracy. This is due to the very small variation of the shear ratio with cosmology.

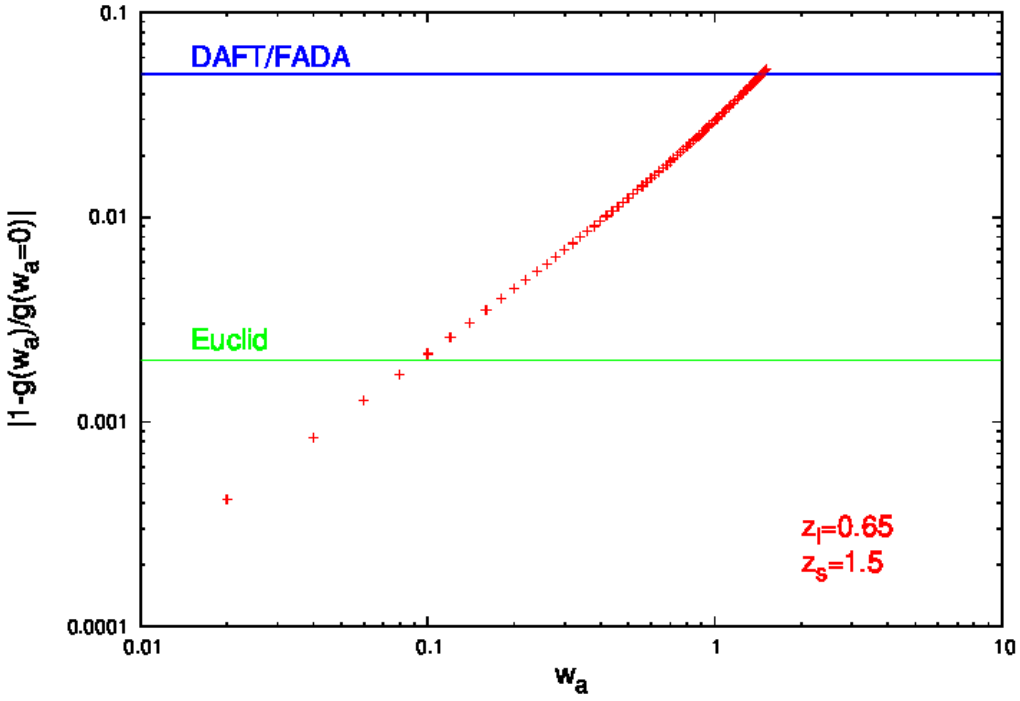

Figure 1.7: Variation of the distance ratio $g = (\chi_s - \chi_l)/\chi_s$ with the DE equation of state parameter w_a. The ordinate is an estimate of the required accuracy to probe the corresponding w_a departure from ΛCDM with WLTC. The blue line corresponds to the shear and photometric redshift accuracy of the DAFT/FADA survey and the green line to the expected accuracy of *Euclid*.

We see in eq. 1.15 that one can estimate a ratio of comoving distances, which depends on cosmology, by only measuring the shape and photometric redshift of background galaxies. The requirement on the accuracy of both measurements is set by the variation of the comoving distance ratio $g(z)$ with cosmology. As the parameter we wish to constrain with the DAFT/FADA survey is the DE equation of state, we rewrite the comoving distance of eq. 1.9 in eq. 1.16 (Linder 2003):

$$\chi(z) = \frac{c}{H_0} \int \frac{dz}{\sqrt{\Omega_M (1+z)^3 + (1-\Omega_M)(1+z)^{3(1+w_0+w_a)} e^{-3w_a z/(1+z)}}}, \tag{1.16}$$

where we introduced the DE equation of state $w = w_0 + w_a(1-a)$, and assumed a flat Universe, with a negligible radiation density parameter, such that $\Omega_R = 0$, $\Omega_K = 0$, and $\Omega_\Lambda = 1 - \Omega_M$. We can now compute the variation of the distance ratio for various values of w_a and compare it to a Universe with non dynamical DE (i.e. $w_a = 0$). This is what is done in Fig. 1.7, where we chose a lens redshift of $z_l = 0.65$ and a source mean redshift of $z_s = 1.5$, which are representative of the DAFT/FADA survey. The variation of the distance ratio $1 - g(w_a)/g(w_a = 0)$ gives an estimate of the required accuracy on both shear and photometric measurements to probe the corresponding departure from ΛCDM: w_a. Our results are compatible with those from Bernstein & Jain (2004) who investigated the required accuracy for probing $w_a = 0.2$. After analyzing a subsample of

the DAFT/FADA survey, we found an accuracy of $\sim 5\%$ on both photometric redshifts (Martinet et al. 2015) and shear (Martinet et al. 2015, A&A submitted). We also plot the value of 0.2% expected for *Euclid* as a comparison. Unfortunately, we see that the systematic errors on redshift and shear in DAFT/FADA only allow us to measure deviation from ΛCDM if $w_a > 1$. With Euclid this should be $w_a > 0.1$, an accuracy more compatible with the present one from Planck: ~ 0.13.

Besides WLTC, the DAFT/FADA project forms a comprehensive database to study clusters and their evolution at $0.4 < z < 0.9$, and this second goal has driven most of the science made with the survey.

1.3.2 Previous results

In addition to the first DAFT/FADA paper establishing the reference basis for the photometric redshift (hereafter photo$-z$) determination (Guennou et al. 2010), results concerning several topics have been obtained by the DAFT/FADA team. Guennou et al. (2012) showed that by stacking data for different clusters it is possible to detect intracluster light (ICL) in the redshift interval $0.4 < z < 0.8$, and that there appears to be no variation in the amount of ICL between $z = 0$ and $z = 0.8$. Guennou et al. (2014a) analyzed the XMM-Newton data available for 42 DAFT/FADA clusters to derive their X-ray luminosities and temperatures, and search for substructures. This study was coupled with dynamical analyses of the 26 clusters with at least 30 spectroscopic redshifts close to the cluster redshift. An interesting result is that the percentage of mass in substructures seems constant with redshift up to $z \sim 0.9$, i.e. just after the completion of the initial cluster building period (see e.g. Ulmer et al. 2009). Using three different methods, Guennou et al. (2014b) determined the mass profile and dynamical status of the z$\sim$0.8 LCDCS 0504 cluster of galaxies characterized by prominent giant gravitational arcs near its center and found differences that may be explained when we analyze a larger sample of DAFT/FADA clusters. Murphy et al. (2014) performed a weak lensing analysis of HST Advanced Camera for Surveys (ACS) mosaic imaging data of ten massive, high-redshift ($z > 0.5$) DAFT/FADA galaxy clusters, made two dimensional surface mass reconstructions, and explored the use of photo$-z$s for background galaxy discrimination.

During my PhD thesis, in addition to participating in the DAFT/FADA paper on substructures (details of my contribution can be found in Appendix A.3), I developed two new projects within the survey. The first one is the study of the galaxy luminosity functions of 31 clusters, using photometric redshifts to assess cluster membership, and separating galaxy populations based on a color criterion. This paper is presented in Sect. 2.1, and refered to as Martinet et al. (2015). The second topic is the cluster mass estimate, and search for filaments with a weak lensing analysis of large field of view images for 16 clusters. This work is reviewed in Sect. 3.2: Martinet et al. (2015, A&A submitted).

Chapter 2

Galaxy magnitudes

This chapter encompasses studies made during the thesis, and based on the galaxy magnitude observable. We first review work that has been done on galaxy luminosity functions in DAFT/FADA medium-high redshift clusters (Sect. 2.1), and then on the fraction of baryons in nearby groups and clusters of galaxies (Sect. 2.2).

2.1 Galaxy luminosity functions

This section presents the results from Martinet et al. (2015): *The evolution of the cluster optical galaxy luminosity function between z=0.4 and 0.9 in the DAFT/FADA survey.* The first subsection briefly summarizes the paper, its context, aims, methods, results, and conclusions. The detailed study can be read in the second subsection, where we display the article.

2.1.1 Summary

Context

There is some disagreement about the abundance of faint galaxies in high-redshift clusters, with contradictory results in the literature arising from studies of the optical GLF for small cluster samples. The GLF is defined as the distribution of galaxies with magnitude and can be studied in different environments. In clusters, some authors find a decreasing faint end at high redshifts, while others find no evolution between $z \sim 1$ and today. Figure 2.1 shows an example of the two behaviors on GLFs represented by Rudnick et al. (2009) for the evolutionary scenario and by De Propris et al. (2013) for the no-evolution scheme. The importance of this debate arises from the fact that in the first case clusters still evolve from high redshift until today, while in the second cluster galaxy populations are frozen at $z \sim 1$.

Aims

We compute GLFs for one of the largest medium-to-high-redshift ($0.4 \leq z < 0.9$) cluster samples to date in order to probe the abundance of faint galaxies in clusters. We also study how the GLF depends on cluster redshift, mass, and substructure and compare the

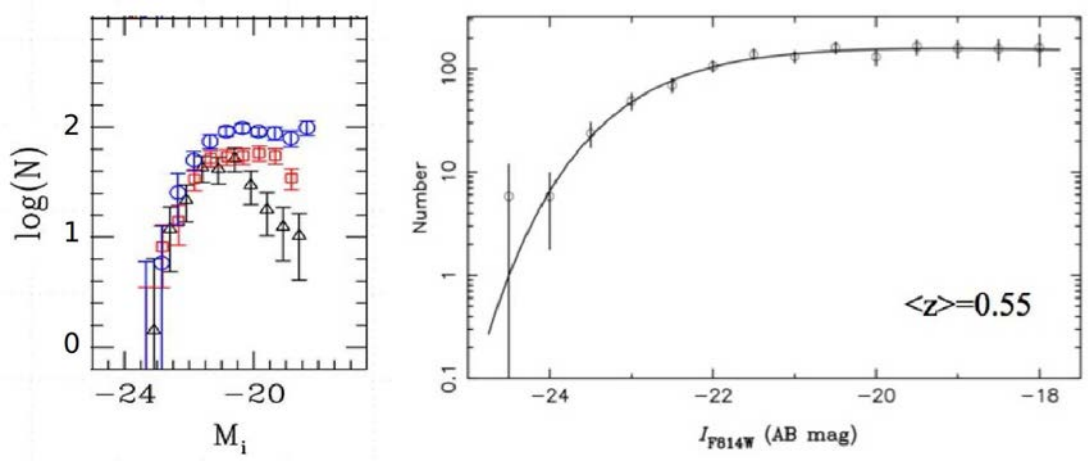

Figure 2.1: The different results for the I band GLF at high redshifts. *Left:* An example where the GLF faint end shows a drop at high redshifts (Rudnick et al. 2009). Blue circles represent SDSS clusters ($z \sim 0.1$), red squares the EDisCS clusters at $0.4 < z < 0.6$ and black triangles at $0.6 < z < 0.8$. *Right:* An example where the GLF faint end shows no evolution at high redshifts (De Propris et al. 2013).

GLFs of clusters with those of the field. We separately investigate the GLFs of blue and red-sequence (RS) galaxies to understand the evolution of different cluster populations.

Methods

We calculated the GLFs for 31 clusters taken from the DAFT/FADA survey in the B, V, R, and I rest-frame bands.

We used photometric redshifts computed from BVRIZJ images to constrain galaxy cluster membership. Photometric redshifts are estimated from interpolating the spectrum of a galaxy from its magnitudes in several bands. Figure 2.2 shows how a typical galaxy spectrum appears at different redshifts, and how it will be covered by the SDSS optical filters. We compute photometric redshifts using the LePhare software (Arnouts et al. 1999; Ilbert et al. 2006) which compares the measured set of magnitudes to a library of spectral energy distributions (SED), determining the most probable redshift. Once galaxies at redshifts close to that of the cluster are selected, we remove background galaxies in a statistical way, using background counts from COSMOS (Ilbert et al. 2009).

We carried out a detailed estimate of the completeness of our data. This step is important not to consider magnitude bins where no galaxies are detected, not because they do not exist, but because data are not deep enough. We distinguished the red-sequence and blue galaxies using a V-I versus I color-magnitude diagram. We studied the evolution of these two populations with redshift. We fitted Schechter functions (Schechter 1976) to our stacked GLFs to determine average cluster characteristics. We then discuss the faint end of the GLF according to the slope α in the Schechter function. $\alpha = -1$ corresponds to a flat slope, while $\alpha < -1$ and $\alpha > -1$ respectively correspond to an increasing and a decreasing slope.

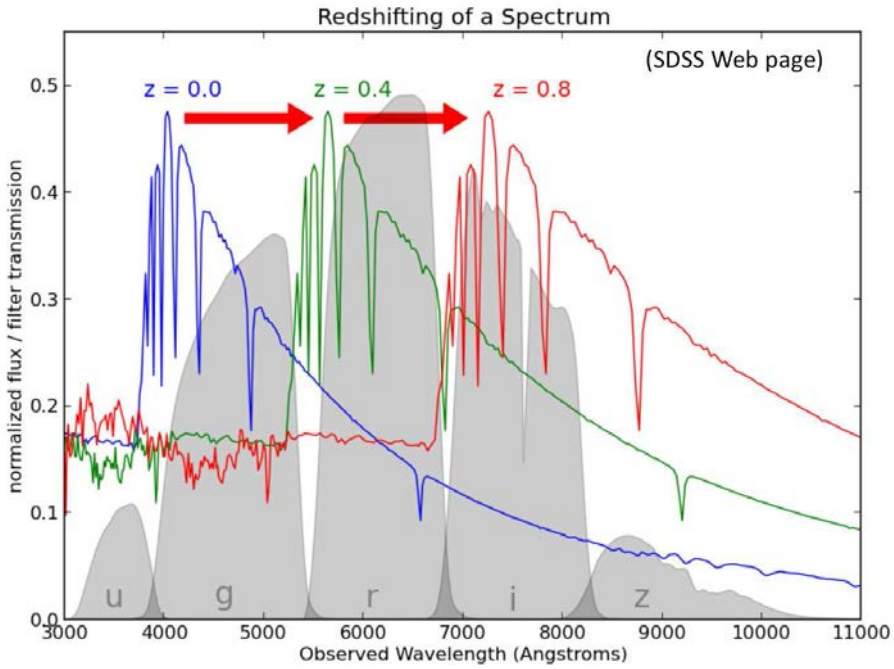

Figure 2.2: Principle of photometric redshifts. The spectrum of a galaxy is interpolated through its observation in several broad band filters. See text for details. Image taken from the SDSS website.

Results

We find that the shapes of our GLFs are similar for the B, V, R, and I bands with a drop at the GLF faint ends of red galaxies, that is more pronounced at high redshift: $\alpha_{\rm red} \sim -0.5$ at $0.40 \leq z < 0.65$ and $\alpha_{\rm red} > 0.1$ at $0.65 \leq z < 0.90$. The GLFs of blue galaxies have a steeper faint end ($\alpha_{\rm blue} \sim -1.6$) than the red GLFs, which appears to be independent of redshift. For the full cluster sample, blue and red GLFs meet at $M_V = -20$, $M_R = -20.5$, and $M_I = -20.3$. We also found an excess of red galaxies in clusters compared to the field, while blue galaxies have more or less identical GLFs. A study of how galaxy types evolve with redshift shows that a large fraction of late-type galaxies appear to become early types between $z \sim 0.9$ and today. Finally, the faint ends of the red GLFs of more massive clusters appear to be richer than less massive clusters, which is more typical of the lower redshift behavior.

Conclusions

Our results indicate that these clusters form at redshifts higher than $z = 0.9$ from galaxy structures that already have an established red sequence. Late-type galaxies then appear to evolve into early types, enriching the red sequence between this redshift and today. This effect is consistent with the evolution of the faint-end slope of the red sequence and the galaxy type evolution that we find. Finally, faint galaxies accreted from the field environment at all redshifts might have replaced the blue late-type galaxies that converted into early types, explaining the lack of evolution in the faint-end slopes of the blue GLFs.

2.1.2 Martinet et al. 2015a

A&A 575, A116 (2015)
DOI: 10.1051/0004-6361/201423796

Astronomy & Astrophysics

The evolution of the cluster optical galaxy luminosity function between z = 0.4 and 0.9 in the DAFT/FADA survey⋆

Nicolas Martinet[1], Florence Durret[1], Lo c Guennou[2,3], Christophe Adami[3], Andrea Biviano[4,1], Melville P. Ulmer[5], Douglas Clowe[6], Claire Halliday[7], Olivier Ilbert[3], Isabel M rquez[8], and Mischa Schirmer[9,10]

[1] UPMC Universit Paris 06, UMR 7095, Institut d'Astrophysique de Paris, 98bis Bd Arago, 75014 Paris, France
e-mail: martinet@iap.fr
[2] Astrophysics and Cosmology Research Unit, University of KwaZulu-Natal, 4041 Durban, South Africa
[3] LAM, OAMP, Universit Aix-Marseille & CNRS, P le de l' toile, Site de Ch teau Gombert, 38 rue Fr d ric Joliot-Curie, 13388 Marseille 13 Cedex, France
[4] INAF/Osservatorio Astronomico di Trieste, via Tiepolo 11, 34143 Trieste, Italy
[5] Dept of Physics and Astronomy & centre for Interdisciplinary Exploration and Research in Astrophysics (CIERA), Northwestern University, Evanston, IL 60208-2900, USA
[6] Department of Physics and Astronomy, Ohio University, 251B Clippinger Lab, Athens, OH 45701, USA
[7] 23 rue d'Yerres, 91230 Montgeron, France
[8] Instituto de Astrof sica de Andaluc a, CSIC, Glorieta de la Astronom a s/n, 18008 Granada, Spain
[9] Gemini Observatory, Casilla 603, La Serena, Chile
[10] Argelander-Institut f r Astronomie, Universit t Bonn, Auf dem H gel 71, 53121 Bonn, Germany

Received 12 March 2014 / Accepted 17 December 2014

ABSTRACT

Context. There is some disagreement about the abundance of faint galaxies in high-redshift clusters, with contradictory results in the literature arising from studies of the optical galaxy luminosity function (GLF) for small cluster samples.
Aims. We compute GLFs for one of the largest medium-to-high-redshift ($0.4 \leq z < 0.9$) cluster samples to date in order to probe the abundance of faint galaxies in clusters. We also study how the GLF depends on cluster redshift, mass, and substructure and compare the GLFs of clusters with those of the field. We separately investigate the GLFs of blue and red-sequence (RS) galaxies to understand the evolution of different cluster populations.
Methods. We calculated the GLFs for 31 clusters taken from the DAFT/FADA survey in the B, V, R, and I rest-frame bands. We used photometric redshifts computed from $BVRIZJ$ images to constrain galaxy cluster membership. We carried out a detailed estimate of the completeness of our data. We distinguished the red-sequence and blue galaxies using a $V - I$ versus I colour–magnitude diagram. We studied the evolution of these two populations with redshift. We fitted Schechter functions to our stacked GLFs to determine average cluster characteristics.
Results. We find that the shapes of our GLFs are similar for the B, V, R, and I bands with a drop at the red GLF faint ends that is more pronounced at high redshift: $\alpha_{\rm red} \sim -0.5$ at $0.40 \leq z < 0.65$ and $\alpha_{\rm red} > 0.1$ at $0.65 \leq z < 0.90$. The blue GLFs have a steeper faint end ($\alpha_{\rm blue} \sim -1.6$) than the red GLFs, which appears to be independent of redshift. For the full cluster sample, blue and red GLFs meet at $M_V = -20$, $M_R = -20.5$, and $M_I = -20.3$. A study of how galaxy types evolve with redshift shows that late-type galaxies appear to become early types between $z \sim 0.9$ and today. Finally, the faint ends of the red GLFs of more massive clusters appear to be richer than less massive clusters, which is more typical of the lower redshift behaviour.
Conclusions. Our results indicate that these clusters form at redshifts higher than $z = 0.9$ from galaxy structures that already have an established red sequence. Late-type galaxies then appear to evolve into early types, enriching the red sequence between this redshift and today. This effect is consistent with the evolution of the faint-end slope of the red sequence and the galaxy type evolution that we find. Finally, faint galaxies accreted from the field environment at all redshifts might have replaced the blue late-type galaxies that converted into early types, explaining the lack of evolution in the faint-end slopes of the blue GLFs.

Key words. galaxies: clusters: general – galaxies: evolution – galaxies: formation – galaxies: luminosity function, mass function

1. Introduction

It is widely accepted that cluster elliptical galaxies are a passively evolving population formed at high redshift ($z > 1$) in a short duration event (e.g. De Propris et al. 1999, 2007, 2013; De Lucia et al. 2004, 2007; Andreon 2006; Muzzin et al. 2008; Mancone et al. 2010, 2012). This scenario is strongly supported by the lack of evolution in the colour–magnitude relation for the bright galaxies in clusters from $z = 1$ to $z = 0$ (e.g. De Lucia et al. 2004). However, there is still a strong debate about whether cluster galaxies migrated from the field to clusters at lower redshift ($z \sim 0.8$; e.g. De Lucia et al. 2004, 2007; Poggianti et al. 2006) or if they joined clusters at higher redshift or still even originally formed in clusters. This debate arises from the different behaviours of the faint-end slope of galaxy luminosity functions (GLFs) observed at high z. At low z, cluster GLFs mainly have flat faint ends populated by low mass galaxies (e.g. Secker et al. 1997; Rudnick et al. 2009). We note that Popesso et al. (2006) find an upturn of the very faint population of the GLF for $M_{\rm g}^* > -18$ in nearby clusters, but our data are not deep enough to investigate this population of dwarf galaxies at high redshift.

⋆ Appendix is available in electronic form at http://www.aanda.org

The faint end of GLFs is found to either decrease with increasing redshift (e.g. Smail et al. 1998; De Lucia et al. 2004, 2007; Tanaka et al. 2005; Stott et al. 2007; Gilbank et al. 2008; Rudnick et al. 2009; Vulcani et al. 2011) or remain constant with redshift (e.g. De Propris et al. 2003, 2007, 2013; Andreon 2006). The first type of behaviour is the most commonly observed, but the cold dark matter scenario predicts a larger number of low mass galaxies (Andreon et al. 2006; Rudnick et al. 2009). Thus, additional processes are often invoked within clusters, such as ram pressure stripping (Gunn & Gott 1972) and harassment (e.g. Moore et al. 1996, 1998). These processes are found to weakly affect the results in the simulation of Lanzoni et al. (2005) and are likely to depend on mass (Muzzin et al. 2008). The study of the abundance of faint galaxies at high redshift is the main objective of this paper.

We also investigate whether GLFs are universal or depend on environment. This can help us determine whether the red cluster galaxy population originates in the field at higher redshift. Many studies find a universal GLF that does not depend on environment (Lugger 1986, 1989; Colless 1989; Gaidos 1997; Rauzy et al. 1998; Trentham 1998; Paolillo et al. 2001; Yagi et al. 2002; Andreon 2004), while others (Dressler 1978; Lopez-Cruz et al. 1997; Lumsden et al. 1997; Valotto et al. 1997; Driver et al. 1998a; Garilli et al. 1999; Goto et al. 2002; De Propris et al. 2003; Christlein & Zabludoff 2003; Popesso et al. 2006; Muzzin et al. 2008; Rudnick et al. 2009) observe differences between clusters and field GLFs. The most widely observed trend is a flattening of the GLF as the environment becomes less dense (see e.g. De Propris et al. 2003 for observations and Lanzoni et al. 2005 for simulations). This behaviour could be explained by either star formation being inhibited in dense environments (Tully et al. 2002; De Propris et al. 2003; Muzzin et al. 2008) or merging processes being more common in the field where the relative velocities of galaxies are lower (Menci et al. 2002). This last explanation does not apply to single objects falling onto groups of galaxies, which can trigger large amounts of star formation (e.g. Adami et al. 2009). In addition, we note that Ilbert et al. (2005) find a steepening of the faint end of the field GLF with increasing redshift such that they do not see the usual flattening of the field GLF at high redshift.

Additional support for the GLF dependence on the environment is the perturbation of the GLF caused by cluster merging (e.g. Durret et al. 2010). Finally, De Propris et al. (2003) and Bou et al. (2008) find different GLFs for cluster cores and outskirts. The first authors find an excess of bright galaxies in cluster cores and the second a steeper faint end in the outskirts.

The Dark energy American French Team (DAFT, in French FADA) survey is ideal for investigating the faint end of the GLF and field to cluster differences at relatively high redshift. The DAFT/FADA survey encompasses ~90 high-redshift ($0.4 \leq z \leq 0.9$) massive ($M \geq 2{\times}10^{14}\ M_{\odot}$) clusters of galaxies with *Hubble* Space Telescope (HST) imaging available, and multi-band optical and near infrared ground based imaging, using 4 m class telescopes, which is now almost complete. The main goals of the survey are to form a comprehensive database to study clusters and their evolution, and to test cosmological constraints geometrically by means of weak lensing tomography. In addition to the first DAFT/FADA paper establishing the reference basis for the photometric redshift (hereafter photo-z) determination (Guennou et al. 2010, hereafter G10), results concerning several topics have been obtained by the DAFT/FADA team[1].

[1] The current status of the survey, with a list of refereed publications, can be found at http://cesam.lam.fr/DAFT/project.php

An outline of the paper is as follows; we first present the photo-z measurements and the improvements that we have made since G10. We then describe our method for computing GLFs. We present the optical GLFs for 31 clusters of the DAFT/FADA survey in the $0.4 \leq z < 0.9$ redshift range for the B, V, R, and I rest-frame bands. The cluster membership of galaxies is based on photo-zs computed with U or B, V, R, I, Z, and J or Ks band data and a field subtraction. We take special care to estimate the completeness of our data, and we show that the GLFs are strongly correlated to the 90% completeness limit. We investigate average cluster behaviours by stacking them and discuss the dependence of GLFs on cluster redshifts, masses, and substructures. We compare the GLF behaviour in the cluster core and outskirts. We also separate blue and red-sequence galaxies to investigate the evolution of different cluster galaxy populations. Finally, we compare our cluster GLFs to the field GLFs computed with COSMOS data (Ilbert et al. 2009) made in the same redshift intervals. We discuss our results in light of the literature. Throughout the paper, we use the standard cosmological model with $\Omega_{\rm M} = 0.3$, $\Omega_{\Lambda} = 0.7$, and $H_0 = 70$ km Mpc^{-1} s^{-1}.

2. Photometric redshifts

2.1. Context

We measure our photo-zs as in G10, with the LePhare package (e.g. Arnouts et al. 1999; Ilbert et al. 2006a,b). We refer the reader to these papers for details but we provide here the salient points of the technique. The aim of the method is to compare observed magnitudes with predicted ones created by templates, in order to estimate the redshift and other parameters such as the photometric type. This type varies between 1 and 31 with the chosen templates (see below). Numbers 1–7 correspond to early-type galaxies, numbers 8–12 to early spiral galaxies, numbers 13–19 to late spiral galaxies, and numbers 20–31 to very blue galaxies. The last category corresponds to very blue templates which have been generated to compensate for the lack of very blue templates in Polletta et al. (2006, 2007).

In a similar way to G10, we select spectral energy distributions (hereafter SEDs) with emission lines from Polletta et al. (2006, 2007), with a Calzetti et al. extinction law (e.g. Calzetti & Heckman 1999) applied to different galaxy classes (see below).

The available spectroscopic redshift catalogues are another important ingredient (as in G10) of our calculations. As LePhare is able to estimate possible shifts in photometric zero points by comparing photometric and spectroscopic redshifts (used as training sets), this allows us to compensate for the various origins of our ground-based images. We collected spectroscopic catalogues for all clusters in the present paper.

2.1.1. Input magnitudes

The first difference from G10 is the photometric bands that we used. As already demonstrated, having near infrared bands is mandatory to obtain a robust estimate of photo-zs at $z \geq 1$. In G10, we used space based IRAC data in the infrared. We did not do so in the present paper for the following reasons:

- These data are unavailable for the entire sample presented here.
- The angular resolution of IRAC is very poor compared to regular ground based data (typically 4 times worse) and this forced us in G10 to estimate correcting factors in order not

to be biased. These factors were typically up to 1.5 mag for small objects.
– Another problem is the small angular extent of our clusters, for which typical galaxy-galaxy separations are often smaller than the IRAC spatial resolution, leading to considerable confusion in the central parts of clusters.
– The IRAC bands are very red (3.6 and 4.5 μm) compared to the reddest optical ground based images at our disposal (typically the z' band at 0.9 μm), leading to a large wavelength gap, and making constraints on redshifts rather poor.

Here, we choose to use J and/or K band data instead of IRAC data. The typical seeings vary between 0.7 and 1.2 arcsec. Simulations similar to the ones we performed in G10 (see their Fig. 9) show that the shifts induced by the different spatial resolutions will be of the order of 0.1 to 0.2 mag, which can be easily compensated for by the capacity of LePhare to adapt the photometric zero points when spectroscopic redshift catalogues are available.

2.1.2. Image registration

Our data reduction procedure uses the Scamp and Swarp packages (Bertin et al. 2002; Bertin 2006) and is identical to that in G10. We produce calibrated median images with cosmic rays and other image defects removed.

The second difference from G10 resides in the image registration between different bands. In G10, we considered data acquired by only three different instruments (IRAC, ESO/FORS2, and CTIO/MOSAIC). It was therefore possible to align precisely all the images and to extract magnitude catalogues with SExtractor (Bertin & Arnouts 1996) in double-image mode.

In the present paper, we consider more than three times as many clusters (31 clusters, compared to 10 in G10) for which we collected near infrared data, in addition to optical band data. Owing to the relatively deep nature of our catalogues (with a typical 90% completeness limit of $I \sim 24$ for stellar objects), this represents a large survey, gathering about 350 h of observations in both hemispheres on 4 m class telescopes. Given also that we used all possible images available in public databases to minimize the amount of new data to be acquired, our project involves a wide range of very different ground-based data: we use data obtained with about 10 different telescopes and more than 12 different cameras (see Table 1). Although we reduced all the data from its raw form to ensure that the final imaging products are as homogeneous as possible, it is impossible to always have image astrometry more precise than 0.5 arcsec everywhere in the fields. Our final images are sometimes still plagued by high frequency astrometric differences of this order. As an example, we show in Fig. 1 the astrometric diagrams for CL J0152.7-1357, for which we collected B, V, R, i', z', and Ks data at SOAR (SOI), Subaru (Suprime), and ESO (HawkI). We see that for a non negligible number of objects, the astrometric shift is larger than 0.5 arcsec. However, the astrometry of sources in the data of CL J0152.7-1357 is among the poorest of all our collated data.

2.1.3. Magnitude homogenization

As already mentioned, we have very different sources for our images, in contrast to G10. It is obviously uninteresting to compute GLFs in several bands that vary from one cluster to another. We therefore choose to take advantage of our spectroscopic catalogues and the ability of LePhare to compute magnitude zero-point shifts. This allows us to convert our various magnitudes homogeneously into a single system (the *common system* in

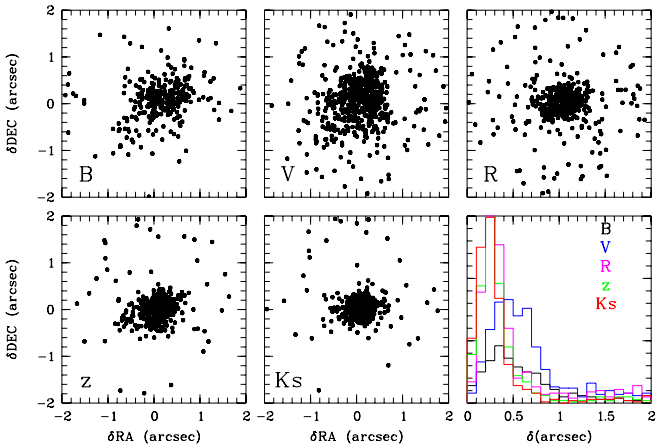

Fig. 1. Astrometric shifts (α, δ) for CL J0152.7-1357 between the objects detected in the i' band and the B, V, R, z', and Ks bands. The figure at the lower right shows the histograms of the shifts between the i' band and the other bands.

the following) that we choose to be VLT/FORS2 B, V, R, I, z' (AB system), and VLT/HawkI J or Ks band (Vega system). These filter shifts are applied after the completion of the photo-z calculations.

We therefore classify our images into several general classes. All U- and B-like magnitudes are translated into VLT/FORS2 B, all V- and g'-like magnitudes into VLT/FORS2 V, all R- and r'-like magnitudes into VLT/FORS2 R, all I- and i'-like magnitudes into VLT/FORS2 I, all z'-like magnitudes into VLT/FORS2 z', all J-like magnitudes into VLT/HawkI J band, and all Ks-like magnitudes into VLT/HawkI Ks band. In the particular case of Abell 851, we also consider the CFHT/WIRCAM Y and H bands directly.

Since we cannot use SExtractor in double image mode here, we choose to apply it in single image mode, computing total magnitudes (MAG_AUTO) in each of the considered bands. We then cross-correlate the different catalogues to generate a final catalogue including all magnitudes for all objects, with an identification distance of 2 arcsec and a minimization of this distance when several objects are within the same radius. This is almost twice the maximum astrometric difference observed between the different bands. We checked that the results obtained with this correlation method do not differ considerably from those of a double image mode detection by comparing the results of both methods for clusters with imaging of good astrometry acquired with the same camera in the 5 optical bands. Both methods agree well except for very faint galaxies, which are detected in larger numbers in double image mode owing to the use of the deepest band (the i band) as the reference detection image for the double image mode. However, this only concerns objects far below the completeness limit of our images. In some cases, there is also a small difference at the bright end of the magnitude distribution because of foreground objects larger than our 2 arcsec criterion.

We also varied the MAG_AUTO minimum aperture radius from 3.5 to 1.5 pixels to verify that we were not missing light in faint objects, as explained in Rudnick et al. (2009). We did not find any significant variation in the magnitude distribution between these two radii.

2.2. Optimization and estimate of the LePhare performances

2.2.1. Zero-point shifts

We entered catalogues of galaxy spectroscopic redshifts into LePhare to correct for small zero-point variations and

Table 1. Data used in our present study.

Cluster	RA	Dec	z	U/B	V	R	I	Z	J/Ks	LF
CL_0016+1609	00 18 33.33	+16 26 35.84	0.5455	WIYN/M B (O)	WIYN/M V (O)	WIYN/M r' (O)	WIYN/M i' (O)	WIYN/M z' (O)	Subaru/M Ks (A)	Y
CL_J0152.7-1357	01 52 40.99	−13 57 45.00	0.8310	SOAR/S B (O)	Subaru/S V (A)	Subaru/S R (A)	SOAR/S I (O)	Subaru/S z' (A)	ESO/H Ks (A)	N
PDCS_018	02 27 25.50	+00 40 04.00	0.4000	CFHT/M u (A)	CFHT/M g' (A)	SOAR/S r' (O)	CFHT/M i' (A)	CFHT/M z' (O)	CFHT/W J (O)	Y
XDCS_cm_J032903.1	03 29 02.81	+02 56 25.18	0.4122	CFHT/M u (A)	CFHT/M g' (A)	CFHT/M r' (A)	SOAR/S i' (O)	SOAR/S z' (O)	CFHT/W J (O)	Y
F1557.19TC	04 12 54.69	−65 50 57.58	0.5100	VLT/F2 B (A)	VLT/F2 V (A)	VLT/F2 R (A)	VLT/F2 I (A)	SOAR/S z' (O)	ESO/H Ks (A)	N
MACS-J0454.1-0300	04 54 10.92	−03 01 07.14	0.5377	VLT/F2 U (A)	VLT/F2 V (A)	VLT/F2 R (A)	VLT/F2 I (A)	Subaru/S z' (A)	ESO/H Ks (A)	Y
MACS_J0647.7+7015	06 47 45.89	+70 15 02.98	0.5907	WIYN/M B (O)	WIYN/M V (O)	WIYN/M R (O)	WIYN/M I (O)	WIYN/M z' (O)	TNG/N J (O)	N
MACS_J0744.9+3927	07 44 51.79	+39 27 33.01	0.6860	WIYN/M B (O)	WIYN/M V (O)	WIYN/M R (O)	WIYN/M I (O)	WIYN/M z' (O)	Subaru/M J (A)	N
RX_J0848.8+4455	08 48 49.30	+44 55 45.98	0.5430	Subaru/S B (A)	Subaru/S V (A)	Subaru/S R (A)	Subaru/S I (A)	Subaru/S z' (A)	MDM/R Y (O)	Y
ABELL_0851	09 42 56.64	+46 59 21.91	0.4069	CFHT/M u (A)	CFHT/M g' (A)	CFHT/M r' (A)	CFHT/M i' (A)	CFHT/M z' (A)	CFHT/W Y (A)	Y
LCDCS_0130	10 40 41.59	−11 55 50.98	0.7043	CTIO/M B (O)	VLT/F2 V (A)	VLT/F2 R (A)	VLT/F2 I (A)	VLT/F2 z' (A)	ESO/H Ks (A)	Y
SEXCLAS_12	10 52 38.20	+57 30 49.28	0.6100	WIYN/M B (O)*	WIYN/M V (O)*	WIYN/M R (O)*	WIYN/M I (O)*	CFHT/M z' (O)	MDM/R Y (O)	N
LCDCS_0173	10 54 43.50	−12 45 50.00	0.7498	CTIO/M B (O)	VLT/F2 V (A)	VLT/F2 R (A)	VLT/F2 I (A)	VLT/F2 z' (A)	ESO/H Ks (A)	Y
MS_1054-03	10 57 00.22	−03 37 27.40	0.8231	VLT/F1 B (A)	VLT/F1 V (A)	VLT/F2 R (A)	VLT/F2 I (A)	GTC/O z'(O)	ESO/H J (A)	Y
RXC_J1206.2-0848	12 06 11.97	−08 48 00.03	0.4400	Subaru/S B (A)	VLT/F1 V (A)	CFHT/M r' (A)	Subaru/S I (A)	VLT/F2 z' (O)	TNG/N J (O)	Y
LCDCS_0504	12 16 45.10	−12 01 17.00	0.7943	CTIO/M B (O)	VLT/F2 V (A)	VLT/F2 R (A)	VLT/F2 I (A)	VLT/F2 z' (A)	ESO/H J (A)	Y
BMW-HRI_J122657.3	12 26 58.00	+33 32 54.09	0.8900	Subaru/S B (A)	Subaru/S V (A)	Subaru/S R (A)	Subaru/S I (A)	Subaru/S z' (A)	Subaru/M J (A)	Y
LCDCS_0531	12 27 53.89	−11 38 20.00	0.6355	CTIO/M B (O)	VLT/F2 V (A)	VLT/F2 R (A)	VLT/F2 I (A)	VLT/F2 z' (A)	ESO/H Ks (A)	Y
HDF:ClG_J1236+6215	12 37 59.99	+62 15 54.00	0.8500	CFHT/M u (A)	CFHT/C V (A)	Subaru/S R (A)	CFHT/C I (A)	Subaru/S z' (A)	CFHT/W J (A)	Y
MJM98_034	13 35 13.78	+37 48 56.30	0.5950	CFHT/M u (A)	CFHT/M g' (A)	Subaru/S R (A)	CFHT/M i' (A)	Subaru/S z' (A)	CFHT/W J (A)	Y
LCDCS_0829	13 47 31.99	−11 45 42.01	0.4510	VLT/F1 B (A)	VLT/F1 V (A)	VLT/F1 R (A)	VLT/F1 I (A)	CFHT/M z' (A)	CFHT/W J (A)	Y
LCDCS_0853	13 54 09.49	−12 30 59.00	0.7627	CTIO/M B (O)	VLT/F2 V (A)	VLT/F2 R (A)	VLT/F2 I (A)	VLT/F2 z' (A)	ESO/H J (A)	N
3C_295_CLUSTER	14 11 20.15	+52 12 09.03	0.4600	CFHT/M u (A)	CFHT/M g' (A)	CFHT/M r' (A)	CFHT/M i' (A)	CFHT/M z' (A)	CFHT/W J (O)	Y
MACS_J1423.8+2404	14 23 48.29	+24 04 46.99	0.5450	Subaru/S B (A)	Subaru/S V (A)	Subaru/S R (A)	Subaru/S I (A)	Subaru/S z' (A)	CFHT/W Ks (A)	Y
GHO_1601+4253	16 03 13.82	+42 45 36.17	0.5391	Subaru/S B (A)	Subaru/S V (A)	Subaru/S R (A)	Subaru/S I (A)	CFHT/M z' (O)	CFHT/W J (O)	Y
GHO_1602+4312	16 04 25.15	+43 04 52.71	0.8950	Subaru/S B (A)	Subaru/S V (A)	Subaru/S R (A)	Subaru/S I (A)	CFHT/M z' (O)	Subaru/M J (A)	N
MACS_J1621.4+3810	16 21 23.99	+38 10 01.99	0.4650	CFHT/M u (A)	Subaru/S V (A)	Subaru/S R (A)	Subaru/S I (A)	CFHT/M z' (O)	CFHT/W J (O)	Y
MACS_J1621.6+3810	16 21 35.99	+38 10 00.01	0.4610	CFHT/M u (A)	Subaru/S V (A)	Subaru/S R (A)	Subaru/S I (A)	CFHT/M z' (O)	CFHT/W J (O)	Y
MACS_J2129.4-0741	21 29 25.99	−07 41 27.99	0.5889	Subaru/S B (A)	Subaru/S V (A)	SOAR/S r' (O)	SOAR/S i' (O)	SOAR/S z' (O)	CFHT/W Ks (A)	Y
GHO_2143+0408	21 46 04.79	+04 23 18.99	0.5310	WIYN/M B (O)	WIYN/M V (O)	WIYN/M R (O)	SOAR/S i' (O)	VLT/F2 z' (O)	CFHT/W J (O)	Y
GHO_2155+0334	21 57 55.37	+03 47 51.53	0.4500	VLT/F2 B (O)	VLT/F2 V (O)	VLT/F2 R (O)	VLT/F2 I (O)	SOAR/S z' (O)	CFHT/W J (O)	N

Notes. (O) represents observed data and (A) data taken from archives. A * indicates that the cluster was only partially observed in the field. The last column states whether we were able to calculate a luminosity function. The LCDCS clusters come from Gonzalez et al. (2001). For clarity, we display an abbreviated name of cameras used, such that WIYN/M corresponds to WIYN/MiniMo, SOAR/S to SOAR/SOI, CFHT/M to CFHT/Megacam, CFHT/W to CFHT/WIRCAM, CFHT/C to CFHT/CFH12K, VLT/F1 and VLT/F2 to VLT/FORS1 and VLT/FORS2, Subaru/S to Subaru/SuprimeCam, Subaru/M to Subaru/MOIRCS, CTIO/M to CTIO/MOSAIC, GTC/O to GTC/Osiris, ESO/H to ESO/HawkI TNG/N to TNG/NICS and MDM/R to MDM/Red4K. In addition, clusters XDCS_cm_J032903.1+025640 and BMW-HRI_J122657.3+333253 are respectively abbreviated to XDCS_cm_J032903.1 and BMW-HRI_J122657.3.

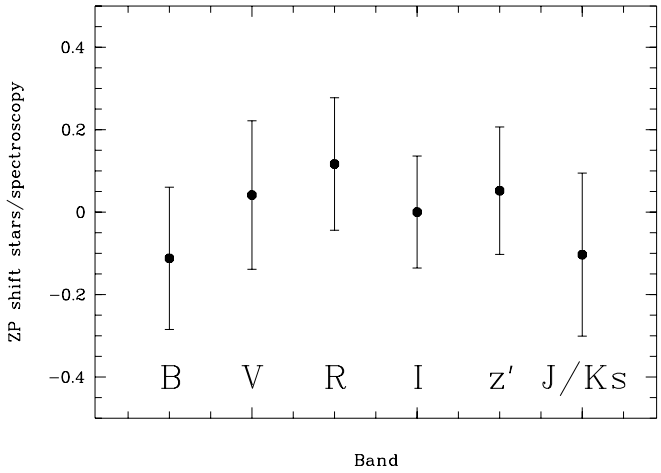

Fig. 2. Mean and uncertainty in the difference between the star and galaxy spectroscopic redshift-based shifts for the different magnitude bands considered over our 31 fields.

compute zero-point shifts when computing magnitudes in our *common system*. We obviously need to estimate the typical errors induced by this process.

The zero-point shift computation in LePhare is a complex interplay between the selected templates, the considered redshifts, and the selection function of the spectroscopic catalogue, which is almost always impossible to compute precisely, owing to the wide range of origins of our spectroscopic redshifts. As a consequence, the only possible way to estimate the errors induced by the LePhare zero-point shift computation is to consider several catalogues of objects for which the redshifts are known.

We could have divided our galaxy spectroscopic catalogues into several subsamples and checked the robustness of the resulting magnitude zero-point shifts. However, this would only have been possible for a few clusters for which we have a sufficient number of spectroscopic redshifts. We therefore choose another approach, considering the only other object class for which the redshifts are known: the stars in our fields.

We select stars with both ground-based and space-based HST data. This is done by plotting all the detected objects in diagrams of central surface brightness versus total magnitude. Space-based data allow us to detect very faint stars albeit in rather limited sky areas, while ground-based data allow us to detect relatively bright stars across larger areas of the sky. By applying LePhare to these star catalogues and fixing the redshifts to 0, we can compute zero-point shifts for these star catalogues. The same is done for the catalogues of galaxies with a known spectroscopic redshift, giving us a second estimate of the zero-point shifts.

Both shifts have no reason to be identical, as we consider in one case only stellar templates (which are not adapted to our galaxy catalogues) and in the other case galaxy templates at various redshifts. However, we expect not to obtain dramatically different values, since galaxy templates are theoretically nothing but combinations of stellar templates.

In Fig. 2, we show the mean value and the uncertainty in the difference between these two shifts for the various magnitude bands considered. As expected, the mean differences are always smaller than 0.2 mag. Similarly, typical uncertainties in the mean differences are of the order of 0.2 mag. The numbers of spectroscopic redshifts and stars used in the calibration are given in Fig. 3. On the one hand, this shows that we cannot exclude the hypothesis that the two shifts are the same, whatever

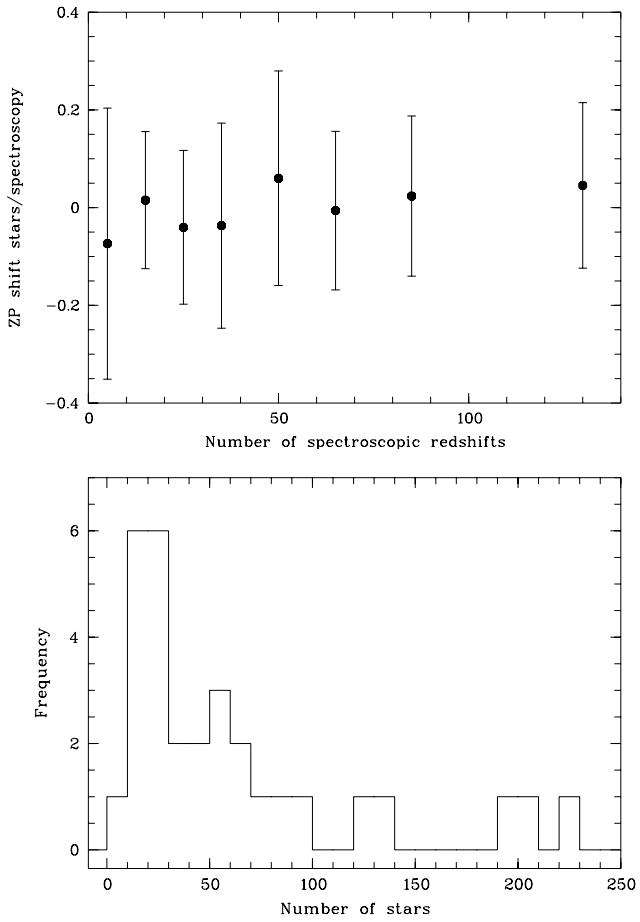

Fig. 3. *Top*: mean and uncertainty on the difference between the star and galaxy spectroscopic redshift-based shifts in the *I* band versus the number of spectroscopic redshifts available over our 31 fields. *Bottom*: histogram of the number of stars used for the calibration of each cluster.

the photometric band. On the other hand, this also means that given the uncertainties in the differences, it would be incorrect to use only star catalogues to estimate the zero-point shifts of our galaxy catalogues. A 0.2 mag shift is indeed large enough to induce significant errors in our photo-z estimates (see e.g. G10). Thus, star-based zero-point shifts were only used to roughly assess the spectroscopic redshift based shifts.

We also test how varying the number of spectroscopic redshifts affects our photo-z estimates. In Fig. 3, we plot the mean and uncertainty in the difference of the two shifts in the *I* band for different numbers of spectroscopic redshifts available in the considered catalogues. Except for the very sparse spectroscopic catalogues ($\leq$10 redshifts) with uncertainties of about 0.3 mag, all shift differences are consistent with zero and all uncertainties are smaller than 0.2 mag. We therefore choose to consider only clusters for which we have at least 10 spectroscopic redshifts along the line of sight.

To conclude, our method of translating all our magnitudes to a *common system* is robust, but cannot be efficiently applied without spectroscopic catalogues of at least 10 galaxies per cluster.

2.2.2. Extinction and photometric redshifts

One of the main results of G10 was that the precision of our photometric redshifts was sometimes degraded by a factor of

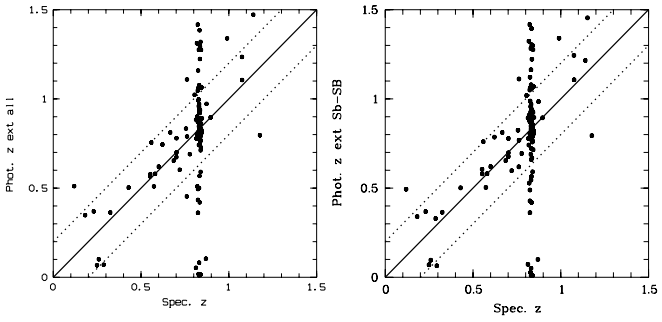

Fig. 4. Photometric versus spectroscopic redshifts when allowing extinction in all galaxies (*left*) or only in spiral galaxies (*right*) for the MS1054-03 field. The full lines show the lines of equality of the photometric and spectroscopic redshifts and the dotted lines show the scatter at ±0.2. See text for details.

two when considering cluster galaxies (see also Adami et al. 2011). This is probably due to a lack of galaxy templates typical of high density regions. Even the reddest galaxy templates are sometimes not red enough. Indeed, the mean type of cluster galaxies is 15 when taking all galaxies into account and 22 when taking only galaxies with photo-zs differing from spectroscopic redshifts by more than 1σ. These numbers highlight the lack of red templates (templates get bluer from type 1 to 31), and force LePhare to increase the galaxy redshifts.

In this framework, we note that in G10, we allowed LePhare to include extinction only in spiral galaxies. This was in good agreement with the galaxy properties generally observed, even though early-type galaxies are not always unobscured (e.g. Martini et al. 2013). Here, we allow LePhare to artificially introduce extinction in early-type galaxies, permitting galaxy templates to become redder. We are aware that this artificial extinction might not be physical but we choose to apply it nonetheless because it significantly improves the accuracy of our photo-zs.

To illustrate the effect of this approach, we show the example of MS 1054-03 at redshift $z = 0.8231$. The extinction in the I band is 0.3 ± 0.3 mag for early types and 0.4 ± 0.3 mag for late types. Figure 4 shows the photometric versus spectroscopic redshifts when allowing extinction only in spiral galaxies and in all galaxies. We achieve a higher photometric redshift accuracy when allowing extinction also in early-type galaxies. More quantitatively, the dispersion in the mean difference between the photometric and spectroscopic redshifts of cluster members is $\sigma_{|z_{\rm phot}-z_{\rm spec}|} = 0.20$ when allowing extinction in early-type galaxies, while it is 0.30 when allowing extinction only in late-type galaxies. We therefore improve the quality of our photometric redshift estimates in the cluster by ∼50% when allowing extinction in early-type galaxies. Outside the cluster, the effect is clearly less evident because the dispersion in the mean difference between photometric and spectroscopic redshifts is 0.22 when permitting extinction in early-type galaxies and 0.21 when allowing extinction only in late-type galaxies.

Permitting extinction in early-type galaxies therefore does not drastically change photometric redshifts outside the cluster but increases their accuracy by 50% within the cluster, enabling us to reach the same precision inside and outside the cluster. Furthermore, the number of catastrophic errors inside the cluster is reduced by more than 25% when extinction is allowed in early-type galaxies.

2.2.3. Photometric redshift quality

We now discuss the quality of our photometric redshifts and compare our results with those of G10. The dotted lines in Fig. 5

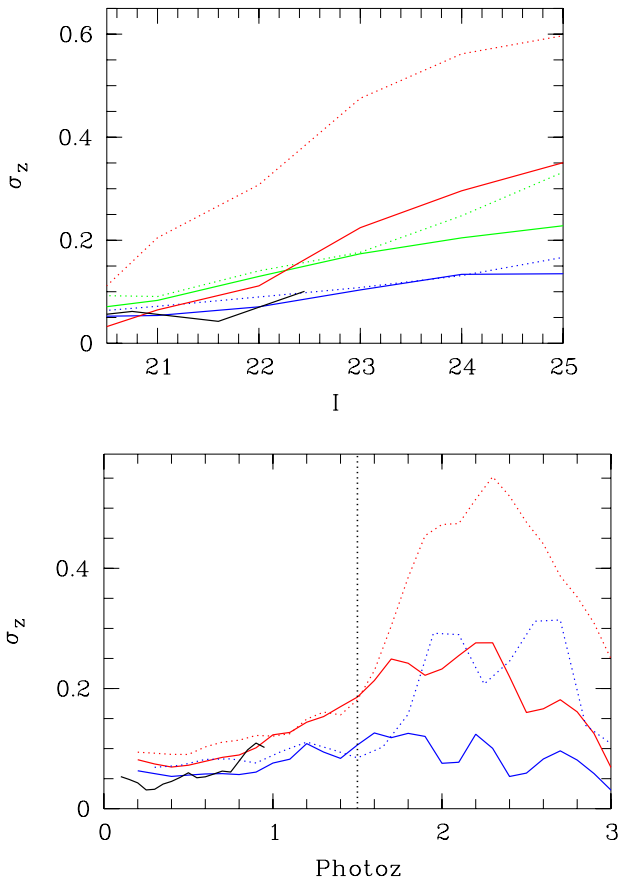

Fig. 5. *Top*: mean individual photo-z uncertainties as a function of I magnitude in three redshift intervals, colour coded as: blue: z = [0.; 1.05], green: z = [1.05; 2.0], red: z = [2.0; 2.5]. *Bottom*: mean individual photo-z uncertainties as a function of photo-z for various I magnitude intervals, colour coded as: blue: I = [19.5; 22.5], red: $F814W$ = [19.5; 24.5]. The vertical dotted line shows the $z \leq 1.5$ limit we suggested to adopt in G10. In both plots, dotted lines correspond to G10 and continuous lines to the present work. The black curves correspond to the CFHTLS with $I < 22.5$ and $z < 1.05$ and should be compared with the blue curves (see text for details).

come from G10 with slightly different redshift and magnitude intervals. At $z \leq 1.5$ and $I \leq 22.5$, our photometric redshifts have slightly smaller uncertainties than those of G10. The improvement is much more significant at $I \geq 22.5$ and $z \geq 1.5$.

We also compare our photo-zs to those of the CFHTLS (Coupon et al. 2009). To do so, we select cluster galaxies in the XXM-LSS survey (e.g. Adami et al. 2011) with spectroscopic redshifts and check their corresponding photo-zs in the CFHTLS. We then calculate the photo-z uncertainties for this sample ($I < 22.5$ and $z < 1.05$) using LePhare and plot them in Fig. 5. The precision of our photo-zs is comparable to that of the CFHTLS, and becomes higher for redshifts higher than $z = 0.8$ owing to the use of near infrared data.

Similarly, we reproduce Figs. 14 and 15 of G10 in Fig. 6, using data drawn only from spectroscopic catalogues. We find that our present photometric redshift computations lead to a modest improvement in the photometric redshift quality for field galaxies. However, cluster galaxy photometric redshifts are systematically improved for early-type galaxies, as expected, thanks to the extinction artificially allowed for such types.

As a conclusion, the present photometric redshift computations allow us to achieve a constant photometric redshift

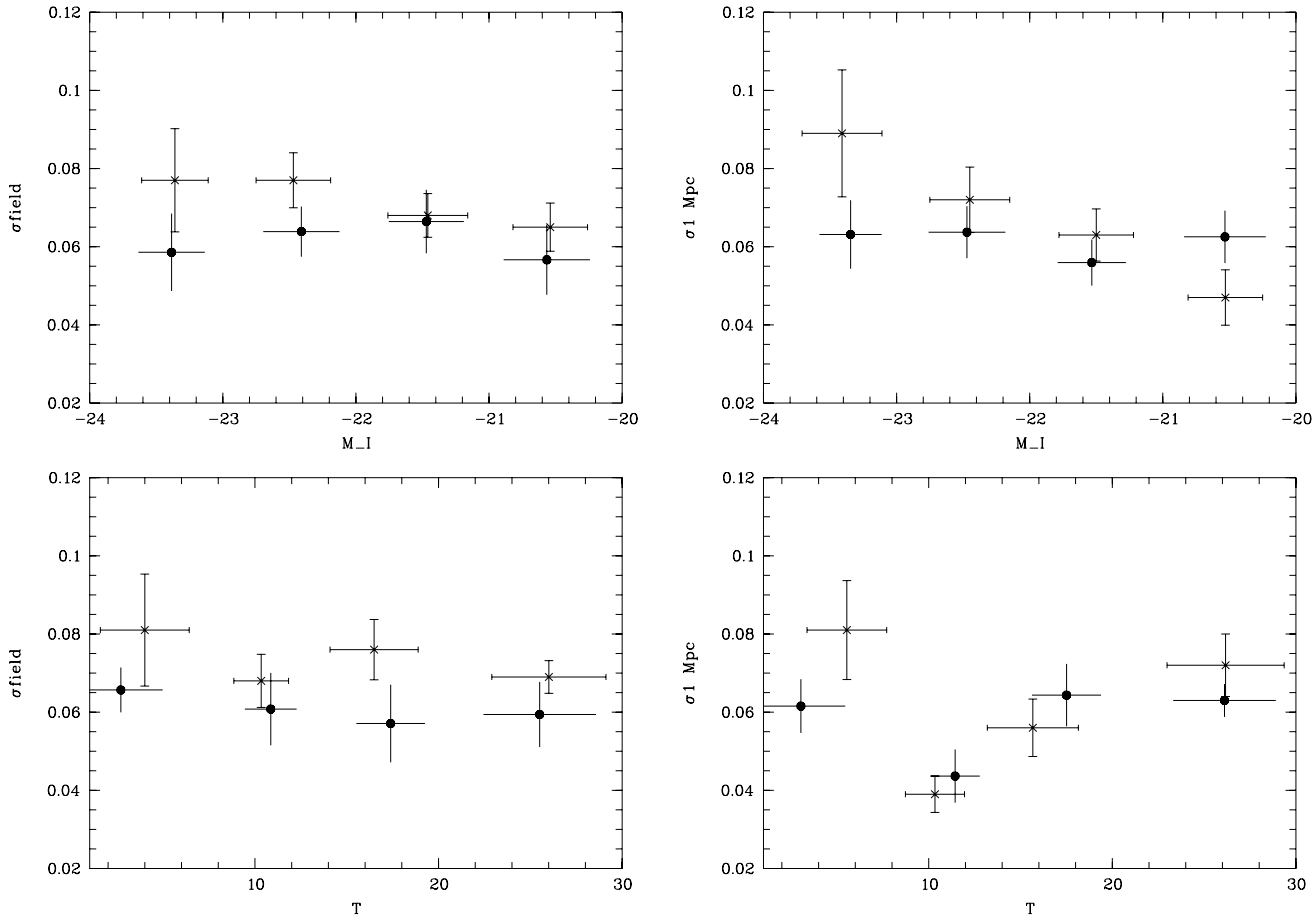

Fig. 6. Reduced σ of photo-zs versus I band absolute magnitude (*top*) and versus galaxy photometric type T (*bottom*). *Left*: field galaxies, and *right*: cluster galaxies inside a 1 Mpc radius. Error bars for the reduced σ are Poissonian and therefore directly proportional to the inverse square root of the number of galaxies within the considered bin. Error bars for each type are simply the second order momentum of the galaxy type distributions in the selected type bins ([1; 7], [8; 12], [13; 19], [20; 31]). Crosses correspond to the G10 values, and circles to the present values. Shifts in types and magnitudes arise from plotting average values for two different samples. Refer to Sect. 2.1 for details of the photometric types.

precision of $\sigma_z \sim 0.06$ for all galaxy environments (field or cluster), magnitudes, and galaxy types.

2.2.4. Improvement achieved by the use of more than one near infrared band

While the interest of having several near infrared bands is evident at $z \geq 1$, the effect at $z \leq 1$ (where all our clusters are) is not so clear. We test this with Abell 851. This cluster has a comprehensive range of data, with Y, J, H, and Ks near infrared bands available. Our spectroscopic redshift catalogue typically extends from $z \sim 0.2$ to $z \sim 0.8$, so is perfectly suited to testing the photometric redshift quality over the entire redshift range covered by our cluster sample. We therefore compute photometric redshifts for this cluster by considering, in addition to the optical bands, the z' band, then the z' and Y bands, the z', Y, and J bands, the z', Y, J, and H bands, and finally the z', Y, J, H, and Ks bands.

The mean photometric redshift precision (with catastrophic errors removed) between $z = 0.2$ and 0.8 does not depend significantly on the number of near infrared bands included. However, the number of completely wrong photometric redshifts (i.e. for which the difference between the spectroscopic and photometric redshift is greater than 0.3) tends to increase when the number of bands decreases. In the case of Abell 851, this percentage is close to 25% when at least one band is used among Y, J, H, or Ks, in addition to B, V, R, I, and z', while it suddenly jumps to 38% when only B, V, R, I, and z' are used.

This shows that within the redshift range considered (typically $z \leq 1$), the photo-z accuracy is not significantly improved by collecting data for more than one band among Y, J, H, or Ks. However, including data for at least one of these bands will notably diminish the number of catastrophic errors.

3. Galaxy luminosity functions

We now compute the B, V, R, and I rest-frame band GLFs for 31 clusters, using photo-zs to estimate the cluster membership of galaxies.

We consider that a galaxy belongs to the cluster when its photo-z is within a ± 0.2 interval centred on the cluster redshift. Once a galaxy is identified as a potential cluster member, we set its photo-z to the cluster redshift and re-run LePhare to obtain better estimates of redshift dependent parameters (such as absolute magnitude, colour, k-correction, etc.). We then subtract galaxy field counts measured in the same redshift interval using COSMOS data (Ilbert et al. 2009) to exclude galaxies at ± 0.2 from the cluster redshift that are not cluster members.

When single band catalogues are merged to estimate galaxy photo-zs, all objects that are not detected in every band are rejected from the catalogue. Galaxies missed in this approach

are mainly very faint galaxies, and we need to correct for this incompleteness to have the same number of galaxies in each band than in the original single band catalogue. Schechter functions are fitted up to the limiting magnitude at which our galaxy catalogues are 90% complete. We measure the completeness independently within each image by inserting and re-detecting stars simulated with the image point spread function (PSF). We obtain the 90% completeness limit in absolute magnitude by applying the k-correction and distance modulus.

Further details of our analysis are described step by step in the rest of this section.

3.1. Completeness

For each image, we first measure the PSF by fitting the stars with a Gaussian light distribution using the PSFEx software (Bertin 2011). With this PSF, we can model a set of Gaussian stars of various magnitudes. For each bin of 0.5 apparent magnitude, we simulate a hundred stars, insert them into the image, and try to re-detect them with SExtractor. The 90% completeness limit corresponds to the faintest magnitude bin in which we still re-detect at least 90 stars. This star completeness limit can be transformed to an approximate galaxy completeness limit by subtracting 0.5 from the magnitude (e.g. Adami et al. 2006).

In some cases, it is impossible to measure the PSF accurately because there are too few stars in the field. We then take the magnitude of the bin just brighter than the peak of the selected band magnitude histogram to be the 90% completeness limit. We verified that in most cases both methods give the same completeness limit estimate for the clusters for which it was possible to measure the PSF in the I band. The I band completeness limits for both methods are equal for 40% of the clusters and always differ by less than 1 mag. The average galaxy 90% completeness limit of our sample in the I band is 23.2.

We then translate these apparent magnitude completeness limits to absolute magnitude completeness limits by applying the k-correction and distance modulus. LePhare uses galaxy SED model libraries to estimate the theoretical k-corrections, which depend on galaxy types and redshifts. For each type, we measure the mean and the dispersion of the k-correction over galaxy templates in a redshift range of ±0.1 around the cluster redshift. This redshift interval is narrower than the one chosen for cluster membership to avoid too much contamination from foreground and background galaxies. The redshift range for cluster membership is larger as we then subtract field counts. We then define our corrections to be the mean values plus 2σ to be representative of 95% of our galaxy population. To keep a 90% completeness limit for all types of galaxies, the final k-corrections are set to the maximal values over all types. This step is illustrated in Eq. (1), where C_X and C_x are the completeness limit in absolute and apparent magnitude in the x band, $DM(z)$ the distance modulus, $k_x(z)$ the k-correction in the x band at redshift z, and T the galaxy type:

$$C_X = C_x - DM(z) - \max_T \left(\langle k_x(z)\rangle + 2\sigma_{k_x(z)}\right). \quad (1)$$

3.2. Computation of galaxy luminosity functions

We use the output catalogue of LePhare with photo-zs, positions, magnitudes, and absolute magnitudes for the B, V, R, I, Z, and J or Ks band data acquired by the original telescopes, and the magnitudes computed as if they had been observed with the VLT filters. We remove objects near saturated stars identified by eye in all our catalogues. Some stars are not assigned a null photo-z by LePhare. We then add an I band central surface brightness versus magnitude criterion to remove those stars. We correct for the dust extinction of the Milky Way using the cirrus maps of Schlegel et al. (1998). We assume that this correction is constant over each field and take the mean value of the extinction map area corresponding to the cluster position. This assumption is validated by the small area of our clusters compared to the resolution of the extinction maps. A cluster rarely occupies more than 4×4 pixel area of the cirrus map.

When combining all catalogues into a single one, we delete objects that are not detected in all 6 bands. We can estimate this loss of galaxies by comparing the number of galaxies in the merged catalogue to the single band catalogues. We first remove stars in single band catalogues using a surface brightness to magnitude diagram. This step mostly eliminates some very bright objects (bright and saturated stars) and faint spurious detections. We then measure the ratio of the numbers of galaxies from each of the single band catalogues to the combined catalogue in bins of 0.5 apparent magnitude. As we do not have the redshifts of the galaxies for which we wish to account for by applying this incompleteness correction, we apply these ratios as a weight coefficient to all galaxies belonging to the same apparent magnitude bin. Owing to the application of a k-correction, galaxies in the same apparent magnitude bin do not necessarily lie in the same absolute magnitude bin. Thus, applying this corrective factor directly to the magnitude bins instead of applying it to each galaxy would distort the absolute magnitude distribution. As we perform this correction on single band catalogues, we use the apparent magnitudes measured within the images. All subsequent steps are done using the magnitudes simulated by LePhare, which are as if they had been acquired with the VLT. This allows a more reliable comparison of clusters with each other.

We select galaxy cluster members as galaxies with photo-zs of ±0.2 around the cluster redshift. We verify in a $V - I$ versus I colour−magnitude diagram that this subsample has a red sequence that agrees with that of simulated elliptical galaxies of Bruzual & Charlot (2003) at the cluster redshift. Once this preselection is done, we fix galaxy redshifts to the cluster redshift and re-run LePhare on this subsample without varying photo-zs. This allows LePhare to determine both the k-corrections and the absolute magnitudes of the cluster members more accurately because they are redshift dependent properties. The k-correction strongly depends on redshift at high redshift (Chilingarian et al. 2010). For example, mistaking a galaxy at $z = 0.4$ with a galaxy at $z = 0.5$ leads to a difference of 0.3 mag in the r band for an elliptical galaxy and 0.2 for a spiral galaxy, when adopting the galaxy colours $g - r = 1.5$ and 0.9 given in Fukugita et al. (1995) and using the on-line k-correction calculator of Chilingarian[2].

We then perform a field galaxy background subtraction using COSMOS data (Ilbert et al. 2009), which are suitable for this subtraction because they include our redshift range and have accurate photo-zs. We first convert COSMOS magnitudes into our own set of filters by applying a correction factor that depends on galaxy type and redshift. Magnitudes in the COSMOS catalogue are already corrected for dust extinction. To avoid any k-correction effect, we do the background subtraction in apparent magnitude. Indeed, for our clusters, we compute the k-correction by setting all galaxies to the cluster redshift, while in COSMOS we have access to the k-correction of galaxies at their own photo-z. We apply the same photometric redshift cut applied to select our cluster members. We then count cluster and field galaxies in bins of 0.5 mag and apply a weight to all

[2] http://kcor.sai.msu.ru/

galaxies in each bin equal to the ratio of cluster to field galaxies in the bin. Field counts are first normalized to the cluster area assuming that the COSMOS field of view is 1.73 deg^2 after eliminating the masked regions. This subtraction removes line of sight galaxies that are in our cluster redshift interval. Owing to the relatively small fields covered by our J band data, field counts cannot be estimated from our images, hence we use robust field counts taken from the literature. For the same reason, we are unable to investigate the properties of clusters at very large radii. We assume that our clusters lie in a region of radius 1 Mpc around their optical centre (position of the BCG or in some cases barycentre of bright galaxies). Once field counts are subtracted, we normalize GLFs by dividing by the 1 Mpc area converted to square degrees. We choose this normalization to compare our results to those of other authors who calculated GLFs normalized to 1 deg^2.

We study the behaviour of clusters by fitting their B, V, R, and I band GLFs with a Schechter function (Eq. (2), Schechter 1976):

$$N(M) = 0.4\log(10)\phi^* \left[10^{0.4(M^*-M)}\right]^{\alpha+1} \exp\left(-10^{0.4(M^*-M)}\right), \quad (2)$$

where ϕ^* is the characteristic number of galaxies per unit volume, M^* the characteristic absolute magnitude, and α the faint-end slope of the GLF. We obtain these three parameters by applying a χ^2 minimization algorithm. The error bars in these parameters are given by the covariance matrix (i.e. the second derivative matrix of the χ^2 function with respect to its free parameters, evaluated at the best parameter values).

Since our clusters are rather distant, the numbers of points available to fit their GLFs do not justify the inclusion of a second function (either a second Schechter function, or a Gaussian) to fit our data, as sometimes found in the literature. Since we are particularly interested in the faint-end slope of the GLF, a single Schechter function is therefore appropriate.

3.3. Red-sequence and blue galaxy luminosity functions

To understand clearly the cluster properties, it is interesting to study their different galaxy populations. To do so, we need to distinguish the red sequence (RS) from the blue galaxies. The first roughly correspond to early-type galaxies and the second to late types.

To perform this separation, we use a $V - I$ versus I colour−magnitude diagram plotting only galaxies selected as cluster members based on their photo-zs. As it has been observed that the RS slope does not evolve across our redshift range (e.g. De Lucia et al. 2007), we assume a fixed slope of −0.0436, as in Durret et al. (2011). For the ordinate of the RS, we first interpolate the elliptical galaxy colour value given in Fukugita et al. (1995) to each cluster redshift and select a wide RS with a width of 0.6 in magnitude. We then fit this preliminary RS with a free ordinate to get the final RS equation on which we set the smaller width of 0.3 used in De Lucia et al. (2007). We check that slightly modifying the value from Fukugita et al. (1995) does not significantly affect our RS selection: a shift of 0.2 to our first ordinate estimate results in only a few galaxies changing their population type.

Once we select our two galaxy populations, we compute GLFs for each population following the same method used for the whole sample. Field galaxies are separated using the red sequence calculated for each cluster.

The upper absolute magnitude limit for the Schechter fit is the magnitude corresponding to the 90% completeness and the lower limit is set to the magnitude of the cluster BCG, which is defined to be the brighest red sequence galaxy in the I band. Blue galaxies brighter than the BCG are removed as they are probably foreground galaxies incorrectly assumed to lie at the cluster redshift.

4. Results on galaxy luminosity functions

We present in this section our fitted Schechter functions to the GLFs of our clusters. We first analyse our fits to individual cluster GLFs and then study average behaviours by stacking the GLFs of several clusters. We consider the dependence of the Schechter parameters on redshift, mass, and cluster substructuring when our GLFs are stacked. For the stacked GLFs and their dependence on environment, we also derive GLFs for blue and red-sequence populations. To separate clusters in terms of redshifts, masses, and substructures, we limit our analysis to the RS galaxy population as there are too few blue galaxies for the considered number of clusters. This study will be conducted in a future paper when we have data for more clusters in hand.

4.1. Individual cluster GLFs

We discuss individual cluster GLFs fitted with a Schechter function to the 90% magnitude completeness limits. These fits are done in the B, V, R, and I restframe bands and separately for red-sequence and blue galaxies. Two of our GLFs are shown in Fig. 7. All individual GLFs, and their Schechter fits when possible, are displayed for blue and RS populations in Appendix A (Fig. A.1 and Table A.1). As in Fig. 7, we only show galaxy counts when the selected cluster population has more than 20 members after removal of the background. We only display Schechter fits when they converge. In many cases, the fits indeed do not converge, probably because the completeness limit is too bright, even when the clusters have a relatively high number of galaxy counts. We display these clusters novertheless in Table A.1, as they are included in the stacked GLFs.

Figure 7 displays the GLFs for two clusters that span our redshift range: CL0016+1609 at $z = 0.55$ and LCDCS0504 at $z = 0.79$. CL0016+1609 represents our low-redshift clusters. We find rather flat RS GLFs but note the small decrease at the faint end characterized by an α parameter of about −0.5 in the V, R, and I restframe bands. In most of our low-redshift clusters, the observed cluster members lie primarily on the RS and too few blue galaxies are available to produce a blue GLF. LCDCS0504 represents our high-redshift clusters. Its RS GLFs sharply decline at their faint end. In contrast, its blue GLFs are rather flat except in the B band. For the high-redshift clusters, there are sometimes insufficient RS galaxies to obtain GLFs, as here in the B band. The large uncertainties in both counts and Schechter parameters highlight the need for stacking to draw any clear conclusion about the GLF behaviour.

For some clusters, the completeness limit is too bright to permit GLF fitting, especially for high-redshift clusters. This is true for CL_J0152.7-1357 and LCDCS 0853 for which deeper images would be required. Sometimes, the galaxy counts are too low to allow any fit of the GLF, placing in doubt the high masses assumed for these clusters. The masses we considered to select the DAFT/FADA clusters are drawn from X-ray surveys. The X-ray selection is often assumed to be superior to optical selection, because the X-ray flux is proportional to the gas density squared, while the rest-frame optical flux is roughly proportional to the galaxy density. However, compact X-ray sources may not have been subtracted reliably from many X-ray observations of

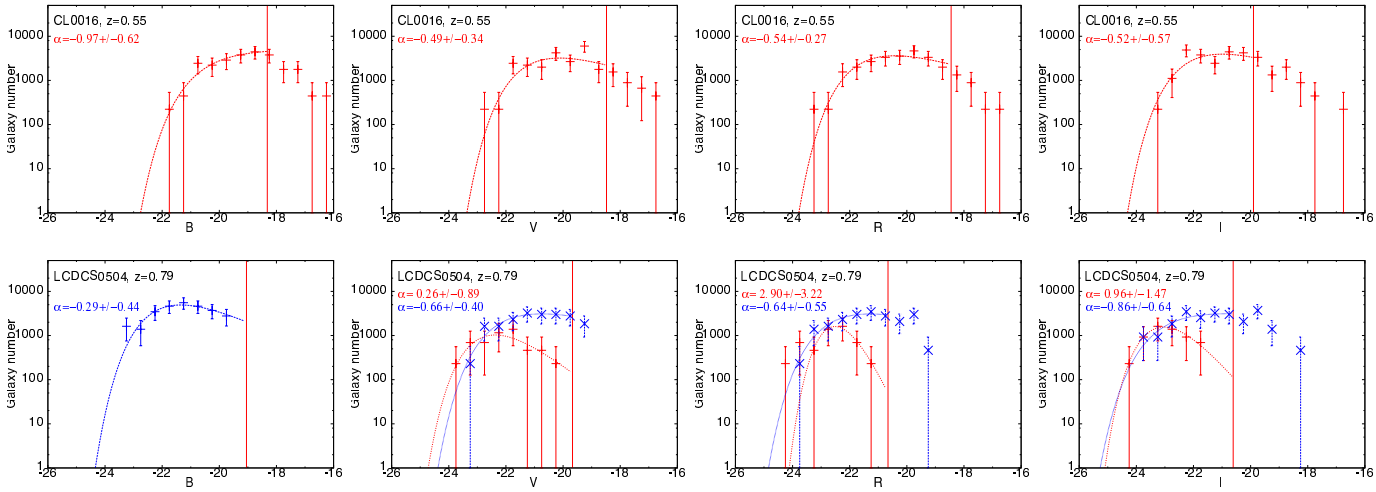

Fig. 7. Our GLFs in the B, V, R, and I rest-frame bands (*from left to right*) for CL0016+1609 (*top*) and LCDCS0504 (*bottom*). Red and blue points correspond to red-sequence and blue GLFs normalized to 1 deg^2. The red vertical lines indicate the 90% completeness limit. The red and blue curves show the best Schechter fits to red-sequence and blue galaxies, and the faint-end slope parameter (α) is displayed in the corresponding colour. Only galaxies brighter than the 90% completeness limit are taken into account in the fits. In addition, we display GLFs only when more than 20 cluster galaxies are within the colour RS or blue bins and after subtracting the field.

our clusters (especially for ROSAT data), leading to overestimates of the cluster X-ray masses. This is true in particular for MACS J0647.7+7015, for which a bright source is very near the cluster in the XMM image. Clusters with a similarly small number of galaxy counts are F1557.19TC, MACS J0647.7+7015, MACS J0744.9+3927, SEXCLAS 12, GHO 1602+4312, and GHO 2155+0334. We eliminate them from our analysis.

As shown in Table A.1, the Schechter parameters derived for individual clusters can differ, even after removing the problematic clusters. The large error bars are due to the use of Poissonian errors and the large photo-z interval for cluster membership selection which causes more background galaxies to be subtracted. In the following parts we stack these clusters to study how the cluster properties depend on average on redshift, mass, substructures, and environment.

4.2. Stacked GLFs

We stack our clusters using the standard Colless method (Colless 1989) described in Popesso et al. (2006). The idea is to average cluster counts in each magnitude bin including all clusters that are 90% complete in this bin. Clusters first have to be normalized to the same area, chosen to be 1 deg^2, and to a fixed richness. This richness is set to the number of galaxies detected to the completeness limit that encloses 90% of our sample. We do not choose our worst completeness limit because this would result in too few galaxies for the normalization. Also, we only include clusters that have more than 20 galaxies above the background for a given galaxy population (red or blue), to avoid a domination of the stack by the poorest clusters.

This method allows us to use the maximum amount of information for all our clusters. A more classical method would remove the information for the most complete bins as we would only be able to stack clusters reaching the same completeness limit. We could also stack different numbers of clusters for different completeness limits. This approach would allow to better control the evolution with completeness but it would generate many sets of figures partially containing the same information, thus affecting the legibility of the results.

For any method, the more complete our data, the farther we are from an average cluster. In a standard method, this problem affects only the stacks with the fewer clusters, while with the Colless method it affects the faintest bins of the GLF. We investigate this bias by stacking fixed numbers of clusters in each stack. We find that for the same completeness limit the stacked GLFs do not change much once we have four clusters in the stack. Thus, we require to have at least four clusters in each magnitude bin to take into account in the Colless stack, to avoid being dominated by individual cluster behaviours.

Error bars are calculated using the χ^2 fit to our galaxy counts normalized to 1 deg^2. Galaxy counts and their errors are summed following Eqs. (3) and (4) below, where $N(j)$ and $\sigma(j)$ are the stacked galaxy counts and galaxy count errors in magnitude bins j, the index i indicates single cluster values, S_i is the area of cluster i, $N_c(j)$ the number of clusters in bin j, and $N_{0,i}$ and $\langle N_0(j)\rangle$ are the richness of the cluster i and the mean richness of clusters in bin j:

$$N(j) = \frac{\langle N_0(j)\rangle}{N_c(j)} \sum_i \frac{N_i(j)}{S_i N_{o,i}}, \tag{3}$$

$$\sigma(j) = \frac{\langle N_0(j)\rangle}{N_c(j)} \sqrt{\sum_i \left(\frac{\sigma_i(j)}{S_i N_{o,i}}\right)^2}. \tag{4}$$

Individual variances are weighted by the square of the cluster area, as for the galaxy counts, and not simply the area. This is to retain the Poissonian distribution of the counts. We also fit Schechter functions to the stacked GLFs.

Stacked GLFs are shown in Fig. 8 for the RS and blue populations of the full cluster sample in the B, V, R, and I restframe bands. Results of their best Schechter fits are given in Table 2, along with the 90% completeness limit, the numbers of clusters in the stack, and the mean redshifts of the clusters in the stack.

We see a common behaviour for the V, R, and I bands. The RS GLF is close to that at low redshift but with a slight decline at the faint end. M^* is almost the same for the three bands and α is slightly higher in the I band than in the other two bands. The blue GLFs are also very similar for these three bands, with steeper faint ends. In the I band, however, blue galaxy counts

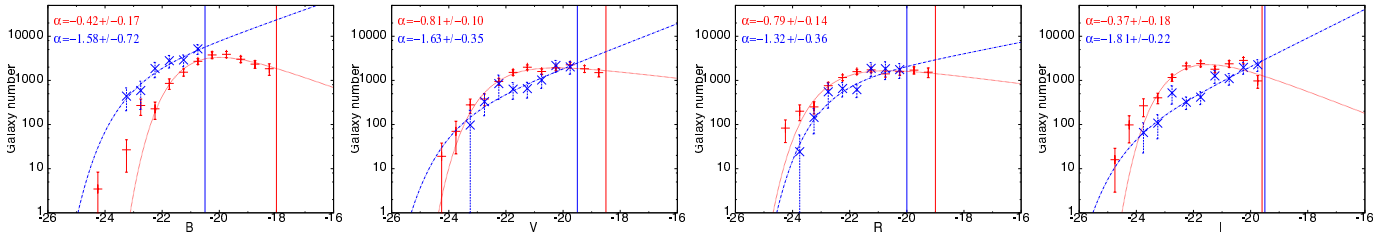

Fig. 8. Our GLFs in the B, V, R and I rest-frame bands (*from left to right*) for clusters stacked together. Red and blue points respectively correspond to red-sequence and blue GLFs normalized to 1 deg^2. The red and blue curves show the best Schechter fits to red-sequence and blue galaxies and the red and blue vertical lines indicate the corresponding 90% completeness limits. The slope of the fit α is given for each population. Refer to Table 2 for all Schechter fit parameters.

Table 2. Parameters of the best Schechter function fits for stacked cluster GLFs normalized to 1 deg^2 for red-sequence and blue galaxies.

	$N_{\rm clus}$	Comp	$\langle z \rangle$	α	M^*	ϕ^* (deg^{-2})
All clusters				red-sequence GLFs		
B	14	–18	0.61	-0.42 ± 0.17	-20.6 ± 0.2	8837 ± 1456
V	16	–18.5	0.58	-0.81 ± 0.10	-22.0 ± 0.2	3434 ± 671
R	16	–19	0.58	-0.80 ± 0.14	-22.4 ± 0.2	3059 ± 690
I	13	–19.6	0.54	-0.37 ± 0.18	-22.0 ± 0.2	6204 ± 930
All clusters				blue GLFs		
B	5	–20.5	0.70	-1.58 ± 0.72	-22.9 ± 1.7	1888 ± 4514
V	6	–19.5	0.62	-1.63 ± 0.35	-23.7 ± 2.1	238 ± 555
R	6	–20	0.62	-1.32 ± 0.36	-22.4 ± 0.5	1163 ± 880
I	7	–19.5	0.53	-1.81 ± 0.22	-24.1 ± 1.7	104 ± 209

Notes. "$N_{\rm clus}$" is the number of clusters in the stack, "Comp" is the 90% completeness limit and "$\langle z \rangle$" is the mean redshift of the stack. See Fig. 8 for the GLF plots.

are smaller: as expected, blue galaxies are fainter in redder photometric bands. Blue and red GLFs cross at around $V = -20$, $R = -20.5$, and $I = -20.3$. These results represent clusters of mean redshift about $z = 0.6$. Results are quite different for the B band. The RS GLF also has a shallow decline at the faint end but the blue counts are higher than the red ones, implying that the blue galaxies are indeed brighter in the bluer bands.

There is also an excess of red-sequence galaxies at the bright end compared to the Schechter function, especially for the B and I bands. This kind of excess is often observed in clusters and some authors prefer to fit GLFs with a combination of a Schechter and a Gaussian (e.g. Biviano et al. 1995). However, this excess is puzzling for the B band, leading to very bright red-sequence galaxies for this optical band. This distribution of bright galaxies probably results from a complex interplay of intrinsic properties and applied k-correction. On examining the images, we indeed found that some BCGs appearing very bright in the I band are quite faint in the B band compared to other bright galaxies. The bright end of the red-sequence B band GLF is then dominated by the k-correction factor, which can be as high as 3 mag at these redshifts. It would be very useful to compare bright cluster galaxies in the B and I bands but this is beyond the scope of this paper. In the present study, we merely conclude that a Schechter function cannot simultaneously fit the bright and faint ends of the B band RS GLFs. In the rest of the paper, we concentrate mainly on the faint end of the GLFs, which is well constrained.

We wish to highlight several caveats of our method. The number of clusters with a sufficient number of blue galaxies to be stacked is two to three times lower than the number for RS galaxies. Thus, the blue GLFs are far more poorly constrained, as can be seen from their larger error bars for their best fit Schechter function parameters. In addition, as we used only clusters with a sufficient number of galaxies for each population, the RS GLF is biased toward red-galaxy rich clusters and the blue GLF toward blue-galaxy rich clusters. It would be more rigorous to consider the same clusters in both subsamples, but this would require deeper images. As a sanity check, we compared our GLFs with those obtained by considering only the few clusters presenting both large red and blue populations. Results are in good agreement, but error bars on the latest GLFs are much larger due to the very low number of clusters in the stack. When applying the Colless method for stacking, data for different clusters are stacked in different magnitude bins. As our survey spans a large redshift range ($0.4 \leq z < 0.9$), each magnitude bin has a different mean redshift. Since the completeness limit is brighter for high-redshift clusters, the faint end of any stacked GLF will be dominated by lower redshift clusters. In the next subsection, we study GLFs in separate narrower redshift ranges to avoid this problem. We compare our stacked GLFs with field GLFs in Sect. 5.2.

4.3. Evolution of GLFs with redshift

To investigate the evolution of the GLF with redshift, we apply the same analysis as previously, but separate our clusters between low ($0.4 \leq z < 0.65$) and high ($0.65 \leq z < 0.9$) redshifts. We obtain about 13 low and 4 high-redshift clusters, which each have more than 20 red-sequence galaxies depending on the photometric band. Unfortunatly, there are an unsufficient number of blue cluster galaxies to fit blue GLFs for these two redshift intervals. Our results for red-sequence galaxies are displayed in Fig. 9 and Table 3.

For the low-redshift sample, the faint end of the GLFs is similar to that of the stacked GLF for all clusters. This is evident from the similarity of the α parameters for both samples (Tables 2 and 3). This means that the faint end of our stacked

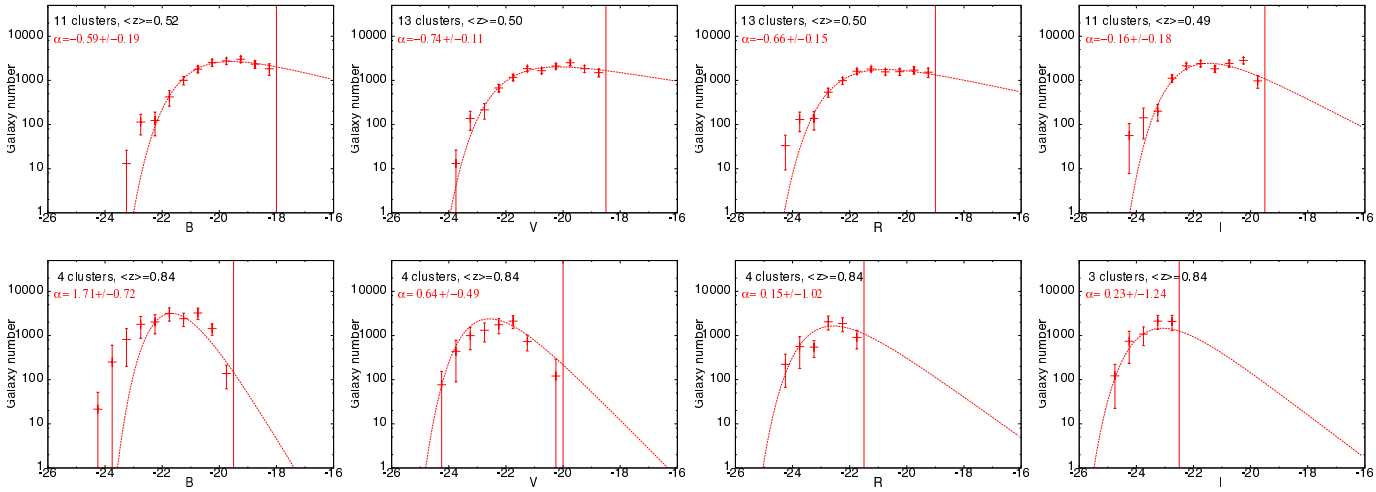

Fig. 9. Evolution of red-sequence GLFs with redshift in the B, V, R and I rest-frame bands (*from left to right*) for clusters stacked together. The first line of figures is for clusters with redshifts $0.40 \leq z < 0.65$ and the last line of figures is for clusters with redshifts $0.65 \leq z < 0.90$. Red crosses are red-sequence GLFs normalized to 1 deg^2. The vertical red lines indicate the 90% completeness limit. Red curves are the best Schechter fits to red-sequence galaxies. The slope of the fit α is given with the number of clusters and the mean redshift of the stack. Refer to Table 3 for all Schechter fit parameters.

Table 3. Parameters of the best Schechter function fits for stacked cluster GLFs normalized to 1 deg^2 for red sequence.

	$N_{\rm clus}$	Comp	$\langle z \rangle$	α	M^*	ϕ^* (deg^{-2})
Clusters at				red-sequence GLFs		
$0.40 \leq z < 0.65$						
B	11	–18	0.52	-0.59 ± 0.19	-20.5 ± 0.3	6278 ± 1366
V	13	–18.5	0.50	-0.74 ± 0.11	-21.6 ± 0.2	4062 ± 724
R	13	–19	0.50	-0.66 ± 0.15	-21.9 ± 0.2	3898 ± 734
I	11	–19.5	0.49	-0.16 ± 0.18	-21.6 ± 0.2	7101 ± 747
Clusters at				red-sequence GLFs		
$0.65 \leq z < 0.90$						
B	4	–19.5	0.84	1.71 ± 0.72	-20.6 ± 0.5	3476 ± 2285
V	4	–20	0.84	0.64 ± 0.49	-22.0 ± 0.4	5936 ± 1130
R	4	–21.5	0.84	0.15 ± 1.01	-22.4 ± 1.0	4795 ± 972
I	3	–22.5	0.84	0.23 ± 1.24	-22.9 ± 0.6	4212 ± 1605

Notes. The *top* part is for clusters with redshifts $0.40 \leq z < 0.65$ and the *bottom* is for clusters with redshifts $0.65 \leq z < 0.90$. "$N_{\rm clus}$" is the number of clusters in the stack, "comp" is the 90% completeness limit and "$\langle z \rangle$" is the mean redshift of the stack. See Fig. 9 for the plots of the GLFs.

GLF for all clusters is dominated by the low-redshift clusters. This is not surprising as there are fewer high redshift clusters than low-redshift ones. In addition, low-redshift clusters tend to have fainter completeness limits, hence are more likely to contribute to the faintest bins of the GLF than the high-redshift clusters.

The red GLFs of high-redshift clusters decline far more sharply at their faint end than the low-redshift clusters. The α parameter is significantly higher even with those large error bars. On the other hand, M^* is slightly brighter than at low redshift and equal to that for the fit of all clusters taken together, meaning that the bright end is dominated by the high-redshift clusters. There may be more bright galaxies in high redshift clusters but this result can also be due to the k-correction which is higher for high-redshift clusters and tends to distort the bright end of the GLF such that the Schechter function is not appropriate any more. This can be clearly seen in the B band where there is a significantly larger number of red bright galaxies than predicted by the Schechter fit. The best-fit Schechter parameters for the B band are therefore unreliable for our high-redshift sample. We also note that there are very few clusters at high redshift, so that we need to target more high-redshift clusters to decrease the error bars in both the galaxy counts and Schechter parameters. In this particular case we took into account every magnitude bin with at least two clusters, a number that could be increased if we observed more clusters.

These dependences of the GLF properties on redshift are interpreted in terms of physical processes in our discussion.

We also note that overestimating the completeness limit in apparent magnitude would also lead to a sharp decline in the faint end of GLFs. This drop would also increase with redshift, because the completeness limit in absolute magnitude would be brighter at high redshift. Since we compute accurate 90% completeness limits for every image, we should not be affected by this effect.

4.4. Dependence of GLFs on cluster X-ray luminosity

We can similarly investigate the dependence of the GLF on a mass proxy. To achieve this, we separate clusters according to their X-ray luminosity, as measured in Guennou et al. (2014) who analysed the *XMM-Newton* data available for

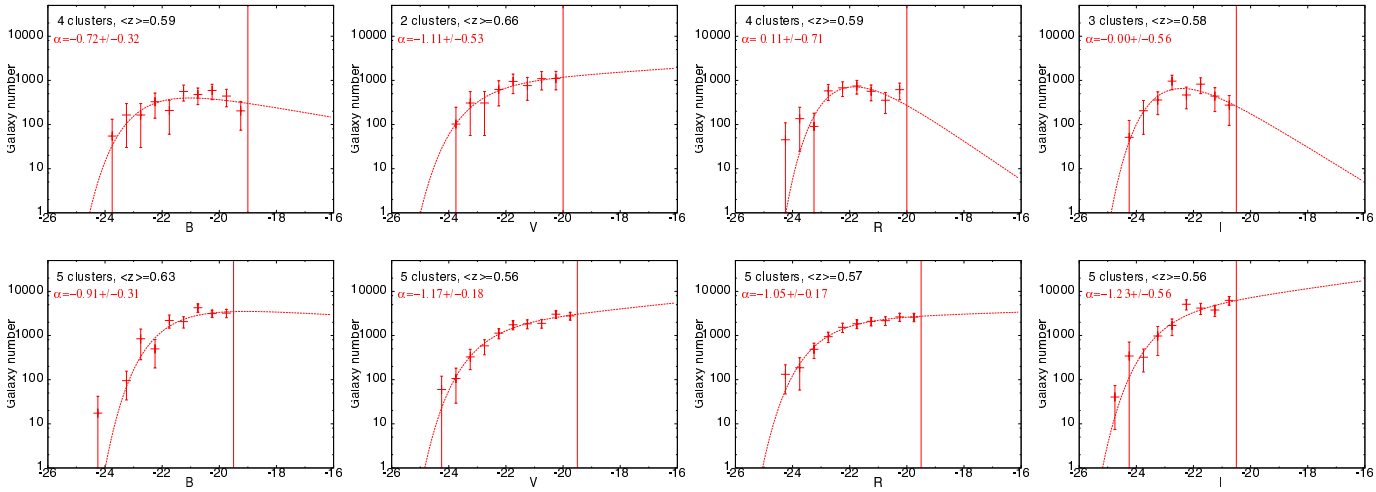

Fig. 10. Dependence of red-sequence GLFs on cluster X-ray luminosity in the *B*, *V*, *R*, and *I* rest-frame bands (*from left to right*) for clusters stacked together. The *top line* is for clusters with X-ray luminosities $8 \times 10^{43} < L_X < 10^{45}$ erg s^{-1} and the *bottom line* is for clusters with X-ray luminosities $L_X > 10^{45}$ erg s^{-1}. Red crosses are red-sequence GLFs normalized to 1 deg^2. The vertical red lines indicate the 90% completeness limit. Red curves are the best Schechter fits to red-sequence galaxies. The slope of the fit α is given with the number of clusters and the mean redshift of the stack.

42 DAFT/FADA clusters to derive their X-ray luminosities and temperatures, and search for substructures. We have about 5 clusters with a luminosity greater than 10^{45} erg s^{-1} and 4 with a lower luminosity depending on the considered optical band. These numbers are for RS galaxies; we do not have enough clusters with more than 20 blue galaxy members to compile blue GLFs in this case. We do not have accurate X-ray luminosities for the remaining clusters.

We find a steeper faint end for high-mass clusters than low-mass ones in every photometric band (Fig. 10). This could mean that the drop at the faint end of RS GLFs is essentially due to low mass clusters. In addition, the number of member galaxies is much larger for high X-ray luminosity clusters, which seems logical. However, we note that the number of clusters, especially for low-mass clusters, is small. In this particular case we recall that we consider every magnitude bin with at least two clusters. More data are needed to produce larger samples that cover a wide range of mass but similar in redshifts, and also to study the variations in the blue and red GLFs with mass. When our DAFT/FADA sample of about 90 clusters is complete, we should be able to draw conclusions about the GLF dependence on mass and redshift, provided that we have the same proportion of clusters with good completeness as in the present subsample. We also note that our clusters all have quite high X-ray luminosities. Our results therefore only concern clusters with X-ray luminosities $L_X > 8 \times 10^{43}$ erg s^{-1}.

4.5. Dependence of GLFs on substructures

We also search for differences between clusters with and without substructures. We consider clusters with substructures detected both with optical spectroscopy and X-ray data by Guennou et al. (2014). We have 3 clusters with substructures and 2 that are relaxed and sufficiently rich in red galaxies. For the remaining clusters, we have been unable to robustly confirm either the presence or absence of substructures and therefore discard these clusters in this subsection.

It is difficult to draw any conclusions about relaxed clusters as they are too few in number here and their completeness limit is too bright. Hence, we only study stacked clusters with substructures (Fig. 11). In this particular case we allow some bins to contain as few as two clusters to be able to draw the red-sequence GLFs. There is no clear difference in either the slope or M^* of the Schechter function from those parameters for stacks containing all clusters, given the large error bars caused by the low number of clusters. In the *I* band, the very bright completeness limit does not allow us to study the faint part of the GLF.

For stacks of clusters with substructures, we also have higher counts for *B* band data than for other bands. This is consistent with a burst of star formation being produced as the clusters merge. These faint blue galaxies might also be the debris of any merging processes. However, we need data with a fainter completeness limit to investigate whether these debris dwarf galaxies exist.

Given the error bars in our Schechter parameters, our interpretations of the analysis of our substructured clusters are not statistically significant. We could reduce our error bars by either reducing the number of background galaxies, i.e. adding more clusters to the stacks, or computing more accurate photometric redshifts for field and cluster galaxies.

4.6. Cluster cores and outskirts

In some cases, stellar formation can be triggered by in-fall in the outskirts of clusters (e.g. Biviano et al. 2011). To investigate whether this is true for clusters in general, we compute GLFs for the core ($r \leq 500$ kpc) and outskirts ($500 < r \leq 1000$ kpc) of clusters. We present the stacked GLFs for blue and red-sequence galaxies in different environments in Fig. 12. This figure is to be compared with Fig. 8 which displays cluster GLFs for the same cluster galaxies but in both the core and outskirt regions.

We only consider clusters which are richer than 20 galaxies once background galaxies have been subtracted, in the particular cluster area and for the selected colour population. For red-sequence GLFs, we see no difference between the faint ends for each cluster region. The α parameters are the same within the error bars for the cluster cores, outskirts, and both regions combined. However, the brighest galaxies tend to lie in cluster cores,

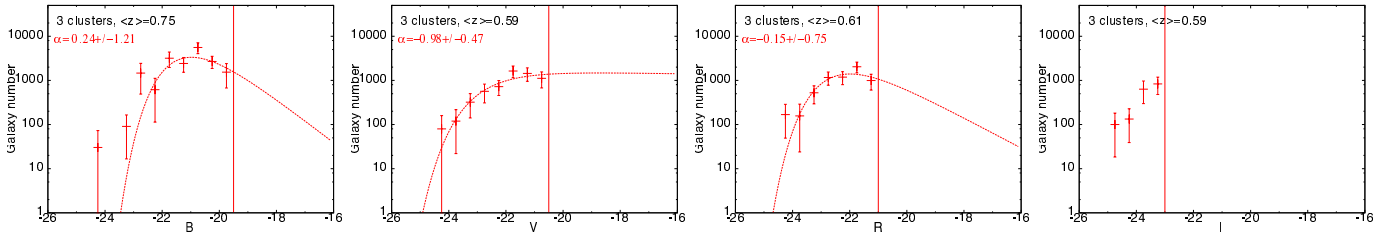

Fig. 11. Dependence of red-sequence GLFs on cluster substructures in the B, V, R, and I rest-frame bands (*from left to right*) for clusters stacked together. Only clusters with detected substructures are considered here (cf. Guennou et al. 2014). Red crosses are red-sequence GLFs normalized to 1 deg^2. The vertical red lines indicate the 90% completeness limit. Red curves are the best Schechter fits to red-sequence galaxies. The slope of the fit α is given with the number of clusters and the mean redshift of the stack.

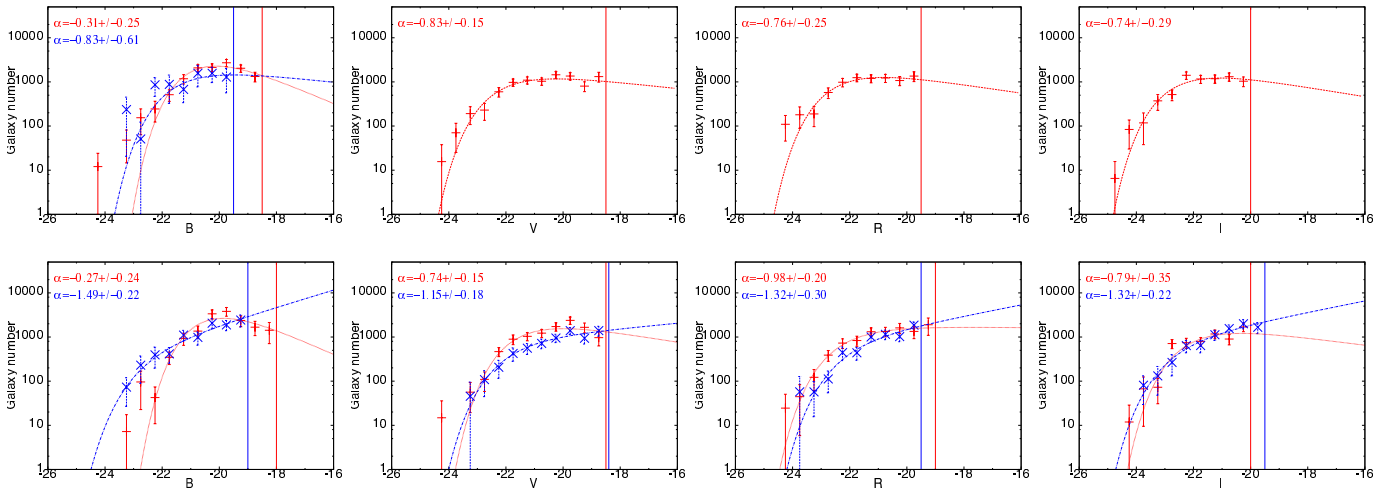

Fig. 12. Galaxy luminosity functions in the B, V, R, and I rest-frame bands (*from left to right*) for stacked clusters in cores and outskirts. The *first line* of figures is for cluster cores ($r \leq 500$ kpc) and the *second line* of figures for cluster outskirts ($500 < r \leq 1000$ kpc). Red and blue points, respectively, correspond to red-sequence and blue GLFs normalized to 1 deg^2. The red and blue curves show the best Schechter fits to red-sequence and blue galaxies and the red and blue vertical lines indicate the corresponding 90% completeness limits. The slope of the fit α is given for each population.

so the excess seen at the bright end of GLFs diminishes in the cluster outskirts.

We find that there are more blue galaxies in the outskirts than in the cores, so blue GLFs in cluster cores can only be plotted for the B band for our data. In the B band, the blue core stacked GLF is much closer to the red-sequence GLF than when taking galaxies from all the regions together. In the outskirts, blue and red-sequence galaxies seem to equally contribute to the cluster population at any magnitude to our completeness limits for V, R, and I bands. However, the faint end of the GLF is steeper for blue galaxies, implying that at fainter magnitudes, blue galaxies are more numerous than red ones in cluster outskirts. In the B band, we detect far more bright blue galaxies than red-sequence galaxies, which indicates that the bright end of the blue B band GLF seen in Fig. 8 is dominated by the outskirts of clusters.

To conclude, we find an excess of blue galaxies in the outskirts compared to the core of clusters but in the cluster outskirts the GLFs of blue and red galaxies are very similar. This can be interpreted as an infall of blue galaxies on cluster outskirts from the field populations or by a burst of stellar formation.

5. Discussion

5.1. The faint end of the GLF

The GLF faint end depends on both colour and redshift. We have investigated this evolution by stacking cluster counts for blue and RS galaxies separated within colour-magnitude diagrams, and at either low redshift ($0.40 \leq z < 0.65$) or high redshift ($0.65 \leq z < 0.90$). We now interpret Fig. 8 and Table 2 in terms of colour evolution, and Fig. 9 and Table 3 in terms of redshift evolution.

Taking our full redshift cluster sample, we find steep blue GLFs with $\alpha_{\rm blue} \sim -1.6$ for all bands, owing to the large error bars caused by the small amount of clusters with a sufficient number of blue galaxies. This is more or less consistent with similar analyses for clusters at lower redshifts. For red-sequence galaxies, we see a small drop at the faint end with a slope $\alpha_{\rm red} \sim -0.4$ for B and I bands and $\alpha_{\rm red} \sim -0.8$ for V and R, while lower-redshift clusters usually present a flat faint end for the red-sequence population. In our redshift range, red galaxies dominate the blue population for magnitudes brighter than $V = -20$, $R = -20.5$, and $I = -20.3$. Above these magnitudes, blue faint counts become higher than red ones. In the B band, the blue galaxies dominate over red ones at all magnitudes, possibly because blue galaxies are brighter in the blue band. We note however that we draw this conclusion for only five clusters with sufficient blue galaxies in the B band.

If we now separate our clusters between high and low redshift, we find that the red-sequence faint-end drop is more important at high redshift. At low redshift, the slope is comparable to that for all clusters combined. This is because we perform our stacking using the Colless method, in which the faint end of

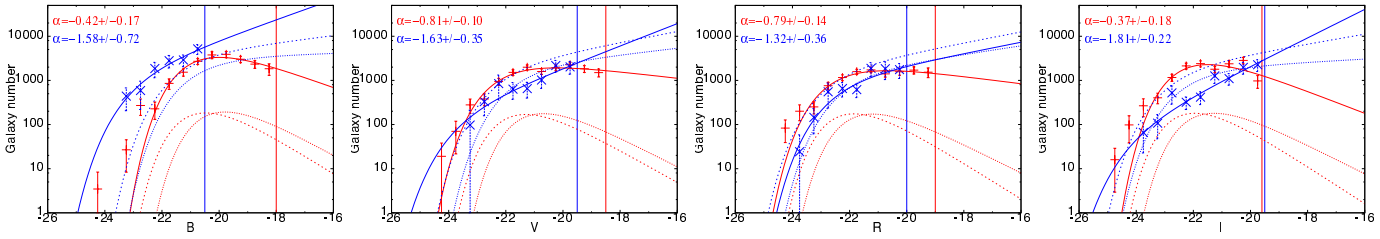

Fig. 13. Cluster and field GLFs in the B, V, R, and I rest-frame bands (*from left to right*). Red and blue points respectively correspond to red-sequence and blue stacked cluster GLFs normalized to 1 deg^2. The red and blue plain curves show the best Schechter fits to red-sequence and blue galaxies and the red and blue vertical lines indicate the corresponding 90% completeness limits. The slope of the fit α is given for each population. Refer to Table 2 for cluster best Schechter fit parameters. The thin dotted and dashed curves correspond to the COSMOS field GLFs centered at redshifts $z = 0.5$ and $z = 0.7$ normalized to 1 deg^2. The separation between red and blue field galaxies is done the same way than for clusters at the corresponding redshift (see text for details).

the GLF is dominated by the low-redshift clusters in the stack. At higher redshifts, we find slopes of between $\alpha_{\rm red} \sim 0.1$ and $\alpha_{\rm red} \sim 0.7$. We have only a few clusters at high redshift, though the error bars in the slope are in the range 0.5 to 1. Data for more high-redshift clusters are needed to fully investigate this behaviour. We also have insufficient clusters with enough blue galaxies to produce blue GLFs at these redshifts.

When interpreting these results in terms of galaxy evolution, we can conclude that blue star forming galaxies are quenched in dense cluster environments to enrich the red-sequence population between high redshifts and today. However, that the properties of blue galaxies in clusters are similar at $z \sim 0$ and our redshift range ($0.4 \leq z < 0.9$) implies that clusters continue to accrete galaxies from the field across a wide range of redshift.

This deficit of faint red galaxies at $z \sim 0.7$ has already been observed by many authors (e.g. Tanaka et al. 2005; De Lucia et al. 2007; Rudnick et al. 2009; Stott et al. 2007; Gilbank et al. 2008; Vulcani et al. 2011). In particular, our strong change in the RS faint-end slope is in good agreement with that found for EDisCs clusters (see Fig. 5 of Rudnick et al. 2009, and our Fig. 9). Kodama et al. (2004) also observed a compensation for the decrease in the faint red galaxy counts by those of bluer galaxies. Furthermore, this evolution agrees with the empirical model of Peng et al. (2010) which predicts a difference between the blue and red faint-end slopes of the order of unity owing to mass quenching being proportional to the star formation rate (SFR) of galaxies in our redshift range.

On the other hand, some authors find no evolution in the RS GLFs with redshift (e.g. Andreon 2006; De Propris et al. 2007, 2013). De Propris et al. (2013) wrote that surface brightness selection effects could account for claims of evolution at the faint end. Observations with various surface brightness limits are required to confirm this hypothesis.

We can only compare our results with GLFs that have been fitted by a single Schechter function. It is sometimes useful to fit GLFs with both a Gaussian and a Schechter function (Biviano et al. 1995) or with two Schechter functions (Popesso et al. 2006). The first case allows to better account for the excess of very bright galaxies observed in certain clusters, while the second fits well the upturn of very faint counts that can exist for dwarf galaxies at fainter magnitudes than the usual GLF flat faint end. In the present study, we chose to use a single Schechter fit, as our data are insufficiently complete to investigate the upturn of very faint galaxies found in Popesso et al. (2006). More sophisticated fitting with a higher number of degrees of freedom for the fit would require a larger number of data points and a fainter completeness limit. We cannot compare our results with those of the following authors because their approaches differ from ours:

- Mancone et al. (2012) studied GLFs only in apparent magnitude. Thus, the k-correction is not taken into account and it is difficult to know exactly which population is studied and the precise completeness limit, particularly since they consider high-redshift clusters ($1 < z < 1.5$);
- Muzzin et al. (2008) fixed the slope of the faint end $\alpha = -0.8$ and fit the two other parameters (ϕ^* and M^*).

5.2. Dependence on environment

Another important debate concerns the interaction between clusters and their environment. To properly address this problem, it is necessary to investigate it on three different scales. First, we compare cluster GLFs to field GLFs, then study the dependence of GLFs on various cluster properties before finally studying the variations inside clusters.

We first compare our cluster GLFs calculated in Sect. 4.2 with field GLFs derived from COSMOS data (Ilbert et al. 2009). We compute two field GLFs for redshifts of 0.5 and 0.7 with a width of ±0.2 around these redshifts to be consistent with the way we made our cluster GLFs. We separate blue from red field galaxies by applying a colour-magnitude relation similar to the one used for our clusters. The ordinate of this red sequence is equal to the colour of elliptical galaxies at the central redshift taken from Fukugita et al. (1995) and the width of the RS is ±0.3 in colour. This allows us to compare cluster and field GLFs computed in the same way with the same separation between red and blue galaxies. Results are shown in Fig. 13.

The GLFs of blue galaxies are similar for the field and clusters in the V, R, and I bands, while we find more blue galaxies in our clusters than the field for the B band but with a similar shape. The shape of the red-sequence GLFs are also almost identical. However, there are about ten times more red galaxies in clusters than the field. Another difference is the GLF of cluster RS galaxies has a sharper drop at the faint end at high redshift, while the field red GLFs remain unchanged across our redshift range. This apparent lack of evolution in early-type field galaxies was assessed in Zucca et al. (2006), who proposed that it highlights an efficient transformation of blue to red galaxies in higher density environments. Inside clusters, interactions between galaxies are more likely to happen, boosting this evolution, while in the field galaxy interactions are less frequent and the red population increases at a far lower rate.

We wrote above that the average cluster GLF of RS galaxies depends on mass. GLFs of more massive clusters ressemble

more the GLFs of nearby clusters with a flat faint end. This implies that these high-redshift massive clusters are more evolved than their companions at the same redshift either because they formed earlier or in a denser environment.

We find no remarkable difference between the properties of general GLF and those of the GLF of only substructured clusters. However, we have only three clusters that can be studied in this way, leading to large error bars. We know that the merging of galaxy clusters can strongly affect the slope of the GLF, as illustrated by studies of cluster pairs or violently merging clusters (e.g. Durret et al. 2010, 2011, 2013). Hence we would expect that substructured clusters present a variation of their faint-end slope compared to others. More data at different stages of the merging process are needed before we can draw stronger conclusions.

Finally, we find differences in GLF behaviours between cluster cores and outskirts. We find more bright galaxies in the core compared to the outskirts, in agreement with CDM models that predict the most massive galaxies to lie at the cluster cores. We also find more blue galaxies in the outskirts than in the core. This larger number of blue galaxies in the outskirts could be explained by infalls from the field. However, the red GLF faint end remains the same in any part of the cluster. Some authors found steeper faint-end slopes in cluster outskirts (e.g. Adami et al. 2008; Bou et al. 2008). In particular, strong variations in α have been observed in the highly structured Coma cluster, which can be probed with high completeness and quality due to its proximity (Adami et al. 2007a,b).

5.3. Evolution of cluster galaxy types with redshift

With colour-selected populations, we analyse the variations of the galaxy types within clusters. We consider blue and red galaxies selected in a colour−magnitude diagram and for which field galaxies have been subtracted. We also remove galaxies that are outside disks of 1 Mpc radius centered on cluster optical centres. We compute the percentages of each type for every cluster and then average them over clusters by stacks of four clusters. Error bars correspond to the dispersion in values over all clusters within a stack. This allows us to study the evolution of cluster galaxy types with redshift from $z = 0.4$ to $z = 0.9$. We limit our sample to galaxies brighter than $I = -21$ and only consider clusters that are at least 90% complete at this magnitude.

Looking at Fig. 14, we note a clear decrease in the fraction of early-type galaxies from low to high redshift, while the fraction of late-type galaxies increases with redshift. This scenario agrees with galaxy-evolution scenarios where spiral galaxies evolve into ellipticals. Furthermore, it is consistent with the evolution of early-type and late-type GLF faint ends that we discussed in Sect. 5.1.

Our early-type fraction decreases from $f_{\rm red} = 0.81 \pm 0.17$ at $z = 0.42$ to $f_{\rm red} = 0.50 \pm 0.27$ at $z = 0.66$. We compare these results to spectral classifications from Ellingson et al. (2001), and also to the morphology-density relation found by Smith et al. (2005) and Postman et al. (2005). In the first case, we overplot on Fig. 14 their best fit to the blue fraction of clusters between $0.18 < z < 0.55$. The blue galaxies taken into account in this study are spectroscopic cluster members and are separated in a colour–magnitude diagram. They are also brighter than $R = -20$, such that it is very close to the low-redshift sample of galaxies we use. We find a very good agreement between our blue fraction and the one from Ellingson et al. (2001) at all redshifts. We do not attempt to separate our sample into high-density (cluster cores) and medium-density regions, so our results should compare with the $\Sigma = 100$ Mpc^{-2} and $\Sigma = 1000$ Mpc^{-2} curves

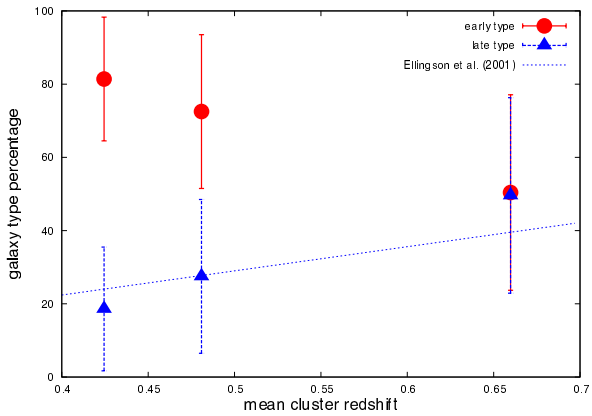

Fig. 14. Evolution of cluster galaxy type percentages with redshift. Each point represents the mean value of a percentage over four clusters. Red dots are red (early type) galaxies and blue triangles correspond to blue (late type) galaxies. The blue dashed line corresponds to the blue fraction from Ellingson et al. (2001).

in Fig. 3 of Smith et al. (2005) and Fig. 13 of Postman et al. (2005). We find an overall good agreement. At intermediate redshift ($z = 0.4$), our early-type fraction lies within the fractions of medium and high density of the cited authors ($f_{E+S0} = 0.6$ and $f_{E+S0} = 0.85$). At higher redshifts ($z = 0.7$), our values are also consistent with the interval $0.55 < f_{E+S0} < 0.8$ found by the previous authors, but only when taking our error bars into account. However, one must note that previous authors used a classification based on galaxy shapes while our work relies on the galaxy colours. The trend of a decreasing early-type fraction with increasing redshift is clearly seen whichever method is used. A comparison of both spectral and morphological methods for the same galaxy sample would help understanding the different biases of each method. Apart from possible biases, the morphological and spectral evolutions might also be different.

5.4. A scenario for the evolution of clusters

Peng et al. (2010) empirically showed that the red sequence is fed by two different types of quenching that happen at different redshifts. At high redshift ($z > 2$), environmental effects dominate and the red sequence grows through the quenching of blue star forming galaxies that fall into the dark matter halo of the forming group ("environment quenching"). At lower redshift ($0 < z < 1$), galaxies are quenched proportionally to their star forming rate and progressively enrich the red sequence ("mass quenching").

Cosmological models of cluster mass assembly predict the most intense mass growth of clusters at redshifts earlier than $z \sim 0.8$ to 1 (e.g. Adami et al. (2013) from the Millennium simulation). In this redshift interval, clusters grow through accretion of major groups, and this already provides a pre-processed galaxy population formed by the cited "environment quenching". This explains the fact that clusters at $z > 1$ already exhibit a red sequence (Gobat et al. 2011; Fassbender et al. 2011).

At lower redshifts ($z < 0.8$), group accretion only concerns more modest groups in terms of relative mass and Guennou et al. (2014) have shown in our survey that this accretion only involves less than 10% to 15% of the cluster mass. In the $0 < z < 0.8$ redshift interval, the galaxies accreted by clusters are therefore not only coming from red populations preprocessed in groups but also from regular blue field galaxy populations. In the meantime,

blue galaxies evolve into red ones following the "mass quenching" defined in Peng et al. (2010).

We can show that this evolutionary scenario for clusters is assessed by the main results of our paper as follows:

1) Red-sequence cluster galaxies show a drop at their faint end which is more significant at higher redshift.
2) Blue cluster GLFs are steeper than those of RS galaxies and are similar across our redshift range and at lower redshift.
3) There is a large excess of red galaxies in clusters compared to the field while the blue galaxies behave more or less in the same way. The red GLFs of clusters continue to evolve across our redshift range, while for the field there is little evolution.
4) There is a strong decrease of the early-type fraction in clusters with increasing redshift.
5) There might be infalls of blue galaxies from the field to the cluster outskirts. This could explain why we find so few blue galaxies in cluster cores compared to the outskirts.
6) When considering our more massive clusters, we find a red-sequence GLF that is consistent with those observed at $z = 0$ with a flat faint end.

The result 1) shows that clusters are formed at redshifts higher than $z = 0.9$. A possible explanation of the redshift dependent drop at the faint end of the red GLFs (point 1) would reside in the blue to red colour evolution in cluster galaxies populating the faint part of the GLF (point 4). This agrees with the mass quenching expected at these redshifts from Peng et al. (2010). The evolution of the red cluster GLFs with redshift compared to the field GLFs (point 3) suggests that red galaxy formation is more efficient in high-density environments. At the same time, a non-negligible infall of faint galaxies from the field (point 5) could explain how the blue GLF faint end remains the same from $z \sim 0.9$ to 0 (point 2). Our discovery that very massive clusters have the same red GLF faint end as clusters in the nearby Universe (point 6) indicates that cluster evolution can be faster in denser environments or that some clusters formed earlier than others.

6. Conclusion

We have computed GLFs in the B, V, R, and I rest-frame bands for 31 clusters of the DAFT/FADA survey using photo-zs, the largest medium-to-high redshift ($0.4 \leq z < 0.9$) cluster sample to date.

To overcome the problem of lower photometric redshift precision in clusters mainly due to a lack of red enough spectral templates, we have artificially allowed the inclusion of extinction in early-type galaxies. This process does not affect drastically photometric redshifts outside clusters but increases their quality by ~50% inside clusters, allowing us to reach the same precision inside and outside the cluster.

Another result of this paper is that GLFs are strongly correlated to the completeness of the data. This should be kept in mind when comparing GLFs from different studies.

We have shown that GLFs have similar properties for the B, V, R, and I rest-frame bands with small differences for the B band blue GLFs. We found a sharp decline in the red faint end that increases with redshift: $\alpha_{\rm red} \sim -0.5$ at $0.40 \leq z < 0.65$ and $\alpha_{\rm red} > 0.1$ at $0.65 \leq z < 0.90$. High mass clusters appear to have a flat faint end which may indicate that galaxy evolution is more rapid in denser environments or different formation epochs for clusters of different masses. Blue GLFs are steeper with $\alpha_{\rm blue} \sim -1.6$ and do not seem to evolve with redshift.

Our study of galaxy types with redshift shows an evolution of late-type galaxies to early types from high z until today that could account for the drop found at the red faint end.

We also found an excess of red galaxies in clusters compared to the field, while blue galaxies have more or less identical GLFs.

Our results imply that clusters have formed at high redshift ($z > 0.9$) and that blue cluster galaxies are efficiently quenched into red ones between $z \sim 0.9$ and today. During this time interval, galaxy clusters continue to accrete faint galaxies from the field environment.

Finally, we note an inversion of the red to blue population dominance at magnitudes $V = -20$, $R = -20.5$, and $I = -20.3$ at redshift $0.40 \leq z < 0.90$. We plan to compute stellar mass functions (SMFs) in a future paper, to see whether the blue and red populations have comparable behaviours in mass and luminosity. This would allow us to compare our results with simulations of galaxy cluster formation.

Acknowledgements. We thank Greg Rudnick for useful discussions. We also thank Eric Jullo, Marceau Limousin, Dennis Zaritsky for comments on earlier versions of this paper. We are grateful to the referee for interesting comments. F.D. acknowledges long-term financial support from CNES. I.M. acknowledges financial support from the Spanish grant AYA2010-15169 and from the Junta de Andalucia through TIC-114 and the Excellence Project P08-TIC-03531. Based on observations made with the FORS2 multi-object spectrograph mounted on the Antu VLT telescope at ESO-Paranal Observatory (programme 085.A-0016, 089A-0666, 191.A-0268; PI: C. Adami). Also based on observations made with the Italian Telescopio Nazionale *Galileo* (TNG) operated on the island of La Palma by the Fundaci n Galileo Galilei of the INAF (Istituto Nazionale di Astrofisica) at the Spanish Observatorio del Roque de los Muchachos of the Instituto de Astrof sica de Canarias. Based on observations obtained with MegaPrime/MegaCam, a joint project of CFHT and CEA/IRFU, at the Canada-France-Hawaii Telescope (CFHT) which is operated by the National Research Council (NRC) of Canada, the Institut National des Science de l'Univers of the Centre National de la Recherche Scientifique (CNRS) of France, and the University of Hawaii. This work is based in part on data products produced at Terapix available at the Canadian Astronomy Data Centre as part of the Canada-France-Hawaii Telescope Legacy Survey, a collaborative project of NRC and CNRS. Also based on observations obtained at the WIYN telescope (KNPO). The WIYN Observatory is a joint facility of the University of Wisconsin-Madison, Indiana University, Yale University, and the National Optical Astronomy Observatory. Kitt Peak National Observatory, National Optical Astronomy Observatory. It is operated by the Association of Universities for Research in Astronomy (AURA) under cooperative agreement with the National Science Foundation. Also based on observations obtained at the MDM observatory (2.4 m telescope). MDM consortium partners are Columbia University Department of Astronomy and Astrophysics, Dartmouth College Department of Physics and Astronomy, University of Michigan Astronomy Department, The Ohio State University Astronomy Department, and the Ohio University Dept. of Physics and Astronomy. Also based on observations obtained at the Southern Astrophysical Research (SOAR) telescope, which is a joint project of the Minist rio da Ci ncia, Tecnologia, e Inova o (MCTI) da Rep blica Federativa do Brasil, the US National Optical Astronomy Observatory (NOAO), the University of North Carolina at Chapel Hill (UNC), and Michigan State University (MSU). Also based on observations obtained at the Cerro Tololo Inter-American Observatory, National Optical Astronomy Observatory, which are operated by the Association of Universities for Research in Astronomy, under contract with the National Science Foundation. Also based on observations made with the Gran Telescopio Canarias (GTC), installed at the Spanish Observatorio del Roque de los Muchachos of the Instituto de Astrof sica de Canarias, on the island of La Palma. Also based on archive data collected at the Subaru Telescope, which is operated by the National Astronomical Observatory of Japan. Finally, this research has made use of the VizieR catalogue access tool at the CDS, Strasbourg, France.

References

Adami, C., Picat, J. P., Savine, C., et al. 2006, A&A, 451, 1159
Adami, C., Durret, F., Mazure, A., et al. 2007a, A&A, 462, 411
Adami, C., Picat, J.-P., Durret, F. et al. 2007b, A&A, 472, 749
Adami, C., Ilbert, O., Pell , R., et al. 2008, A&A, 491, 681
Adami, C., Le Brun, V., Biviano, A., et al. 2009, A&A, 507, 1225
Adami, C., Mazure, A., Pierre, M., et al. 2011, A&A, 526, A18

Adami, C., Durret, F., Guennou, L., & Da Rocha, C. 2013, A&A, 551, A20
Andreon, S. 2004, A&A, 416, 865
Andreon, S. 2006, MNRAS, 369, 969
Andreon, S., Cuillandre, J.-C., Puddu, E., & Mellier, Y. 2006, MNRAS, 372, 60
Arnouts, S., Cristiani, S., Moscardini, L., et al. 1999, MNRAS, 310, 540
Bertin, E. 2006, ASP Conf. Ser., 351, 112
Bertin, E. 2011, ASP Conf. Ser., 442, 435
Bertin, E., & Arnouts, S. 1996, A&AS, 317, 393
Bertin, E., Mellier, Y., Radovich, M., et al. 2002, ASP Conf. Ser., 281, 228
Biviano, A., Durret, F., Gerbal, D., et al. 1995, A&A, 297, 610
Biviano, A., Fadda, D., Durret, F., Edwards, L. O. V., & Marleau, F. 2011, A&A, 532, A77
Bou , G., Adami, C., Durret, F., Mamon, G. A., & Cayatte, V. 2008, A&A, 479, 335
Bruzual, G., & Charlot, S. 2003, MNRAS, 344, 1000
Calzetti, D., & Heckman, T. M. 1999, ApJ, 519, 27
Chilingarian, I. V., Melchior, A.-L., & Zolotukhin, I. Y. 2010, MNRAS, 405, 1409
Christlein, D., & Zabludoff, A. 2003, ApJ, 591, 764
Colless, M. 1989, MNRAS, 237, 799
Coupon, J., Ilbert, O., Kilbinger, M., et al. 2009, A&A, 500, 981
De Lucia, G., Poggianti, B. M., Arag n-Salamanca, A., et al. 2004, ApJ, 610, L77
De Lucia, G., Poggianti, B. M., Aragoń-Salamanca, A., et al. 2007, MNRAS, 374, 809
De Propris, R., Stanford, S. A., Eisenhardt, P. R., Dickinson, M., & Elston, R. 1999, AJ, 118, 719
De Propris, R., Colless, M., Driver, S. P., et al. 2003, MNRAS, 342, 725
De Propris, R., Stanford, S. A., Eisenhardt, P. R., Holden, B. P., & Rosati, P. 2007, AJ, 133, 2209
De Propris, R., Phillipps, S., & Bremer, M. N. 2013, MNRAS, 434, 3469
Dressler, A. 1978, ApJ, 223, 765
Driver, S. P., Fernandez-Soto, A., Couch, W. J., et al. 1998, ApJ, 496, L93
Durret, F., Lagan , T. F., Adami, C., & Bertin, E. 2010, A&A, 517, A94
Durret, F., Lagan , T., & Haider, M. 2011, A&A, 529, A38
Durret, F., Perrot, C., Lima Neto, G. B., et al. 2013, A&A, 560, A78
Ellingson, E., Lin, H., Yee, H. K. C., & Carlberg, R. G. 2001, ApJ, 547, 609
Fassbender, R., Nastasi, A., B hringer, H., et al. 2011, A&A, 527, L10
Fukugita, M., Shimasaku, K., & Ichikawa, T. 1995, PASP, 107, 945
Gaidos, E. J. 1997, AJ, 113, 117
Garilli, B., Maccagni, D., & Andreon, S. 1999, A&A, 342, 408
Gilbank, D. G., Yee, H. K. C., Ellingson, E., et al. 2008, ApJ, 673, 742
Gobat, R., Daddi, E., Onodera, M., et al. 2011, A&A, 526, A133
Gonzalez, A. H., Zaritsky, D., Dalcanton, J. J., & Nelson, A. 2001, ApJS, 137, 117
Goto, T., Okamura, S., McKay, T. A., et al. 2002, PASJ, 54, 515
Guennou, L., Adami, C., Ulmer, M. P., et al. 2010, A&A, 523, A21
Guennou, L., Adami, C., Durret, F., et al. 2014, A&A, 561, A112
Gunn, J. E., & Gott, J. R. III 1972, ApJ, 176, 1
Ilbert, O., Tresse, L., Zucca, E., et al. 2005, A&A, 439, 863
Ilbert, O., Arnouts, S., McCracken, H. J., et al. 2006a, A&A, 457, 841
Ilbert, O., Lauger, S., Tresse, L., et al. 2006b, A&A, 453, 809
Ilbert, O., Capak, P., Salvato, M., et al. 2008, ApJ, 690, 1236
Kodama, T., Yamada, T., Akiyama, M., et al. 2004, MNRAS, 350, 1005
Lanzoni, B., Guiderdoni, B., Mamon, G. A., Devriendt, J., & Hatton, S. 2005, MNRAS, 361, 369
Lopez-Cruz, O., Yee, H. K. C., Brown, J. P., Jones, C., & Forman, W. 1997, ApJ, 475, 97
Lugger, P. M. 1986, ApJ, 303, 535
Lugger, P. M. 1989, ApJ, 343, 572
Lumsden, S. L., Collins, C. A., Nichol, R. C., Eke, V. R., & Guzzo, L. 1997, MNRAS, 290, 119
Mancone, C. L., Gonzalez, A. H., Brodwin, M., et al. 2010, ApJ, 720, 284
Mancone, C. L., Baker, T., Gonzalez, A. H., et al. 2012, ApJ, 761, 141
Martini, P., Dicken, D., & Storchi-Bergmann, T. 2013, ApJ, 766, 121
Menci, N., Cavaliere, A., Fontana, A., Giallongo, E., & Poli, F. 2002, ApJ, 575, 18
Moore, B., Katz, N., Lake, G., Dressler, A., & Oemler, A. 1996, Nature, 379, 613
Moore, B., Lake, G., & Katz, N. 1998, ApJ, 495, 139
Muzzin, A., Wilson, G., Lacy, M., Yee, H. K. C., & Stanford, S. A. 2008, ApJ, 686, 966
Paolillo, M., Andreon, S., Longo, G., et al. 2001, A&A, 367, 59
Peng, Y.-J., Lilly, S. J., Kovac, K., et al. 2010, ApJ, 721, 193
Poggianti, B. M., von der Linden, A., De Lucia, G., et al. 2006, ApJ, 642, 188
Polletta, M., Wilkes, B. J., Siana, B., et al. 2006, ApJ, 642, 673
Polletta, M., Tajer, M., Maraschi, L., et al. 2007, ApJ, 663, 81
Popesso, P., Biviano, A., B hringer, H., & Romaniello, M. 2006, A&A, 445, 29
Postman, M., Franx, M., Cross, N. J. G., et al. 2005, ApJ, 623, 721
Rauzy, S., Adami, C., & Mazure, A. 1998, A&A, 337, 31
Rudnick, G., Von der Linden, A., Pell , R., et al. 2009, ApJ, 700, 1559
Secker, J., Harris, W. E., & Plummer, J. D. 1997, PASP, 109, 1377
Schechter, P. 1976, ApJ, 203, 297
Schlegel, D. J., Finkbeiner, D. P., & Davis, M. 1998, ApJ, 500, 525
Smail, I., Edge, A. C., Ellis, R. S., & Blandford, R. D. 1998, MNRAS, 293, 124
Smith, G. P., Treu, T., Ellis, R. S., Moran, S. M., & Dressler, A. 2005, ApJ, 620, 78
Stott, J. P., Smail, I., Edge, A. C., et al. 2007, ApJ, 661, 95
Tanaka, M., Kodama, T., Arimoto, N., et al. 2005, MNRAS, 362, 268
Trentham, N. 1998, MNRAS, 294, 193
Tully, R. B., Somerville, R. S., Trentham, N., & Verheijen, M. A. W. 2002, ApJ, 569, 573
Valotto, C. A., Nicotra, M. A., Muriel, H., & Lambas, D. G. 1997, ApJ, 479, 90
Vulcani, B., Poggianti, B., Arag n-Salamanca, A., et al. 2011, MNRAS, 412, 246
Yagi, M., Kashikawa, N., Sekiguchi, M., et al. 2002, AJ, 123, 66
Zucca, E., Ilbert, O., Bardelli, S., et al. 2006, A&A, 455, 879

Pages 19 to 24 are available in the electronic edition of the journal at http://www.aanda.org

Appendix A: Individual cluster GLFs

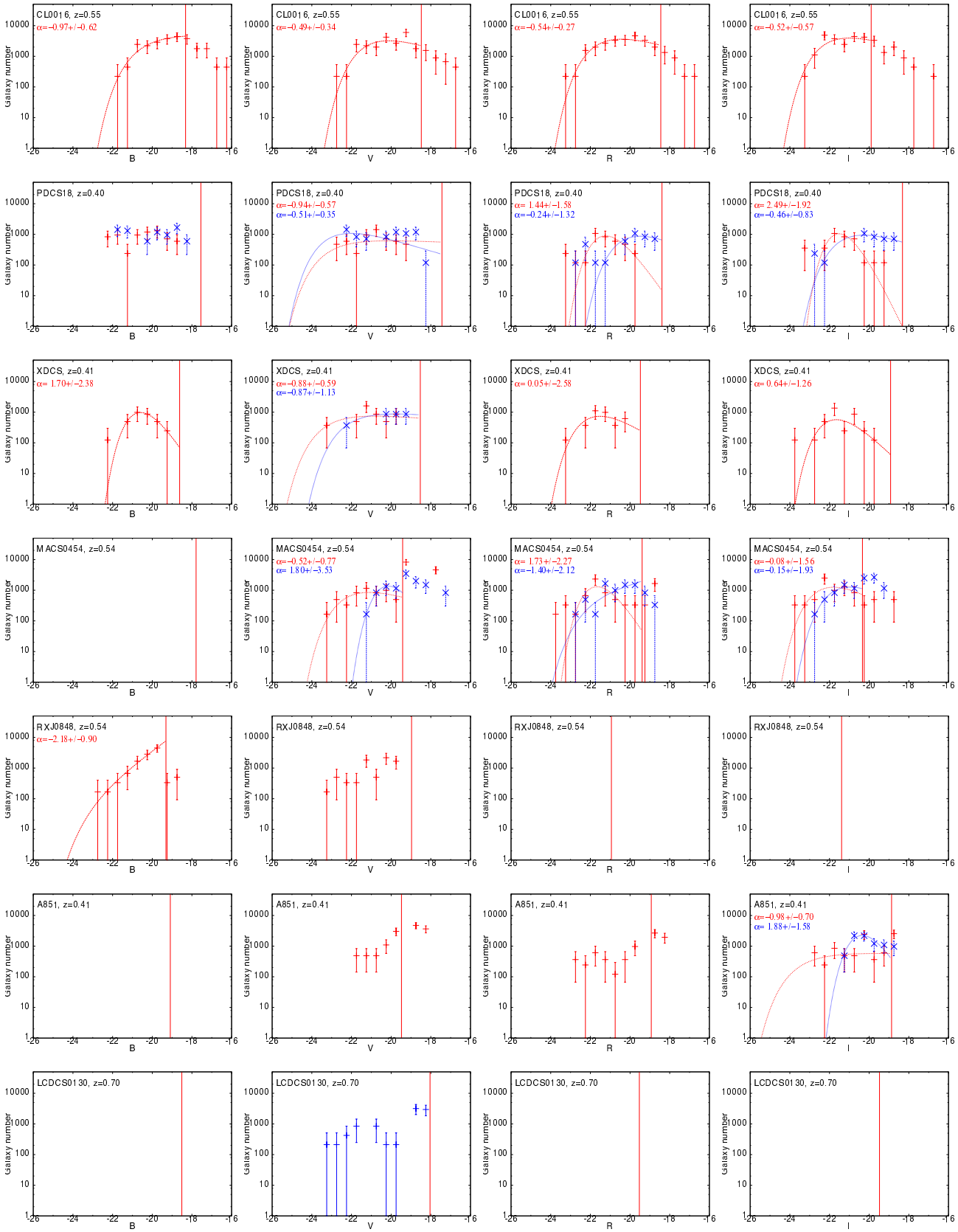

Fig. A.1. GLFs in the B, V, R and I rest-frame bands (*from left to right*) for individual clusters ordered by right ascension. Red and blue points correspond to red-sequence and blue GLFs normalized to 1 deg^2. The red vertical lines indicate the 90% completeness limit. The red and blue curves show the best Schechter fits to red sequence and blue galaxies, and the faint-end slope parameter (α) is displayed in the corresponding colour. Only galaxies brighter than the 90% completeness limit are taken into account in the fits. Also, we only show GLFs richer than 20 galaxies after the colour separation and after subtracting the field.

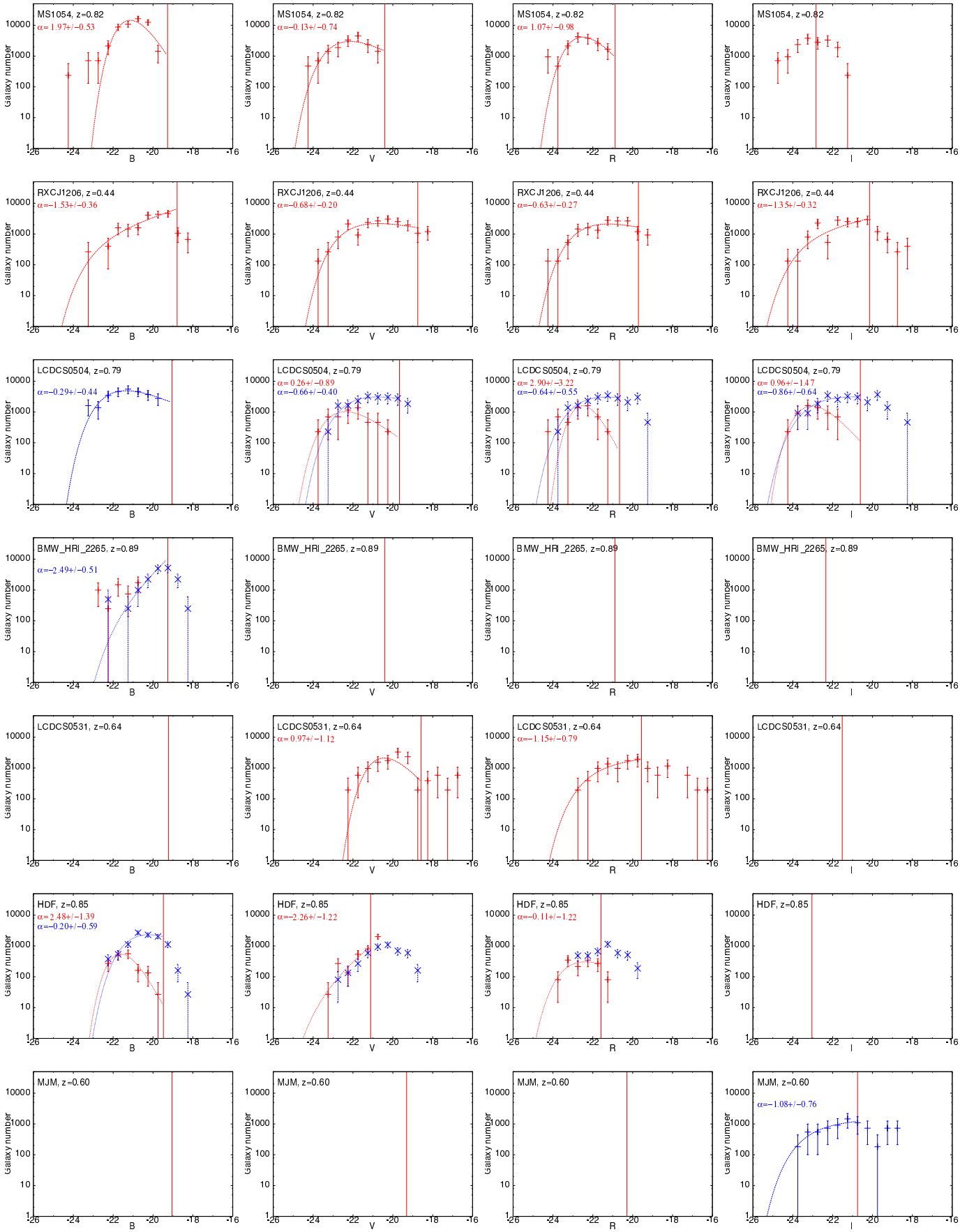

Fig. A.1. continued.

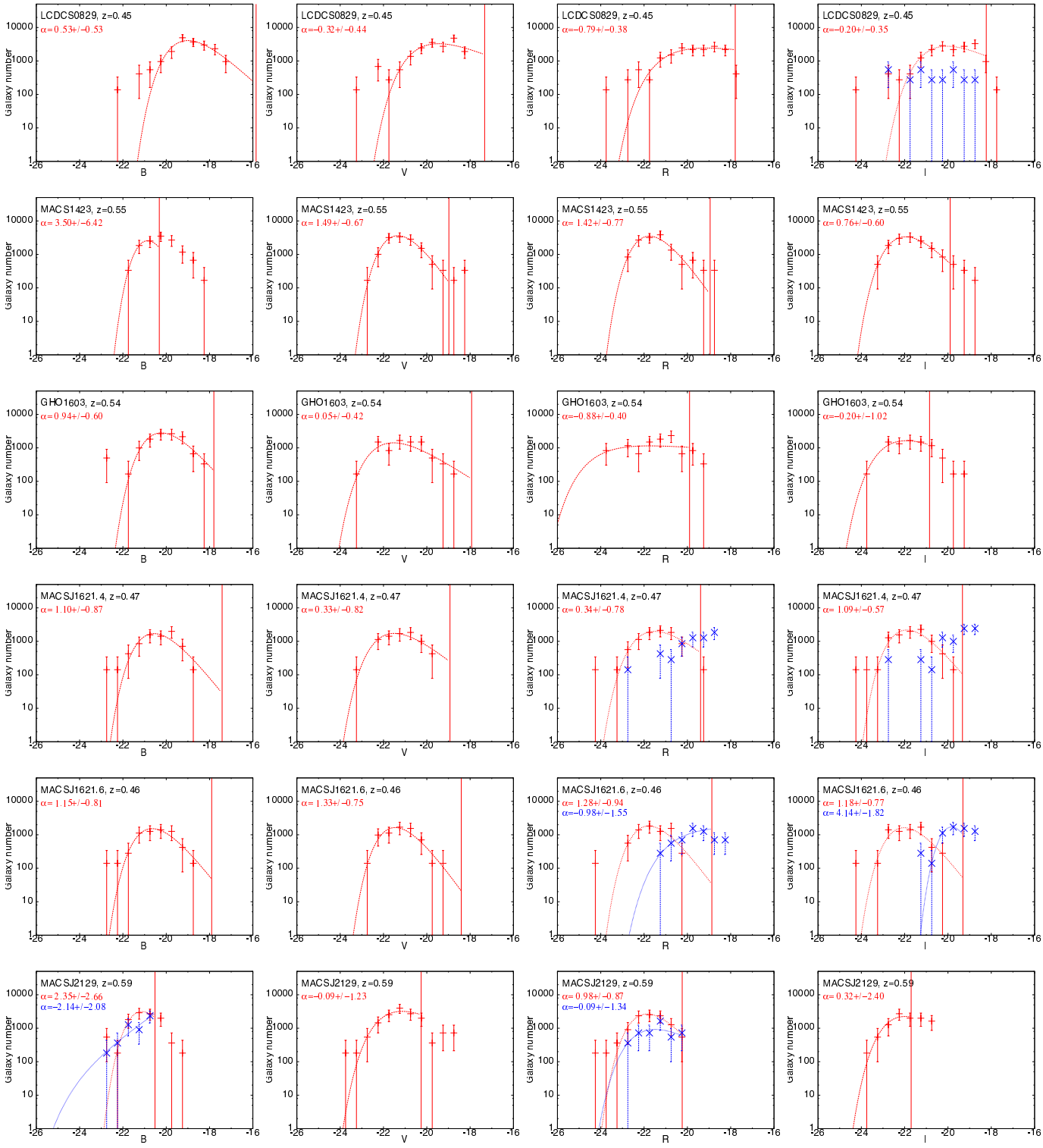

Fig. A.1. continued.

Table A.1. Parameters of the best Schechter function fit for every cluster normalized to 1 deg^2.

			Red-sequence GLFs			Blue GLFs		
	z	comp	α	M^*	ϕ^* (deg^{-2})	α	M^*	ϕ^* (deg^{-2})
CL0016	0.55							
B		−18.3	−0.97 ± 0.62	−20.4 ± 0.8	6052 ± 5477	–	–	–
V		−18.5	−0.49 ± 0.34	−20.9 ± 0.4	8154 ± 2893	–	–	–
R		−18.5	−0.54 ± 0.27	−21.3 ± 0.4	8890 ± 3012	–	–	–
I		−19.9	−0.52 ± 0.57	−21.8 ± 0.5	9801 ± 4369	–	–	–
PDCS18	0.40							
B		−17.5	–	–	–	–	–	–
V		−17.4	−0.94 ± 0.57	−23.1 ± 3.3	848 ± 1401	−0.51 ± 0.35	−22.8 ± 2.7	2708 ± 976
R		−18.4	1.44 ± 1.58	−20.3 ± 0.6	1264 ± 1478	−0.24 ± 1.32	−19.8 ± 1.2	2487 ± 1518
I		−18.3	2.49 ± 1.92	−20.2 ± 0.6	474 ± 1020	−0.46 ± 0.83	−20.9 ± 1.0	2451 ± 2304
XDCS	0.41							
B		−18.6	1.70 ± 2.38	−19.5 ± 1.1	1074 ± 2218	–	–	–
V		−18.5	−0.88 ± 0.59	−23.1 ± 2.0	1184 ± 1611	−0.87 ± 1.13	−22.0 ± 2.6	1412 ± 3337
R		−19.5	0.05 ± 2.58	−21.5 ± 2.5	2165 ± 1106	–	–	–
I		−18.9	0.64 ± 1.26	−21.1 ± 0.8	1416 ± 643	–	–	–
MACS0454	0.54							
B		−17.8	–	–	–	–	–	–
V		−19.4	−0.52 ± 0.77	−21.9 ± 1.3	2114 ± 1841	1.80 ± 3.53	−19.0 ± 1.0	1364 ± 4734
R		−19.4	1.73 ± 2.27	−20.6 ± 0.8	1402 ± 2655	−1.40 ± 2.12	−22.0 ± 7.0	925 ± 6462
I		−20.3	−0.08 ± 1.56	−21.9 ± 1.4	3687 ± 1988	−0.15 ± 1.93	−21.1 ± 1.3	3700 ± 1604
RXJ0848	0.54							
B		−19.3	−2.18 ± 0.90	−22.9 ± 6.5	173 ± 1607	–	–	–
V		−19.0	–	–	–	–	–	–
R		−20.9	–	–	–	–	–	–
I		−21.4	–	–	–	–	–	–
A851	0.41							
B		−19.1	–	–	–	–	–	–
V		−19.5	–	–	–	–	–	–
R		−18.9	–	–	–	–	–	–
I		−18.9	−0.98 ± 0.70	−23.4 ± 6.2	691 ± 1625	1.88 ± 1.58	−19.2 ± 0.5	2047 ± 3034
LCDCS0130	0.70							
B		−18.5	–	–	–	–	–	–
V		−18.0	–	–	–	–	–	–
R		−19.5	–	–	–	–	–	–
I		−19.5	–	–	–	–	–	–
MS1054	0.82							
B		−19.3	1.97 ± 0.53	−20.0 ± 0.2	12219 ± 6210	–	–	–
V		−20.4	−0.13 ± 0.74	−22.3 ± 0.9	8736 ± 3317	–	–	–
R		−20.9	1.07 ± 0.98	−21.7 ± 0.5	7890 ± 4505	–	–	–
I		−22.8	–	–	–	–	–	–

Notes. Fits are done to the cluster 90% completeness limit in the selected band. A "–" means the fit has not converged due to a too bright completeness limit or because the selected cluster population is poorer than 20. Clusters with too few galaxy counts in every band (see Sect. 4.1 for details) are not displayed. As noted above, clusters for which the fit with a Schechter function does not converge are kept in the table when they are taken into account in the stacked GLFs. There can be large differences between our parameters and the literature for some clusters, as we do not adapt the completeness limit nor any step of our method to individual clusters. This choice is made not to bias the study of stacked GLFs.

Table A.1. continued.

			Red-sequence GLFs			Blue GLFs		
	z	comp	α	M^*	ϕ^* (deg^{-2})	α	M^*	ϕ^* (deg^{-2})
RXCJ1206	0.44							
B		−18.8	−1.53 ± 0.36	−22.6 ± 1.9	1108 ± 2244	–	–	–
V		−18.8	−0.68 ± 0.20	−22.0 ± 0.5	4719 ± 1692	–	–	–
R		−19.7	−0.63 ± 0.27	−22.3 ± 0.4	4830 ± 1798	–	–	–
I		−20.1	−1.35 ± 0.32	−23.3 ± 0.9	1355 ± 1463	–	–	–
LCDCS0504	0.79							
B		−19.0	–	–	–	−0.29 ± 0.44	−21.7 ± 0.6	13 856 ± 4540
V		−19.7	0.26 ± 0.89	−22.1 ± 0.8	2945 ± 928	−0.66 ± 0.40	−21.9 ± 0.6	6768 ± 3392
R		−20.7	2.90 ± 3.22	−21.0 ± 1.0	427 ± 1710	−0.64 ± 0.55	−22.4 ± 0.7	6929 ± 3919
I		−20.6	0.96 ± 1.47	−22.3 ± 0.7	3216 ± 2523	−0.86 ± 0.64	−22.9 ± 1.2	5148 ± 5522
BMW HRI 2265	0.89							
B		−19.3	–	–	–	−2.49 ± 0.51	−21.4 ± 0.4	760 ± 280
V		−20.4	–	–	–	–	–	–
R		−20.9	–	–	–	–	–	–
I		−22.3	–	–	–	–	–	–
LCDCS0531	0.64							
B		−19.2	3.02 ± 6.97	−18.6 ± 1.7	298 ± 2694	–	–	–
V		−18.6	0.97 ± 1.12	−19.7 ± 0.9	4316 ± 2356	–	–	–
R		−19.6	−1.15 ± 0.79	−22.1 ± 1.6	1661 ± 2945	–	–	–
I		−21.5	–	–	–	–	–	–
HDF	0.85							
B		−19.5	2.48 ± 1.39	−20.3 ± 0.5	253 ± 397	−0.20 ± 0.59	−20.5 ± 0.5	6700 ± 1326
V		−21.1	−2.26 ± 1.22	−23.3 ± 3.3	101 ± 705	–	–	–
R		−21.6	−0.11 ± 1.22	−22.5 ± 0.9	898 ± 298	–	–	–
I		−23.0	–	–	–	–	–	–
MJM	0.60							
B		−19.0	–	–	–	–	–	–
V		−19.3	–	–	–	–	–	–
R		−20.3	–	–	–	–	–	–
I		−20.8	–	–	–	−1.08 ± 0.76	−23.2 ± 1.7	1237 ± 2135
LCDCS0829	0.45							
B		−15.9	0.53 ± 0.53	−18.5 ± 0.4	10 607 ± 1628	–	–	–
V		−17.3	−0.32 ± 0.44	−19.9 ± 0.5	9134 ± 2822	−1.28 ± 0.69	−25.1 ± 5.3	169 ± 1395
R		−17.8	−0.79 ± 0.38	−20.8 ± 0.7	4557 ± 2803	–	–	–
I		−18.2	−0.20 ± 0.35	−20.3 ± 0.4	7954 ± 1915	–	–	–
MACS1423	0.55							
B		−20.3	3.50 ± 6.42	−19.2 ± 1.1	289 ± 2779	–	–	–
V		−19.0	1.49 ± 0.67	−20.3 ± 0.3	4896 ± 2472	–	–	–
R		−19.0	1.42 ± 0.77	−20.8 ± 0.4	5075 ± 2773	–	–	–
I		−19.9	0.76 ± 0.60	−21.3 ± 0.4	7855 ± 2017	–	–	–
GHO1603	0.54							
B		−17.8	0.94 ± 0.60	−19.5 ± 0.4	5867 ± 1806	–	–	–
V		−17.9	0.05 ± 0.42	−21.5 ± 0.6	4176 ± 1046	–	–	–
R		−19.9	−0.88 ± 0.40	−24.1 ± 2.2	1798 ± 1822	–	–	–
I		−20.9	−0.20 ± 1.02	−22.2 ± 0.8	4730 ± 1836	–	–	–

Table A.1. continued.

			Red-sequence GLFs			Blue GLFs		
	z	comp	α	M^*	ϕ^* (deg^{-2})	α	M^*	ϕ^* (deg^{-2})
MACSJ1621.4	0.47							
B		−17.4	1.10 ± 0.87	−19.8 ± 0.6	3178 ± 1590	–	–	–
V		−18.9	0.33 ± 0.82	−21.2 ± 0.9	4839 ± 977	–	–	–
R		−19.4	0.34 ± 0.78	−21.2 ± 0.6	5552 ± 1098	–	–	–
I		−19.3	1.09 ± 0.57	−21.1 ± 0.3	4098 ± 1396	–	–	–
MACSJ1621.6	0.46							
B		−17.9	1.15 ± 0.81	−19.8 ± 0.5	2735 ± 1358	–	–	–
V		−18.4	1.33 ± 0.75	−20.5 ± 0.4	2554 ± 1344	–	–	–
R		−18.9	1.28 ± 0.94	−20.9 ± 0.5	2974 ± 1916	−0.98 ± 1.55	−20.5 ± 2.1	2120 ± 4595
I		−19.3	1.18 ± 0.77	−21.2 ± 0.4	2855 ± 1412	4.14 ± 1.82	−18.1 ± 0.3	71 ± 210
MACSJ2129	0.59							
B		−20.5	2.35 ± 2.66	−19.8 ± 0.6	1702 ± 5290	−2.14 ± 2.08	−24.0 ± 9.0	81 ± 1959
V		−20.3	−0.09 ± 1.23	−21.2 ± 0.9	9395 ± 2567	–	–	–
R		−20.2	0.98 ± 0.87	−21.1 ± 0.5	5394 ± 2441	−0.09 ± 1.34	−21.6 ± 1.3	2702 ± 1393
I		−21.7	0.32 ± 2.40	−21.7 ± 1.2	6318 ± 4242	–	–	–

2.2 Fraction of baryons

This section presents the results from Laganá et al. (2013): *A comprehensive picture of baryons in groups and clusters of galaxies*. The first subsection briefly summarizes the paper, its context, aims, methods, results, and conclusions. The detailed study can be read in the second subsection, where we display the article.

2.2.1 Summary

Context

While cluster formation processes imply that they form by hierarchical merging of small groups (see Sect. 1.1.2), the observations of groups of galaxies show that they are not the scaled-down version of galaxy clusters (e.g. Mulchaey 2000; Ponman et al. 2003; Voit 2005). Since galaxy groups are cooler with shallower potential wells, non-gravitational effects defined in Sect. 1.1.3 play a more significant role in less massive systems, altering the gas to galaxy mass ratio. In clusters, the gas is the baryon-dominant component (about 6 times more massive than the stellar mass). While in groups, the gas mass is significantly lower: it is of the same order as the stellar mass and in some cases, even lower than the stellar component (e.g. Giodini et al. 2009).

The analysis of both components is critical for observational cosmology when using groups and clusters to constrain the Ω_M parameter from the observed baryon mass fraction (see Sect. 1.2.2), defined as $f_{\rm b} = (M_{\rm gas} + M_{\rm star})/M_{\rm tot}$.

Aims

Based on XMM-Newton, Chandra, and SDSS data, we investigate the baryon distribution in groups and clusters and its use as a cosmological constraint. For this, we considered a sample of 123 systems with temperatures $kT_{500} = 1.0 - 9.0$ keV, total masses in the mass range $M_{500} = (\sim 10^{13} - 4 \times 10^{15}) h_{70}^{-1} M_{\odot}$, and redshifts $0.02 < z < 1.3$. Among these systems, 9 are groups of galaxies with masses lower than $8 \times 10^{13} M_{\odot}$.

Methods

The gas masses and total masses are derived from X-ray data under the assumption of spherical symmetry. The surface brightness profile is fitted by a β-model and the temperature profile by an empirical relation (see Fig. 2.3). The gas mass is then obtained by integration of the gas mass density expressed as a function of the β parameter, and assuming it is isothermal. The total mass is computed from the derivative of the density and temperature profiles with respect to the distance to the cluster center, and assuming hydrostatic equilibrium.

The stellar masses are based on SDSS-DR8 optical photometric data, and computed from the sum of the luminosity of every galaxy in the cluster redshift area, using photometric redshifts from the SDSS. A background correction is then performed by subtracting the mass of every galaxy in the same redshift range, but in an annulus centered on the cluster, with a large inner radius, and normalized to the cluster area.

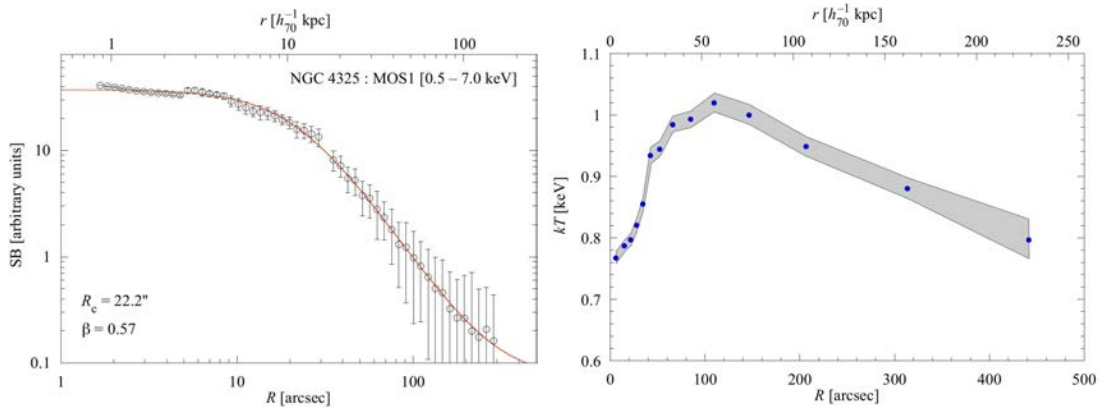

Figure 2.3: X-ray gas surface brightness (*Left*) and temperature profiles (*Right*) for my favorite group: NGC4325. The red curve in the left panel corresponds to the fit by a β-model.

For the 37 systems out of 123 that had both optical and X-ray data available, we investigated the gas, stellar, and total baryon mass fractions inside r_{2500} and r_{500} and the differential gas mass fraction within the spherical annulus between r_{2500} and r_{500} , as a function of total mass. For the other objects, we investigated the gas mass fraction only.

Results

We find that the gas mass fraction inside r_{2500} and r_{500} depends on the total mass. However, the differential gas mass fraction does not show any dependence on total mass for systems with $M_{500} > 10^{14} M_{\odot}$. The stellar mass fraction inside r_{2500} and r_{500} increases towards low-mass systems more steeply than the $f_{\rm gas}$ decreases with total mass. Adding the gas and stellar mass fractions to obtain the total baryonic content, we find it to increase with cluster mass, reaching the WMAP-7 value for clusters with $M_{500} \sim 10^{14} M_{\odot}$.

Conclusions

The gas mass fraction dependence on total mass observed for groups and clusters could be due to the difficulty for low-mass systems to retain gas inside the inner region ($r < r_{2500}$). Because of their shallower potential well, non-thermal processes are more effective in expelling the gas from their central regions outwards. Since the differential gas mass fraction is nearly constant, it provides better constraints for cosmology. Moreover, we find that the gas mass fraction does not depend on redshift at a 2σ level. Using our total $f_{\rm b}$ estimates together with WMAP-7 priors on $\Omega_{\rm b}$ from Jarosik et al. (2011), we put constraints on the matter density parameter Ω_M as described in eq. 1.11 of Sect. 1.2.2. Our results imply $\Omega_M < 0.55$, and taking the highest significant estimates for $f_{\rm b}$, $\Omega_M > 0.22$.

2.2.2 Laganá et al. 2013

A&A 555, A66 (2013)
DOI: 10.1051/0004-6361/201220423

Astronomy & Astrophysics

A comprehensive picture of baryons in groups and clusters of galaxies⋆

T. F. Lagan [1], N. Martinet[2], F. Durret[2], G. B. Lima Neto[1], B. Maughan[3], and Y.-Y. Zhang[4]

[1] IAG, USP, R. do Mat o 1226, 05508-090 S o Paulo/SP, Brazil
e-mail: tflagana@astro.iag.usp.br
[2] UPMC – CNRS, UMR7095, Institut d'Astrophysique de Paris 98bis Bd Arago, 75014 Paris, France
[3] H. H. Wills Physics Laboratory, University of Bristol, Tyndall Ave, Bristol BS8 1TL, UK
[4] Argelander-Institut f r Astronomie, Universit t Bonn, Auf dem H gel 71, 53121 Bonn, Germany

Received 20 September 2012 / Accepted 22 April 2013

ABSTRACT

Aims. Based on *XMM-Newton*, *Chandra*, and SDSS data, we investigate the baryon distribution in groups and clusters and its use as a cosmological constraint. For this, we considered a sample of 123 systems with temperatures kT_{500} = 1.0–9.0 keV, total masses in the mass range $M_{500} = (\sim 10^{13}–4 \times 10^{15})\ h_{70}^{-1}\ M_{\odot}$, and redshifts $0.02 < z < 1.3$.
Methods. The gas masses and total masses are derived from X-ray data under the assumption of hydrostatic equilibrium and spherical symmetry. The stellar masses are based on SDSS-DR8 optical photometric data. For the 37 systems out of 123 that had both optical and X-ray data available, we investigated the gas, stellar, and total baryon mass fractions inside r_{2500} and r_{500} and the differential gas mass fraction within the spherical annulus between r_{2500} and r_{500}, as a function of total mass. For the other objects, we investigated the gas mass fraction only.
Results. We find that the gas mass fraction inside r_{2500} and r_{500} depends on the total mass. However, the differential gas mass fraction does not show any dependence on total mass for systems with $M_{500} > 10^{14}\ M_{\odot}$. The stellar mass fraction inside r_{2500} and r_{500} increases towards low-mass systems more steeply than the $f_{\rm gas}$ decrease with total mass. Adding the gas and stellar mass fractions to obtain the total baryonic content, we find it to increase with cluster mass, reaching the WMAP-7 value for clusters with $M_{500} \sim 10^{14}\ M_{\odot}$. This led us to investigate the contribution of the intracluster light to the total baryon budget for lower mass systems, but we find that it cannot account for the difference observed.
Conclusions. The gas mass fraction dependence on total mass observed for groups and clusters could be due to the difficulty of low-mass systems to retain gas inside the inner region ($r < r_{2500}$). Because of their shallower potential well, non-thermal processes are more effective in expelling the gas from their central regions outwards. Since the differential gas mass fraction is nearly constant, it provides better constraints for cosmology. Moreover, we find that the gas mass fraction does not depend on redshift at a 2σ level. Using our total $f_{\rm b}$ estimates, our results imply $\Omega_{\rm m} < 0.55$, and taking the highest significant estimates for $f_{\rm b}$, $\Omega_{\rm m} > 0.22$.

Key words. galaxies: clusters: general – cosmological parameters – galaxies: clusters: intracluster medium

1. Introduction

Considering the hierarchical scenario of structure formation, the groups we observe today are the building blocks of future galaxy clusters. Although they collapse and merge to form progressively larger systems, the observations of groups of galaxies show that they are not the scaled-down version of galaxy clusters (e.g., Mulchaey 2000; Ponman et al. 2003; Voit 2005). Cluster scaling relations (e.g. the L–T relation) show deviations from self-similar relations at the low-mass end (e.g., Voit 2005, but see also Eckmiller et al. 2011), providing evidence of the importance of baryon physics.

Since galaxy groups are cooler with shallower potential wells, non-gravitational processes (e.g., galactic winds, cooling, active galactic nucleus, AGN, feedback, etc.) play a more significant role in less massive systems. Also, the matter composition in groups is different from that in clusters. Baryons in galaxy groups and clusters can be divided into two major components, the hot gas between galaxies and the stars in galaxies. A minor component is the intra-cluster light. In clusters, the gas is the baryon-dominant component (about 6 times more massive than the stellar mass). While in groups, the gas mass is significantly lower: it is of the same order as the stellar mass (e.g., Lagan et al. 2011) and in some cases, even lower than the stellar component (e.g., Giodini et al. 2009). The analysis of both components is critical for observational cosmology when using groups and clusters to constrain the $\Omega_{\rm m}$ parameter from the observed baryon mass fraction (e.g., Allen et al. 2002; Vikhlinin et al. 2009).

The total baryon mass fraction is defined as the ratio between the gas+stars and the total mass: $f_{\rm b} = (M_{\rm gas} + M_{\rm star})/M_{\rm tot}$. In very massive galaxy clusters ($M_{500} \sim 10^{15}\ M_{\odot}$), the baryon content is supposed to closely match the Seven-year *Wilkinson* Microwave Anisotropy Probe (WMAP-7) value ($f_{\rm b}^{\rm WMAP-7} = 0.169 \pm 0.009$, Jarosik et al. 2011). However, it is found that the total baryon mass fraction (and the gas mass fraction) decreases towards low-mass systems when analyzing a wide range of masses (e.g., Lin et al. 2003; Gonzalez et al. 2007; Giodini et al. 2009; Sun et al. 2009; Lagan et al. 2011; Zhang et al. 2011; Sun 2012). On the other hand, the stellar mass fraction seems to increase from clusters to groups of galaxies. A straightforward

⋆ Table 1 and Appendices are available in electronic form at http://www.aanda.org

interpretation can be that the gas mass fraction is directly related to cooling and to the star formation rate, and thus, a smaller gas mass fraction in groups may be related to an efficient cooling. However, the gas mass fraction can also be affected by AGN feedback, which, as mentioned before, is more significant in groups than in clusters. As shown in recent numerical simulations performed by Puchwein et al. (2010), the amount of gas removed by AGN heating from the central regions of clusters and are driven outwards ($r > r_{500}$) depends on cluster mass and is higher in low-mass systems.

The baryon fraction in clusters and groups is an important cosmological probe (e.g., Allen et al. 2004), and therefore scaling relations, such as $f_{\rm gas}$–kT or $f_{\rm gas}$–M_{500}, need to be well understood if we want to use them as a cosmological tool. We will explore here the baryon distribution in the form of gas and stellar mass fractions in groups and compare them with the observed baryon fractions observed in clusters. We will consider in particular the baryon fractions inside the characteristic radii r_{2500} and r_{500}, which are commonly observed with the present generation of X-ray telescopes.

Previous works have presented an analysis of the gas fraction in groups, but few have measured the gas properties up to r_{500}: Vikhlinin et al. (2006) and Gonzalez et al. (2007) derived the gas mass fraction within r_{500} for four low-temperature systems. Sun et al. (2009) determined gas properties up to r_{500} for 11 out of 43 groups. In groups of galaxies, the stellar mass is of the order of the gas mass. To understand the dependence of the total baryon fraction on total mass, it is important to compute both components, the stellar and gas mass fractions, in a homogeneous way. We thus present here the analysis of nine galaxy groups based on *XMM-Newton* and Sloan Digital Sky Survey (SDSS DR8) data, for which we could reliably measure gas properties up to r_{500}. We also included 114 galaxy clusters from Maughan et al. (2012, hereafter M12) to investigate the gas mass component inside r_{2500} and r_{500}, and for 28 of these 114 clusters, we could also estimate the stellar mass fraction.

The paper is organised as follows. The sample is described in Sect. 2. The data reduction is divided in two sections: Sect. 3 describes the SDSS-DR8 data reduction, the colour–magnitude diagrams (CMD) constructed to select group galaxies, and the procedure to compute the stellar masses; Sect. 4 describes the X-ray analysis, gas estimates, and total mass estimates. In Sect. 5, we present our results and compare them to previous results, which are finally summarized in Sect. 7. A ΛCDM cosmology with $H_0 = 70$ km s^{-1} Mpc^{-1} and $\Omega_M = 0.3$ is adopted throughout, and all errors are quoted at the 68% confidence level.

2. The sample

To analyse the baryon mass fraction dependence (gas and stellar mass) on total cluster mass, it is important to consider a sample that covers a wide range of mass, and the objects must have optical and X-ray masses available.

In the present work, we analyse the sample of 114 clusters from Maughan et al. (2008), which were updated in M12, in the redshift range $0.11 < z < 1.3$ and with temperatures ranging from 2.0 keV up to 8.9 keV. 28 out of 114 have optical data available.

To complete our analysis, we also included nine low-mass systems, which were selected as follows. We first selected all groups with available *XMM-Newton* and SDSS-DR8 data, imposing an X-ray flux limit of $L_{\rm X} = 1.9 \times 10^{43}$ erg/s, which corresponds to $kT \sim 2$ keV (Eckmiller et al. 2011). We had 19 groups (without considering the Hickson groups, which are very particular) fulfilling these conditions. However, nine out of 19 had very shallow X-ray observations (low exposure times) that did not allow us to constrain the gas mass. For this reason, we had to exclude those groups. Another group was on the border of the X-ray detector, so it was excluded too.

We ended with a large sample of 123 systems ($0.02 < z < 1.3$) with total masses between $10^{13}\ M_\odot$ and $4 \times 10^{15}\ M_\odot$. These groups and clusters are listed in Table 1. We emphasize that we analysed a sample of nine groups and 28 clusters for the total baryon budget. For the gas mass fraction analysis, we worked with 9 groups and 114 clusters from M12. Thus, the sample is mainly composed by clusters in the latter part.

3. Optical data analysis and stellar mass determination

In this section we describe the method adopted to compute the total stellar mass (in galaxies) for our nine groups of galaxies and 28 galaxy clusters from M12. To be homogeneous, the procedure adopted in this work was the same for groups and clusters, and we followed the steps described in Giodini et al. (2009) and Bolzonella et al. (2010) that consider statistical membership, background correction, and mass completeness as a function of redshift, and a geometrical correction.

We used SDSS-DR8 data, from DERED magnitude tables (already corrected for internal galaxy extinction) for all sources in the GALAXY catalog. The GALAXY catalogue is essentially complete down to 21.3 i-magnitude (SDSS-DR8 summary[1]).

To obtain stellar masses, we first transformed apparent magnitudes to absolute magnitudes with the distance modulus, assuming K-correction values, K(z), according to the morphological type (tables from Poggianti 1997):

$$M = m - 25 - 5\log(d_{\rm L}/1\ {\rm Mpc}) - K(z), \quad (1)$$

where, $d_{\rm L}$ is the luminosity distance.

Absolute magnitudes are converted to luminosities, assuming an absolute magnitude of 4.58 for the Sun in the i-band (Blanton et al. 2003). Luminosities are then converted to masses assuming two different mass-to-light ratios (from Kauffmann et al. 2003): $(M/L_i)_\star = 0.74\ M_\odot/L_\odot$ for late-type and $(M/L_i)_\star = 1.70\ M_\odot/L_\odot$ for early-type galaxies, as described in Lagan et al. (2008). All morphological classification used here is based on the galaxy distribution in a CMD, as explained below. Thus, morphological type simply means "early" (red) or "late" (blue) type galaxies.

3.1. Completeness

To compare the stellar masses of groups and clusters, we defined the completeness in stellar mass ($\mathcal{M}^{\rm star}_{\rm lim}$), or galaxy absolute magnitude, as a function of redshift (as adopted in Giodini et al. 2009; Bolzonella et al. 2010; Pozzetti et al. 2010). This is the lowest mass at which the galaxy stellar mass function can be considered as reliable and unaffected by incompleteness.

For each galaxy, we computed the "limiting mass", which is the stellar mass that this galaxy would have if its apparent magnitude was equal to the sample limit magnitude (i.e., $i = 21.3$): $\log \mathcal{M}^{\rm star}_{\rm lim} = \log \mathcal{M} + 0.4 \times (i - 21.3)$, where $\mathcal{M}$ is the stellar mass of the galaxy with apparent magnitude i. We then computed

[1] http://www.sdss3.org/dr9/scope.php

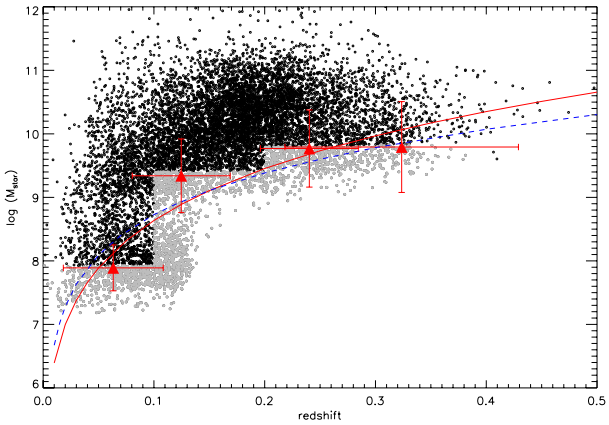

Fig. 1. Stellar mass completeness for our system, which is computed from the fit (red line) to the 95% percentile of the distribution in the limiting mass, for galaxies in the 20% lower percentile in magnitude (grey points) as a function of redshift. The black points represent all galaxies inside r_{500} in the photometric redshift range with $i < 21.3$. The blue-dashed line represents the theoretical value, assuming no K-correction and a constant value for the mass-to-light ratio, as stated in the text.

this value in small redshift bins by considering the 20% faintest galaxies (the grey points in Fig. 1), that is, those contributing to the faint-mass end of the galaxy stellar mass function. For each redshift bin, we define the value corresponding to 95% of the distribution of limiting masses as a minimum mass. The systems were divided into four bins of redshift, and we fit the limiting mass values as a function of redshift: $\log \mathcal{M}^{\rm star}_{\rm lim}(z) = 11.67 \times z^{0.13}$ (the red line in Fig. 1). We thus adopted $\mathcal{M}^{\rm star}_{\rm lim}$ as the lowest galaxy stellar mass that will be considered in our analysis to compute the stellar masses for the groups and clusters. As a check, we also computed the theoretical values for the limiting mass, assuming no K-correction and a constant value for the mass-to-light ratio (M/L) as $\log \mathcal{M}^{\rm star}_{\rm lim} \propto DM(z)/2.5$, where DM is the distance modulus. We see that the adopted function for the limiting mass (red line in Fig. 1) is close to the theoretical predicted value for $\mathcal{M}^{\rm star}_{\rm lim}$ (blue-dashed line in Fig. 1).

We estimated the contribution from galaxies that are less massive than $\mathcal{M}_{\rm lim}$ in each redshift bin. We assumed that the fraction of galaxies that are not considered is $f = 1 - [\mathcal{M}_{\rm star}(\mathcal{M} > \mathcal{M}_{\rm lim})/\mathcal{M}_{\rm star_{tot}}]$ and can be estimated using a stellar mass function. Thus,

$$f = 1 - \frac{\int_{\mathcal{M}_{\rm lim}}^{\mathcal{M}_{\rm max}} \mathcal{M} f(\mathcal{M}) {\rm d}\mathcal{M}}{\int_{\mathcal{M}_{\rm min}}^{\mathcal{M}_{\rm max}} \mathcal{M} f(\mathcal{M}) {\rm d}\mathcal{M}}, \quad (2)$$

where $\mathcal{M}_{\rm lim}$ is the limiting mass values for each redshift bin defined by the red points in Fig. 1, and $\mathcal{M}_{\rm min}$ and $\mathcal{M}_{\rm max}$ are the minimum and maximum mass values for the stellar mass in cluster galaxies, respectively. We assumed that $\mathcal{M}_{\rm min} = 10^8\ M_\odot$ and $\mathcal{M}_{\rm max} = 10^{13}\ M_\odot$. Considering that the stellar mass function is described by a single Schechter function, we used typical values from Bell et al. (2003) ($M^* = 10^6/h^2$, $\alpha = -0.6$) to estimate the fraction of stellar mass that is missing in each redshift bin because of completeness correction. We found that the fractional contribution to the total stellar mass budget of galaxies with $10^8\ M_\odot < \mathcal{M} < \mathcal{M}_{\rm lim}(z)$ varies from less than 1% up to 4% (for clusters with $z > 0.3$). These small fractions (also in agreement with Lin et al. 2003; Giodini et al. 2009) show that the stellar masses computed in this work are reliable.

3.2. Statistical membership, background correction, and geometrical correction

As a first step to estimate the projected total stellar mass, which is the sum of all potential member galaxies (with masses greater than the limiting mass), we first have to define candidate members inside r_{2500} and r_{500}. Those members are defined as all the galaxies inside a projected distance equal to r_{2500} or r_{500}, which is defined from the X-ray centroid of a group/cluster and with photometric redshift in the range $z = z_{\rm c} \pm 0.1 \times (1 + z^{\rm SDSS}_{\rm photo})$ (where $z_{\rm c}$ is the central redshift taken from NED, and $z^{\rm SDSS}_{\rm photo}$ is the photometric redshift taken from SDSS-DR8). We note that we used a range of 0.1, which is of the order of the error on photometric redshifts in the SDSS catalogue.

We constructed CMD for each group/cluster to identify the red-sequence (RS). For each system, we linearly fit the red-sequence and considered all galaxies within the RS best-fit ±0.3 mag as early-type objects. Late-type galaxies were classified as the objects that are bluer than the lower limit of the RS. We summed the masses of all the early-type and late-type galaxies that obeyed our criteria.

We corrected for background/foreground contamination by measuring the total stellar mass of early-type and late-type galaxies, assuming the same photometric redshift criterium, in an annulus of inner and outer radii of $8 \times r_{500}$ and $9 \times r_{500}$, respectively (as already described in Lin et al. 2003; Lagan et al. 2008). The background regions do not overlap other structures and were chosen to represent a field environment. We applied early- and late-type definitions of the cluster to the background region. Thus, field galaxies are selected by following the same criteria as group/cluster potential members. We then summed the masses of all late- and early-type galaxies in the background area.

Finally, we added up the stellar masses of all early-type galaxies from our systems and subtracted the stellar masses of background early-type galaxies normalised to the cluster area. The same was done for late-type galaxies. Then, To compute the total stellar mass of the system, we summed the total corrected values for early- and late-type stellar masses, considering our limiting mass for the cluster/groups redshift.

There is one last correction to be applied. The values derived for the stellar masses refer to a cylinder section projected perpendicularly to the line of sight. On the other hand, the gas and total masses are measured inside spheres of radii, r_{2500} and r_{500}. To compare stellar masses to total and gas masses, we need to apply a geometrical correction to correct the cylindrical volume to a spherical volume (see Appendix B for more details). The concentration parameters are taken to be 2 ± 1 and 3 ± 1 for clusters and groups, respectively. These values lead to a multiplicative factor on the stellar mass of 0.68 for clusters and 0.74 for groups within r_{500} and 0.53 for clusters and 0.61 for groups within r_{2500}. One can note that the concentration parameter of clusters is chosen to be lower than the parameter of groups, according to results from Hansen et al. (2005).

3.3. Uncertainties

We have three major uncertainties: the photometric magnitude uncertainty (about 14% of the stellar mass), the uncertainty arising from the geometrical correction (about 6% within r_{500} and 9% within r_{2500}), and the uncertainty on the mass to light ratio (about 26%). The error bars are approximated to be the quadrature sum of the three uncertainties, i.e., about 30%. The

uncertainty on the geometrical correction has been calculated, assuming the concentration parameter is known at ±1. In most cases, our error bars are mainly because of the uncertainty on the mass-to-light ratio. Thus, it could improve with better constraints on mass-to-light ratios. It is also interesting to note that errors are of the same order within r_{2500} and r_{500}, which shows there are enough galaxies within r_{2500} to calculate statistical uncertainties. Stellar masses with error bars are given in Table 1.

4. X-ray data analysis, gas and total mass determinations

For the nine groups of our sample, we reduced the X-ray data with the *XMM-Newton* Science Analysis System (SAS) v11.0 and calibration database using all the updates available prior to February 2012. The initial data screening was applied using recommended sets of event patterns – i.e., 0–12 and 0–4 for the MOS and PN cameras, respectively. The light curves in the energy range of [1–10] keV were filtered to reject periods of high background. We used the background maps for the 3 EPIC instruments from Read & Ponman (2003). The background was normalised with a spectrum obtained in an annulus (between 9–11 arcmin), where the cluster emission is no longer detected. A normalised spectrum was then subtracted, yielding a residual spectrum. This normalisation parameter was then used in the spectral fit. This procedure was already adopted in Lagan e et al. (2008) and Durret et al. (2010, 2011).

We also considered the 114 clusters from Maughan et al. (2012) in the redshift range of $0.1 < z < 1.3$, and observed with *Chandra*. Their temperatures ranged from 2.0 keV to 16 keV. This sample was first presented in Maughan et al. (2008), where the full analysis procedure is described. In M12 the sample was reanalysed with updated versions of the CIAO software package (version 4.2) and the *Chandra* Calibration Database (version 4.3.0).

4.1. Gas and total mass determinations for the groups

To compute the gas mass, we first converted the surface brightness distribution into a projected emissivity profile that was modelled by a β-model (Cavaliere & Fusco-Femiano 1978). The gas mass is given by:

$$M_{\rm gas}(r) = 4\,\pi\,m_{\rm p}\,\mu_{\rm e}\int_0^{r_\Delta} n_{\rm e}(r) r^2 {\rm d}r, \tag{3}$$

and for the β-model, we can write

$$n_{\rm e} = \frac{n_0}{\left[1+\left(\frac{r}{r_{\rm c}}\right)^2\right]^{\frac{3\beta}{2}}}, \tag{4}$$

where $r_{\rm c}$ is the characteristic radius, β is the slope of the surface brightness profile, $\mu_{\rm e} = 0.81$, and n_0 is the central density obtained from the normalization parameter from the spectra.

To compute the total mass based on X-ray data, we rely on the assumption of hydrostatic equilibrium (HE) and spherical symmetry. The total mass can be calculated using the deprojected surface brightness and temperature profiles. The total mass is given by:

$$M_{\rm tot}(<r_\Delta) = -\frac{k_{\rm b}Tr}{G\mu{\rm m_p}}\left(\frac{{\rm dln}\,\rho}{{\rm dln}\,r}+\frac{{\rm dln}\,T}{{\rm dln}\,r}\right), \tag{5}$$

where r_Δ is the radius inside which the mean density is higher than the critical value by a factor of Δ (in our case, $\Delta = 2500$, or $\Delta = 500$); $k_{\rm b}$ is the Boltzman constant; T is the mean gas temperature; $m_{\rm p}$ is the proton mass; μ is the molecular weight; and ρ is the gas density. Here, we assumed that the systems are isothermal, and we used a global temperature (measured within 300 h_{70}^{-1} kpc) to compute the dynamic mass. To determine the temperature, the MOS and PN data were jointly fit with a MEKAL plasma model (bremsstrahlung plus line emission). We fixed the hydrogen column density at the local Galactic value, using the task *nH* from FTOOLS (an interpolation from the LAB *nH* table, Kalberla et al. 2005) to estimate it. The gas and total masses (derived inside r_{2500} and r_{500}) and the other quantities derived from X-ray observations are in Table 1.

Assuming that the gas temperature for groups is roughly isothermal, r_{500} is given by Lima Neto et al. (2003):

$$r_\Delta = r_{\rm c}\left[\frac{2.3\times10^8\,\beta\langle kT\rangle}{\Delta\,h_{70}^2E^2(z;\Omega_{\rm m},\Omega_\lambda)\,\mu\,r_{\rm c}^2}\right]^{1/2}, \tag{6}$$

where $r_{\rm c}$ is the characteristic radius (given in kpc); β is the slope given by the β-model fit for the surface brightness profile; $\langle kT\rangle$ is the mean temperature (given in keV); and $E^2(z;\Omega_{\rm m},\Omega_\Lambda) = (\Omega_{\rm m}(1+z)^3+(1-\Omega_{\rm m}-\Omega_\Lambda)(1+z)^2+\Omega_\Lambda)$ describes the redshift evolution of the Hubble parameter. It is important to mention that the surface brightness and temperature profiles reach r_{500} without extrapolation for all systems.

4.2. Gas and total mass determinations for the Maughan et al. (2012) sample

The gas density profile of each cluster was determined by converting the observed surface brightness profile (measured in the 0.7–2 keV band) into a projected emissivity profile, which was then modelled in M12 by modifying the β-model (see e.g., Pointecouteau et al. 2004; Vikhlinin et al. 2006; Maughan et al. 2008) to take into account the power-law-type cusp instead of a flat core in the centre of relaxed clusters. Also, the cluster gas temperature, gas mass and r_{500} were then determined iteratively in M12. The procedure was as follows: to extract a spectrum within an estimated r_{500} (with the central 15 percent of that radius excluded), integrate the gas density profile to determine the gas mass within the estimated r_{500} and thus calculate $Y_{\rm X}$, which is the product of the temperature and gas mass, a low scatter proxy for the total mass (Kravtsov et al. 2006). A new value of r_{500} was then estimated from the $Y_{\rm X}-M_{\rm tot}$ scaling relation of Vikhlinin et al. (2009). The process was repeated until r_{500} converged. All the details are in Sect. 2 of M12.

For the gas mass, we used Eq. (3), but we assumed the modified β-model (as in M12) given by

$$n_{\rm e}^2 = n_0^2\frac{(r/r_{\rm c})^{-\alpha}}{(1+r^2/r_{\rm c}^2)^{3\beta-\alpha/2}}\times(1+(r/r_{\rm s})^\gamma)^{-\epsilon/\gamma}, \tag{7}$$

where the additional term describes a change of slope by ϵ near the radius $r_{\rm s}$, and the parameter γ controls the width of the transition region. Gas masses were then determined from Monte Carlo realisations of the projected emissivity profile based on the best-fitting projected model to the original data. The errors in the gas mass determination were calculated using a Gaussian distribution for all gas mass values, and the standard deviation was assumed to be the full width at half maximum of this distribution.

To test the assumption of isothermality, we computed here the characteristic radius r_{500} and r_{2500}, by its definition,

$$\langle\rho(r_\delta)\rangle \equiv \frac{M_{\rm tot}(<r_\delta)}{4\pi r_\delta^3/3}, \tag{8}$$

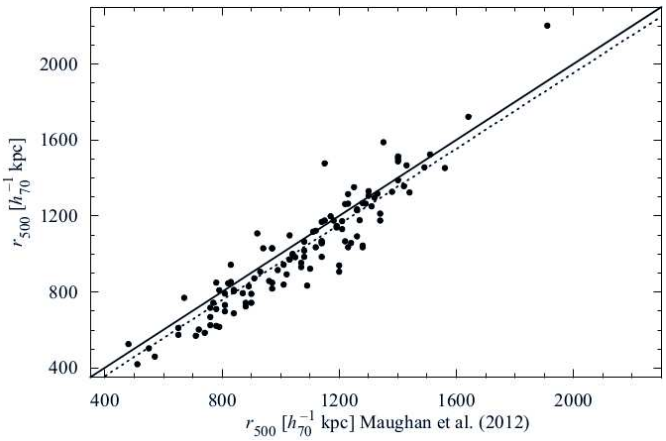

Fig. 2. Comparison of the r_{500} values determined by Maughan et al. (2012) and those computed with Eq. (6) to determine r_{2500} and r_{500} in a homogeneous way for our sample.

where δ is the density contrast, $\rho_{\rm cr}(z)$ is the critical density at the cluster redshift, and $\langle\rho(r_\delta)\rangle$ is the mean total density inside r_δ. The radius r_δ is then found by numerically solving the following equation:

$$r_\delta^3 = -\frac{3}{4\pi\delta}\rho_{\rm cr}^{-1}(z)\frac{r_\delta\, kT}{\mu m_{\rm H} G}\left.\frac{{\rm dlog}\,\rho}{{\rm dlog}\,r}\right|_{r=r_\delta}. \quad (9)$$

Spherical symmetry and hydrostatic equilibrium are assumed, and kT and ρ are the gas temperature and density, respectively. To solve this equation, we used the gas density profile from Eq. (7) and an isothermal temperature. As shown in Fig. 2, the values agree with those derived in M12, although they are systematically lower. They may be because the M12 values were derived using a scaling relation, and we assume hydrostatic equilibrium (more discussion in Appendix A).

We computed the total mass using Eq. (5) and assuming a modified β-model for the gas density profile and an isothermal profile, as in the case for the groups. In Appendix A, we test the assumption of isothermality. By showing this, we are not introducing any systematic error, and we show that the total masses derived in this work are robust. The gas and total masses inside radii r_{2500} and r_{500} are presented in Table 1. The errors on the total mass determinations are mainly because of the assumption of an isothermal gas.

It is important to state that Piffaretti & Valdarnini (2008) have shown that masses can be underestimated by about 5%, even for the most relaxed clusters. Nagai et al. (2007) found that the gas mass is measured quite accurately (<~6%) in all clusters, while the hydrostatic estimate biases the total mass towards lower values by about 5%–20% throughout the virial region, when compared to the gravitational mass estimates. Thus, we incorporated a 10% error into our $f_{\rm gas}$ error budget for all systems (clusters and groups).

5. Results

We present our results in four different sub-sections. In the first part, we present and discuss the star formation efficiency as a function of total mass computed inside r_{2500} and r_{500} for our sample of 37 systems (nine groups and 28 clusters) with both optical and X-ray available data. In Sect. 5.2, we investigate the difference in mass between the estimated total baryon budget and the WMAP-7 value. Then, we discuss in Sect. 5.3 the gas mass fraction enclosed in r_{2500} and r_{500}, and also the differential mass fraction as a function of total mass for our entire sample of 123 systems. Finally, we address the use of clusters, or more precisely, the total baryon budget and the gas mass fraction as a function of redshift, as cosmological tools in Sect. 5.4. Given the large scatter observed, we adopt the robust Spearman correlation coefficient ρ and determine the significance of its deviation from zero P (where a small value of P indicates a stronger correlation) to evaluate the significance of the correlations (see Press et al. 1992).

5.1. Cold baryon fraction and star formation efficiency

In this section, we investigate the star formation efficiency and the cold baryon fraction dependences on total mass of the system. The star formation efficiency can be defined as the ratio of stellar to gas mass, and the cold baryon fraction is the ratio between the stellar mass and the total baryon (stars plus ICM) mass. In Fig. 3, we show the star formation efficiency and the cold-baryon fraction as a function of total mass computed for r_{2500} and r_{500}.

From Fig. 3, we see a clear trend, which suggests that the cold baryon fraction and star formation efficiency decrease with increasing total mass (as reported previously by David et al. 1990; Roussel et al. 2000). We obtained a Spearman correlation coefficient of $\rho = -0.73$ with $P = 10^{-7}$ for the correlations within r_{500} and $\rho = -0.84$ with $P = 10^{-11}$ for the correlations within r_{2500}. In both cases, we had a strong correlation between the cold baryon fraction/star formation efficiency and the total mass.

The star formation efficiency decreases by an order of magnitude for both r_{2500} and r_{500} from groups to massive clusters. From the analysis of twelve groups and clusters, David et al. (1990) also found a strong correlation for $M_{\rm star}/M_{\rm gas} \times M_{\rm tot}$, showing that the $M_{\rm star}/M_{\rm gas}$ ratio varies by more than a factor of five from low to high-mass systems.

5.2. Difference between the observed and WMAP-7 baryon fractions

In Fig. 4, we show the stellar, gas, and total baryon budgets as a function of total mass of the system. We also show the ratio between the total baryon fraction determined by the sum of $f_{\rm star}$ and $f_{\rm gas}$ and the WMAP-7 value as a function of total mass in the bottom panel. The solid lines represent the best linear fits for the total, gas and stellar mass fractions as a function of total mass. We also represent the fits for the stellar mass fraction for groups and clusters separately. As we see, the best fits for the stellar mass fractions differ by more than 3σ if we separate the 28 clusters from the 9 groups. This suggests that groups and clusters form two distinct populations in terms of stellar content.

The total baryon mass fraction, as shown in Fig. 4, for the mass range analysed here indicates a decrease towards groups and poor-clusters (as mentioned previously). The discrepancy between the total baryon mass fraction and the WMAP-7 value becomes larger with decreasing mass (as already pointed out by some previous works, such as in Gonzalez et al. 2007; Giodini et al. 2009; Andreon 2010). To use the total baryon fraction of galaxy clusters as a cosmological tool, one thus should consider carefully the sample. These structures range in mass from $M_{500} \sim 10^{13}\ M_\odot$ to $10^{15}\ M_\odot$, and $f_{\rm baryon}$ is not constant for the entire range of mass. We discuss this further in Sect. 6.

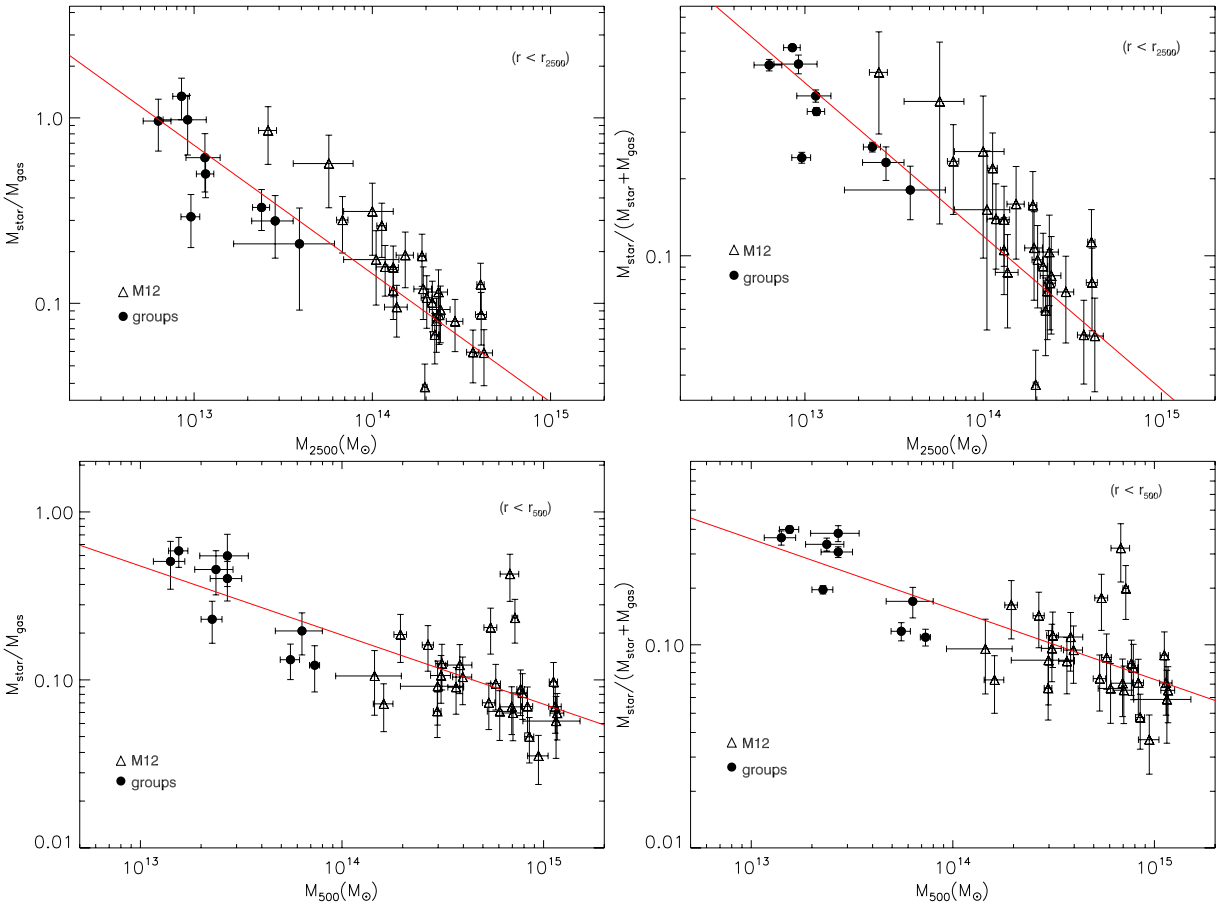

Fig. 3. Cold baryon fraction, $M_{\rm star}/(M_{\rm gas}+M_{\rm star})$ and star formation efficiency, $M_{\rm star}/M_{\rm gas}$, as a function of total mass, computed inside r_{2500} (*upper panels*) and r_{500} (*lower panels*).

5.3. Gas mass fraction within r_{500}, and r_{2500}, and the differential gas mass fraction ($f_{gas,diff}$)

The gas mass fraction of clusters of galaxies can be used as a cosmological tool, as first done by Allen et al. (2002) and refined later by (Allen et al. 2004, 2008). These studies show an agreement between the gas mass fraction and the ΛCDM cosmology. Recently, more sophisticated X-ray analyses were done by Ettori et al. (2009) and Mantz et al. (2010). All these studies rely upon the assumption that the gas mass fraction of the cluster sample considered is constant with total mass and redshift.

In this section, we present our results concerning the gas mass fraction dependence on the total mass, making use of our entire sample of 123 objects. We present our results in Fig. 5. We show the strong cool-core clusters in blue (RCC is defined in Maughan et al. 2012, these are the most relaxed clusters in the sample). Cool-core clusters are generally defined by a drop of temperature in the centre which is associated with denser cores that are cooling hydrostatically via bremsstrahlung. They are associated with dynamically relaxed clusters, where the hydrostatic equilibrium equation is valid. However, it seems to be a general agreement between the "true" masses (measured through weak-lensing) and the X-ray derived values inside r_{500}, independent of the dynamical state of the system (Zhang et al. 2010).

In Fig. 5, we show the gas mass fraction inside r_{2500}, and r_{500} and the differential gas mass fraction as a function of total mass. The differential gas mass fraction, $f_{\rm gas,diff}$, is defined as the mass fraction within the spherical shell of radii r_{2500} and r_{500}; that is, $[M_{\rm gas,500}-M_{\rm gas,2500}]/[M_{\rm tot,500}-M_{\rm tot,2500}]$. We see that there is a $f_{\rm gas}$ dependence on total mass for total masses enclosed in both radii. If we assume a linear dependence (BCES bisector) for $f_{\rm gas,2500}-M_{\rm tot,2500}$ $f_{\rm gas,2500}\propto M_{2500}^{0.17\pm0.02}$ (with a $\rho=0.47$ and $P=2.8\times10^{-8}$) is compatible with the relation computed for r_{500} within the measurement errors $f_{\rm gas,500}\propto M_{500}^{0.14\pm0.02}$ (with a $\rho=0.16$ and $P=0.006$). Both relations are steeper than the relation found for the differential gas mass fraction, $f_{\rm gas,diff}\propto M_{\rm tot,500}^{0.02\pm0.02}$, that is compatible with a flat distribution. We must stress that the trend found here for $f_{\rm gas,500}-M_{\rm tot,500}$ is not as steep as the one presented in Lagan e et al. (2011) within 1σ, which may be because of two major factors: first, we computed the total mass from a scaling relation using the gas mass as a proxy in the previous work, imposing a $f_{\rm gas}$ dependence on $M_{\rm tot}$ and diminishing the scatter in the relation; second, we have assumed an isothermal gas to compute the total mass in the present work, instead of considering the temperature profile. However, the slopes agree within 2σ.

The differential gas mass fraction shown in Fig. 5 is higher than the cumulative measures, reaching the universal baryon fraction for systems with mass $M_{500}\sim10^{14}\ M_{\odot}$. Clearly, the differential gas mass fraction is constant at the 1σ level and provides a better constraint for cosmology, although the statistical scatter is very large. For groups (i.e., the systems in our sample with $M_{500}<10^{14}\ M_{\odot}$), we still observe lower values for the differential gas mass fraction when compared to the WMAP-7 result. Since our sample includes few systems in this mass regime, we cannot derive firm conclusions.

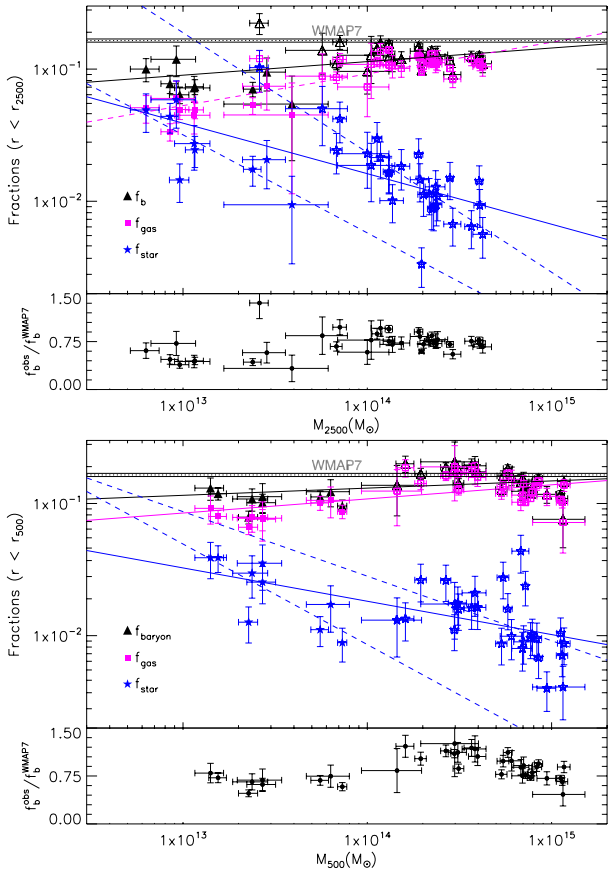

Fig. 4. Stellar (blue stars), gas (magenta squares), and total baryon (black triangles) mass fractions as a function of total mass for r_{2500} (*top panel*) and r_{500} (*lower panel*). The solid lines correspond to the best linear fit for each relation. The two blue dashed lines correspond to the fits for the groups and clusters separately. On the bottom of each panel, we show the ratio between the total baryon fraction determined by the sum of $f_{\rm star}$ and $f_{\rm gas}$ and the WMAP-7 value as a function of total mass.

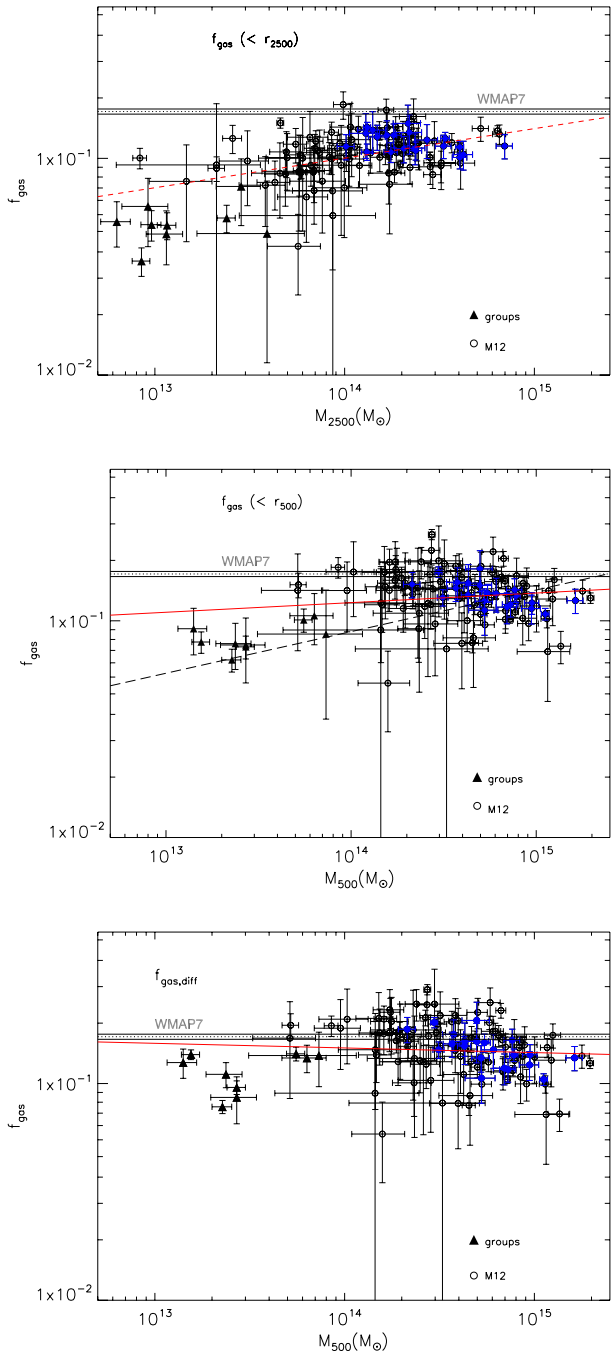

Fig. 5. Gas mass fraction as a function of total mass computed within r_{2500} (*upper panel*), and within r_{500} (*middle panel*); the differential gas mass fraction, $[M_{\rm gas,500} - M_{\rm gas,2500}]/[M_{\rm tot,500} - M_{\rm tot,2500}]$, as a function of $M_{\rm tot,500}$ (*lower panel*). The triangles represent the nine groups, while the circles represent the 114 clusters from M12 (we show in blue the strong cool-core clusters). The red lines show the best fits for the entire sample. The dashed line in the middle panel corresponds to the best fit found by Lagan et al. (2011).

Comparing the three plots in Fig. 5, we conclude that the observed $f_{\rm gas}$–$M_{\rm tot}$ trend found for groups and clusters is due to the lack of gas enclosed inside r_{2500} for groups and poor clusters, as proposed by Sun (2012), owing to non-thermal processes, such as supernova feedback, that are more efficient in low mass systems because of the shallower potential well. From their hydrodynamical simulations, Young et al. (2011) reported that the injection of entropy has removed gas from the cores of the low-mass systems and pushed the gas out to larger radii between r_{500} and r_{200}.

5.4. Cosmological constraints from the total baryon budget and from the f_{gas} vs. redshift relation

As mentioned before, the X-ray data analysis of galaxy clusters can provide reliable constraints on cosmology from the total baryon budget and the gas mass fraction dependence on the redshift. One of the classical methods to infer $\Omega_{\rm m}$ assumes that the baryon-to-total mass ratio should closely match the cosmological values, and thus $\Omega_{\rm b}/\Omega_{\rm m} \sim M_{\rm b}/M_{\rm tot}$ (White et al. 1993; Evrard 1997). Combining $\Omega_{\rm b} = 0.0456$ (Jarosik et al. 2011) with our values for the baryon fraction obtained in Sect. 5.1, our results imply $\Omega_{\rm m} < 0.55$ (assuming the lowest $f_{\rm b}$ value and agreeing with Ettori & Fabian 1999), and if we take the highest significant estimates for $f_{\rm b}$, $\Omega_{\rm m} > 0.22$.

In addition to the calculation of $\Omega_{\rm m}$ based on the total baryon budget, the gas mass fraction has been used to obtain more rigorous constraints on cosmology that probes the acceleration of the universe. The apparent behaviour of $f_{\rm gas}$ with redshift can constrain the cosmic acceleration, as studied in Ettori & Fabian (1999) and Allen et al. (2004, 2008). This constraint

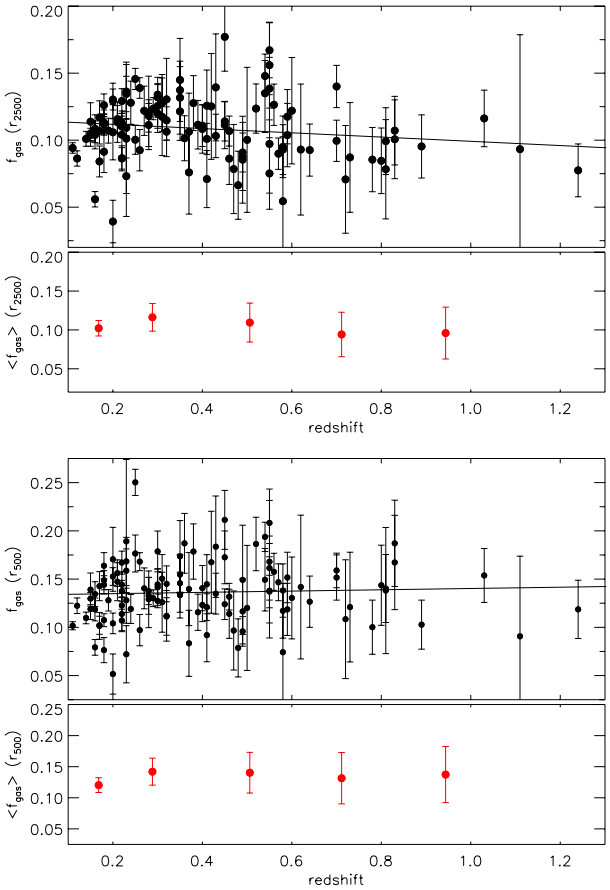

Fig. 6. Gas fraction as a function of redshift for r_{2500} (*upper panel*) and r_{500} (*lower panel*). The black lines represent the best linear fit for the data.

originates because f_{gas} measurements depend on the distance to the cluster ($f_{gas} \propto d^{1.5}$).

The gas mass fraction for the present sample was computed, assuming the default ΛCDM cosmology, and we show the gas mass fraction determined inside r_{2500} ($f_{gas,2500}$) and r_{500} ($f_{gas,500}$) as a function of redshift in Fig. 6. On the bottom of each panel, we show with red points the mean gas mass fraction value computed for bins of 0.2 in redshift as a function of the mean redshift, and the errors are the standard errors on the mean.

From this figure, we can see that the gas mass fraction values determined for r_{2500} and r_{500} show little variation with redshift. Assuming $f_{gas(z)} = A + B \times z$, we obtained $A = 0.130 \pm 0.009$ and $B = 0.010 \pm 0.015$ for r_{500}, and determined $A = 0.110 \pm 0.008$ and $B = -0.019 \pm 0.013$ for r_{2500}. From these results, we verified that the enclosed gas mass fraction does not depend on redshift at a 2σ level in both cases.

From our analysis, we cannot attribute the slight decrease of $f_{gas,2500}$ with redshift to evolution of f_{gas}. Selection biases may have led to the enhanced mean gas mass fraction at around $z = 0.3$ and may have driven the observed trend, as recently reported by Landry et al. (2013).

6. Discussion

In this section, we further discuss the results obtained in this work and compare them to previous observational and theoretical ones.

6.1. Stellar and gas mass dependence on total mass

The trends shown in Fig. 3 can be explained by a decrease in the stellar mass with an increase in cluster mass. Alternatively, the gas mass can increase for more massive systems. From previous results in the literature (David et al. 1990; Lin et al. 2003; Lagan et al. 2008; Giodini et al. 2009; Lagan et al. 2011; Zhang et al. 2011), we observe both behaviours, but the decrease in stellar mass fraction as a function of total mass is more significant than the gas mass increase in the same range. This provides evidence that there is no well-tuned balance between the gas and stellar mass fractions. This evidence suggests that the variation in star formation efficiency is because of the variation in stellar mass, which arises from the decrease in efficiency of tidal interactions among galaxies, the removal of the gas reservoir of galaxies due to the motion of galaxies through the ICM, or feedback processes that may quench star-formation. Recent numerical simulation results from Dubois et al. (2013) supported this scenario. According to their results, AGN feedback alone is able to significantly alter the stellar mass content by quenching star formation.

During mergers to form rich clusters, the gas within the system will be shocked and heated to the virial temperature. As mergers progress, more massive systems are formed, and the gas is progressively heated to higher temperatures. Thus, cooling and galaxy formation are inhibited. Since rich clusters are formed from many mergers, this explains why this large gas fraction of the gas is not consumed to form stars. In contrast, less massive systems, such as groups, have experienced fewer mergers. Therefore their gas is cooler and more stars are formed within the galaxies. As a consequence, the star formation efficiency is higher in groups, which indicates that physical mechanisms that depend on the virial mass, such as ram-pressure stripping, are driving galaxy evolution within clusters and groups. This result is important to provide constraints on the role of thermodynamical processes for groups and clusters and seems to agree with theoretical expectations from hydrodynamical simulations by Springel & Hernquist (2003). In their models, the integrated star formation efficiency as a function of halo mass, which varies from 10^8 to 10^{15} $M_\odot$, falls by a factor of five to ten over the cluster mass scale, due to the less efficient formation of cooling flows for more massive haloes (in their case, with temperature above 10^7 K, what comprises the entire range of mass analysed in this work).

Recently, Planelles et al. (2013) carried out two sets of simulations including radiative cooling, star formation and feedback from supernovae and in one of which they also accounted for the effect of feedback from AGN. These authors found that both radiative simulation sets predict a trend of stellar mass fraction with cluster mass that tends to be weaker than the observed one. However this tension depends on the particular set of observational data considered. Including the effect of AGN feedback alleviates this tension on the stellar mass and predicts values of the hot gas mass fraction and total baryon fraction to be in closer agreement with observational results. Also, Zehavi et al. (2012) studied the evolution of stellar mass in galaxies as a function of host halo mass using semi-analytic models, and their results agree with our findings of a varying star formation efficiency. These latter authors found that baryon conversion efficiency into stars has a peaked distribution with halo mass and that the peak location shifts toward lower mass from $z \sim 1$ to $z \sim 0$. Another difference between low- and high-mass haloes is that the stellar mass in low-mass haloes grows mostly by star formation since $z \sim 1$. In contrast, most of the stellar mass is assembled by mergers in high-mass haloes.

6.2. The ICL contribution to the total baryon budget

To account for the difference in baryons at the low-mass end (see Fig. 4), where the total baryon budget is still significantly below the value of WMAP-7, there are two possibilities. The first possibility is that the discrepancy in baryon mass fraction is because of feedback mechanisms, as expected by many studies (including Bregman 2007; Giodini et al. 2009). Recent numerical simulations performed by Dai et al. (2010) proposed that the baryon loss mechanism is primarily controlled by the depth of the potential well: the baryon loss is not significant for deep potential wells (rich clusters), while for lower-mass clusters and groups the baryon loss becomes increasingly important. Baryons can be expelled from the central regions beyond r_{500}. The second possibility is to account for baryons in other forms: for example, the increase in the stellar light via intra-cluster light (ICL), which increases the stellar mass.

ICL is one of the most important sources of unaccounted baryons, and observational results have shown that it may represent from 10% to 40% of the total cluster light (e.g., Feldmeier et al. 2002; Zibetti et al. 2005; Krick & Bernstein 2007; Gonzalez et al. 2007). However, recently, Burke et al. (2012) found that the ICL constitutes only 1–4% of the total cluster light within r_{500} in high-z clusters.

To investigate the ICL contribution as a function of system total mass, we computed the difference between the observed total baryon budget and the WMAP-7 value, which is taken to be: $M_{\rm diff} = (f_b^{\rm WMAP-7} - f_b^{\rm obs}) \times M_{500}$, where $f_b^{\rm WMAP-7}$ is the WMAP-7 value; $f_b^{\rm obs}$ is the observed baryon mass fraction that we computed for our systems; and M_{500} is the total mass computed in the r_{500} radius. We then assumed that this difference in mass is under the form of luminous matter. To compute the corresponding "missing stellar surface brightness", we assumed a mass-to-light ratio for ellipticals of $M/L = 1.7\ M_\odot/L_\odot$ (Kauffmann et al. 2003) to convert the difference in mass into a difference in luminosity. We then convert the luminosity in surface brightness by dividing the area inside r_{500}.

In Fig. 7, we show the missing stellar mass divided by the total stellar mass as a function of total mass (upper panel), the missing stellar surface brightness as a function of total mass (middle panel), and the ratio between the stellar surface brightness and the BCG magnitude as a function of total mass. Since the stellar mass fraction decreases for massive clusters (Fig. 4) one could conclude that the ICL could be more important in clusters of galaxies because the measured stellar light fraction of the ICL has not been considered. As a direct consequence of the stellar mass dependence on total mass, we observe an increase of the missing-to-total stellar mass ratio as a function of the total mass of the system, as shown in the upper panel of Fig. 7. In this panel, groups and clusters seem to be two distinguished populations, which are comparable to the behaviour observed in Fig. 4. Then, if we think in terms of missing surface brightness, groups seems to present fainter values than clusters. This means that it would be easier to detect the ICL contribution is clusters than in groups.

However, from the values obtained here, the stellar component would have to increase by a factor of three to be able to explain the baryon deficit with intra-cluster light for low-mass systems. Moreover, such a high amount of ICL would be visible in current observations. Although a large sample of clusters and groups is needed for further constraints on the photometrical properties and for the ICL formation mechanism, it is very unlikely that the ICL will be able to answer the baryon deficit problem.

Even by considering the uncertainties associated with our total baryon fraction and the WMAP-7 measurement, the two values are discrepant at the 5σ level for systems with mass $M_{500} < 10^{14}\ M_\odot$. It is therefore probable that either the baryon mass fraction within r_{500} in groups is different from the universal value, or that there are still unaccounted baryons (other than ICL) in the low-mass regime.

7. Conclusions

We have investigated the baryon content of a sample of 123 galaxy clusters and groups, whose mass spans a broad range (from groups of $M_{500} \sim 10^{13}\ M_\odot$ up to clusters of $M_{500} = 4 \times 10^{15}\ M_\odot$). We measured the cluster gas and total masses from X-ray data analysis, and we computed the stellar masses for 37 out of 123 galaxy clusters and groups using DR8-SDSS data. We summarise our results and discussions in the following points:

- For a subsample of 37 systems for which we had both optical and X-ray data, we derived quantities inside r_{2500} and r_{500} to investigate the stellar, gas and total mass fractions dependence on total mass. We confirmed the previous trend found in the literature: the star formation efficiency is lower for more massive clusters. It decreases by an order of magnitude from groups to clusters inside both r_{2500} and r_{500}. We observe a decrease of the cold baryon fraction and of the star formation efficiency from r_{2500} to r_{500}.
- Star-formation efficiency is lower in galaxy clusters than in groups, which suggests that the gas reservoir of the galaxies during cluster formation in more massive clusters are more affected by mechanisms, such as ram-pressure, that quench the star formation. Physical mechanisms depending on the total mass of the system may be driving galaxy evolution in groups and clusters. This observational result agrees with hydrodynamical simulations.
- For the entire sample of 123 systems, we analysed the gas mass fraction inside r_{2500}, and r_{500} and also the differential gas mass fraction ($f_{\rm gas,2500} - f_{\rm gas,500}$) dependence on total mass. We found that the gas fraction depends on the total mass inside both radii, with the dependence being steeper for the inner radius. However, we found that for systems more massive than $M_{\rm tot} > 10^{14}\ M_\odot$, the differential gas mass fraction shows no dependence on total mass, which provides evidence that groups cannot retain gas in the inner parts in the same way clusters do. Since groups have shallower potential wells, non-thermal processes are more important than in clusters, and AGN feedback, for instance, could expel the gas towards the outer radii of groups. This result is an indication that such processes must play a more important role in the centres of low-mass systems than in massive clusters.
- The differential gas mass fraction is higher than the cumulative measures and clearly more constant as a function of total mass, which provides better constraints for cosmology.
- Combining the baryon-to-total mass fraction with primordial nucleosynthesis measurements, our results indicate that $0.17 < \Omega_{\rm m} < 0.55$. We also observed that the gas mass fraction that is enclosed within r_{2500} and r_{500} does not depend on redshift at the 2-sigma level, which is very important in the use of clusters of galaxies as a cosmological tool to constrain the cosmic acceleration.
- Our results show that non-thermal processes play different but important roles on galaxy evolution in groups and clusters. While in groups, the gas is more affected because of

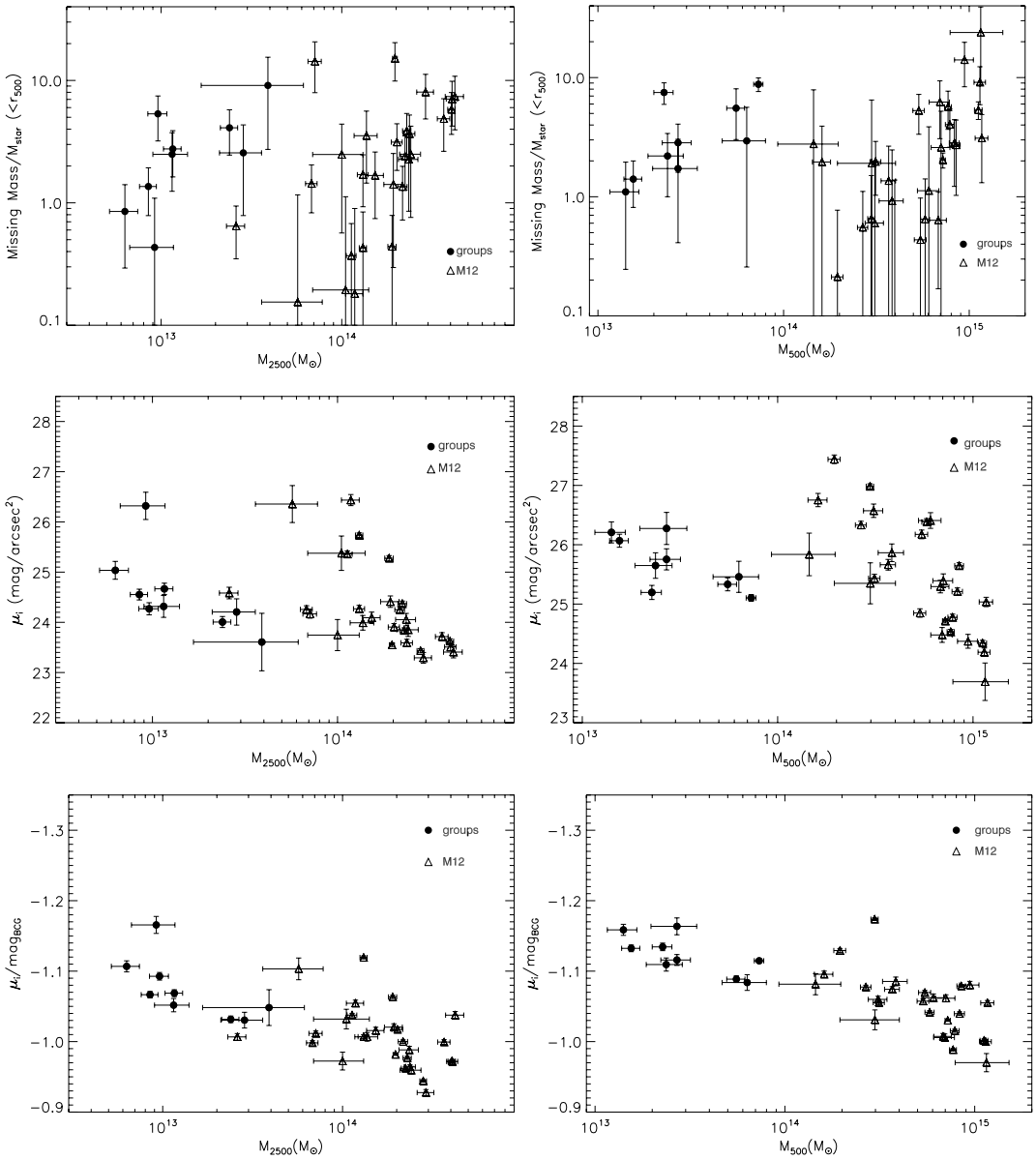

Fig. 7. *Top*: "missing stellar mass" to total stellar mass ratio as a function of M_{2500} (*left panel*) and M_{500} (*right panel*); *Middle*: "missing stellar surface brightness" as a function of total mass for r_{2500} (*left panel*) and r_{500} (*right panel*); *Bottom*: "missing stellar surface brightness" to BCG magnitude ratio as a function of M_{2500} (*left panel*) and M_{500} (*right panel*).

the lower potential well, in galaxy clusters, the cold baryons (stars in galaxies) are more affected due to ram-pressure stripping. These mechanisms make the baryon distribution in these two structures different. Many studies have indeed reported systematic differences between the physical properties of groups and the clusters.

– To investigate the contribution of the ICL to the baryon budget, we computed the difference in mass between the WMAP-7 value and the observed baryon fraction in terms of surface brightness. The values found here for the expected missing surface brightness for clusters of galaxies are similar to the ICL surface brightness detected in the literature, which span the range of $\sim 24 < \mu_r < 28$. If the difference between the observed baryon fraction and the WMAP-7 value is because of luminous matter that is spread throughout the volume of the system, as a direct consequence of $M_{\rm star}$ dependence on $M_{\rm tot}$, we observe a small increase in Missing Mass/$M_{\rm star}$ with total mass, and groups and clusters seem to be separated into two distinct populations. However, we have a high scatter inside both r_{2500} and r_{500}. In terms of missing surface brightness, we observe a small decrease as a function of total mass also for the ratio between the missing surface brightness and the BCG magnitude inside r_{500}, but it is difficult to spot a clear trend from these panels.

Acknowledgements. We are very grateful to Christophe Adami and Emmanuel Bertin for their advice during the early stages of this work. We are also grateful to the anonymous referee who carefully read this paper and gave important suggestions. We acknowledge financial support from CNES and CAPES/COFECUB program 711/11. T.F.L. acknowledges financial support from FAPESP (grant: 2008/0431-8). Y.Y.Z. acknowledges support from the German BMWi through the Verbundforschung under the grant NO 50 OR 1103.

References

Allen, S. W., Schmidt, R. W., & Fabian, A. C. 2002, MNRAS, 334, L11
Allen, S. W., Schmidt, R. W., Ebeling, H., Fabian, A. C., & van Speybroeck, L. 2004, MNRAS, 353, 457

Allen, S. W., Rapetti, D. A., Schmidt, R. W., et al. 2008, MNRAS, 383, 879
Andreon, S. 2010, MNRAS, 407, 263
Bell, E. F., McIntosh, D. H., Katz, N., & Weinberg, M. D. 2003, ApJS, 149, 289
Blanton, M. R., Hogg, D. W., Bahcall, N. A., et al. 2003, ApJ, 592, 819
Bolzonella, M., Kovač, K., Pozzetti, L., et al. 2010, A&A, 524, A76
Bregman, J. N. 2007, ARA&A, 45, 221
Burke, C., Collins, C. A., Stott, J. P., & Hilton, M. 2012, MNRAS, 425, 2058
Cavaliere, A., & Fusco-Femiano, R. 1978, A&A, 70, 677
Dai, X., Bregman, J. N., Kochanek, C. S., & Rasia, E. 2010, ApJ, 719, 119
David, L. P., Arnaud, K. A., Forman, W., & Jones, C. 1990, ApJ, 356, 32
Dubois, Y., Pichon, C., Devriendt, J., et al. 2013, MNRAS, 428, 2885
Durret, F., Lagan , T. F., Adami, C., & Bertin, E. 2010, A&A, 517, A94
Durret, F., Lagan , T. F., & Haider, M. 2011, A&A, 529, A38
Eckmiller, H. J., Hudson, D. S., & Reiprich, T. H. 2011, A&A, 535, A105
Ettori, S., & Fabian, A. C. 1999, MNRAS, 305, 834
Ettori, S., Morandi, A., Tozzi, P., et al. 2009, A&A, 501, 61
Evrard, A. E. 1997, MNRAS, 292, 289
Feldmeier, J. J., Mihos, J. C., Morrison, H. L., Rodney, S. A., & Harding, P. 2002, ApJ, 575, 779
Giodini, S., Pierini, D., Finoguenov, A., et al. 2009, ApJ, 703, 982
Gonzalez, A. H., Zaritsky, D., & Zabludoff, A. I. 2007, ApJ, 666, 147
Hansen, S. M., McKay, T. A., Wechsler, R. H., et al. 2005, ApJ, 633, 122
Jarosik, N., Bennett, C. L., Dunkley, J., et al. 2011, ApJS, 192, 14
Kalberla, P. M. W., Burton, W. B., Hartmann, D., et al. 2005, A&A, 440, 775
Kauffmann, G., Heckman, T. M., White, S. D. M., et al. 2003, MNRAS, 341, 33
Kravtsov, A. V., Vikhlinin, A., & Nagai, D. 2006, ApJ, 650, 128
Krick, J. E., & Bernstein, R. A. 2007, AJ, 134, 466
Lagan , T. F., Lima Neto, G. B., Andrade-Santos, F., & Cypriano, E. S. 2008, A&A, 485, 633
Lagan , T. F., Zhang, Y.-Y., Reiprich, T. H., & Schneider, P. 2011, ApJ, 743, 13
Landry, D., Bonamente, M., Giles, P., Maughan, B., & Joy, M. 2013, MNRAS, submitted [arXiv:1211.4626]
Lima Neto, G. B., Capelato, H. V., Sodr , L. Jr., & Proust, D. 2003, A&A, 398, 31
Lin, Y.-T., Mohr, J. J., & Stanford, S. A. 2003, ApJ, 591, 749
Mantz, A., Allen, S. W., Rapetti, D., & Ebeling, H. 2010, MNRAS, 406, 1759
Maughan, B. J., Jones, C., Forman, W., & Van Speybroeck, L. 2008, ApJS, 174, 117
Maughan, B. J., Giles, P. A., Randall, S. W., Jones, C., & Forman, W. R. 2012, MNRAS, 421, 1583
Mulchaey, J. S. 2000, ARA&A, 38, 289
Nagai, D., Vikhlinin, A., & Kravtsov, A. V. 2007, ApJ, 655, 98
Navarro, J. F., Frenk, C. S., & White, S. D. M. 1997, ApJ, 490, 493
Piffaretti, R., & Valdarnini, R. 2008, A&A, 491, 71
Planelles, S., Borgani, S., Dolag, K., et al. 2013, MNRAS, 431, 1487
Poggianti, B. M. 1997, A&AS, 122, 399
Pointecouteau, E., Arnaud, M., Kaastra, J., & de Plaa, J. 2004, A&A, 423, 33
Ponman, T. J., Sanderson, A. J. R., & Finoguenov, A. 2003, MNRAS, 343, 331
Pozzetti, L., Bolzonella, M., Zucca, E., et al. 2010, A&A, 523, A13
Press, W. H., Teukolsky, S. A., Vetterling, W. T., & Flannery, B. P. 1992, Numerical recipes in FORTRAN. The art of scientific computing
Puchwein, E., Springel, V., Sijacki, D., & Dolag, K. 2010, MNRAS, 406, 936
Read, A. M., & Ponman, T. J. 2003, A&A, 409, 395
Roussel, H., Sadat, R., & Blanchard, A. 2000, A&A, 361, 429
Springel, V., & Hernquist, L. 2003, MNRAS, 339, 312
Sun, M. 2012, New J. Phys., 14, 045004
Sun, M., Voit, G. M., Donahue, M., et al. 2009, ApJ, 693, 1142
Vikhlinin, A., Kravtsov, A., Forman, W., et al. 2006, ApJ, 640, 691
Vikhlinin, A., Burenin, R. A., Ebeling, H., et al. 2009, ApJ, 692, 1033
Voit, G. M. 2005, Rev. Mod. Phys., 77, 207
White, S. D. M., Navarro, J. F., Evrard, A. E., & Frenk, C. S. 1993, Nature, 366, 429
Young, O. E., Thomas, P. A., Short, C. J., & Pearce, F. 2011, MNRAS, 413, 691
Zehavi, I., Patiri, S., & Zheng, Z. 2012, ApJ, 746, 145
Zhang, Y., Okabe, N., Finoguenov, A., et al. 2010, ApJ, 711, 1033
Zhang, Y.-Y., Lagan , T. F., Pierini, D., et al. 2011, A&A, 535, A78
Zibetti, S., White, S. D. M., Schneider, D. P., & Brinkmann, J. 2005, MNRAS, 358, 949

Pages 12 to 16 are available in the electronic edition of the journal at http://www.aanda.org

Table 1. General properties, X-ray parameters and stellar masses derived for our sample.

Groups												
Name	z	RA	Dec	r_{2500} (h_{70}^{-1}) kpc	r_{500} (h_{70}^{-1}) kpc	$\langle kT \rangle$ (keV)	$M_{\rm gas,2500}$ (10^{12} $M_\odot$)	$M_{\rm gas,500}$ (10^{12} $M_\odot$)	$M_{\rm tot,2500}$ (10^{13} $M_\odot$)	$M_{\rm tot,500}$ (10^{13} $M_\odot$)	$M_{\rm star,2500}$ (10^{12} $M_\odot$)	$M_{\rm star,500}$ (10^{12} $M_\odot$)
NGC1132	0.023	02h52m51.9s	−01d16m29s	171.5	383.5	0.98 ± 0.10	0.29 ± 0.03	1.24 ± 0.03	0.85 ± 0.09	1.55 ± 0.17	0.37 ± 0.09	0.60 ± 0.12
RBS461	0.030	03h41m21.7s	+15d24m18s	262.4	586.8	2.14 ± 0.46	0.55 ± 0.09	2.09 ± 0.39	0.92 ± 0.25	2.70 ± 0.73	0.54 ± 0.15	0.95 ± 0.25
NGC4104	0.028	12h06m39.0s	+28d10m27s	224.7	502.5	1.63 ± 0.18	0.57 ± 0.05	2.05 ± 0.09	1.16 ± 0.13	2.70 ± 0.48	0.28 ± 0.07	0.69 ± 0.18
NGC4325	0.026	12h23m06.7s	+10d37m16s	182.1	408.6	0.89 ± 0.11	0.47 ± 0.05	1.50 ± 0.02	0.96 ± 0.12	2.27 ± 0.27	0.14 ± 0.04	0.29 ± 0.08
NGC5098	0.037	13h20m16.2s	+33d08m39s	154.1	344.6	0.94 ± 0.17	0.32 ± 0.05	1.30 ± 0.21	0.63 ± 0.11	1.41 ± 0.25	0.31 ± 0.08	0.55 ± 0.14
Abell1991	0.059	14h54m30.2s	+18d37m51s	251.9	563.3	2.20 ± 0.57	2.11 ± 0.46	6.68 ± 0.12	2.85 ± 0.74	6.33 ± 1.66	0.59 ± 0.18	1.09 ± 0.30
AWM4	0.032	16h04m57.0s	+23d55m14s	245.0	547.8	2.40 ± 0.26	1.27 ± 0.12	5.60 ± 0.29	2.39 ± 0.26	5.55 ± 0.61	0.42 ± 0.10	0.62 ± 0.14
IC1262	0.033	17h33m02.0s	+43d45m35s	284.8	636.9	2.64 ± 1.51	1.75 ± 0.64	6.36 ± 0.65	3.90 ± 1.23	7.32 ± 4.20	0.37 ± 0.11	0.65 ± 0.18
RXCJ2315.7-0222	0.027	23h15m44.1s	−02d22m59s	191.0	427.1	1.39 ± 0.23	0.51 ± 0.06	1.86 ± 0.19	1.15 ± 0.25	2.37 ± 0.51	0.31 ± 0.09	0.70 ± 0.20
Clusters from M12												
Name	z	RA	Dec	r_{2500} (h_{70}^{-1}) kpc	r_{500} (h_{70}^{-1}) kpc	$\langle kT \rangle$ (keV)	$M_{\rm gas,2500}$ (10^{13} $M_\odot$)	$M_{\rm gas,500}$ (10^{13} $M_\odot$)	$M_{\rm tot,2500}$ (10^{14} $M_\odot$)	$M_{\rm tot,500}$ (10^{14} $M_\odot$)	$M_{\rm star,2500}$ (10^{13} $M_\odot$)	$M_{\rm star,500}$ (10^{13} $M_\odot$)
MS0015.9+1609	0.54	00h18m33.631s	+16d26m13.56s	445.6	1092.6	8.3 ± 0.5	3.34 ± 0.17	12.9 ± 0.6	2.26 ± 0.14	6.67 ± 0.40	–	–
RXJ0027.6+2616	0.37	00h27m46.051s	+26d16m19.92s	328.4	914.8	4.8 ± 1.0	0.78 ± 0.14	4.5 ± 0.8	0.74 ± 0.15	3.19 ± 0.66	–	–
CLJ0030+2618	0.50	00h30m33.948s	+26d18m08.28s	291.2	811.4	4.1 ± 1.7	0.60 ± 0.21	3.1 ± 1.1	0.60 ± 0.25	2.60 ± 1.08	–	–
MS0015.9+1609	0.54	00h18m33.631s	+16d26m13.56s	445.6	1092.6	8.3 ± 0.5	3.34 ± 0.17	12.9 ± 0.6	2.26 ± 0.14	6.67 ± 0.40	–	–
RXJ0027.6+2616	0.37	00h27m46.051s	+26d16m19.92s	328.4	914.8	4.8 ± 1.0	0.78 ± 0.14	4.5 ± 0.8	0.74 ± 0.15	3.19 ± 0.66	–	–
CLJ0030+2618	0.50	00h30m33.948s	+26d18m08.28s	291.2	811.4	4.1 ± 1.7	0.60 ± 0.21	3.1 ± 1.1	0.60 ± 0.25	2.60 ± 1.08	–	–
A68	0.26	00h37m06.089s	+09d09m33.04s	559.6	1352.7	7.8 ± 1.0	2.98 ± 0.32	8.8 ± 0.9	3.22 ± 0.41	9.10 ± 1.17	–	–
A115	0.20	00h55m50.688s	+26d24m37.80s	429.4	1035.7	6.7 ± 1.0	1.45 ± 0.18	6.5 ± 0.8	1.37 ± 0.20	3.84 ± 0.57	0.14 ± 0.04	0.81 ± 0.24
A209	0.21	01h31m53.520s	−13d36m46.44s	479.9	1213.1	7.4 ± 0.5	2.23 ± 0.13	9.7 ± 0.5	1.93 ± 0.13	6.22 ± 0.42	–	–
CLJ0152.7-1357S	0.83	01h52m39.888s	−13d58m26.76s	239.7	625.3	4.9 ± 1.1	0.50 ± 0.09	3.0 ± 0.6	0.50 ± 0.11	1.77 ± 0.40	–	–
A267	0.23	01h52m42.144s	+01d00m41.29s	404.3	953.3	4.4 ± 0.5	1.61 ± 0.15	5.2 ± 0.5	1.18 ± 0.13	3.10 ± 0.35	0.25 ± 0.07	0.55 ± 0.16
CLJ0152.7-1357N	0.83	01h52m44.280s	−13d57m19.08s	239.0	621.1	4.9 ± 0.9	0.53 ± 0.08	3.2 ± 0.5	0.49 ± 0.09	1.73 ± 0.32	–	–
MACSJ0159.8-0849	0.41	01h59m49.368s	−08d50m00.42s	570.7	1296.3	10.2 ± 0.9	4.09 ± 0.30	11.5 ± 0.8	4.05 ± 0.36	9.49 ± 0.84	–	–
CLJ0216-1747	0.58	02h16m32.856s	−17d47m32.28s	318.9	849.9	5.6 ± 3.8	0.47 ± 0.27	2.4 ± 1.4	0.87 ± 0.59	3.28 ± 2.22	–	–
RXJ0232.2-4420	0.28	02h32m18.216s	−44d20m49.56s	539.0	1317.5	8.0 ± 1.4	3.58 ± 0.52	11.2 ± 1.6	2.97 ± 0.52	8.68 ± 1.52	–	–
MACSJ0242.5-2132	0.31	02h42m35.856s	−21d32m26.16s	439.9	985.5	5.5 ± 0.7	2.14 ± 0.23	5.7 ± 0.6	1.67 ± 0.21	3.76 ± 0.48	–	–
A383	0.19	02h48m03.432s	−03d31m45.87s	425.1	971.2	4.5 ± 0.3	1.40 ± 0.08	4.0 ± 0.2	1.31 ± 0.09	3.13 ± 0.21	0.22 ± 0.07	0.49 ± 0.15
MACSJ0257.6-2209	0.32	02h57m41.328s	−22d09m14.40s	455.5	1199.4	6.7 ± 0.9	1.99 ± 0.22	7.6 ± 0.9	1.87 ± 0.25	6.83 ± 0.92	–	–
MS0302.7+1658	0.42	03h05m31.656s	+17d10m10.56s	308.9	697.8	3.3 ± 0.8	0.82 ± 0.17	2.5 ± 0.5	0.66 ± 0.16	1.51 ± 0.37	–	–
CLJ0318-0302	0.37	03h18m33.456s	−03d02m57.30s	435.4	1030.8	5.4 ± 1.7	1.31 ± 0.34	3.8 ± 1.0	1.73 ± 0.54	4.58 ± 1.44	–	–
MACSJ0329.6-0211	0.45	03h29m41.520s	−02d11m45.99s	349.9	839.6	4.5 ± 0.5	1.74 ± 0.16	5.7 ± 0.5	0.98 ± 0.11	2.72 ± 0.30	–	–
MACSJ0404.6+1109	0.36	04h04m32.664s	+11d08m16.80s	343.1	834.5	5.5 ± 0.7	0.84 ± 0.09	4.5 ± 0.5	0.83 ± 0.11	2.39 ± 0.30	–	–
MACSJ0429.6-0253	0.40	04h29m35.952s	−02d53m06.21s	456.1	1065.8	6.5 ± 0.7	2.27 ± 0.20	6.5 ± 0.6	2.05 ± 0.22	5.24 ± 0.56	–	–
RXJ0439.0+0715	0.23	04h39m00.672s	+07d16m03.75s	440.1	1169.6	5.3 ± 0.4	2.05 ± 0.13	7.3 ± 0.5	1.52 ± 0.12	5.72 ± 0.43	–	–
RXJ0439+0520	0.21	04h39m02.304s	+05d20m43.26s	387.7	848.8	3.9 ± 0.4	1.15 ± 0.10	3.1 ± 0.3	1.02 ± 0.10	2.14 ± 0.22	–	–
MACSJ0451.9+0006	0.43	04h51m54.408s	+00d06m19.13s	363.0	892.7	5.0 ± 1.1	1.50 ± 0.27	5.9 ± 1.1	1.07 ± 0.24	3.19 ± 0.70	–	–
A521	0.55	04h54m11.184s	−03d00m53.85s	292.4	906.2	4.8 ± 0.2	0.67 ± 0.02	6.8 ± 0.2	0.46 ± 0.02	2.73 ± 0.11	–	–
A520	0.25	04h54m06.576s	−10d13m15.24s	447.1	1251.2	6.5 ± 0.3	2.02 ± 0.08	10.3 ± 0.4	1.55 ± 0.07	6.78 ± 0.31	–	–
MS0451.6-0305	0.20	04h54m09.600s	+02d55m28.63s	447.1	1148.9	7.6 ± 1.2	3.60 ± 0.47	12.6 ± 1.7	2.31 ± 0.36	7.83 ± 1.24	–	–
CLJ0522-3625	0.47	05h22m14.832s	−36d24m57.60s	318.7	845.2	4.3 ± 1.4	0.60 ± 0.16	2.8 ± 0.7	0.76 ± 0.25	2.84 ± 0.93	–	–
CLJ0542.8-4100	0.64	05h42m50.208s	−41d00m04.32s	346.4	872.4	6.2 ± 1.0	1.11 ± 0.15	4.8 ± 0.7	1.20 ± 0.19	3.83 ± 0.62	–	–
MACSJ0647.7+7015	0.58	06h47m50.160s	+70d14m55.68s	533.6	1231.0	11.3 ± 2.1	3.88 ± 0.60	11.8 ± 1.8	4.09 ± 0.76	10.04 ± 1.86	–	–
1E0657-56	0.30	06h58m30.000s	−55d56m39.12s	692.9	1722.6	11.7 ± 0.5	8.57 ± 0.31	25.0 ± 0.9	6.40 ± 0.27	19.66 ± 0.84	–	–
MACSJ0717.5+3745	0.55	07h17m31.680s	+37d45m31.68s	400.9	1513.0	10.6 ± 1.0	2.77 ± 0.22	24.4 ± 1.9	1.66 ± 0.16	17.81 ± 1.68	–	–
A586	0.17	07h32m20.160s	+31d37m55.92s	557.8	1265.8	7.6 ± 0.8	2.45 ± 0.22	6.9 ± 0.6	2.91 ± 0.31	6.81 ± 0.72	0.2 ± 0.06	2.97 ± 0.89
MACSJ0744.9+3927	0.70	07h44m52.320s	+39d27m26.64s	392.2	1017.6	8.1 ± 0.7	2.60 ± 0.19	10.3 ± 0.7	1.86 ± 0.16	6.49 ± 0.56	–	–
A665	0.18	08h30m57.360s	+65d50m33.36s	481.6	1357.3	7.8 ± 0.4	2.39 ± 0.10	12.6 ± 0.5	1.90 ± 0.10	8.50 ± 0.44	0.43 ± 0.13	0.58 ± 0.17
A697	0.28	08h42m57.600s	+36d21m55.80s	578.7	1455.7	10.2 ± 0.8	4.34 ± 0.28	16.1 ± 1.1	3.67 ± 0.29	11.68 ± 0.92	0.34 ± 0.11	0.70 ± 0.21
CLJ0848.7+4456	0.57	08h48m47.760s	+44d56m13.92s	199.7	460.7	2.0 ± 0.2	0.19 ± 0.02	0.8 ± 0.1	0.21 ± 0.02	0.52 ± 0.05	–	–
ZWCLJ1953	0.32	08h50m06.960s	+36d04m17.40s	441.9	1057.0	6.1 ± 0.6	1.96 ± 0.16	6.8 ± 0.6	1.71 ± 0.17	4.67 ± 0.46	–	–
CLJ0853+5759	0.48	08h53m14.880s	+57d59m57.48s	298.5	943.1	5.1 ± 1.5	0.42 ± 0.10	3.1 ± 0.8	0.63 ± 0.18	3.97 ± 1.17	–	–
MS0906.5+1110	0.18	09h09m12.720s	+10d58m32.88s	405.7	923.0	4.7 ± 0.3	1.28 ± 0.07	4.4 ± 0.2	1.13 ± 0.07	2.67 ± 0.17	0.28 ± 0.09	0.92 ± 0.31
RXJ0910+5422	1.11	09h10m44.880s	+54d22m07.68s	161.6	524.9	2.7 ± 1.9	0.20 ± 0.12	1.3 ± 0.8	0.21 ± 0.15	1.45 ± 1.02	–	–
A773	0.22	09h17m53.040s	+51d43m39.72s	506.2	1306.3	7.4 ± 0.4	2.52 ± 0.11	9.6 ± 0.4	2.29 ± 0.12	7.86 ± 0.42	0.20 ± 0.06	0.80 ± 0.24
A781	0.30	09h20m26.160s	+30d30m02.52s	332.0	984.4	5.5 ± 0.5	0.85 ± 0.06	6.6 ± 0.5	0.71 ± 0.06	3.68 ± 0.33	0.30 ± 0.10	0.60 ± 0.18
CLJ0926+1242	0.49	09h26m36.480s	+12d43m03.36s	306.2	804.2	4.5 ± 1.0	0.61 ± 0.11	2.9 ± 0.5	0.69 ± 0.15	2.50 ± 0.56	–	–

Table 1. continued.

Name	z	RA	Dec	r_{2500}	r_{500}	$\langle kT \rangle$	$M_{\rm gas,2500}$	$M_{\rm gas,500}$	$M_{\rm tot,2500}$	$M_{\rm tot,500}$	$M_{\rm star,2500}$	$M_{\rm star,500}$
				(h_{70}^{-1}) kpc	(h_{70}^{-1}) kpc	(keV)	$(10^{13}\ M_\odot)$	$(10^{13}\ M_\odot)$	$(10^{14}\ M_\odot)$	$(10^{14}\ M_\odot)$	$(10^{13}\ M_\odot)$	$(10^{13}\ M_\odot)$
RBS797	0.35	09h47m12.960s	+76d23m13.56s	509.5	1139.7	7.3 ± 1.0	3.30 ± 0.38	8.1 ± 0.9	2.72 ± 0.37	6.08 ± 0.83	–	–
MACSJ0949.8+1708	0.38	09h49m51.840s	+17d07m07.68s	457.2	1057.7	7.3 ± 0.9	2.59 ± 0.27	9.0 ± 0.9	2.03 ± 0.25	5.03 ± 0.62	–	–
CLJ0956+4107	0.59	09h56m03.360s	+41d07m12.72s	278.8	792.9	4.0 ± 0.7	0.61 ± 0.09	3.2 ± 0.5	0.58 ± 0.10	2.69 ± 0.47	–	–
A907	0.15	09h58m21.840s	−11d03m49.32s	471.0	1063.7	5.4 ± 0.2	1.79 ± 0.06	5.2 ± 0.2	1.72 ± 0.06	3.97 ± 0.15	–	–
MS1006.0+1202	0.22	10h08m47.520s	+11d47m42.36s	469.4	1122.1	6.0 ± 0.5	1.58 ± 0.11	5.4 ± 0.4	1.83 ± 0.15	5.01 ± 0.42	–	–
MS1008.1-1224	0.30	10h10m32.400s	−12d39m30.24s	353.4	997.7	4.6 ± 0.4	1.13 ± 0.08	5.5 ± 0.4	0.85 ± 0.07	3.84 ± 0.33	–	–
ZW3146	0.29	10h23m39.600s	+04d11m12.08s	561.6	1267.8	7.8 ± 0.4	4.18 ± 0.18	10.1 ± 0.4	3.39 ± 0.17	7.79 ± 0.40	–	–
CLJ1113.1-2615	0.73	11h13m05.280s	-26d15m38.88s	262.2	610.7	3.6 ± 1.3	0.50 ± 0.15	1.8 ± 0.5	0.57 ± 0.21	1.45 ± 0.52	–	–
A1204	0.17	11h13m20.400s	+17d35m40.92s	383.0	858.1	3.7 ± 0.3	1.10 ± 0.07	3.0 ± 0.2	0.94 ± 0.08	2.12 ± 0.17	0.29 ± 0.09	0.19 ± 0.06
CLJ1117+1745	0.55	11h17m30.000s	+17d44m52.44s	245.6	569.4	3.3 ± 0.9	0.29 ± 0.07	1.3 ± 0.3	0.38 ± 0.10	0.95 ± 0.26	–	–
CLJ1120+4318	0.56	11h20m57.360s	+23d26m30.12s	341.2	906.2	5.2 ± 1.3	1.33 ± 0.28	5.3 ± 1.1	1.09 ± 0.27	4.08 ± 1.02	–	–
RXJ1121+2327	0.60	11h20m07.200s	+43d18m05.76s	51.5	709.7	3.2 ± 0.3	0.00 ± 0.00	3.0 ± 0.2	0.00 ± 0.00	1.87 ± 0.18	–	–
A1240	0.16	11h23m37.920s	+43d05m37.32s	111.2	1108.8	3.8 ± 0.3	0.01 ± 0.00	3.6 ± 0.2	0.02 ± 0.00	4.52 ± 0.36	–	–
MACSJ1131.8-1955	0.31	11h31m55.200s	−19d55m50.88s	501.0	1466.2	9.5 ± 1.8	2.88 ± 0.45	15.5 ± 2.4	2.45 ± 0.46	12.27 ± 2.33	–	–
MS1137.5+6625	0.78	11h40m22.320s	+66d08m15.72s	368.7	853.6	6.5 ± 1.4	1.46 ± 0.26	4.2 ± 0.8	1.71 ± 0.37	4.24 ± 0.91	–	–
MACSJ1149.5+2223	0.55	11h49m35.040s	+22d24m10.08s	402.8	1044.2	8.5 ± 1.1	2.32 ± 0.25	12.2 ± 1.3	1.68 ± 0.22	5.85 ± 0.76	–	–
A1413	0.14	11h55m18.000s	+23d24m17.28s	556.4	1330.7	7.1 ± 0.3	2.84 ± 0.10	8.4 ± 0.3	2.81 ± 0.12	7.69 ± 0.32	0.42 ± 0.13	0.74 ± 0.22
CLJ1213+0253	0.41	12h13m34.800s	+02d53m46.39s	316.0	809.7	3.9 ± 0.9	0.49 ± 0.09	2.1 ± 0.4	0.69 ± 0.16	2.32 ± 0.54	–	–
RXJ1221+4918	0.70	12h21m26.400s	+49d18m30.24s	302.2	789.3	5.9 ± 0.7	0.85 ± 0.08	4.6 ± 0.5	0.85 ± 0.10	3.04 ± 0.36	–	–
CLJ1226.9+3332	0.89	12h26m57.840s	+33d32m47.76s	436.8	1029.6	10.0 ± 1.9	3.08 ± 0.49	8.7 ± 1.4	3.23 ± 0.61	8.46 ± 1.61	–	–
RXJ1234.2+0947	0.23	12h34m17.50s	+09d45m58.48s	382.0	1477.9	7.6 ± 2.4	0.73 ± 0.19	8.3 ± 2.2	1.00 ± 0.31	11.53 ± 3.64	0.23 ± 0.08	0.47 ± 0.14
RDCS1252-29	1.24	12h52m54.960s	−29d27m20.88s	195.2	503.3	4.6 ± 0.9	0.33 ± 0.05	1.7 ± 0.3	0.43 ± 0.08	1.47 ± 0.29	–	–
A1682	0.23	13h06m50.880s	+46d33m30.24s	388.0	939.2	5.8 ± 2.0	1.15 ± 0.33	5.6 ± 1.6	1.05 ± 0.36	2.98 ± 1.03	0.20 ± 0.06	0.52 ± 0.16
MACSJ1311.0-0310	0.49	13h11m01.680s	−03d10m36.87s	450.6	1030.4	6.5 ± 0.8	2.01 ± 0.21	5.1 ± 0.5	2.21 ± 0.27	5.29 ± 0.65	–	–
A1689	0.18	13h11m29.520s	−01d20m29.68s	619.6	1487.5	8.4 ± 0.4	4.56 ± 0.18	12.0 ± 0.5	4.05 ± 0.19	11.20 ± 0.53	0.58 ± 0.17	1.17 ± 0.35
RXJ1317.4+2911	0.81	13h17m20.880s	+29d11m15.00s	161.2	418.9	2.2 ± 0.8	0.11 ± 0.03	0.7 ± 0.2	0.15 ± 0.05	0.51 ± 0.19	–	–
CLJ1334+5031	0.62	13h34m19.200s	+50d31m05.52s	324.4	742.2	5.2 ± 2.1	0.89 ± 0.30	3.3 ± 1.1	0.96 ± 0.39	2.30 ± 0.93	–	–
A1763	0.22	13h35m18.240s	+40d59m59.28s	496.4	1328.3	8.1 ± 0.5	2.45 ± 0.13	11.5 ± 0.6	2.17 ± 0.13	8.32 ± 0.51	0.25 ± 0.07	0.79 ± 0.24
RXJ1347.5-1145	0.45	13h47m30.720s	−11d45m10.44s	672.0	1524.6	14.2 ± 1.4	7.95 ± 0.65	20.2 ± 1.7	6.97 ± 0.69	16.28 ± 1.61	–	–
RXJ1350.0+6007	0.80	13h50m48.480s	+60d07m55.20s	240.6	602.6	4.5 ± 1.0	0.41 ± 0.08	2.2 ± 0.4	0.49 ± 0.11	1.53 ± 0.34	–	–
CLJ1354-0221	0.55	13h54m17.280s	−02d21m50.97s	228.7	585.3	3.1 ± 0.9	0.30 ± 0.07	1.7 ± 0.4	0.31 ± 0.09	1.03 ± 0.30	–	–
CLJ1415.1+3612	1.03	14h15m11.040s	+36d12m03.60s	229.7	574.1	4.3 ± 0.6	0.64 ± 0.07	2.7 ± 0.3	0.55 ± 0.08	1.73 ± 0.24	–	–
RXJ1416+4446	0.40	14h16m28.080s	+44d46m43.32s	321.9	793.7	3.9 ± 0.5	0.78 ± 0.08	3.0 ± 0.3	0.72 ± 0.09	2.17 ± 0.28	–	–
MACSJ1423.8+2404	0.54	14h23m47.760s	+24d04m41.88s	380.1	943.4	6 ± 1.0	1.90 ± 0.26	6.4 ± 0.9	1.41 ± 0.23	4.30 ± 0.72	–	–
A1914	0.17	14h26m00.960s	+37d49m33.96s	623.9	1503.5	8.5 ± 0.6	4.36 ± 0.26	11.7 ± 0.7	4.08 ± 0.29	11.42 ± 0.81	0.38 ± 0.12	0.81 ± 0.24
A1942	0.22	14h38m22.080s	+03d40m06.38s	337.6	818.6	4.2 ± 0.3	0.59 ± 0.04	2.8 ± 0.2	0.68 ± 0.05	1.95 ± 0.14	0.17 ± 0.05	0.51 ± 0.16
MS1455.0+2232	0.26	14h57m15.120s	+22d20m35.52s	414.7	930.3	4.7 ± 0.2	1.83 ± 0.06	5.0 ± 0.2	1.31 ± 0.06	2.97 ± 0.13	0.21 ± 0.06	0.33 ± 0.10
RXJ1504-0248	0.22	15h04m07.440s	−02d48m18.50s	621.6	1388.6	9.4 ± 1.1	4.40 ± 0.43	10.7 ± 1.0	4.23 ± 0.49	9.43 ± 1.10	0.21 ± 0.08	0.38 ± 0.12
A2034	0.11	15h10m12.480s	+33d30m28.08s	499.2	1315.5	6.3 ± 0.2	1.85 ± 0.05	7.3 ± 0.2	1.97 ± 0.06	7.21 ± 0.23	0.07 ± 0.02	1.71 ± 0.50
A2069	0.12	15h24m39.840s	+29d53m26.33s	334.1	1173.2	5.9 ± 0.3	0.51 ± 0.02	6.3 ± 0.3	0.59 ± 0.03	5.13 ± 0.26	0.27 ± 0.09	0.22 ± 0.06
RXJ1525+0958	0.12	15h24m09.600s	+29d53m07.80s	218.0	687.6	3.5 ± 0.4	0.32 ± 0.03	3.0 ± 0.3	0.26 ± 0.03	1.61 ± 0.18	–	–
RXJ1532.9+3021	0.35	15h32m53.760s	+30d20m59.28s	476.2	1068.4	6.3 ± 1.0	2.89 ± 0.38	7.2 ± 1.0	2.20 ± 0.35	4.96 ± 0.79	–	–
A2111	0.23	15h39m41.280s	+34d25m10.92s	441.0	1035.7	6.4 ± 0.7	1.55 ± 0.14	6.3 ± 0.6	1.53 ± 0.17	3.97 ± 0.43	0.28 ± 0.09	0.65 ± 0.19
A2125	0.25	15h41m08.880s	+66d15m53.28s	166.1	616.2	2.4 ± 0.2	0.08 ± 0.01	1.5 ± 0.1	0.08 ± 0.01	0.85 ± 0.07	–	–
A2163	0.20	16h15m45.840s	−06d08m54.52s	722.0	2203.3	15.2 ± 1.2	8.45 ± 0.56	38.7 ± 2.5	6.54 ± 0.52	37.16 ± 2.93	–	–
MACSJ1621.3+3810	0.46	16h21m24.720s	+38d10m09.48s	422.1	971.9	6.2 ± 0.5	1.87 ± 0.13	5.6 ± 0.4	1.75 ± 0.14	4.28 ± 0.35	–	–
MS1621.5+2640	0.43	16h23m35.520s	+26d34m20.64s	357.7	1000.7	5.8 ± 0.7	1.05 ± 0.11	6.0 ± 0.6	1.02 ± 0.12	4.47 ± 0.54	–	–
A2204	0.15	16h32m47.040s	+05d34m32.52s	586.4	1323.8	8.4 ± 0.8	3.78 ± 0.30	10.6 ± 0.8	3.32 ± 0.32	7.64 ± 0.73	–	–
A2218	0.18	16h35m52.320s	+66d12m36.00s	479.2	1130.0	6.0 ± 0.3	2.08 ± 0.09	7.0 ± 0.3	1.86 ± 0.09	4.87 ± 0.24	–	–
CLJ1641+4001	0.46	16h41m53.040s	+40d01m27.48s	291.5	742.9	3.5 ± 0.6	0.50 ± 0.07	2.2 ± 0.3	0.58 ± 0.10	1.91 ± 0.33	–	–
RXJ1701+6414	0.45	17h01m22.800s	+64d14m11.40s	311.5	723.4	4.1 ± 0.5	0.77 ± 0.08	3.0 ± 0.3	0.70 ± 0.08	1.74 ± 0.21	–	–
RXJ1716.9+6708	0.81	17h16m49.440s	+67d08m25.80s	310.4	731.5	5.7 ± 1.1	1.05 ± 0.17	3.9 ± 0.6	1.06 ± 0.20	2.77 ± 0.53	–	–
A2259	0.16	17h20m10.080s	+27d39m03.28s	461.6	1117.1	5.2 ± 0.4	1.70 ± 0.11	5.5 ± 0.4	1.64 ± 0.13	4.65 ± 0.36	0.24 ± 0.07	1.50 ± 0.45
RXJ1720.1+2638	0.39	17h20m16.800s	+26d38m06.60s	522.0	1178.4	6.8 ± 0.5	2.57 ± 0.16	7.3 ± 0.4	2.37 ± 0.17	5.46 ± 0.40	0.30 ± 0.09	0.56 ± 0.17
MACSJ1720.2+3536	0.16	17h20m08.400s	+27d40m10.20s	479.7	1176.6	7.2 ± 0.9	2.62 ± 0.27	8.0 ± 0.8	2.35 ± 0.29	6.95 ± 0.87	–	–
A2261	0.22	17h22m27.120s	+32d07m56.28s	501.7	1176.8	7.3 ± 0.4	2.90 ± 0.13	9.7 ± 0.4	2.24 ± 0.12	5.79 ± 0.32	0.20 ± 0.06	0.92 ± 0.28
A2294	0.18	17h24m09.120s	+85d53m09.96s	550.7	1588.9	8.4 ± 1.1	2.58 ± 0.28	10.4 ± 1.1	2.83 ± 0.37	13.57 ± 1.78	–	–
MACSJ1824.3+4309	0.49	18h24m18.960s	+43d09m48.96s	267.0	742.4	4.8 ± 1.4	0.39 ± 0.09	2.9 ± 0.7	0.46 ± 0.13	1.96 ± 0.57	–	–
MACSJ1931.8-2634	0.35	19h31m49.680s	−26d34m32.88s	472.2	1066.4	6.7 ± 1.1	3.13 ± 0.43	8.6 ± 1.2	2.16 ± 0.35	4.97 ± 0.82	–	–
RXJ2011.3-5725	0.28	20h11m27.360s	−57d25m09.84s	364.8	829.3	3.6 ± 0.4	1.02 ± 0.09	2.9 ± 0.3	0.92 ± 0.10	2.15 ± 0.24	–	–

Table 1. continued.

Name	z	RA	Dec	r_{2500} (h_{70}^{-1}) kpc	r_{500} (h_{70}^{-1}) kpc	$\langle kT \rangle$ (keV)	$M_{\rm gas,2500}$ ($10^{13}\,M_\odot$)	$M_{\rm gas,500}$ ($10^{13}\,M_\odot$)	$M_{\rm tot,2500}$ ($10^{14}\,M_\odot$)	$M_{\rm tot,500}$ ($10^{14}\,M_\odot$)	$M_{\rm star,2500}$ ($10^{13}\,M_\odot$)	$M_{\rm star,500}$ ($10^{13}\,M_\odot$)
MS2053.7-0449	0.58	20h56m21.120s	−04d37m47.02s	291.3	669.0	3.9 ± 0.6	0.62 ± 0.08	2.2 ± 0.3	0.66 ± 0.10	1.61 ± 0.25	–	–
MACSJ2129.4-0741	0.59	21h29m25.920s	−07d41m30.26s	445.6	1036.3	8.3 ± 1.1	2.83 ± 0.31	9.2 ± 1.0	2.41 ± 0.32	6.06 ± 0.80	–	–
RXJ2129.6+0005	0.24	21h29m40.080s	+00d05m20.31s	465.5	1264.1	6.2 ± 0.6	2.32 ± 0.19	8.6 ± 0.7	1.81 ± 0.18	7.26 ± 0.70	0.26 ± 0.08	0.60 ± 0.19
A2409	0.15	22h00m52.800s	+20d58m27.84s	497.5	1177.1	5.7 ± 0.4	2.12 ± 0.12	6.4 ± 0.4	2.02 ± 0.14	5.35 ± 0.38	0.23 ± 0.07	0.47 ± 0.14
MACSJ2228.5+2036	0.41	22h28m32.880s	+20d37m11.64s	463.4	1265.0	8.6 ± 1.4	2.75 ± 0.37	12.9 ± 1.7	2.18 ± 0.36	8.89 ± 1.45	–	–
MACSJ2229.7-2755	0.32	22h29m45.360s	−27d55m36.48s	402.4	1098.4	5.0 ± 0.9	1.69 ± 0.25	5.9 ± 0.9	1.29 ± 0.23	5.26 ± 0.95	–	–
MACSJ2245.0+2637	0.30	22h45m04.800s	+26d38m03.48s	425.1	983.6	4.9 ± 0.5	1.86 ± 0.16	5.2 ± 0.4	1.49 ± 0.15	3.68 ± 0.38	–	–
RXJ2247+0337	0.20	22h47m28.080s	+03d36m57.78s	320.2	769.9	2.9 ± 0.9	0.22 ± 0.06	0.8 ± 0.2	0.57 ± 0.18	1.58 ± 0.49	–	–
AS1063	0.35	22h48m44.880s	−44d31m44.40s	634.7	1453.2	11.2 ± 1.1	7.16 ± 0.59	19.4 ± 1.6	5.21 ± 0.51	12.52 ± 1.23	–	–
CLJ2302.8+0844	0.72	23h02m48.000s	+08d43m51.56s	300.9	716.5	5.5 ± 2.4	0.61 ± 0.22	2.5 ± 0.9	0.86 ± 0.38	2.33 ± 1.02	–	–
A2631	0.27	23h37m38.160s	+00d16m09.00s	468.9	1234.6	6.9 ± 0.8	2.36 ± 0.23	9.9 ± 1.0	1.93 ± 0.22	7.05 ± 0.82	0.28 ± 0.08	0.62 ± 0.19

Appendix A: Testing the isothermal assumption to compute r_{500} and $M_{\rm tot,500}$

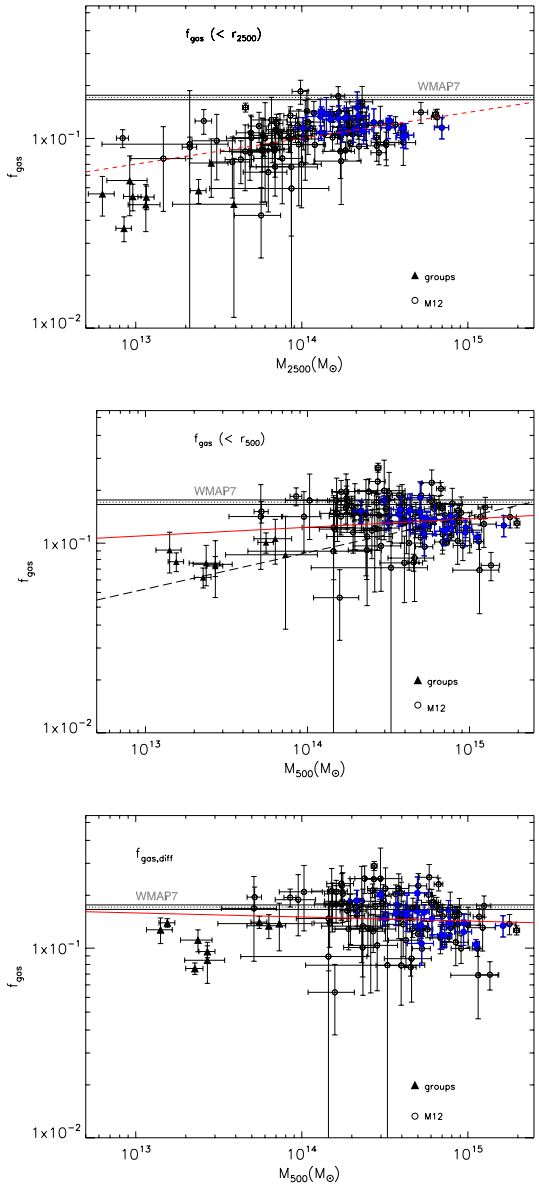

Fig. A.1. *Upper panel*: r_{500} computed assuming an isothermal gas, as a function of r_{500} computed, assuming the temperature profile given in Vikhlinin et al. (2006). *Middle panel*: $M_{\rm tot,500}$ computed, assuming an isothermal gas, as a function of $M_{\rm tot,500}$ computed, assuming the temperature profile given in Vikhlinin et al. (2006). *Lower panel*: $M_{\rm gas,500}$ computed, assuming an isothermal gas as a function of $M_{\rm gas,500}$ computed, assuming the temperature profile given in Vikhlinin et al. (2006).

To test if the assumption of an isothermal cluster would introduce any systematic effect on the total mass determination, biasing low the total mass of cool-core clusters, we consider eight cool-core clusters from Vikhlinin et al. (2006) for which all the necessary parameters were available. We computed r_{500}, $M_{\rm tot,500}$ and $M_{\rm gas,500}$ by considering their Eq. (6) to describe the temperature profile and a mean temperature, $T_{\rm mg}$, in the isothermal case. For both cases, the emission measure profile is given by the sum of a modified β-model profile and a second β-model component with a small core radius, as stated in their Eq. (2).

In Fig. A.1, we show the comparison between r_{500}, $M_{\rm tot,500}$ and $M_{\rm gas,500}$ which is computed in both ways, using a temperature profile and assuming an isothermal case. To compute the gas mass, we do not use the temperature profile, since the values of r_{500} change. The enclosed $M_{\rm gas,500}$ will also change, and for completeness we thus, show the comparison for the gas masses computed in both ways in Fig. A.1.

As we can see from Fig. A.1, the assumption of isothermality does not introduce any systematic error in either the total mass or r_{500}. Moreover, the values are in good agreement, which is shown even for cool-core clusters, that the derived values in this work are robust.

Appendix B: Geometric correction

The stellar mass is measured in a cone, along the line-of-sight of radius r_{2500} or r_{500} at the group/cluster distance. For simplicity, we will approximate the cone by a cylinder, since the distance of the cluster is much larger than its radius. The length of the cylinder can only be roughly estimated by the given scatter in redshift space, when enough galaxies have a redshift determination. On the other hand, the gas and dynamical masses are measured in spheres of radius r_{2500} or r_{500}. Compared to the sphere, the cylinder will cover a greater volume in space and therefore, a geometric correction is needed.

To estimate this correction, one must assume (or determine) the spatial distribution of galaxies in clusters and groups. Using SDSS data, Hansen et al. (2005) showed that the radial profile of the galaxy distribution is well represented by a NFW profile (Navarro et al. 1997), which is shallower than the dark matter distribution in clusters with a concentration parameter $c \approx 2$–4.

Given a radial profile, the mass excess, Υ, of a cylinder compared to a sphere is:

$$\Upsilon = M_{\rm cyl}/M_{\rm sph}, \tag{B.1}$$

where

$$M_{\rm sph} = 4\pi \int_0^{R_{\rm max}} \rho(r) r^2 {\rm d}r \quad \text{and} \tag{B.2}$$

$$M_{\rm cyl} = 4\pi \int_0^{z_{\rm max}} \int_0^{R_{\rm max}} \rho(R,z) R {\rm d}R\, {\rm d}z. \tag{B.3}$$

Here, $R_{\rm max}$ is the sphere radius of either r_{500} or r_{2500}, and $z_{\rm max}$ is half the length of the cylinder (i.e., we are measuring the mass between $\pm z_{\rm max}$). Although cumbersome, Υ can be determined analytically, if we assume a NFW profile. In terms of the concentration parameter, $c \equiv r_{200}/r_{\rm s}$, we have:

$$\begin{aligned}\Upsilon = & \sqrt{a^2c^2-1} \times [(1+ac)\ln(1+ac) - ac] \times (1+ac)^{-1} \\ & \times \left[\arctan\left(\frac{bc}{\sqrt{a^2c^2-1}}\right) - \arctan\left(\frac{b}{\sqrt{(a^2+b^2)(a^2c^2-1)}}\right)\right. \\ & \left. + \sqrt{a^2c^2-1} \times \ln\left(\frac{a+abc}{b+\sqrt{a^2+b^2}}\right)\right]^{-1},\end{aligned} \tag{B.4}$$

where $a = R_{\rm max}/r_{200}$ and $b = z_{\rm max}/r_{200}$.

For a NFW profile, $r_{500}/r_{200} = 0.61$–0.65 for $c = 2$–4 and $r_{2500}/r_{200} = 0.22$–0.28 also for $c = 2$–4. The mass excess in the cylinder is shown in Fig. B.1:

If we assume that we are including galaxies up to $\sim 3 r_{200}$, then we very roughly have the following mass excesses: $\Upsilon \sim 1.4$ for spheres of r_{500}, and $\Upsilon \sim 1.7$ for spheres of r_{2500}. To compare the stellar mass in galaxies with the gas and dynamical masses, the former should therefore be divided by the above Υ, depending on the extraction radius.

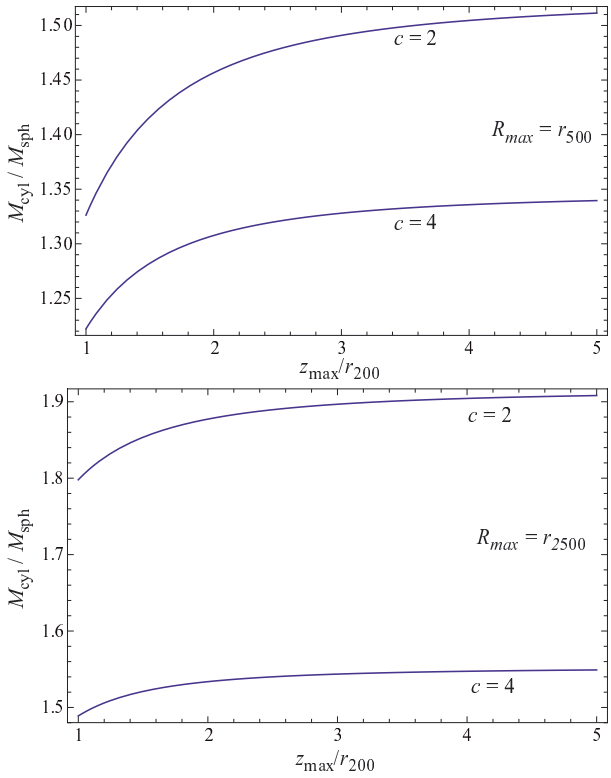

Fig. B.1. *Upper panel*: for a fixed $R_{max} = r_{500}$, mass excess as a function of z_{max}/r_{200}, for two NFW concentration parameters c. *Lower panel*: same as upper panel but for $R_{max} = r_{2500}$.

Chapter 3

Galaxy shapes

In general relativity, massive objects locally distort space-time. An interesting consequence is that light is deflected in the object vicinity. This effect is called gravitational lensing. Every beam of light from a background object, referred to as the source, is deflected in a different way depending on its angular position with respect to the massive object, called the lens. As a result, the image of the source in the lens plane appears distorted.

In the next subsection (Sect. 3.1), we review how one can infer the mass distribution of the lens, by studying the deformation of background sources. We then concentrate on results based on the galaxy shape observable, that we achieved during this thesis. We first present a weak lensing study of DAFT/FADA cluster masses and of the structures in their vicinity using large field of view ground based images (Sect. 3.2). We then introduce the shear peak statistics as a cosmological tool and forecast constraints achievable with a *Euclid*-like survey (Sect. 3.3).

3.1 Weak lensing overview

We only give the salient points of weak lensing necessary for the understanding of this thesis. We refer the reader to the reviews from e.g. Schneider et al. (1992) for general lensing, and Bartelmann & Schneider (2001) for a more detailed description of the weak lensing theory and its applications.

3.1.1 Theory

The effect of gravitational lensing is illustrated in Fig. 3.1, where O, L, S, and I respectively represent, the Observer, the Lens, the Source and the Image of the source in the lens plane. We define the following distances: D_s the distance of the source to the observer, D_l the distance of the lens to the observer, and D_{ls} the distance between the source and the lens. We also define the angular coordinates θ_S for the source position and θ_I for the image position. Finally, we introduce the deflection angle $\hat{\alpha}$ due to the presence of the lens. A geometrical analysis gives:

$$\theta_I = \theta_S + \alpha, \tag{3.1}$$

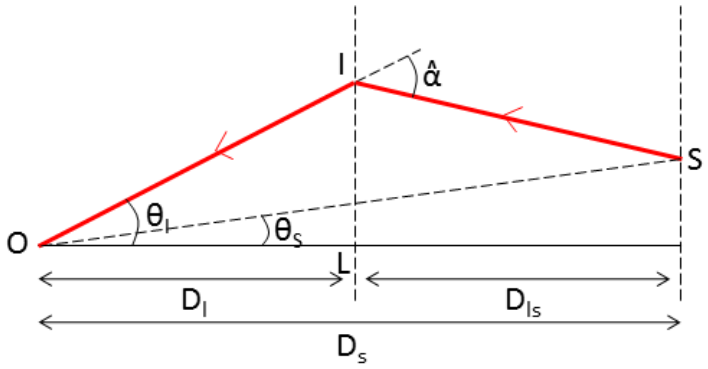

Figure 3.1: Illustration of the lensing geometry. A light beam (in red) is emitted by the source S, is deflected by the lens L, leading to an image I in the lens plane, that is observed by an observer in O. See text for details.

where we defined the scaled deflection angle $\alpha = \frac{D_{ls}}{D_s}\hat{\alpha}$. Eq. 3.1 is called the lens equation and defines the image position of the source in the lens plane, knowing the deflection angle. The different solutions of this equation are studied in e.g. Blandford & Narayan (1986). In the particular case of the strong lensing regime, the lens equation has more than one solution, leading to multiple images, called arclets. In the present thesis we are not studying the strong lensing regime and limit ourselves to the weak lensing in which eq. 3.1 has a unique solution for each source. In the following paragraphs, we calculate the deflection angle α as a function of the gravitational potential of the lens.

The metric around a single gravitational potential is the Schwarzschild metric, which in the case of small potentials can be written:

$$ds^2 = -\left(1 + 2\frac{\phi}{c^2}\right)c^2dt^2 + \left(1 - 2\frac{\phi}{c^2}\right)dz^2 + z^2d\Omega^2, \tag{3.2}$$

where c is the light velocity, ϕ the gravitational potential of the lens, z the coordinate along the line of sight and Ω the solid angle for the two other spatial coordinates. For a light beam, $ds = 0$. We also assume that radial components of the metric are null, i.e. $d\Omega = 0$. We can now write the time delay of the beam of light due to the lens, in the weak field approximation (i.e. far enough from the lens to have ϕ small compared to c^2):

$$t = \int_S^O \frac{1}{c}\left(1 - 2\frac{\phi}{c^2}\right)dz. \tag{3.3}$$

It is interesting to note that the first term in the integral of eq. 3.3 corresponds to the geometrical time delay while the second one corresponds to the gravitational delay. It is useful here to introduce the surface mass density of the lens $\Sigma(\vec{\theta})$, which is the integrated density of the lens over the line of sight. We can then replace the potential of the lens and integrate eq. 3.3 to obtain:

$$t = \frac{D_l D_s}{2D_{ls}c}(\vec{\theta}_I - \vec{\theta}_S)^2 - \frac{4G}{c^3}D_l^2 \iint d^2\vec{\theta}'\Sigma(\vec{\theta}')\ln|\vec{\theta}_I - \vec{\theta}'|. \tag{3.4}$$

This equation can be simplified by defining the dimensionless time delay τ (eq. 3.5) and the 2D lensing potential (eq. 3.6):

$$\tau = \frac{D_{ls}}{D_l D_s} ct, \tag{3.5}$$

$$\psi(\vec{\theta_I}) = \frac{4G}{c^2}\frac{D_l D_{ls}}{D_s}\iint d^2\vec{\theta'}\Sigma(\vec{\theta'})\ln|\vec{\theta_I}-\vec{\theta'}| = \frac{1}{\pi}\iint d^2\vec{\theta'}\kappa(\vec{\theta'})\ln|\vec{\theta_I}-\vec{\theta'}|, \tag{3.6}$$

where we introduced the dimensionless surface mass density, the so called convergence κ, which is the ratio of the surface mass density to the critical surface mass density Σ_{cr}:

$$\kappa(\vec{\theta}) = \frac{\Sigma(\vec{\theta})}{\Sigma_{cr}} \qquad \text{and} \qquad \Sigma_{cr} = \frac{c^2}{4\pi G}\frac{D_s}{D_l D_{ls}}. \tag{3.7}$$

Eq. 3.4 can now be very simply rewritten as:

$$\tau(\vec{\theta_I}, \vec{\theta_S}) = \frac{1}{2}(\vec{\theta_I}-\vec{\theta_S})^2 - \psi(\vec{\theta_I}). \tag{3.8}$$

Fermat's principle states that light propagates through the paths that minimize its travel time. In other words, for a given source at position θ_S, the images are located at the stationary points of the total time delay τ. Hence, $\partial\tau/\partial\theta_I = 0$. This principle allows to recover the lens equation through deriving eq. 3.8 with respect to θ_I:

$$\vec{\theta_I} = \vec{\theta_S} + \vec{\nabla}\psi. \tag{3.9}$$

A comparison of eq. 3.9 with its geometrical analog, eq. 3.1, gives the simple relation between the deflection angle and the lens gravitational potential:

$$\vec{\alpha} = \vec{\nabla}\psi. \tag{3.10}$$

Note that in absence of any mass on the light path, or equivalently far enough from a given mass, the lens equation gives $\vec{\theta_I} = \vec{\theta_S}$: the light is not deflected.

The lens equation is the fundamental equation of lensing and describes the resulting images of a point source as a function of the lens potential and the various distances of the problem. For an extended source, each light beam is deflected according to its angular distance to the lens, following the lens equation. It results in a distortion of the source image and an amplification of the light in some regions. This transformation can be written by locally linearising the lens equation (eq. 3.9) with respect to $\vec{\theta_I}$, and corresponds to the Jacobian matrix of the transformation of $\vec{\theta_I}$ to $\vec{\theta_S}$, that we call the amplification matrix A:

$$A = \frac{\partial\vec{\theta_S}}{\partial\vec{\theta_I}} = \left(\delta_{ij} - \frac{\partial^2\psi}{\partial\theta_{Ii}\partial\theta_{Ij}}\right) = \begin{pmatrix} 1-\kappa-\gamma_1 & -\gamma_2 \\ -\gamma_2 & 1-\kappa+\gamma_1 \end{pmatrix}, \tag{3.11}$$

where δ_{ij} is equal to 1 when $i = j$ and 0 otherwise. We also defined the convergence and the two shear components as a function of the second derivatives of the lens potential:

$$\kappa = \frac{1}{2}\left(\frac{\partial^2\psi}{\partial\theta_{I1}\partial\theta_{I1}} + \frac{\partial^2\psi}{\partial\theta_{I2}\partial\theta_{I2}}\right), \tag{3.12}$$

$$\gamma_1 = \frac{1}{2}\left(\frac{\partial^2\psi}{\partial\theta_{I1}\partial\theta_{I1}} - \frac{\partial^2\psi}{\partial\theta_{I2}\partial\theta_{I2}}\right), \qquad \gamma_2 = \frac{\partial^2\psi}{\partial\theta_{I1}\partial\theta_{I2}}. \tag{3.13}$$

The convergence defined in eq. 3.12 is the same quantity than the scaled surface mass density described in eq. 3.7. The shear is defined by its two components as a complex quantity: $\gamma = \gamma_1 + i\gamma_2 = |\gamma|e^{2i\Phi}$. Note that the shear is a spinner of spin 2 and not a vector as it transforms as $e^{2i\Phi}$ under rotation.

Liouville's theorem states that a function of distribution is constant along any trajectory in the phase space. Hence, lensing conserves the surface brightness distribution of the source. If we note $I(\vec{\theta_S})$ and $I(\vec{\theta_I})$ the surface brightness of the source and the image, and if $\vec{\theta}_{I0}$ is the image corresponding to the source point $\vec{\theta}_{S0}$, we can use the linearised lens equation (eq. 3.11) to compute the surface brightness distribution of the image:

$$I(\vec{\theta_I}) = I(\vec{\theta_S}) = I(\vec{\theta}_{S0} + A(\vec{\theta}_{I0}).(\vec{\theta_I} - \vec{\theta}_{I0})) \tag{3.14}$$

Since A is symmetric it can be diagonalized. Eq. 3.14 shows that the image is stretched compared to the source, of an amount quantified by the inverses of the eigenvalues of A, which are $1 - \kappa \pm |\gamma|$. In the particular case of a circular source, the resulting image is an ellipse, and the ratio of the source radius to the image semi-axis are equal to the eigenvalues of A. The same equation shows that the solid angle of the source is not conserved by lensing and the ratio of the image to the source areas is equal to the inverse of the determinant of A, i.e. the inverse of the Jacobian of the transformation of $\vec{\theta_I}$ to $\vec{\theta_S}$. As the surface brightness is conserved, this surface ratio corresponds to a magnification ratio between the source and the image, noted μ:

$$\mu = \frac{1}{\det A} = \frac{1}{(1-\kappa)^2 - |\gamma|^2}. \tag{3.15}$$

Thus, the size distortion of the image is due to both the convergence and the shear, while the distortion of the shape is only due to the shear, as the convergence acts identically on both space directions, as stated by the eigenvalues of A.

In some cases, $\det A = 0$. The ensemble of points in the lens plane on which this property is verified is called the critical line, and the corresponding points in the source plane form the caustic line. On the critical line, the magnification should be infinite, but remains finite due to the spatial extension on sources. In the WL regime, $(\kappa, |\gamma|) \ll (1, 1)$ and the magnification depends only on the convergence at the first order.

One can factorize the $(1-\kappa)$ term in A, leading to the following writing of the matrix:

$$A = (1-\kappa)\begin{pmatrix} 1-g_1 & -g_2 \\ -g_2 & 1+g_1 \end{pmatrix}, \tag{3.16}$$

where we have defined the reduced shear g:

$$g = \frac{\gamma}{1-\kappa}. \tag{3.17}$$

Eq. 3.16 shows that the reduced shear g is the only quantity affecting the shape of the image, the factor $(1-\kappa)$ only affecting the size, and therefore g is the true observable in the lensing theory. Note that in the WL regime, $g \simeq \gamma$. The surface mass density κ can only be computed from an integration of the shear, and is thus known to within an integration constant for a finite space. This is the so-called mass-sheet degeneracy.

In the following section we review the different methods that have been developed to measure the shear of weakly lensed galaxies.

3.1.2 Shear measurement

Weak lensing can provide tight constraints on cosmology when large data sets are explored, but this requires highly unbiased measurements of galaxy shapes. Unfortunately, the shape distortion due to lensing (i.e. the shear) is of the order of a percent, and therefore small compared to both the noise from the intrinsic ellipticity of galaxies, and systematic distortions caused by the light traveling through the atmosphere and the telescope optics. The problem of the intrinsic shape of galaxies is solved by averaging over many sources, assuming that galaxies are randomly oriented. For a sufficient number of galaxies, the intrinsic ellipticity thus averages to zero. The hypothesis that galaxies are randomly oriented seems reasonable as only background galaxies are retained for lensing, thus they should not be gravitationally bound together. Note however, that intrinsic alignment can become an issue when studying the correlation of galaxy shapes within structures, such as in cosmic shear surveys (e.g. Hirata et al. 2007). The second problem is more challenging, and requires a very accurate understanding of every observational bias. A major source of bias is the image point spread function, and must be measured at the percent level accuracy. This work is eased if the atmosphere bias, called the seeing, is low, and even more for space telescopes. The common idea is to measure the PSF on stars, as they are quasi-point like sources, and then to correct galaxies for the measured bias. The precision required for next generation large WL surveys (STAGE IV DE surveys), such as *Euclid* (Laureijs et al. 2011), WFIRST (Spergel et al. 2013), or LSST (LSST Science Collaboration et al. 2009), makes shear measurements a very active field. Several methods have been developed, and we will review here the different approaches to this problem.

The first step is to define the shape of a galaxy. For this purpose, we assume galaxies are ellipticals and introduce their ellipticity ϵ defined as a complex quantity, with norm the geometrical ellipticity $|\epsilon| = (1 - b/a)(1 + b/a)$, where a and b are the major and minor semi-axis of the ellipse, and with an orientation angle defined by the direction of the major axis. In the case where $|g| \leq 1$, the ellipticity of the image ϵ_I is linked to the ellipticity of the source ϵ_S through:

$$\epsilon_I = \frac{\epsilon_S + g}{1 + g^* \epsilon_S}, \tag{3.18}$$

where a star denotes the conjugate quantity. In the WL regime, $|g| \ll 1$ and $\epsilon_I \simeq \epsilon_S + g$. Finally, averaging over many galaxies, and assuming galaxies are randomly oriented, $\langle \epsilon_I \rangle \simeq g$.

Another parameterization, called the distortion χ, is through the second moments Q_{ij} of the surface brightness distribution of an image $I(\vec{\theta})$:

$$\chi = \frac{Q_{11} - Q_{22} + 2iQ_{12}}{Q_{11} + Q_{22}}, \quad \text{with} \quad Q_{ij} = \frac{\int d^2\theta I(\vec{\theta}) W(\vec{\theta}) \theta_i \theta_j}{\int d^2\theta I(\vec{\theta}) W(\vec{\theta})}, \tag{3.19}$$

W being a weighting function. The two definitions of complex ellipticity are related through eq. 3.20:

$$\chi = \frac{2\epsilon}{1 + |\epsilon|^2}. \tag{3.20}$$

In the regime of WL and assuming galaxies are randomly oriented, we have $\langle \chi_I \rangle \simeq 2g$. The choice of one definition over another depends on the measurement method.

The first technique to have been developed is based on the measurement of the moments of the distribution of the surface brightness of objects, and was proposed by Kaiser et al. (1995) (then referred as the KSB method, for Kaiser, Squires, and Broadhurst). Defining the ellipticity as in eq. 3.19, the authors introduce two operators that describe an object response to the PSF (the smear polarizability tensor $P^{\rm sm}$) and to the shear (the shear polarizability tensor $P^{\rm sh}$), that are computed from the different order moments of an object light distribution. Note however that $P^{\rm sm}$ and $P^{\rm sh}$ are not the objects general response to smearing and shearing but are calculated from linear perturbations, so higher order terms have been neglected. This is the reason why it is unlikely to ever reach an accuracy better than 1% with the KSB method. One can then measure the PSF and shear response on stars and correct for it on galaxies to evaluate their ellipticity. This technique led to many developments, which are still widely used, especially in the case of only moderately weak lensing regime, i.e. around galaxy clusters (e.g. Okabe et al. 2010; von der Linden et al. 2014; Hoekstra et al. 2015; Martinet et al. 2015, A&A submitted). An example of an application of a KSB-like technique is presented in part 3.2 of this work.

Apart from KSB, several methods have been developed to accurately measure the shapes of galaxies, and to link it to the shear signal. We can regroup them in three main categories: 1) the moments of light distribution; 2) the galaxy modeling ; 3) machine learning. Method 1) gathers all methods based on the measurement of the moments of the surface brightness distribution, i.e. the KSB-like techniques. The 2$^{\rm nd}$ method is based on the direct measurement of the profile of the overall light distribution. Several different techniques have been developed in that sense. Some authors assume a galaxy profile with about 10 degrees of freedom, and fit it to the objects, based on maximum likelihood statistics (e.g. sFIT: Jee et al. 2013, or Amalgam at IAP). An example of this method is shown in the next paragraph. Others decompose the object image in an orthonormal basis, requiring hundreds of parameters but better taking into account irregularities in the shape (e.g. shapelets: Massey & Refregier 2005). Another major branch is the stacking of objects before fitting a galaxy profile (e.g. Lewis 2009). However, this technique is hardly applicable to non-constant shear fields. The last method is to fit the galaxy profile in a Bayesian framework rather than a maximum likelihood estimator (e.g. LENSFIT: Miller et al. 2007, Bernstein & Armstrong 2014). Method 3), also refered to as neural network, infers the galaxy shear through comparison with a known sample of input and output galaxy shapes (e.g. Gruen et al. 2010, MegaLUT: Tewes et al. 2012). This method is very fast, but needs to be trained on a known sample, which can be challenging for real

data.

The variety of methods used to measure the shear led to challenges organized by the community, aiming at evaluating the different systematics of each method, and selecting the most reliable ones, based on simulations. There have been five such challenges so far, with different specific points being tested: STEP1 (Heymans et al. 2006), STEP2 (Massey et al. 2007a), GREAT08 (Bridle et al. 2010), GREAT10 (Kitching et al. 2012), and GREAT3 (Mandelbaum et al. 2014). All these challenges consist in blindly measuring the galaxy shears in simulated images to compare them afterwards to the input values. The winning method has evolved from one test to another, given new developments in both shear measurement techniques, and challenges' maturity. The last challenge to date includes true galaxy morphology taken from HST imaging, multiple exposure stacking as done in real observing data, and a PSF estimation from stars rather than a given PSF. This last challenge showed the advent of maximum likelihood galaxy modeling, which is the method used by the three best teams. However, the Bayesian likelihood and the supervised machine learning techniques obtained promising results, considering they are more recent techniques, still in development. Another important result is that the best techniques now achieve the STAGE IV dark energy survey requirements for the shear accuracy ($\sim 10^{-3}$ in the case of *Euclid*), but under some simplifications in the simulations, and providing that the sample is limited to high signal to noise galaxies ($S/N > 20$). Among these simplifications are the choices of neglecting the wavelength-dependent effects and of placing galaxies on grids which avoids blending objects.

The observation of galaxies in broad-band filters leads to a bias in the shape measurement due to the PSF being chromatic. One can correct for this effect using a color-weighted PSF that depends on the spectral energy distribution (SED) of the galaxy (Cypriano et al. 2010). However, the problem gets more complicated if the SED of the galaxy varies spatially, what is called the color gradient. A typical example of this effect appears for a galaxy presenting a red bulge and a blue star-forming disc. The wavelength-dependence of the PSF biases the shape measurement of such objects, if the variation of the SED across the galaxy is not accounted for. Semboloni et al. (2013) found that color gradient biases the shape measurements at a level of a few 10^{-3}, using simulated galaxies. The effect of color gradient is then of the same order as the required accuracy of *Euclid*, and must therefore be taken into consideration. A way to correct for this bias is to measure the spatial dependence of the SED, which can be interpolated from at least two magnitude bands. In the same study, they demonstrated that a correction to the required precision is in principle possible, using some 10,000 galaxies observed in the F606W and F814W filters of the Hubble Space Telescope (HST).

The blending issue has not been studied in detail so far, and we usually resort to discarding galaxies that are too close to each other when performing shape measurements, because they are hard to disentangle in the fitting process. Further work is needed to quantify the effect of blending along with the proportion of blended objects. While identified blended galaxies can be discarded, it is important to know the fraction of galaxies that are blended but that we cannot detect and what effect they have on shear measurement. The problem is more difficult at high redshift ($z \sim 1.5$), because optical data correspond to the UV restframe band at these redshift. Thus, near-infrared is needed to check whether an identified high redshift galaxy is blended or if we are observing two

star-forming regions of the same galaxy. A technique to accurately measure the shape of blended objects would increase the number of galaxies usable for the cosmological probe, boosting their efficiency. Several tracks can be followed, such as the fit of joint galaxy profiles.

The next challenges are then to calibrate color gradients, to reach the low end of the S/N distribution (i.e. $S/N < 20$), and to properly fit the light profiles of overlapping galaxies. The first issue needs to be addressed if one wants to reach the required accuracy of coming STAGE IV DE surveys while solving the other two will result in a huge gain in the global shear signal, probably more than doubling the number of available galaxies for shear based cosmological probes.

The afore-mentioned challenges were performed in the very weak lensing regime, with DE surveys in mind. Hence, even if the moment methods seem ruled out in this regime, they are still used for the intermediate weak regime, in the vicinity of clusters, and this is why we decided to use them in part 3.2. The lack of simulation tests in the cluster regime is being investigated in the context e.g. of LSST. The ARCLETS (http://www.het.brown.edu/people/ian/ClustersChallenge/index.html) challenge is designed in this sense, providing simulations with shear typical of that produced by a galaxy cluster. Even if these simulations are not as accurate as the previous challenges yet, they imply some new features appearing at moderately weak lensing, such as the flexion, which is the deformation of an object due to the shear not being constant over its area. I participated in this challenge within the Amalgam team at IAP, applying one of the most advanced galaxy maximum likelihood model fittings.

The Amalgam@IAP method follows the simple steps of modeling the PSF, fitting a galaxy modeled convolved with the PSF to the galaxies, and weighting each shear measurement. The PSF measurement is done using the PSFEx software (Bertin 2011). The different detected PSFs are re-centered, and fitted with polynomials in a χ^2 minimization. A set of PSFs is computed, to take the PSF variation across the field into account. The local PSF model is then convolved with a Sérsic model (Sérsic 1963, and eq. 3.21) and fitted to each galaxy in a χ^2 minimization using SExtractor (Bertin & Arnouts 1996). The Sérsic model gives the intensity I at a distance R from the center along the major semi-axis:

$$I(R) = I_e \exp\left(-b_n\left[\left(\frac{R}{R_e}\right)^{1/n} - 1\right]\right), \tag{3.21}$$

with I_e the amplitude at the effective radius R_e, n the Sérsic index, and b_n a term fixed by n and defined through the formula $\Gamma(2n) = 2\gamma(2n, b_n)$ where Γ and γ here represent the complete and incomplete gamma functions. The Sérsic index describes the shape of the profile: $n = 1$ usually fits well spiral galaxies, while $n = 4$ is well adapted for ellipticals and corresponds to the de Vaucouleurs profile (de Vaucouleurs 1948).

Note that other models can be used, such as a combination of two Sérsics applied to the bulge and to the disk of the galaxy, but the single Sérsic was found to perform very well. There are seven degrees of freedom in the fitted model which are the center coordinates, the amplitude, the effective radius, the aspect ratio, the position angle, and the Sérsic index. The detections are then weighted by the inverse variance, where the

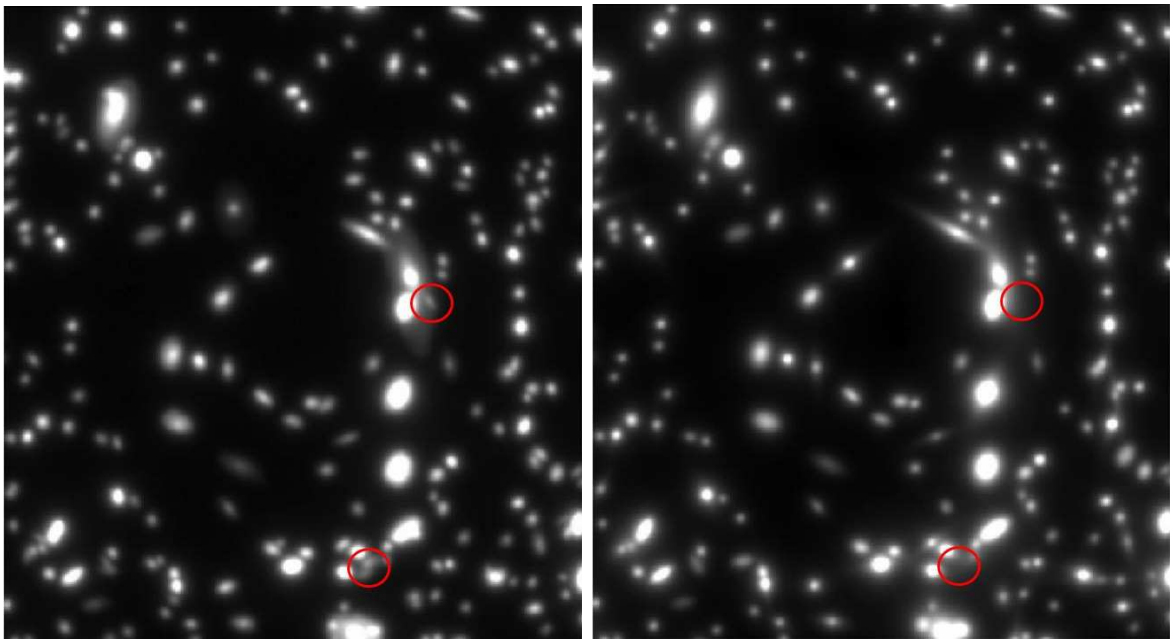

Figure 3.2: Example of an ARCLETS LSST-like simulation (left) and the image reconstructed with the fitted galaxy models applying the Amalgam@IAP method (right). We note a good overall agreement except in the case of faint blended galaxies that are not recovered (e.g. in the two red circles).

variance is a combination of measurement errors for both ellipticity coordinates and shape noise. The technique seems to work also very well in the cluster regime, except for some blending and flexion issues, as seen in Fig. 3.2. Indeed, some faint blended galaxies are not modeled, and the flexion is smoothed in the reconstructed map. The challenge is not closed yet, and we are working on the improvement of the method. Note that only large signal-to-noise objects are provided in these simulations, such that the noise bias issue cannot be tested in this case.

3.2 WL in clusters

This section presents the results from Martinet et al. (2015, A&A submitted): *Weak lensing study of 16 DAFT/FADA clusters: substructures and filaments*. The first subsection briefly summarizes the paper, its context, aims, methods, results, and conclusions. The detailed study can be read in the second subsection, where we display the article.

3.2.1 Summary

Context

While our current cosmological model places galaxy clusters at the nodes of a filament network (see Sect. 1.1.2), we still struggle to detect these filaments at high redshifts.

In addition, accurate estimates of cluster masses are required to calibrate the observable-mass relation used in cluster abundance cosmological probes (cf. Sect. 1.2.2).

Aims

We perform a weak lensing study for a sample of 16 massive, medium-high redshift ($0.4 < z < 0.9$) galaxy clusters from the DAFT/FADA survey, that are imaged in at least three optical bands with Subaru/SuprimeCam or CFHT/MegaCam. Taking advantage of the large field of view of our data, we study cluster environments, adding information from galaxy density maps at the cluster redshift and from X-ray images when available.

Methods

We estimate the shear of each galaxy through a KSB-like method. Background galaxies are then selected in a color-color diagram. We estimate the cluster masses using an NFW fit to the shear profile. We also compute convergence maps and select structures within, securing their detection with bootstrap re-sampling techniques. We compare convergence contour levels, with X-ray contours from *XMM*–Newton and *Chandra* observations, and galaxy light density contours for galaxies selected in a color-magnitude diagram to be approximately at the same redshift as the cluster.

Results

Using this new sample of cluster masses, we contribute to the calibration of the observable-mass relation required for cluster abundance cosmological studies.

Studying cluster environments, we find that they show a large variety of weak lensing maps at large scales and that most of them may be embedded in filamentary structures at megaparsec scale.

We classify clusters in three categories according to the smoothness of their weak lensing contours and to the amount of substructures: relaxed ($\sim$ 7%), past mergers ($\sim$ 21.5%), recent or present mergers ($\sim$ 71.5%).

Finally, we report the detection of particularly intense filaments in six cluster fields.

Conclusions

We note that spherical NFW profiles might be insufficient to accurately fit every cluster mass profile on scales larger than their inner core region.

The fraction of clusters undergoing merging events observationally supports the hierarchical scenario of cluster growth, and implies that massive clusters are strongly evolving at the studied redshifts.

The intense filaments detected will constitute a first test sample to study the properties of galaxies inside filaments at these redshifts.

3.2.2 Martinet et al. 2015c

Astronomy & Astrophysics manuscript no. wl
September 30, 2015

Weak lensing study of 16 DAFT/FADA clusters: substructures and filaments. ⋆

Nicolas Martinet[1], Douglas Clowe[2], Florence Durret[1], Christophe Adami[3], Ana Acebrón[3], Lorena Hernandez-García[4], Isabel Márquez[4], Loic Guennou[5], Florian Sarron[1], Mel Ulmer[6]

[1] Sorbonne Universités, UPMC Univ Paris 6 et CNRS, UMR 7095, Institut dAstrophysique de Paris, 98 bis bd Arago, 75014 Paris, France
[2] Department of Physics and Astronomy, Ohio University, 251B Clippinger Lab, Athens, OH 45701, USA
[3] LAM, OAMP, Université Aix-Marseille & CNRS, Pôle de l'Etoile, Site de Château Gombert, 38 rue Frédéric Joliot-Curie, 13388 Marseille 13 Cedex, France
[4] Instituto de Astrofísica de Andalucía, CSIC, Glorieta de la Astronomía s/n, 18008, Granada, Spain
[5] Institut dAstrophysique Spatiale, CNRS (UMR8617) Université Paris-Sud 11, Bâtiment 121, Orsay, France
[6] Dept of Physics and Astronomy & Center for Interdisciplinary Exploration and Research in Astrophysics (CIERA), Evanston, IL 60208-2900, USA

Preprint online version: September 30, 2015

ABSTRACT

While our current cosmological model places galaxy clusters at the nodes of a filament network (the cosmic web), we still struggle to detect these filaments at high redshifts. We perform a weak lensing study for a sample of 16 massive, medium-high redshift ($0.4 < z < 0.9$) galaxy clusters from the DAFT/FADA survey, that are imaged in at least three optical bands with Subaru/Suprime-Cam or CFHT/MegaCam. We estimate the cluster masses using an NFW fit to the shear profile measured in a KSB-like method, adding our contribution to the calibration of the observable-mass relation required for cluster abundance cosmological studies. We compute convergence maps and select structures within, securing their detection with noise re-sampling techniques. Taking advantage of the large field of view of our data, we study cluster environment, adding information from galaxy density maps at the cluster redshift and from X-ray images when available. We find that clusters show a large variety of weak lensing maps at large scales and that they may all be embedded in filamentary structures at megaparsec scale. We classify them in three categories according to the smoothness of their weak lensing contours and to the amount of substructures: relaxed (~ 7%), past mergers (~ 21.5%), recent or present mergers (~ 71.5%). The fraction of clusters undergoing merging events observationally supports the hierarchical scenario of cluster growth, and implies that massive clusters are strongly evolving at the studied redshifts. Finally, we report the detection of particularly intense filaments in CLJ0152, MACSJ0454, MACSJ0717, A851, BMW1226, MACSJ1621, and MS1621.

Key words. Galaxies: cluster: general - Gravitational lensing: weak - Cosmology: large-scale structure of Universe

1. Introduction

In Cold Dark Matter (CDM) theories, our Universe can be represented as an ensemble of Large Scale Structures (LSS) made of voids and galaxy clusters that are connected through filamentary structures (Bond et al. 1996). In this scenario, matter collapses into halos that then grow through accretion and merging with other halos. Galaxy clusters are the highest density structures resulting from this hierarchical formation. N-body simulations (e.g. Millennium: Springel et al. 2005) and low redshift observations (e.g. SDSS: Tegmark et al. 2004) have confirmed this evolutionary scheme.

In this framework, galaxy clusters can be used to constrain cosmological models. Indeed, the distribution of clusters with mass and redshift contains information on the mentioned hierarchical formation scenario (e.g. Allen et al. 2011). The main challenge is to calibrate the so-called observable-mass relation, that links true cluster masses to the mass proxy used in the survey. With its ability of being insensitive to the matter dynamical state, Weak Lensing (WL) appears as a major tool in determining the masses of galaxy clusters with sufficient precision to derive cosmological constraints. However, this technique requires a large amount of clusters, and therefore more and more WL surveys with increasing numbers of clusters are conducted (e.g. Dahle et al. 2002; Cypriano et al. 2004; Clowe et al. 2006; Gavazzi & Soucail 2007; Hoekstra 2007; Okabe et al. 2010; von der Linden et al. 2014; Hoekstra et al. 2015). In a similar idea, Martinet et al. (2015a) recently showed that counting shear peaks can constrain cosmological parameters almost as well as counting galaxy clusters, without requiring any knowledge of the observable-mass relation, but needing a large number of cosmological simulations.

As it directly traces the matter density, WL also allows to study the LSSs of our Universe. However, the low density of filaments compared to clusters makes their detection difficult. Several studies pioneered in using WL to detect such structures

Send offprint requests to: Nicolas Martinet, e-mail: martinet@iap.fr

⋆ Based on observations obtained with MegaCam, a joint project of CFHT and CEA/IRFU, at the Canada-France-Hawaii Telescope (CFHT) which is operated by the National Research Council (NRC) of Canada, the Institut National des Sciences de l'Univers of the Centre National de la Recherche Scientifique (CNRS) of France, and the University of Hawaii. Also based on archive data collected at the Subaru Telescope, which is operated by the National Astronomical Observatory of Japan. This research made use of data obtained from the *Chandra* Data Archive provided by the *Chandra* X-ray Center (CXC), and data obtained from the *XMM*–Newton Data Archive provided by the *XMM*–Newton Science Archive (XSA).

in the vicinity of clusters either by reporting low significance detection or questioning previous claims of detection (e.g. Clowe et al. 1998; Kaiser et al. 1998; Gray et al. 2002; Gavazzi et al. 2004; Dietrich et al. 2005; Heymans et al. 2008; Dietrich et al. 2012). Note that Massey et al. (2007b) found evidence for a cosmic network of filaments in the COSMOS field galaxy survey. Mead et al. (2010) used the Millennium Simulation (Springel et al. 2005) to test the ability of various WL techniques to detect nearby cluster filaments, and concluded that background galaxy density is key to filament detection. Future space-based missions are likely to detect many filaments, but today, the narrow field of view of the Advanced Camera for Surveys (ACS) on the Hubble Space Telescope (HST) does not allow such detection in a simple way. In this context, deep ground-based imaging can be very efficient as it often has a much wider field of view, and offers the possibility to cover clusters and their vicinity in a single image with Subaru/Suprime-Cam or CFHT/Megacam. Recently, Jauzac et al. (2012) reported the first WL detection of a $z = 0.54$ cluster with a filament, MACSJ0717.5+3745 based on a mosaic of HST/ACS images. This detection was latter confirmed by Medezinski et al. (2013) from a Subaru/Suprime-Cam WL analysis.

In this paper, we present the WL analysis of 16 clusters from the Dark energy American French Team (DAFT, in French FADA) survey. All are medium-high redshift ($0.4 \leq z \leq 0.9$) massive ($M \geq 2 \times 10^{14}$ $M_\odot$) clusters of galaxies selected through their X-ray luminosities. This sample is comparable to other X-ray selected cluster studies such as LOCUSS at $0.15 \leq z \leq 0.3$ (Okabe et al. 2010), Weighting the Giants at $0.15 \leq z \leq 0.7$ (von der Linden et al. 2014), and CCCP at $0.15 \leq z \leq 0.55$ (Hoekstra 2007; Hoekstra et al. 2015), with a slightly higher redshift, but with fewer clusters than the mentioned surveys which respectively contain 30, 51, and 50 galaxy clusters. Apart from estimating cluster masses, we take advantage of the large field of view of our images (8 CFHT/Megacam images with 1 deg^2 f.o.v. and 7 Subaru/Suprime-Cam images with 34×27 arcmin^2 f.o.v. - one of the Subaru images contains two clusters) to investigate galaxy cluster environments. In particular, we report the WL detection of several filaments.

This paper is structured as follows. Sect. 2 describes our data set, Sect. 3 presents in detail the shear measurement we apply, and Sect. 4 the mass reconstruction process. In Sect.5, we estimate the cluster masses and in Sect. 6 we focus on the environment of clusters: substructures, mergers, and filaments. We conclude in Sect. 7. Throughout the paper, we use a fiducial flat ΛCDM cosmology with $\Omega_M = 0.3$, $\Omega_\Lambda = 0.7$, and $H_0 = 70$ km Mpc^{-1} s^{-1}.

2. Data

2.1. DAFT/FADA

DAFT/FADA is a survey of $\sim$ 90 high-redshift ($0.4 \leq z \leq 0.9$) massive ($M \geq 2 \times 10^{14}$ $M_\odot$) clusters of galaxies selected through their X-ray luminosities. All of the clusters have Hubble Space Telescope (HST) imaging available with either WFPC2 or ACS cameras. We also gathered multi-band optical and near infrared ground based imaging, using 4m class telescopes for most of the sample. This data set allows to accurately measure the ellipticity of galaxies from space and their photometric redshifts (hereafter photo-z) from the ground. The main goals of the survey are to form a comprehensive database to study galaxy clusters and their evolution, and to test cosmological constraints geometrically by means of weak lensing tomography. Several steps have been made towards the achievement of these two goals, and the current status of the survey, with a list of refereed publications, can be found at http://cencosw.oamp.fr/DAFT/index.php.

Among other papers, Murphy et al. (2015, A&A submitted) performed a WL analysis of HST/ACS mosaic imaging data of ten massive, high-redshift ($z > 0.5$) DAFT/FADA galaxy clusters. Using the photo-zs calculated by Guennou et al. (2010), they explored their use for background galaxy discrimination. Our team is currently increasing this small sample of HST/ACS shear measurements to a larger number of clusters and also aims at combining ground-based and space-based shear catalogs to build a shear analysis which is both deep in the cluster central region and extended on larger scales. This will serve as the reference catalog to perform Weak Lensing Tomography with Clusters (WLTC) as described in Jain & Taylor (2003).

2.2. This study

In this study, we focus on 16 galaxy clusters for which we have Subaru/Suprime-Cam or CFHT/Megacam wide field images for at least three optical bands among the v, r, i, and z bands. Having three bands is mandatory to be able to perform a color-color cut to remove foreground galaxies that dilute the lensing signal. The shear measurements are performed in the r or i bands depending on the image seeing. This choice is made to maximize the number of source galaxies as these bands are the deepest optical bands. The use of Suprime-Cam (34×27 arcmin^2 field) and Megacam (1×1 deg^2 field) imaging allows to study clusters within their virial radius and also to see how they interplay with the surrounding LSS at the selected redshifts ($0.4 \leq z \leq 0.9$). These fields of view are much wider than what can be achieved from current space telescopes, as the HST/ACS field of view is only 3.4×3.4 arcmin^2. Besides, the Megacam and Suprime-Cam cameras present rather stable Point Spread Functions (PSFs) and contain a large number of stars within each pointing allowing to accurately estimate the PSF distortion due to the instrument and atmospheric biases. A list of the data for each cluster can be found in Table 1.

Some of the clusters from the present study have been analyzed in previous DAFT/FADA papers. Guennou et al. (2014) derived X-ray luminosities and temperatures for 12 out of these 16 clusters. A comparison of WL and X-ray total masses will be performed in Sect. 5.2. Guennou et al. (2014) also searched for substructures using both X-ray data and optical galaxy spectroscopy. Martinet et al. (2015b) studied the optical emission of galaxy clusters and measured the Galaxy Luminosity Functions (GLFs) for 7 out of these 16 clusters. We indicate in Table 1 for each cluster in which study it was included.

With the present DM study, we will have a full understanding of the matter content of a sample of galaxy clusters: the DM halo, the X-ray Intra Cluster Medium (ICM), and the stars contained in galaxies. Even if we do not include all the clusters in each analysis, we will have a general knowledge of cluster behaviors as observed through WL, X-rays, and optical.

2.3. Image reduction

The Subaru and CFHT data presented here are archive data, either from previous studies, or from the early phases of DAFT/FADA.

The CFHT/Megacam data have been reduced by the TERAPIX team at the Institut d'Astrophysique de Paris, using the astromatic softwares (http://www.astromatic.net/).

Table 1. Data used in this study. The different columns correspond to #1: cluster ID, #2: right ascension, #3: declination, #4: redshift, #5: telescope/camera, #6: filters; we give first the band on which we perform shape measurements and in parenthesis the two other bands used for the color-color cut, #7: seeing for the band on which we perform shape measurements. Column #8 (G14) and #9 (M15) show if the cluster has been studied in Guennou et al. (2014) or Martinet et al. (2015b). In the first case, we know if it presents substructures based on X-ray images, and in most cases, also on optical galaxy spectroscopy. For RX_J1716.4+6708, we have spectroscopy but no *XMM* image. In the second, we have photo-zs in the inner part, and in most cases, an optical galaxy luminosity function for the cluster. Hereafter, we will use abridged names.

Cluster	RA	DEC	z	Instrument	Filters	Seeing	G14	M15
XDCScmJ032903	03 29 02.81	+02 56 25.18	0.4122	CFHT/Megacam	r+(v,i)	0.73”	Y	Y
MACSJ0454.1-0300	04 54 10.92	-03 01 07.14	0.5377	CFHT/Megacam	r+(v,z)	0.76”	Y	Y
ABELL0851	09 42 56.64	+46 59 21.91	0.4069	CFHT/Megacam	i+(v,z)	0.80”	Y	Y
LCDCS0829	13 47 31.99	-11 45 42.01	0.4510	CFHT/Megacam	r+(v,i)	0.83”	Y	Y
MS1621.5+2640	16 23 35.50	+26 34 13.00	0.4260	CFHT/Megacam	r+(v,i)	0.65”	Y	N
OC02J1701+6412	17 01 22.60	+64 14 09.00	0.4530	CFHT/Megacam	r+(i,v)	0.73”	N	N
NEP0200	17 57 19.39	+66 31 31.00	0.6909	CFHT/Megacam	i+(v,r)	0.97”	N	N
RXJ2328.8+1453	23 28 49.90	+14 53 12.01	0.4970	CFHT/Megacam	r+(v,i)	0.70”	Y	N
CLJ0152.7-1357	01 52 40.99	-13 57 45.00	0.8310	Subaru/Suprime-Cam	r+(v,z)	0.70”	Y	Y
MACSJ0717.5+3745	07 17 33.79	+37 45 20.01	0.5458	Subaru/Suprime-Cam	r+(v,z)	0.69”	N	N
BMW-HRIJ122657	12 26 58.00	+33 32 54.09	0.8900	Subaru/Suprime-Cam	r+(i,z)	0.80”	Y	Y
MACSJ1423.8+2404	14 23 48.29	+24 04 46.99	0.5450	Subaru/Suprime-Cam	i+(v,r)	0.88”	Y	Y
MACSJ1621.4+3810	16 21 23.99	+38 10 01.99	0.4650	Subaru/Suprime-Cam	i+(v,r)	0.62”	N	Y
RXJ1716.4+6708	17 16 49.60	+67 08 30.01	0.8130	Subaru/Suprime-Cam	r+(v,z)	0.63”	Y/N	N
CXOSEXSIJ205617*	20 56 17.16	-04 41 55.10	0.6002	Subaru/Suprime-Cam	r+(v,i)	0.61”	Y	N
MS2053.7-0449*	20 56 22.37	-04 37 43.42	0.5830	Subaru/Suprime-Cam	r+(v,i)	0.61”	Y	N

*CXOSEXSI_J205617 and MS_2053.7-0449 are on the same image.

Sources are detected with SExtractor (Bertin & Arnouts 1996) and an astrometric solution is found using SCAMP (Bertin 2006). The stacking of the dithered exposures is then performed using SWarp (Bertin et al. 2002). We measure the seeing by fitting a Gaussian surface brightness profile to the bright stars of the image with PSFEx (Bertin 2011).

The images obtained with the Subaru telescope and Suprime-Cam were retrieved in raw form from the SMOKA archive (http://smoka.nao.ac.jp/), together with calibration files (bias and sky flat field exposures), except the images of MACSJ0717, that were taken from Medezinski et al. (2013). They were reduced in the usual way, by subtracting an average bias and dividing by the normalized flat field in each filter exactly in the same way as the images we observed ourselves. The reduced images were then calibrated astrometrically using the SCAMP and SWarp tools, and combined for each filter. The photometric calibration was made in priority with SDSS catalogs when available in the field and in the corresponding band. If not available, we used the observed standard stars.

3. Shear measurement

The main idea of lensing is to reconstruct the mass distribution of a foreground object, designated as the lens, through the deflection it induces on the background object light, namely galaxy sources. In the WL regime, the deflection is smaller than the typical intrinsic ellipticity of a galaxy (of the order of the percent), so that we must take the mean of many shear measurements from individual galaxies to reach a high signal-to-noise (S/N) detection of the shear. For a complete description of this phenomenon, check e.g., the review by Bartelmann & Schneider (2001). The main difficulty of the method is to take into account all the galaxy shape distortions that are not due to the shear signal, such as atmospheric variations and instrumental biases. To correct for these biases, we apply a KSB+ method, initially proposed by Kaiser et al. (1995) and later refined by Luppino & Kaiser (1997); Hoekstra et al. (1998). The KSB method suits well shear measurements in cluster fields as assessed by the various large surveys choosing this technique (Okabe et al. 2010; von der Linden et al. 2014; Hoekstra et al. 2015). In addition, it has been accurately tested on simulated images such as, e.g. the STEP2 simulations by Massey et al. (2007a). Most of the WL reduction presented here is similar to the technique applied in Clowe et al. (2012).

We first detect objects using SExtractor and clean the catalog from spurious detections (Sect. 3.1). We separate stars from galaxies and measure the instrument Point Spread Function (PSF) variation on stars (Sect. 3.2) using the IMCAT software (Kaiser (2011): http://www.ifa.hawaii.edu/~kaiser/imcat/) with some additional developments. We correct galaxy shapes for the PSF anisotropies to obtain an individual object shear catalog (Sect. 3.3). We then smooth the shear measurement noise (Sect. 3.4) and correct for the methodology biases by testing our reduction on the STEP2 (Massey et al. 2007a) shear simulations (Sect. 3.5).

3.1. Source detection

We use SExtractor to detect objects and measure their photometry in our images. In most cases, the precise alignments of the three bands are sufficient to allow a detection in double image mode. We then perform the initial detection in the band used for shape measurements and detect objects in the same apertures and positions in the two other images. For some Subaru images, we did not manage to align precisely the images from all three bands. The detection is then performed separately in each band and measurements are associated to those in the band on which the ellipticity measurement is done. This cross correlation is done through a minimization of matched object distances with a 2 arcsec limit. We detect all objects which lie on at least three pixels above 1.5 times the sky background after convolving the surface brightness profile with a Gaussian kernel of 7×7 pixel size and 3 pixel FWHM. We use 32 deblending sub-thresholds with

a deblending contrast close to zero in order to remove most of the possible blended objects that would have a modified shape. Object magnitudes are measured with the MAG_AUTO keyword.

We then compute the signal-to-noise ratio of each object using the *getsig* IMCAT tool. This command convolves the object surface brightness profile with a Gaussian filter of increasing smoothing radius r_g and selects the value of r_g that maximizes the signal-to-noise. We obtain at the same time the best signal-to-noise ratio for the object and an estimate of its size with the r_g parameter. The local background is computed by fitting a mean sky level and a 2-d linear slope of the sky brightness in an annulus centered on the object, ignoring all the pixels within $3r_g$ of any object to avoid contamination. Once this accurate signal-to-noise is computed, we remove all objects with signal-to-noise lower than 10.

We measure the 1st to 4th order of the surface brightness profile of each object in a circular aperture of size $3r_g$ using a Gaussian weighting with $\sigma = r_g$, through the *getshapes* IMCAT command. We reject objects for which the first moment of the surface brightness profile does not coincide within one pixel, with the object peak position as detected by SExtractor. We adjust the position of the remaining objects to the first moment of the surface brightness profile which represents a sub-pixel estimate of the object peak position and re-measure the object shape centered on this new position.

We then apply a series of cuts to remove likely spurious detections. We first remove all objects that have a smaller size than the instrument PSF, i.e. having a radius r_g smaller than the minimum radius of stars, selected in a magnitude versus r_g diagram. We also remove all objects located at less than 20 pixels from the image edges to avoid measuring truncated objects. Finally, we remove bad pixel detection and only keep objects that do not have any neighbor within 10 pixels of their center.

This catalog is then separated between stars and galaxies in a half light radius r_h versus magnitude plot, as shown in Fig. 1. Stars are selected as objects lying on the constant radius sequence and with appropriate magnitudes. This magnitude range is set by hand to avoid saturated stars and too faint objects. Galaxies are selected as all objects larger than the star sequence at the same magnitude excluding the saturated objects that can be seen in the bright part of the diagram.

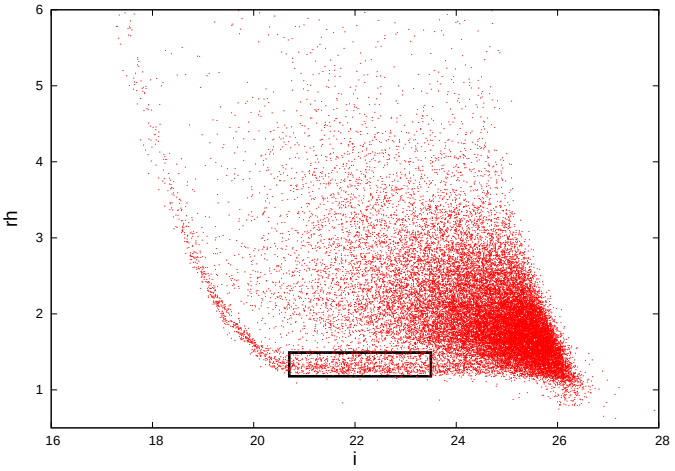

Fig. 1. Half light radius r_h (in pixels) versus i-band magnitude diagram for MACSJ1621. Red dots are catalog objects. The star selection is represented by the black polygon. The sequence of saturated stars on the left part is removed and all remaining objects above the star sequence are considered as galaxies.

3.2. PSF measurement

The PSF of a given image represents the response of the instrument to a point like source in the conditions of observation. Its variations across the image are due to the instrument characteristics and to the weather conditions. CFHT/Megacam and Subaru/Suprime-Cam have rather stable PSFs suitable for WL. Having a good seeing also diminishes the PSF correction that we need to apply. As stars are point like sources, they are suitable for measuring the PSF of an image. The large field of view of our images enables us to have enough stars in a single frame to correct for the PSF anisotropies, on the contrary of smaller field of view cameras that often require to use stars across several images.

A general image distortion can be expressed by the two following quantities: the smear polarizability tensor $\boldsymbol{P}^{\rm sm}$ that describes the object response to the PSF anisotropy, and the shear polarizability tensor $\boldsymbol{P}^{\rm sh}$ that describes its response to the shear. These two tensors are measured from the 0th, 2nd and 4th order moments of an object surface brightness distribution. We refer the reader to Kaiser et al. (1995) and Hoekstra et al. (1998) for the expression of these tensors. The ellipticity $\boldsymbol{e}$, is estimated from the 2nd order moments of this distribution. In the next subsection we will use the following quantities, as measured on stars, to infer the true shape of galaxies: $\boldsymbol{P}^{\rm sm}_{\rm star}$, $\boldsymbol{P}^{\rm sh}_{\rm star}$, and $\boldsymbol{e}_{\rm star}$.

Before measuring those quantities, we refine the star catalog to the cleanest objects. We first remove all objects that are closer than 40 pixels to any other object. We then fit the star ellipticities with a two dimension polynomial of the 6th order and generate modeled ellipticities at each object position using this polynomial. Objects that have a measured ellipticity differing by more than 0.05 from their modeled ellipticity are rejected. This step is repeated three times, and permits to remove galaxies that might have been considered as stars. We chose an ellipticity cut at 0.05 as we found that it removes objects that are mainly out of the whole sample ellipticity distribution. Finally, a visual inspection is carried out to remove all remaining objects that could still suffer from blending issues or being close to saturated stars. The final catalogs contain $\sim$ 1000 and $\sim$ 3000 stars in average for Subaru and Megacam images respectively, leading to an average star density of 1.0 arcmin^{-2} and 0.8 arcmin^{-2} respectively for Subaru and Megacam.

Star shapes are measured using the *getshapes* IMCAT tool. As $\boldsymbol{P}^{\rm sm}$ and $\boldsymbol{P}^{\rm sh}$ depend on object sizes, we have to measure them for various sets of weighting radii. Hence, we compute a series of tensors for each r_g between 1 and 10 pixels with a step of 0.5 pixels, so that we can use the tensors corresponding to the galaxy radius when correcting for the PSF. Final quantities are fitted by 6th-order 2D polynomials as a function of position in order to have continuous functions defined at every point of the image. Here we chose to measure the PSF over the entire image, using a high order polynomial fit. However, in the case of large field-of-view images, one could also divide the frame into several small patches, and fit the PSF in each tile with a lower order polynomial. While the second approach is used in various studies (Okabe et al. 2010; Umetsu et al. 2011), von der Linden et al. (2014) applied and validated the first approach in the case of Subaru/Suprime-Cam images. For the CFHT/Megacam data, while fitting the PSF on each chip, Hoekstra (2007) found negligible discontinuities in the PSF anisotropy between chips. Following e.g. Massey et al. (2005), we compute the auto-correlation function of star ellip-

ticities before and after the PSF correction and the cross correlation function between galaxy shear and star ellipticities in Appendix A, validating our PSF correction.

3.3. PSF correction

In the absence of noise the shear of a background galaxy ($\boldsymbol{g}_{\rm gal}$) can be computed from the following equation:

$$\boldsymbol{g}_{\rm gal} = \left(\boldsymbol{P}^{\rm g}_{\rm gal}\right)^{-1} \boldsymbol{\delta e}_{\rm gal}, \quad (1)$$

where $\boldsymbol{P}^{\rm g}_{\rm gal}$ is the shear susceptibility tensor defined in eq. 2, and $\boldsymbol{\delta e}_{\rm gal}$ the apparent change in ellipticity, described in eq. 3. Note that in this equation we neglect the intrinsic ellipticity that should be subtracted to the apparent ellipticity change ($\boldsymbol{\delta e}_{\rm gal}$). This is true if a sufficient number of galaxies is taken into account: the galaxies being randomly oriented, the intrinsic ellipticity is null in average.

The shear susceptibility tensor represents the PSF corrected distortion, i.e. only due to the shear. We define it as in Luppino & Kaiser (1997):

$$\boldsymbol{P}^{\rm g}_{\rm gal} = \boldsymbol{P}^{\rm sh}_{\rm gal} - \boldsymbol{P}^{\rm sh}_{\rm star} \left(\boldsymbol{P}^{\rm sm}_{\rm star}\right)^{-1} \boldsymbol{P}^{\rm sm}_{\rm gal}, \quad (2)$$

where the $_{\rm gal}$ index is for tensors measured on galaxies, and $_{\rm star}$ for tensors measured on stars. The apparent change in ellipticity is:

$$\boldsymbol{\delta e}_{\rm gal} = \boldsymbol{e}_{\rm gal} - \boldsymbol{P}^{\rm sm}_{\rm gal} \left(\boldsymbol{P}^{\rm sm}_{\rm star}\right)^{-1} \boldsymbol{e}_{\rm star}, \quad (3)$$

where $\boldsymbol{e}$ represents the object ellipticity. In order to compute a galaxy shear, we then need to measure its ellipticity vector, and its smear polarizability and shear polarizability tensors. This is again done with the *getshapes* tool. We also generate the star quantities corresponding to each galaxy radius r_g using the polynomials computed in the last section.

Prior to measuring the shape of galaxies, we reject QSOs and cosmic rays by removing objects that lie away from the principal sequence in a maximum flux versus magnitude diagram. We also remove objects in regions where the sky level is too bright to avoid star diffraction halos. We restrict our catalogs to objects larger than 1.5 times the PSF size, defined as the minimum star radius r_g, deleting objects on which the PSF deconvolution could be too noisy. Finally, we visually inspect the images to remove any object close to saturated stars or reduction artifacts that could have survived our previous cleaning.

3.4. Noise smoothing and co-addition

The individual shear values are noisy due to the sky noise in the measurements of the higher order moments of the light distribution of objects. As these moments are subtracted one to each other when computing the shear polarizibility tensor, the final signal value is reduced while the noise increases. We then have to smooth the noise in the shear polarizibility tensor measurement to avoid it dominating the shear measurement, using its distribution across the image. We fit each component of the shear polarizability tensor $\boldsymbol{P}^{\rm g}_{\rm gal}$ as a function of one component of the ellipticity and of the object size r_g by a 4th order two dimension polynomial. We chose a 4th order polynomial after testing several orders, as we found that it was minimizing the noise. Also, we find that the shear polarizability tensor weakly depends on the ellipticity but is more sensitive to the object size. We then use this modeled tensor to re-generate the shear values of each object following eq. 1. We note that this step removes the noise that would cause negative values of the shear polarizability tensor. We verify that after this fitting procedure, we do not have $\boldsymbol{P}^{\rm g}_{\rm gal}$ values lower than 0.1.

Finally, we weight the individual shear values according to their significance compared to their neighbors in the (r_g,S/N) plane. In practice, this weight factor is set to the inverse of the root mean square of the shear of the 50 nearest neighbors for a region around each galaxy size and significance. Generally, the small, faint galaxies are given a low weight and larger, bright galaxies are given a high weight, due to the larger galaxies being affected only by the intrinsic shape noise while the smaller, fainter galaxies also have a significant noise component coming from sky noise in their shear measurements. In addition, sub-areas presenting a large shear dispersion will contribute less than sub-areas with a low shear dispersion.

Table 2. Multiplicative (m) and additive (c) shear biases derived from applying our WL reduction pipeline to the STEP2 simulations with a Subaru PSF and a seeing of 0.8" (PSF C). See eq. 4 and text for details.

	m	c
γ_1	-0.053 ± 0.021	0.004 ± 0.001
γ_2	-0.021 ± 0.030	0.001 ± 0.001

3.5. Bias calibration

We measure the bias of our method on the STEP2 simulations (Massey et al. 2007a) that provide images computed with various PSFs, and with an added constant shear across each image. We use the sets of images characterized by a Subaru PSF with a seeing of 0.8 arcsec (PSF C). This PSF suits well our data as about half of our images are from Subaru and our image seeing lies between $0.6 < \epsilon < 1.0$ arcsec. However, note that the STEP2 images are 7×7 arcmin^2 size, while our images are of the order of 34×27 arcmin^2 for Suprime-Cam and 60×60 arcmin^2 for MegaCam. Hence, the PSF should be better sampled in the true images.

Applying our reduction pipeline, we calculate the average shear of each of the 64 simulated galaxy fields and fit the difference between our shear estimate and the true shear as a function of the true shear, according to the notation of eq. 4 from Massey et al. (2007a):

$$\gamma_i - \gamma_i^{\rm true} = m_i \times \gamma_i^{\rm true} + c_i, \quad (4)$$

where i is the index for both shear components. The values we have found for the multiplicative biases m_1 and m_2 and the additive biases c_1 and c_2 are shown in Table 2.

Our results compare well with the ones from other methods as described in the STEP2 challenge (Massey et al. 2007a). As expected, the additive bias is rather negligible and the shear is slightly underestimated with the KSB method. The multiplicative bias can be seen as an evaluation of the quality of the shear measurement. Our results hence show that we can measure the galaxy shear with an accuracy better than $\sim 5\%$. We correct each component of the shear for the multiplicative bias, and thus obtain our final shear catalog. Note that we do not correct for the additive bias which is strongly PSF dependent, and rather prefer to leave it as a potential systematic bias, small compared to the other sources of errors.

4. Mass reconstruction

We then translate the measured shear signal to a mass estimate. We first apply the standard Seitz & Schneider (1995) inversion technique based on the Kaiser & Squires (1993) algorithm to calculate a convergence density map (Sect. 4.2). This technique allows to draw significance contour levels on the cluster image to search for structures but does not allow to recover the true masses of objects. Indeed, the integration of the shear over a finite space introduces a constant called the mass sheet degeneracy that cannot be properly taken into account without a magnification study. To avoid this problem, we fit NFW shear profiles on clusters to infer their 3D mass distribution in Sect. 4.3. In any case, we first have to select galaxies that lie behind the structures we aim to detect, to avoid diluting the shear signal. This is done in Sect. 4.1, where we also estimate the mean background galaxy redshift, as this quantity is required to convert the shear and the convergence into mass.

4.1. Background galaxies

Foreground and cluster galaxies are not lensed by the cluster. Hence, they will appear as noise in the co-adding of individual shear measurements, and have to be deleted. The most accurate way to select background galaxies is to use spectroscopic redshifts, but it requires too much observational time. Photometric redshifts are more promising, as less time-consuming, and are starting to give accurate redshift estimations. However, we do not have spectroscopic or photometric redshifts for all galaxies and therefore we must consider galaxy colors. Galaxy colors are linked to the galaxy formation history and can be used as a crude approximation of the galaxy redshift.

We select background galaxies in a color-color diagram, comparing our galaxy colors to those from galaxy templates computed at various redshifts. We generate templates for early and late type galaxies using EzGal (Mancone & Gonzalez 2012) with Bruzual & Charlot (2003) models, assuming a Chabrier (2003) Initial Mass Function (IMF), a formation redshift of $z_{\rm form} = 4$, and a solar metallicity. The red early type galaxies are modeled with a single starburst model and the blue late type galaxies by an exponentially decaying star formation model. We remove all galaxies that correspond to the color-color area covered by template galaxies at redshift $z < z_{\rm clus} + 0.2$. For example, we show the color-color diagram of MACSJ1621 with the removed area in Fig. 2. Note that the colors we use vary from one cluster to another according to the available optical bands (see Table 1). We also cut all the remaining galaxies with magnitudes brighter than $i = 22$ or $r = 22.5$ (depending on the image on which the shear measurement is performed), as they are very likely foreground galaxies given the high redshift of our clusters. In the same manner, galaxies fainter than $i = 25$ or $r = 25.5$ are removed as they are fainter than the depth of our images, and therefore not reliable.

Another issue is to measure the distances of the lens and of the background galaxies. These observables are required to estimate the mass of the lens, which depends on the ratio of the source to observer distance over the source to lens distance: D_s/D_{ls}. We estimate the lens distance through the spectroscopic redshift of the cluster. The classical way of estimating the mean background galaxy distance is to average the distance ratio D_s/D_{ls} over all source galaxies. See also Applegate et al. (2014) for a method that uses all galaxy background photometric redshifts in a Bayesian formalism.

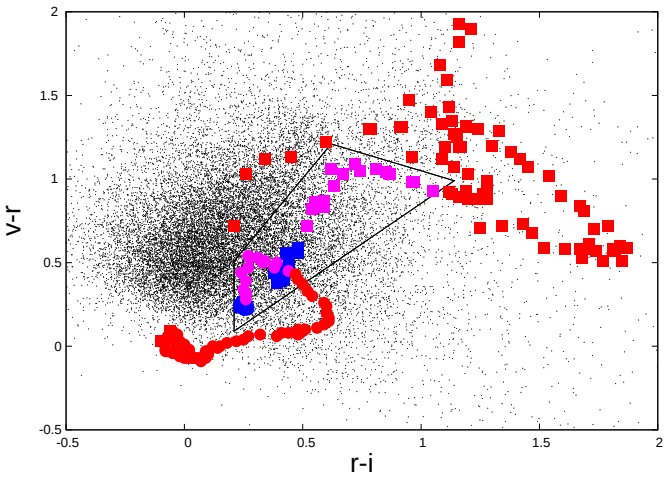

Fig. 2. (v-r) versus (r-i) color-color diagram for MACSJ1621. Black dots represent galaxies from our catalog. Circles are late type galaxy templates and squares early types. Magenta is for templates at ±0.2 around the cluster redshift, blue for lower-redshift galaxy templates and red for higher-redshift galaxy templates. The black polygon circling magenta and blue points correspond to the color area we remove from our catalog. See text for details on used galaxy templates.

As we do not have photometric redshifts for background galaxies, we consider an external redshift distribution. We use the COSMOS data (Ilbert et al. 2009) as our redshift distribution. These data are well suitable as they cover a large area of about 1.7 deg^2 after masking, down to a magnitude of $i = 25$, and are adapted to our redshift range. Furthermore, the photometric redshifts of COSMOS are computed with a high precision, using 30 bands from near-UV to mid-IR. We first apply the same magnitude and color cuts than those applied to our shear catalog. We then remove all galaxies that have a photometric redshift smaller than that of the cluster and calculate the mean of the ratio of the source to lens versus source distances D_{ls}/D_s, applying an appropriate weight. The weighting function is generated on the COSMOS galaxy sub-sample from a 2D polynomial fitted on the shear weighting function in our data in a half-light radius versus magnitude plane. We use the magnitude instead of the S/N ratio as the second coordinate because the S/N in COSMOS and in our data can vary significantly. Finally, the weights generated on COSMOS are re-normalized to 1. The mean redshift of background galaxies is then set to the one that allows to find the measured mean distance ratio D_{ls}/D_s. These redshifts can be found in Table 3.

4.2. 2D mass map

We reconstruct the projected convergence field by inverting the shear in Fourier-space, following Seitz & Schneider (1995). This technique is an iterative application of the Kaiser & Squires (1993) algorithm to correct for the fact that we measure the reduced shear, which is equal to the shear γ divided by $1 - \kappa$, and not the shear. We reconstruct the first convergence map assuming $\kappa = 0$ in the shear, and then generate a map from the shear where the convergence is set to the previous map in the loop until the process converges. We find that the convergence map remains constant within 0.01% after three realizations. This technique allows to better estimate the mass map around high masses and is therefore particularly suitable for our cluster mass reconstruc-

tion. The convergence field is smoothed with a Gaussian filter of width $\theta_s = 1$ arcmin at each step of the algorithm, before reading off which convergence to use to correct for a given galaxy. The noise level in the final convergence map can be estimated as eq. 5 (van Waerbeke 2000):

$$\sigma_\kappa = \frac{\sigma_\epsilon}{\sqrt{4\pi n_{\rm bg}\theta_s^2}}, \quad (5)$$

where $n_{\rm bg}$ is the density of background galaxies and σ_ϵ the dispersion of the ellipticities of the background galaxies. $n_{\rm bg}$ and σ_ϵ are estimated independently for each image, taking into account the weight function of the shear. σ_ϵ ranges from 0.27 to 0.32 across our data, while $n_{\rm bg}$ can be found in Table 3 for each cluster.

One can then convert the convergence map into a surface mass density map using the definition of the convergence (eq. 6):

$$\kappa = \frac{\Sigma}{\Sigma_{\rm crit}}, \quad (6)$$

where Σ is the surface mass density and $\Sigma_{\rm crit}$ the critical surface mass density defined in eq. 7:

$$\Sigma_{\rm crit} = \frac{c^2}{4\pi G}\frac{D_{\rm s}}{D_{\rm l}D_{\rm ls}}. \quad (7)$$

c is the speed of light, G the gravitational constant, and $D_{\rm s}$, $D_{\rm l}$, and $D_{\rm ls}$ are respectively the distance to the source, the distance to the lens, and the distance between the source and the lens. This conversion hence only requires the knowledge of the lens and source redshifts, calculated in Sect. 4.1. As we cannot properly account for the mass sheet degeneracy in our reconstruction, we did not try to estimate the mass of clusters through the convergence map. These mass maps are thus only used to detect clusters and their surrounding structures, while the cluster masses are estimated in the next section fitting an NFW profile to the shear.

The significance of the detection is computed from a noise re-sampling technique, adding a random ellipticity to every galaxy for each realization. To preserve the shape noise properties of the sample, we draw the added ellipticities from the image galaxy catalog. Doing so, we neglect the additional shear signal as it is very unlikely that it correlates with the detected structures given the large number of galaxies in our catalogs. The shape noise used in eq. 5 is increased by a factor of $\sqrt{2}$ as the ellipticity of galaxies now corresponds to the sum of two Gaussian distributions with a null mean and a width σ_ϵ. We perform a hundred realizations for each catalog, computing the detection level of every structure at each step. The mean and dispersion of these detection levels give a strong estimate of the significance of the detection. We also measure the number of realizations in which the structure is detected at more than 3σ above the map noise. For example we can be very confident in a structure detected at more than 3σ in 95% of the realizations. In addition, this noise re-sampling allows to refine the measure of the position of each structure, computing the mean and dispersion of the local maximum position over all noise realizations. These quantities respectively correspond to an estimate of the structure center and to the error on its position.

For example, we show in Fig. 3 the 3-band-color image with the convergence contours overlaid for MACSJ1621. The contours are spaced in units of the map noise computed from eq. 5, starting at 3σ. We display the same figure for every cluster with X-ray emissivity and galaxy light density contours when available in Sect. 6. As a sanity check, we computed the mass map with shear rotated by 45 degrees (white contours) and found that the signal due to the cluster presence disappears in this map, validating our convergence map reconstruction method. The position of the WL peaks are noted by white crosses with a 1 for the cluster and a 2 for the main secondary structure. The cluster is detected at $(6.8 \pm 1.4)\sigma_\kappa$ in the center region and an elongated structure aligned with the cluster major axis can be seen at a $(5.9 \pm 1.7)\sigma_\kappa$ confidence level computed from the mean and dispersion of a hundred realizations of the noise. These two structures are detected in respectively 97 and 96 % of the realizations. The nature of the secondary peak is discussed in Sect. 6 comparing the WL with other probes (X-ray and optics). The center positions are estimated with a precision of about 200 kpc. Also, we note a slight offset between the Brightest Cluster Galaxy (BCG) marked by a yellow cross and the WL peak.

In spite of all our care to build accurate mass maps, some peaks will arise from the noise. One must evaluate the number of these fake peaks in order to discuss the detection of structures in the mass maps. As the number of fake peaks depends both on the density of background galaxies and on the redshifts of the lens and sources, we compute a fake peak probability for each cluster field. To do so, we assign a random position to each galaxy in the frame, to make sure that no structure from the original position would be left in the simulation. We then use this new ellipticity catalog as an input to our mass map pipeline. The resulting convergence map should be representative of the noise. However, the presence of the cluster also modifies the distribution of fake peaks. To take this into account, we add to the ellipticity of each galaxy, shear values based on the fitted NFW profile of the corresponding cluster (see Sect. 4.3). We find slightly fewer peaks when adding the cluster. This is due to the fact that some noise peaks can be aligned with the cluster, and also because the presence of the cluster is compensated by negative convergence values in the mass map as the mean convergence in the reconstruction is set to zero. We do a hundred realizations to capture the statistical properties of the fake peaks. For MACSJ0717, we also performed 10,000 realizations to check that our 100 realizations are sufficient. We find little difference between the two cases. Quantitatively, we find 11.1 peaks above $3\sigma_\kappa$ and 1.3 above $4\sigma_\kappa$ in the entire Suprime-Cam field for 100 realizations, and 10.9 and 1.2 above $3\sigma_\kappa$ and $4\sigma_\kappa$ for 10,000 realizations. In any case we find less than 0.1 fake peaks above $5\sigma_\kappa$. When discussing the detection of structures in Sect. 6, we give the expected number of fake peaks in the displayed area for each cluster. We note that in Fig. 3, the white contours corresponding to the reconstruction of the orthonormal shear component, are in good agreement with the expected number of fake peaks for the displayed field (2.9 above $3\sigma_\kappa$ and 0.4 above $4\sigma_\kappa$ in the left-hand field).

4.3. Cluster mass fit

To infer the cluster mass distribution, we choose to fit the shear profile centered on the cluster. This avoids having to measure the shear in the cluster core, and partially breaks the mass sheet degeneracy by imposing a given mass profile on the data. We note that using this radial technique on N-body simulated clusters, Becker & Kravtsov (2011); Bahé et al. (2012) found a systematic underestimate of cluster masses of roughly 5%, which we do not correct for as the exact correction factor is likely to be a function of the chosen cosmologcial paramaters (and is small compared to the uncertainties for all of our clusters). The NFW density profile (Navarro et al. 1996) defined in eq. 8 is among

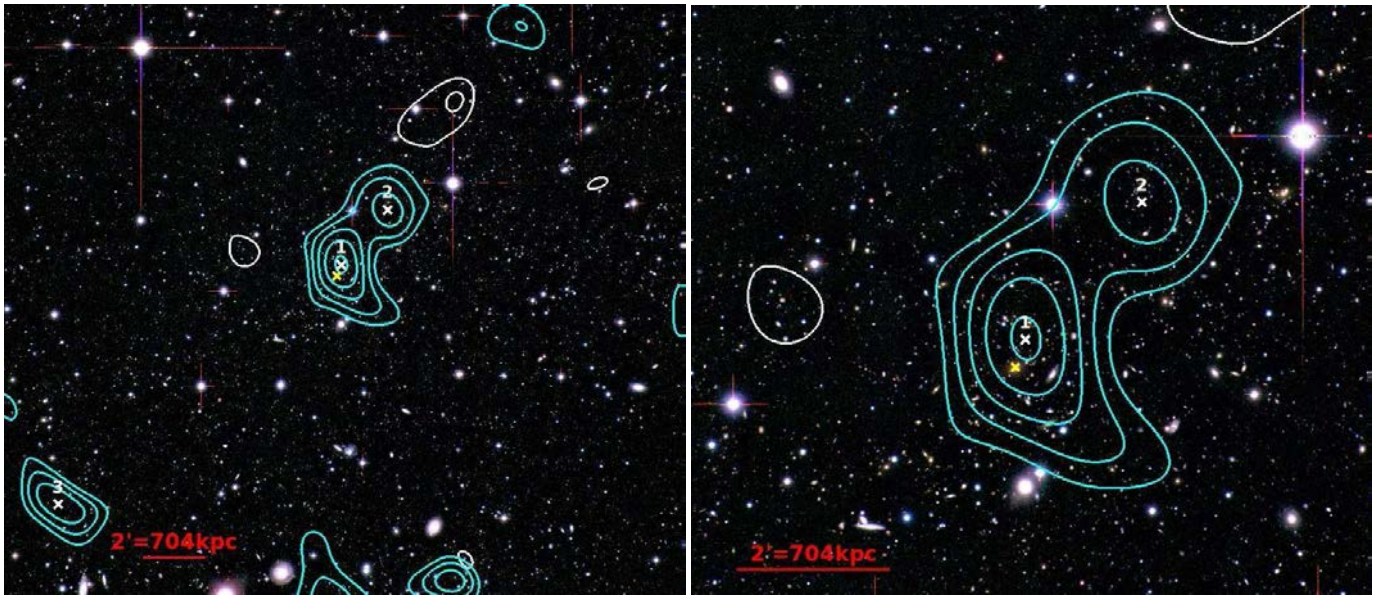

Fig. 3. Convergence density map for MACSJ1621 overlaid on 3-color image. Contour levels (cyan) are in signal-to-noise from $3\sigma_\kappa$ and by step of $1\sigma_\kappa$. The white contours show the convergence density map computed from the rotated shear with the same signal-to-noise levels. We note that the signal corresponding to the cluster disappears in this reconstruction. Weak lensing peaks are noted by a white cross starting with the highest detection. The yellow cross indicates the position of the BCG. Left shows the full image and right a zoom on the cluster region.

the best available profiles to fit observed galaxy clusters (e.g. Umetsu et al. 2011).

$$\rho_{\rm NFW}(r) = \frac{\rho_{\rm s}}{\frac{r}{r_{\rm s}}(1+\frac{r}{r_{\rm s}})^2} \tag{8}$$

where $r_{\rm s}$ is the scale radius and $\rho_{\rm s}$ a density expressed as $\rho_{\rm crit}\delta_{\rm c}$. $\rho_{\rm crit} = 3H^2/8\pi G$ is the critical density of the Universe at the cluster redshift, and $\delta_{\rm c}$ is a dimensionless density that depends on the DM halo, and that can be expressed as a function of the concentration parameter:

$$\delta_{\rm c} = \frac{\Delta}{3}\frac{c_\Delta^3}{\ln(1+c_\Delta) - \frac{c_\Delta}{1+c_\Delta}}, \tag{9}$$

where Δ is the overdensity compared to the critical density, $c_\Delta = r_\Delta/r_s$ is the concentration parameter. By integration of the density under spherical symmetry, the mass $M_{\rm NFW,\Delta}$ in a given radius r_Δ, can be estimated as a function of r_Δ and c_Δ only:

$$M_{\rm NFW,\Delta} = \frac{4\pi\rho_{\rm s} r_\Delta^3}{c_\Delta^3}[\ln(1+c_\Delta) - \frac{c_\Delta}{1+c_\Delta}]. \tag{10}$$

The radial shear profile has an analytic formula derived in e.g. Wright & Brainerd (2000), that we fit to the measured shear to obtain r_Δ and c_Δ which are converted into a cluster mass according to eq. 10. To break the degeneracy between r_Δ and c_Δ, we fix the concentration parameter to $c_{200} = 3.5$, since Gao et al. (2008) demonstrated that very massive clusters have concentration parameters between 3 and 4 at the studied redshifts. This choice of a fixed concentration parameter imposes a systematic error on each individual cluster mass although the average should be correct. We quantify the error on the mass measurement due to the intrinsic scatter of 1.34 on the concentration parameter estimate in Gao et al. (2008) by fixing the concentration parameter to 2.16 and 4.84, which represent the scatter around our chosen value of $c_{200} = 3.5$. We find a variation of the mass of about ±25%. This error is not added to the error budget of Table 3. The fit is done in an annulus where the inner radius is iteratively set to a value larger than the Einstein radius, to remove the area affected by strong lensing. We also require to have a minimum number of objects in every bin, which can push the inner radius to large physical values in the case of high redshift clusters. The outer radius is set to the value at which the output r_Δ does not significantly change (less than 1%) if we probe a larger area. We also ensure that the outer radius is at least larger than the output r_Δ. The fit is performed on the tangential shear computed to the cluster center, which is defined as the closest peak to the cluster position in the convergence map reconstruction. An estimate of the significance of the fit is obtained by computing the $\Delta\chi^2$ between the best fit NFW model and a zero mass model. The tangential shear profiles for every cluster can be found in Appendix B, where the error bars correspond to the orthonormal shear that should be equal to zero in the absence of noise. We measure r_{200} from the best NFW fit and then compute M_{200}, and M_{500}. We note that for clusters where the NFW fit has a low significance value ($\sigma < 3$), the tangential shear profile presents error bars consistent with no signal. We then do not compute a mass for these clusters, as their shear profile is not reliable.

The errors are computed using the same noise re-sampling method than for the mass maps (see Sect. 4.2). A random ellipticity is drawn from our catalog and added to each galaxy. Then, the best NFW fit gives a new value for r_{200} and M_{200}. The mean and the dispersion over a hundred noise realizations are used as the true value and its error. The r_{200} and various mass values are given in Table 3 of Sect. 5.

5. Galaxy clusters

In this section we present the results concerning the 16 galaxy clusters that we have studied. The discussion is based on the masses obtained from the NFW fits presented in Sect. 4.3 and

given in Table 3. After discussing the WL masses (Sect. 5.1), we compare them to the X-ray values from the literature (Sect. 5.2).The comparison of individual cluster masses with other studies is done jointly with the environment discussion in the next section (Sect. 6).

5.1. WL Masses

The results of the best NFW fit are given only when its significance is higher than 3σ, because otherwise such masses would not be reliable. This means that we were not able to constrain the masses of all clusters (see Table 3 and shear profiles in Appendix B). The fact that some of our fits do not converge can have several explanations depending on each case. One obvious limitation is the background galaxy density: as the noise is proportional to the inverse square root of the background density, the deeper the observations, the higher the signal-to-noise of the shear. The data obtained with Subaru, which is an 8m class telescope, are less affected than those obtained with the CFHT, which is only a 4m class telescope. The masses of the clusters and the noise in the images are also important factors. A high mass cluster will tend to be detected even with a low background galaxy density. Finally, we note that the redshift of the cluster also plays a role. For example, BMW-HRI J122657 is a rather massive cluster, but at a redshift of $z = 0.89$. As the lensing effect is measured on the galaxies behind the cluster, the higher the redshift, the more difficult it is to detect the cluster. A redshift of $z \sim 0.9$ is close to the accessible limit, as lensing is most sensitive to structures at redshifts around $z \sim 0.3 - 0.4$.

For the clusters for which we were able to compute masses, we find error bars typical of WL studies. We note however, that using the noise re-sampling method to determine the mass increases our errors over using only the significance of the best NFW fit. We choose to show the former errors because they are more robust and more conservative. We do not statistically compare our masses with other WL studies because we have only few clusters in common. Three of our clusters are studied in the Mahdavi et al. (2013) sample, three in the CCCP sample (Hoekstra et al. 2015), three in the Weighting the Giants sample (Applegate et al. 2014), two in the Foëx et al. (2012) sample, one is studied in Jauzac et al. (2012) and Medezinski et al. (2013), and one in Israel et al. (2014). Nonetheless, a comparison of the WL masses, and also with the X-ray and strong lensing estimates, is done for each cluster in Sect. 6.1. In the next subsection, we compare our WL masses with those derived from X-rays to evaluate potential biases in both measurements.

5.2. X-ray and WL masses

The X-ray masses come from two different samples. Most of them have *XMM*–Newton data and are taken from Guennou et al. (2014). We add four clusters that have *Chandra* data and belong to the Maughan et al. (2012) sample. MACSJ1423 has *Chandra* data but is also part of Guennou et al. (2014). The masses from Guennou et al. (2014) are obtained by applying the Kravtsov et al. (2006) scaling relation to the X-ray derived temperature of the clusters. The error bars have been recomputed taking the scatter of this scaling relation into account, since they were too optimistic in Guennou et al. (2014). The masses from *Chandra* observations have been computed in Laganá et al. (2013) using both the temperatures and surface brightness profiles (see eq. 5 of the mentioned paper).

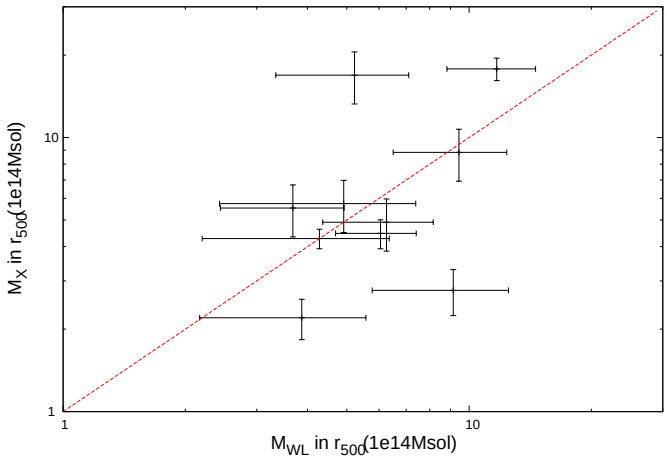

Fig. 4. X-ray versus WL masses. The red dashed line is the first bisector and represents the sequence on which X-ray and WL masses would be equal. All values can be found in Table 3.

We compare in Fig. 4 the cluster masses inferred from X-ray data and from WL, all computed in r_{500}, for the ten clusters that have both data. We see that the points are fairly distributed around the line of equality. Computing the mean ratio of the WL to X-ray masses, we find that WL masses are 22% higher than the X-ray masses in the mean. Finding an offset is quite normal, as the X-ray masses rely on the assumption that clusters are relaxed, which is generally not the case. Weak lensing, on the other part, does not need such an assumption, and WL masses are usually more reliable. This underestimate of about 20% in the X-ray derived total cluster masses is the commonly observed value (Rasia et al. 2006; Nagai et al. 2007; Battaglia et al. 2013). We also note a departure from this relation for LCDCS0829, for which we cannot reproduce the high X-ray mass, and for RXJ1716 which has a very low mass in X-rays compared to its WL mass. In the first case we note that LCDCS0829 is highly asymmetrical as seen from its mass map in Fig. 8 (Sect. 6). Hence, the hypothesis of spherical symmetry that we made for our NFW fit might explain why we find a low mass for this cluster. In general one cannot expect individual WL masses to be very reliable, but in the mean, WL masses tend to be very accurate.

6. Environment

In this section, we use the 2D mass maps computed in Sect. 4.2 to discuss the structures detected in the vicinity of clusters. To have a full understanding of the different mass components we overplot on the images the WL contours at a 3σ significance as well as the X-ray contours and the galaxy light distribution contours. To secure the WL detection of each structure we compute its significance level with respect to the map noise for a hundred realizations of the noise. We also count the percentage of simulations in which the structure is detected at more than 3σ above the background. The last two quantities contain similar information, and are given in Table 4. The significance levels in this table are computed from the hundred realizations of the noise and can slightly differ from the contour levels shown in Figs. 5 to 19 which correspond to the original mass maps. We also compute the number and significance of peaks expected to be due to the noise in the map reconstruction. This enables us to discuss the presence of WL peaks which do not show any optical or X-ray

Table 3. Results on galaxy clusters. The first eight clusters are observed with CFHT/Megacam and the last eight with Subaru/Suprime-cam. The different columns correspond to #1: cluster ID, #2: cluster redshift, #3: mean redshift of background galaxies, #4: mean galaxy density of the background galaxies, #5: r_{200} from the best NFW fit, #6: significance of the NFW fit/significance of the WL peak in the 2D mass map, #7: M_{200}^{NFW} from the best NFW fit centered on the WL peak, #8: M_{500}^{NFW} computed from M_{200}^{NFW} assuming an NFW profile, #9: *XMM* X-ray masses from Guennou et al. (2014) or *Chandra* X-ray masses computed in Laganá et al. (2013) from the Maughan et al. (2012) sample denoted by the symbol ^{M12}.

Cluster	z	$\bar{z}_{\rm bg}$	$n_{\rm bg}$ (arcmin^{-2})	r_{200}^{NFW} (kpc)	σ_{NFW}/σ_{2D}	M_{200}^{NFW} ($10^{14}M_\odot$)	M_{500}^{NFW} ($10^{14}M_\odot$)	M_{500}^{X} ($10^{14}M_\odot$)
XDCS0329	0.4122	0.90	10.20	-	1.2/2.8	-	-	2.9 ± 0.6
MACSJ0454	0.5377	0.99	9.96	-	2.0/5.1	-	-	13.9 ± 3.0
ABELL0851	0.4069	0.92	8.30	1442 ± 178	4.0/7.6	5.5 ± 1.9	3.7 ± 1.2	5.5 ± 1.2
LCDCS0829	0.4510	0.93	8.79	1592 ± 199	4.0/5.5	7.8 ± 2.8	5.2 ± 1.9	16.9 ± 3.6
MS1621	0.4260	0.93	14.13	1704 ± 133	6.4/8.3	9.0 ± 2.0	6.1 ± 1.4	4.5 ± 0.5^{M12}
OC02	0.4530	0.96	13.15	1221 ± 194	3.1/4.7	3.6 ± 1.6	2.4 ± 1.1	-
NEP200	0.6909	1.02	5.80	1783 ± 272	3.1/5.1	14.8 ± 6.1	10.0 ± 4.1	-
RXJ2328	0.4970	0.95	11.46	1400 ± 233	3.2/5.5	5.8 ± 2.5	3.9 ± 1.7	2.2 ± 0.5
CLJ0152	0.8310	1.19	14.94	1673 ± 187	3.8/8.3	14.1 ± 4.4	9.4 ± 2.9	8.8 ± 1.9
MACSJ0717	0.5458	0.98	13.16	2023 ± 172	5.4/10.9	17.4 ± 4.3	11.7 ± 2.9	17.8 ± 1.7^{M12}
BMW1226	0.8900	1.43	10.12	-	1.3/-	-	-	12.1 ± 0.4
MACSJ1423	0.5450	0.93	8.98	1480 ± 265	3.4/5.0	7.3 ± 3.7	4.9 ± 2.5	5.7 ± 1.2
MACSJ1621	0.4650	0.94	16.39	1456 ± 282	4.1/6.8	6.4 ± 3.1	4.3 ± 2.1	4.3 ± 0.4^{M12}
RXJ1716	0.8130	1.17	7.49	1660 ± 217	3.9/7.3	13.6 ± 5.0	9.1 ± 3.4	2.8 ± 0.5^{M12}
MS2053*	0.5830	0.98	14.44	1614 ± 175	4.6/8.7	9.3 ± 2.8	6.3 ± 1.9	4.9 ± 1.1
CXOSEXSI2056*	0.6002	0.98	14.44	-	0.7/4.4	-	-	3.6 ± 0.8

* CXOSEXSI_J205617 and MS_2053.7-0449 are on the same image.

counterpart. We also note that in the case of the optical contours, we tried to select only cluster member galaxies, while the WL is sensitive to any line-of-sight structure, with a higher efficiency for structures at redshift around $z \sim 0.3 - 0.4$. As a result, it is not surprising to find some peaks in the convergence map with no optical counterpart.

The X-ray contours are plotted from *XMM*–Newton EPIC MOS1 or MOS2 images. The *XMM* images suit well our study, as *XMM* has a larger field of view than *Chandra*. However, when no *XMM* data are available, we show contours from *Chandra* images. Even with *XMM*, the field of view is limited to about 30 arcmin in diameter, and in some cases, several structures detected through weak lensing have no X-ray counterparts because only the cluster vicinity is in the X-ray field. The X-ray images have been binned in squares of 64 pixels and then smoothed with a Gaussian filter of 20 pixel width. The significance of the X-ray maps are computed from the dispersion of the values of the respective map avoiding the cluster region, and start at 2σ. We chose a 2σ value to show better how our WL detections are embedded in the baryonic components, and because the X-ray maps are only used for qualitative description.

The light density maps are built with the galaxies selected to have a high probability of being at the same redshift as the cluster. For this, we first extract all the objects from the images in two bands. We separate stars from galaxies as described above and draw color-magnitude diagrams. For each cluster, we superimpose on the color-magnitude diagram the positions of the galaxies with spectroscopic redshifts coinciding with the cluster redshift range. This allows to define the red sequence drawn by the early type galaxies belonging to the cluster and to fit it with a linear function of fixed slope −0.0436, as in Durret et al. (2011). We then select all the galaxies within ±0.3 magnitude of this sequence as probable cluster members and compute the density map of this galaxy catalog, using the same Gaussian kernel than that of the WL analysis. The pixel size chosen to compute these maps is 0.001 deg, and the number of bootstraps is 100. To derive the significance level of our detections, it is necessary to estimate the mean background of each image and its dispersion. For this, we draw for each density map the histogram of the pixel intensities. We apply a 2.5σ clipping to eliminate the pixels of the image that have high values and correspond to objects in the image. We then redraw the histogram of the pixel intensities after clipping and fit this distribution with a Gaussian. For each cluster, the mean value and the width of the Gaussian will respectively give the mean background level and the dispersion, that we will call σ. We then compute the values of the contours corresponding to 3σ detections as the background plus 3σ. In all the figures of the following subsection, we show contours starting at 3σ and increasing by 1σ.

We first discuss individually the mass map of every cluster in Sect. 6.1, and then make general considerations in Sect. 6.2.

6.1. Individual clusters

In addition to discussing the reconstructed convergence maps, in this subsection, we also compare the WL masses computed from the NFW best fit (see Sect. 4.3) to other masses from the literature. However we would like to warn the reader that WL masses from different studies can significantly vary. The reason for that lies in the estimate of the redshift distribution of the background galaxies. In the ideal case where every study selects the same background galaxies and agrees on their redshift distribution, they should get the same masses within errors coming just from the shear measurement. However, in most cases the selection of galaxies and the estimate of their redshift distribution significantly vary from one study to another, introducing large differences on cluster masses. In addition, cluster masses can present a bias, for example introduced by the choice of a given value or range of value for the concentration parameter, in order to break the mass-concentration degeneracy. For large WL cluster surveys, masses thus differ systematically by 20-30% in comparing the masses of each cluster across the survey. However the different teams generally agree with each other regarding which cluster are more massive.

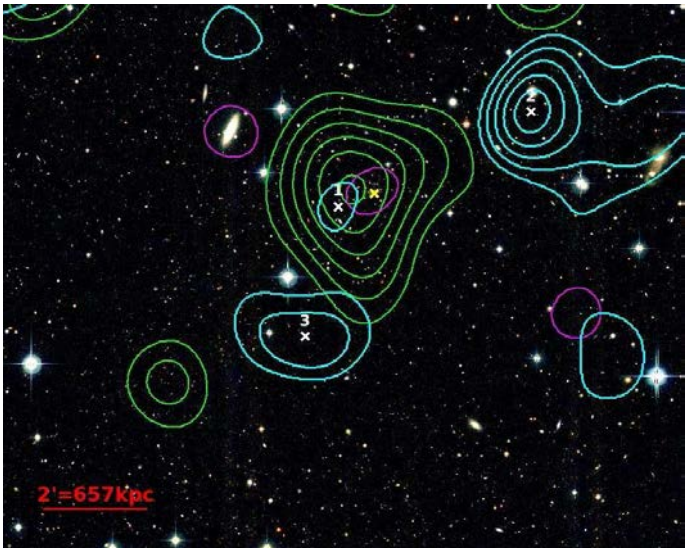

Fig. 5. Convergence density map for XDCS0329 overlaid on the 3-color CFHT/MegaCam image. Contour levels (cyan) are in signal-to-noise from $3\sigma_\kappa$ with steps of $1\sigma_\kappa$. Each weak lensing peak is noted as a white cross. The yellow cross indicates the position of the BCG. The X-ray contours starting at $2\sigma_X$ are in magenta and the light density contours starting at 3σ are in green. We expect 1.3 fake peaks above $3\sigma_\kappa$ and 0.2 above $4\sigma_\kappa$ in the displayed field (see Sect. 4.2 for details).

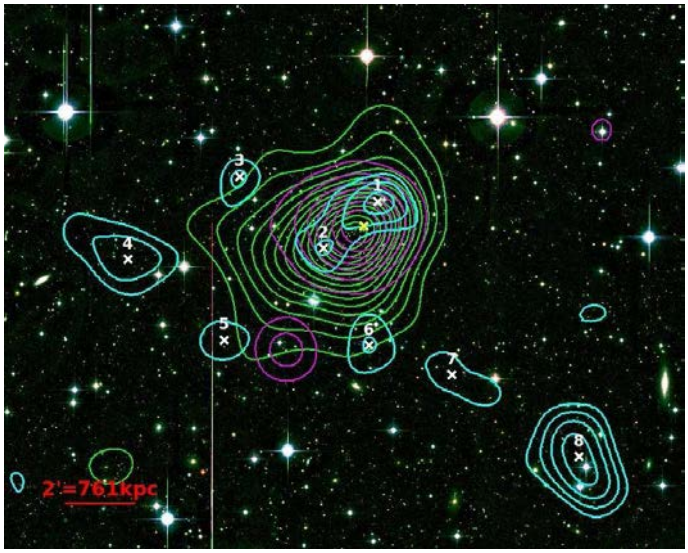

Fig. 6. Same as Fig 5 for MACSJ0454 on the 3-color CFHT/MegaCam image. We expect 3.0 fake peaks above $3\sigma_\kappa$ and 0.6 above $4\sigma_\kappa$ in the displayed field (see Sect. 4.2 for details).

XDCS0329, Fig. 5: XDCS0329 is barely detected, with a significance of only $2.8\sigma_\kappa$. It possesses a weak X-ray and optical counterpart. A larger structure is detected at the south with WL (3: $3.9\sigma_\kappa$) and could correspond to a structure at a different redshift from that of the cluster or to a fake peak but with a weak probability given its signal-to-noise. The most massive structure in this field lies north west of the cluster (2: $5.6\sigma_\kappa$), and does not present any X-ray or optical detection. In addition there are no known structure referenced at this position in NED, and its high significance detection cannot be reproduced by noise in the mass map reconstruction. A spectroscopic survey of the area would help determine the nature and redshift of this massive object. Finally, we note that XDCS0329 is a small cluster given its hydrodynamical mass of $M^X_{500} = (2.9 \pm 0.6) \times 10^{14} M_\odot$ found in Guennou et al. (2014). It is even sometimes considered as a group rather than a cluster (e.g., Mulchaey et al. 2006).

MACSJ0454, Fig. 6: MACSJ0454 has two substructures detected in WL: a first peak at $5.1\sigma_\kappa$, and a second at $4.2\sigma_\kappa$ defining a filamentary structure, as already reported in Kartaltepe et al. (2008). The X-ray and optical contours are centered between these two substructures, and elongated in their direction. The fact that this cluster is highly substructured can explain why the NFW fit fails. In addition, this cluster is probably of low mass as Zitrin et al. (2011) found a central mass of $M^{SL}_{500} = (0.41 \pm 0.03) \times 10^{14} M_\odot$ in their strong lensing analysis. We also detect several faint peaks. They are detected at levels of 4.4, 3.8, 4.2, and $4.0\sigma_\kappa$ for structures 4, 5, 6, and 7 respectively. While structures 5 and 6 might have an optical counterparts, structure 4 and 7 very likely correspond to fake peaks, or to a small group at a different redshift for structure 4. A larger structure is found at the south west (8 at $5.5\sigma_\kappa$), which is not at the cluster redshift, given that it is not detected through the galaxy density contours, but could also be due to a contamination from stars in its vicinity.

ABELL 851, Fig. 7: A851 is a massive cluster, detected at a high significance level ($7.6\sigma_\kappa$). It is highly sub-structured as already found in Guennou et al. (2014), and confirmed here by the presence of three spatially separated components: the dark matter, the X-ray gas, and the galaxies. The most important substructures are those noted 2 and 3, the first to the south with a $5\sigma_\kappa$ significance and the second to the north-east with a $4.3\sigma_\kappa$ significance. These structures are also detected on the galaxy density map and perhaps also in X-rays, the contours of which are extended towards the substructure directions. Finally, we note a fourth and a fifth structures, north-east and south-west of the cluster. These are quite far from the cluster, and while 5 has an optical counterpart, 4 does not, and could either be a fake peak or a group at a different redshift. The 5th structure should lie at the same redshift as the cluster. We note that other studies reported a higher mass than the one we derived for this cluster. We find $M^{NFW}_{500} = (3.7 \pm 1.2) \times 10^{14} M_\odot$ while Mahdavi et al. (2013) found $M_{500} = (10.5 \pm 2.5) \times 10^{14} M_\odot$ and Hoekstra et al. (2015) found $M^{NFW}_{500} = (12.5 \pm 3.0) \times 10^{14} M_\odot$. Finally, we note that the hydrodynamical masses from X-ray studies are lower: $M^X_{500} = (7.4 \pm 2.3) \times 10^{14} M_\odot$ from Mahdavi et al. (2013) and $M^X_{500} = (5.5 \pm 1.2) \times 10^{14} M_\odot$ in the present study.

LCDCS0829, Fig. 8: LCDCS0829 is at first view an isolated cluster, with an elongation to the north-west. It is detected with our three probes. However, at a larger scale there is another structure (3: $4.7\sigma_\kappa$) about 1.5-2 Mpc south-west from the cluster, that could be in interaction, and is detected both with WL and galaxy density. Farther away but still at the same redshift according to our galaxy density map lies a $4.5\sigma_\kappa$ structure (2) that could be a group connecting to the main cluster through a filamentary structure passing by 3, that remains to be detected. For this cluster we find a mass of $M^{NFW}_{500} = (5.2 \pm 1.9) \times 10^{14} M_\odot$, which is low compared to other WL analysis: $M_{500} = (9.3 \pm 2.9) \times 10^{14} M_\odot$ in Mahdavi et al. (2013), and $M^{NFW}_{500} = (17.7 \pm 2.2) \times 10^{14} M_\odot$ in Foëx et al.

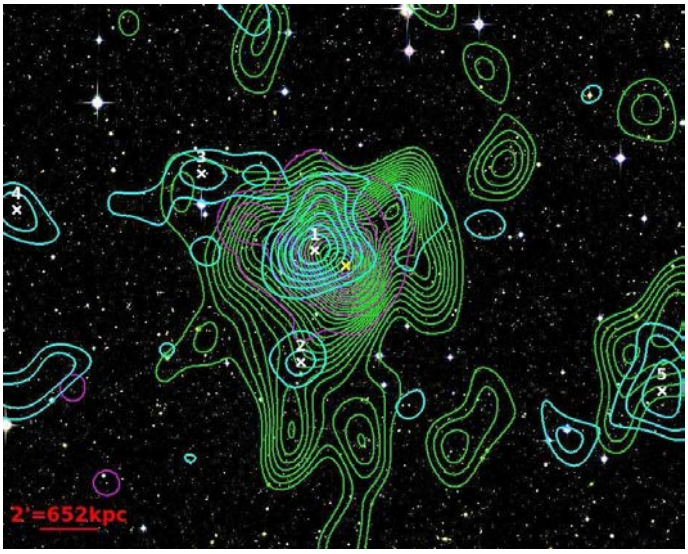

Fig. 7. Same as Fig 5 for A851 on the 3-color CFHT/MegaCam image. We expect 3.8 fake peaks above $3\sigma_\kappa$ and 0.6 above $4\sigma_\kappa$ in the displayed field (see Sect. 4.2 for details).

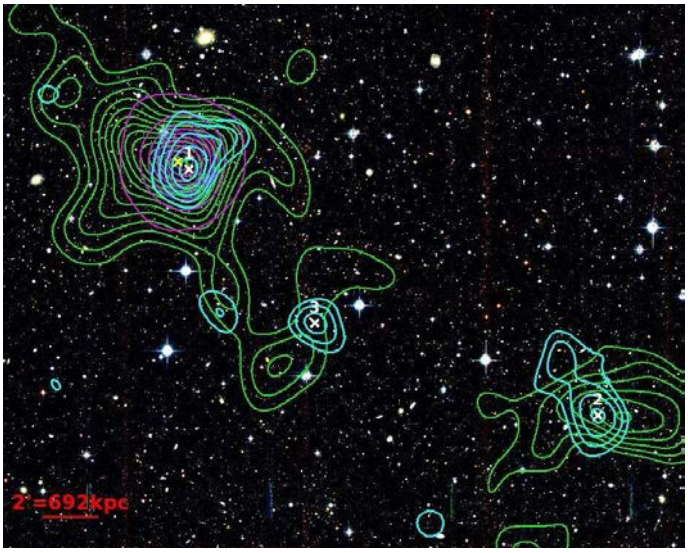

Fig. 8. Same as Fig 5 for LCDCS0829 on a 3-color CFHT/MegaCam image. We expect 4.6 fake peaks above $3\sigma_\kappa$ and 0.8 above $4\sigma_\kappa$ in the displayed field (see Sect. 4.2 for details).

(2012). We note that none of these three values agrees one with another, highlighting the fact that WL masses can significantly differ from one study to another.

MS1621, Fig. 9: This cluster is massive, and highly substructured at large scales. The main cluster is detected at $8.3\sigma_\kappa$, and is also seen on the X-ray and galaxy density maps. It is elongated towards structures 2 and 3 detected at 4.3 and $3.5\sigma_\kappa$, with also an elongation in the X-ray and galaxy density contours. Finally, the galaxy density contours show a structure south-east of substructure 3 that could be a close group. We note that Foëx et al. (2012) found a mass of $M_{500}^{WL} = (8.5 \pm 1.5) \times 10^{14} M_\odot$, slightly higher than our value of $M_{500}^{NFW} = (6.1 \pm 1.4) \times 10^{14} M_\odot$, but in worse agreement with the hydrodynamical mass inferred

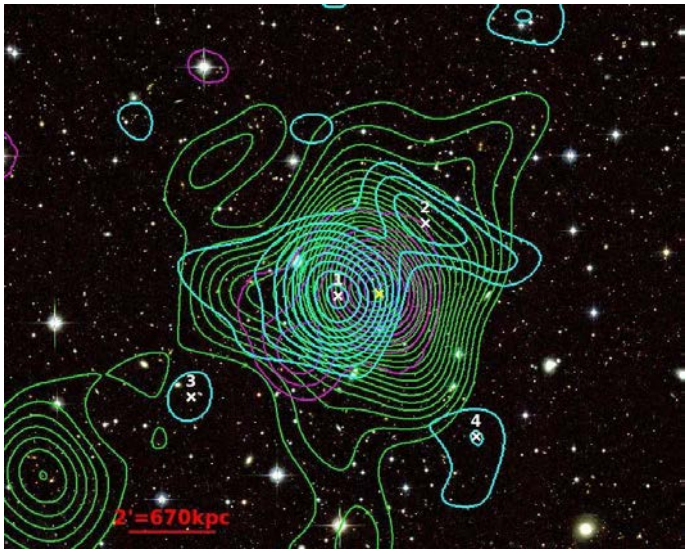

Fig. 9. Same as Fig 5 for MS1621 on the 3-color CFHT/MegaCam image. We expect 2.0 fake peaks above $3\sigma_\kappa$ and 0.4 above $4\sigma_\kappa$ in the displayed field (see Sect. 4.2 for details).

from X-rays: $M_{500}^{X} = (4.5 \pm 0.5) \times 10^{14} M_\odot$.

OC02, Fig. 10: OCO2 is detected with the three probes, with a $4.7\sigma_\kappa$ from WL. It seems to be merging with a smaller group on the south, detected at $4.2\sigma_\kappa$ (3). Finally, we note a massive structure detected at $5.8\sigma_\kappa$, with an X-ray counterpart and only a faint optical counterpart. This means it is a group or cluster, at a different redshift from OC02. By checking on NED, we find that structure 2 corresponds in fact to Abell 2246, a foreground cluster at $z = 0.225$. Finally, OC02, also known as CL1701+6414 is a low mass cluster. We find a mass of $M_{500}^{NFW} = (2.4 \pm 1.1) \times 10^{14} M_\odot$, slightly higher than Israel et al. (2014), who found a WL mass of $M_{500}^{WL} = 0.32 \times 10^{14} M_\odot$ or $M_{500}^{WL} = 1.37 \times 10^{14} M_\odot$ depending on the chosen concentration parameter. We also investigate the bias in the mass estimate from OC02's shear profile due to the presence of the foreground cluster A2246. To do this, we first compute the expected shear profile for the foreground cluster, using an X-ray derived total mass from Wang & Walker (2014): $M_{200}^{X} = (3.3 \pm 0.6) \times 10^{14} M_\odot$, and assuming a concentration parameter of $c_{200} = 3.5$. We note that X-ray derived masses should not be biased by the proximity of both clusters as they are derived in a much smaller region than the WL. We then subtract this expected shear contribution to every galaxy in the field and compute again the mass of OC02 by fitting an NFW profile to its new shear profile. We find a new mass which is 7% lower than the value from Table 3. We conclude that the presence of the foreground cluster only weakly affects the cluster mass estimate in this case, and do not correct for it as it is low compared to the other sources of error, and to avoid biasing our sample in applying a different method to one of our cluster.

NEP200, Fig. 11: NEP200 is detected both in X-rays and WL, with a detection significance of $5.1\sigma_\kappa$. It seems to be merging with a companion on the west (2: $4.6\sigma_\kappa$), but this might also be a projection effect. Spectroscopic redshifts would be needed to confirm this hypothesis. We also note several peaks at $\sim 3\sigma_\kappa$ which could correspond to fake peaks or faint structures at different redshifts. As this cluster has not been widely studied

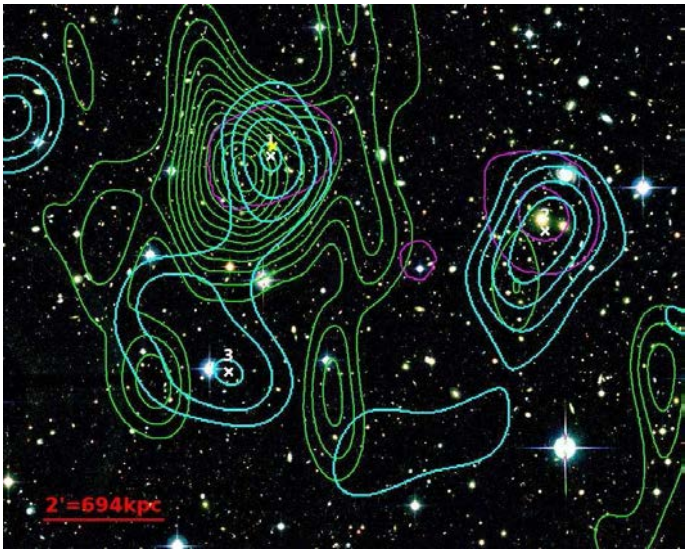

Fig. 10. Same as Fig 5 for OC02 on the 3-color CFHT/MegaCam image. We expect 1.0 fake peaks above $3\sigma_\kappa$ and 0.2 above $4\sigma_\kappa$ in the displayed field (see Sect. 4.2 for details).

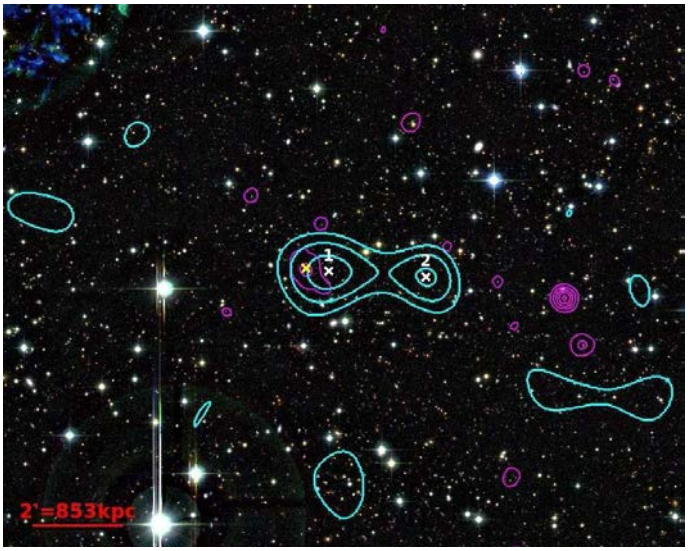

Fig. 11. Same as Fig 5 for NEP200 on the 3-color CFHT/MegaCam image. We expect 1.6 fake peaks above $3\sigma_\kappa$ and 0.3 above $4\sigma_\kappa$ in the displayed field (see Sect. 4.2 for details).

yet, we derive a first WL mass of $M_{500}^{NFW} = (10.0 \pm 4.1) \times 10^{14} M_\odot$ for NEP200.

RXJ2328, Fig. 12: This cluster is detected at $5.5\sigma_\kappa$ from WL, and also has X-ray and optical counterparts. From the WL contours, it seems to be merging with an infalling group detected at $3.9\sigma_\kappa$ in the south. However, this structure is not detected in X-rays or in the galaxy density map, suggesting that it is at a different redshift, and therefore not in interaction with RXJ2328. Note the presence of the Pegasus dwarf galaxy in the south that has been masked in our analysis, but could still bias our measurements. We find a WL mass of $M_{500}^{NFW} = (3.9 \pm 1.7) \times 10^{14} M_\odot$.

CLJ0152, Fig. 13: This cluster is highly sub-structured and has several neighboring groups nearby, implying a complex recent merging history (e.g., Massardi et al. 2010). The cluster

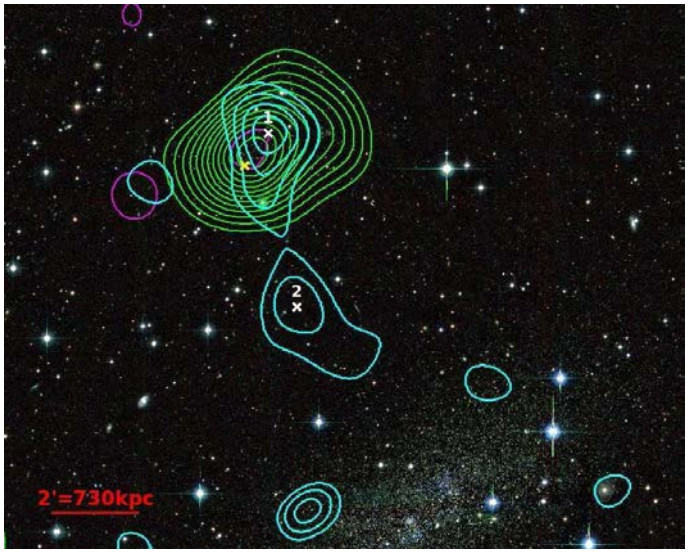

Fig. 12. Same as Fig 5 for RXJ2328 on the 3-color CFHT/MegaCam image. We expect 1.8 fake peaks above $3\sigma_\kappa$ and 0.3 above $4\sigma_\kappa$ in the displayed field (see Sect. 4.2 for details).

is massive ($M_{500}^{NFW} = (9.4 \pm 2.9) \times 10^{14} M_\odot$) and rather elongated in a north-south direction (see structure 2 detected at $6.4\sigma_\kappa$) and in a lesser extent in the east-west direction. Several structures are also detected in the south, and are aligned horizontally: 3 ($4.8\sigma_\kappa$), 4 ($6.6\sigma_\kappa$), 5 ($4.7\sigma_\kappa$), and 6. Structures 3 and 4, and also maybe 5, are detected in X-rays, while 4 and 6 have optical counterparts. Structures detected in WL and X-rays have a high probability to be groups, while those detected through the galaxy density maps should be around the same redshift as CLJ0152. Given the extension of the galaxy density map compared to that of the main cluster, structure 3 is probably a foreground group. One possible explanation is that the cluster recently underwent a merging event with the group 4 that passed through CLJ0152 from the north-west to the south-east. Structure 2 would be a remnant of this merging, while 3 should not have taken part in that scenario. Also structure 6 could have been created in the same event or being now interacting with structure 4. An X-ray temperature map would be valuable to check the direction of the past merger events.

MACSJ0717, Fig. 14: MACSJ0717 is famous for being one of the most massive clusters, as can be seen from its WL contours, which reach a significance of $10.9\sigma_\kappa$. We note also that it is strongly elongated towards a south east structure noted 2 with a $8.2\sigma_\kappa$ significance, and also detected in Kartaltepe et al. (2008). Both structures are also detected from the optical density map, suggesting that they are at the same redshift, but only the main cluster is strongly emitting in X-rays. Structure 2 is thus poor in hot gas, which makes us think that it corresponds to a filament rather than a group which would have produced more hot gas in its formation. The absence of a BCG agrees with this idea. Structure 3 could also be a continuation of this filament. Note that this filament has first been studied by Jauzac et al. (2012) from composite HST data, and later by Medezinski et al. (2013). We compared our WL contours with those from Jauzac et al. (2012), and found good agreement. Concerning the mass of the cluster, Zitrin et al. (2011) and Limousin et al. (2012) found strong lensing masses of respectively $M_{r<350kpc}^{SL} = (7.4 \pm 0.5) \times 10^{14} M_\odot$

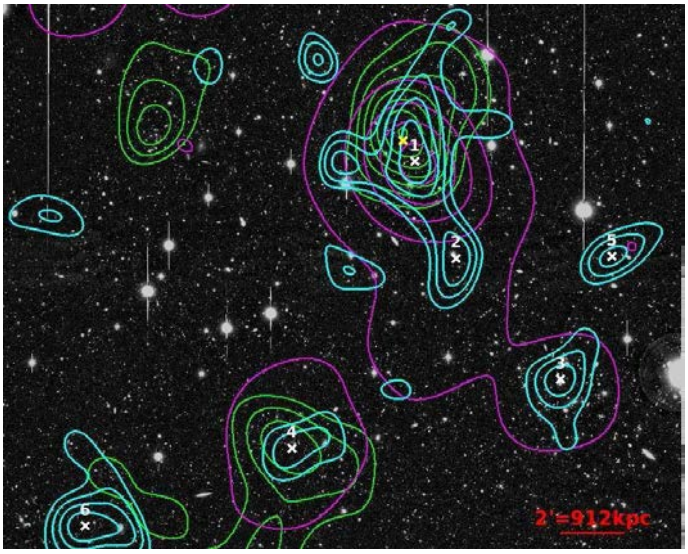

Fig. 13. Same as Fig 5 for CLJ0152 on the r band Subaru/Suprime-Cam image. We expect 4.4 fake peaks above $3\sigma_\kappa$ and 1.1 above $4\sigma_\kappa$ in the displayed field (see Sect. 4.2 for details).

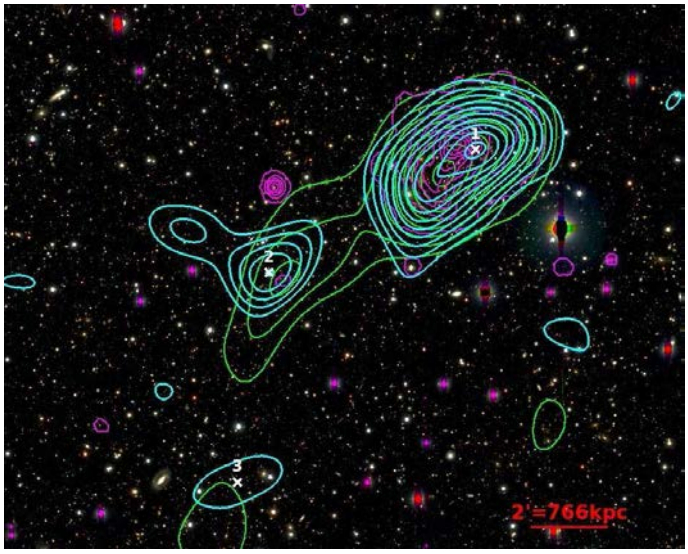

Fig. 14. Same as Fig 5 for MACSJ0717 on the 3-color Subaru/Suprime-Cam image. We expect 1.6 fake peaks above $3\sigma_\kappa$ and 0.3 above $4\sigma_\kappa$ in the displayed field (see Sect. 4.2 for details).

and $M^{SL}_{r<960kpc} = (21.1 \pm 2.3) \times 10^{14} M_\odot$. From WL, various masses have been calculated in different radii. In r_{500}, we have a mass of $M^{WL}_{500} = (11.7 \pm 2.9) \times 10^{14} M_\odot$ to be compared to Mahdavi et al. (2013) and Hoekstra et al. (2015) who respectively found $M^{WL}_{500} = (16.6 \pm 3.4) \times 10^{14} M_\odot$ and $M^{WL}_{500} = (22.3 \pm 5.2) \times 10^{14} M_\odot$. The first estimate agrees with ours within the error bars, but the second is much larger. In a radius of 0.5 Mpc, we have $M^{WL}_{r<0.5Mpc} = (3.7 \pm 0.9) \times 10^{14} M_\odot$, somewhat lower than Jauzac et al. (2012) who found a mass of $M^{WL}_{r<0.5Mpc} = (10.4 \pm 0.8) \times 10^{14} M_\odot$. However we find a good agreement with masses from the CLASH collaboration WL follow up (Medezinski et al. 2013) who found $M^{WL}_{r<0.5Mpc} = (5.4 \pm 1.2) \times 10^{14} M_\odot$. Applegate et al. (2014) also found higher masses within 1.5 Mpc, with $M^{WL}_{r<1.5Mpc} = (25.3 \pm 4.2) \times 10^{14} M_\odot$ or $M^{WL}_{r<1.5Mpc} = (23.1 \pm 3.8) \times 10^{14} M_\odot$, in the first case using the full distribution of photometric redshifts of the background galaxies and in the second the standard color-color cut, while we have $M^{WL}_{r<1.5Mpc} = (13.1 \pm 3.3) \times 10^{14} M_\odot$. We see that the mass estimates vary strongly for this cluster; we tend to find a lower value, but in any study (including ours) MACSJ0717 appears to be one of the most massive cluster.

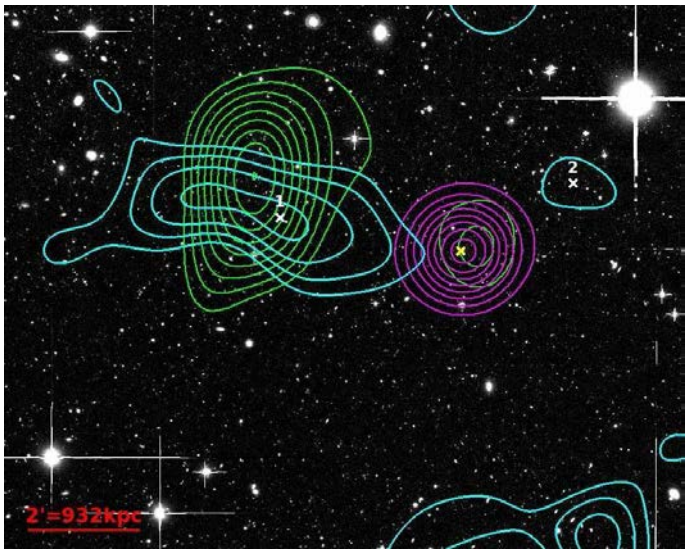

Fig. 15. Same as Fig 5 for BMW1226 on the r-band Subaru/Suprime-Cam image. We expect 1.0 fake peaks above $3\sigma_\kappa$ and 0.1 above $4\sigma_\kappa$ in the displayed field (see Sect. 4.2 for details).

BMW1226, Fig. 15: This cluster is not detected through WL, probably due to its high redshift: $z = 0.89$ which decreases the number of background galaxies usable for the WL reconstruction. However a large elongated structure (1) is detected, and could be a filament linked to BMW1226. It is detected at $5.6\sigma_\kappa$ and has an optical counterpart, such that is should not be too far from the cluster redshift. The small structure (2) west of the cluster is not very significant ($2.9\sigma_\kappa$) and is probably due to the noise in the convergence map reconstruction. This cluster has been studied by Jee & Tyson (2009) under its other name: CLJ1226+3332. Using deep HST data, they manage to have a sufficient number of background galaxies to reconstruct the WL map around the cluster. However, the small field of view of the ACS camera does not allow them to study the filamentary structure that we see east of the cluster.

MACSJ1423, Fig. 16: MACSJ1423 looks rather isolated on small scales, with a good alignment between the WL, X-ray, and optical centers. Kartaltepe et al. (2008) also classified it as a relaxed cluster according to its WL contours. A small structure is detected north-east from WL but not from the optical data and should correspond to a group at a different redshift. The X-ray data come from *Chandra* in this case, so structure 2 has no X-ray imaging. This cluster has been studied in strong lensing by Zitrin et al. (2011) and also by Limousin et al. (2010) who found a single central mass component, which agrees with our smooth contours. Applegate et al. (2014) also computed WL masses for this cluster finding values of $M^{WL}_{r<1.5Mpc} = (3.7 \pm 2.8) \times 10^{14} M_\odot$ or

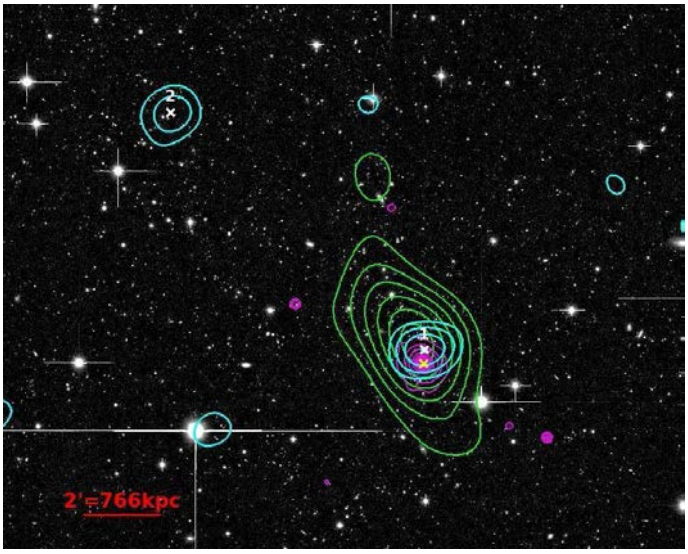

Fig. 16. Same as Fig 5 for MACSJ1423 on the i band Subaru/Suprime-Cam image. We expect 2.1 fake peaks above $3\sigma_\kappa$ and 0.3 above $4\sigma_\kappa$ in the displayed field (see Sect. 4.2 for details).

Fig. 17. Same as Fig 5 for MACSJ1621 on the 3-color Subaru/Suprime-Cam image. We expect 1.2 fake peaks above $3\sigma_\kappa$ and 0.2 above $4\sigma_\kappa$ in the displayed field (see Sect. 4.2 for details).

$M^{WL}_{r<1.5Mpc} = (8.8 \pm 3.6) \times 10^{14} M_\odot$, in the first case using the full distribution of photometric redshifts of the background galaxies and in the second the standard color-color cut. We note that our value of $M^{NFW}_{r<1.5Mpc} = (6.7 \pm 2.7) \times 10^{14} M_\odot$ is in good agreement with the one obtained with the color-color cut method (the one which we used).

MACSJ1621, Fig. 17: MACSJ1621 presents a large substructure (2: $5.9\sigma_\kappa$ significance) that could be an infalling group. Another structure (3) is detected south-east at more than $5\sigma_\kappa$, and could be embedded in a filament linking it to the cluster, as suggested by the galaxy light density map. Note that structure 3 is also detected by von der Linden et al. (2014). An X-ray counterpart is detected only for the cluster and not for structure 2, that has then good chance of being part of the filament rather than being an infalling group. The WL mass that we measure for this cluster agrees with the value of Applegate et al. (2014) within the error bars: we find $M^{NFW}_{r<1.5Mpc} = (5.8 \pm 1.9) \times 10^{14} M_\odot$ and they have $M^{WL}_{r<1.5Mpc} = (8.5 \pm 2.3) \times 10^{14} M_\odot$ or $M^{WL}_{r<1.5Mpc} = (8.8 \pm 2.2) \times 10^{14} M_\odot$ in the first case using the full distribution of photometric redshifts of the background galaxies and in the second the standard color-color cut. However, we do not reproduce the high mass found in Hoekstra et al. (2015): $M^{NFW}_{500} = (11.2 \pm 2.5) \times 10^{14} M_\odot$.

RXJ1716, Fig. 18: RXJ1716 (1: $7.3\sigma_\kappa$) shows a very elongated profile pointing towards two groups: 2 and 3 detected at respectively 4.9 and $5.4\sigma_\kappa$. However those structures are not detected in the galaxy density map and must then lie at a different redshift. The main cluster is also detected with the X-ray and galaxy density contours. The filamentary structure elongated to the north east of the cluster is also seen in the WL reconstruction of Clowe et al. (1998). This is a massive cluster with $M^{NFW}_{500} = (9.1 \pm 3.4) \times 10^{14} M_\odot$.

MS2053/CXOSEXSI2056, Fig. 19: MS2053 is detected with a high level of significance: $8.7\sigma_\kappa$ and with a mass of $M^{NFW}_{500} = (6.3 \pm 1.9) \times 10^{14} M_\odot$. It is also detected in the X-ray and galaxy density contours. CXOSEXSI2056 is a smaller cluster detected at a $4.4\sigma_\kappa$ significance, and also presents an X-ray counterpart. It seems to be merging with a wide structure (3: $4.5\sigma_\kappa$) on the east and might also be linked to the small structure 4 but the significance of the latter structure remains low ($3.2\sigma_\kappa$) and it is more likely a fake peak due to noise. For this field we did not try to estimate the masses of each cluster by removing the contribution from the other, as we did for OC02, because the significance of their detections are too different. CXOSEXSI has little chance to significantly affect the shear profile of MS2053, and on the contrary, removing such a big cluster as MS2053 would introduce an other large bias in the mass estimate of CXOSEXSI. In addition we did not compute any mass for this latter cluster.

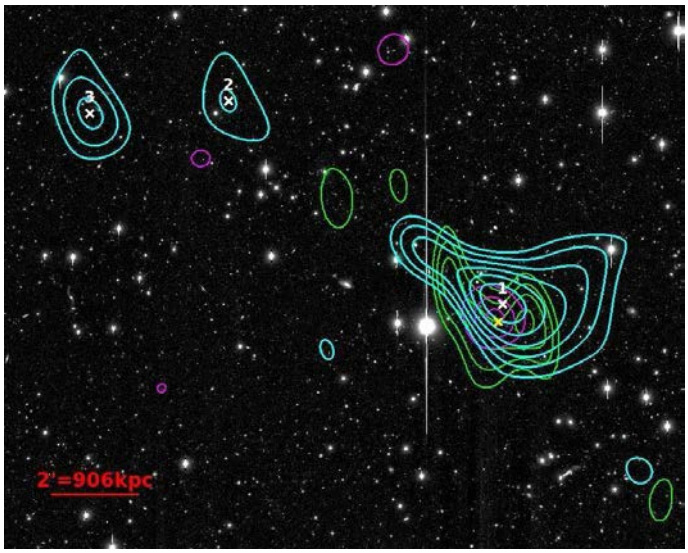

Fig. 18. Same as Fig 5 for RXJ1716 on the r-band Subaru/Suprime-Cam image. We expect 2.1 fake peaks above $3\sigma_\kappa$ and 0.5 above $4\sigma_\kappa$ in the displayed field (see Sect. 4.2 for details).

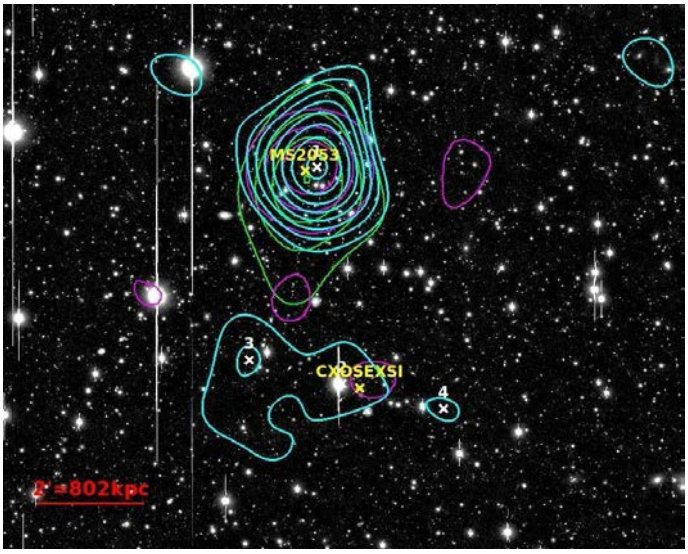

Fig. 19. Same as Fig 5 for MS2053 and CXOSEXSI2056 on the r-band Subaru/Suprime-Cam image. We expect 1.3 fake peaks above $3\sigma_\kappa$ and 0.2 above $4\sigma_\kappa$ in the displayed field (see Sect. 4.2 for details).

6.2. General discussion

We summarize the structure detection in Table 4, where we show the average significance of the WL detection obtained from 100 realizations of the noise along with the percentage of realizations in which the structures are detected at more than 3σ above the map noise defined in eq. 5. We also indicate for each structure if it has X-ray and optical counterparts, and conclude on the current status of the cluster and the possible presence of filaments.

The first conclusion from the study of this sample is that all the clusters appear very different, especially when considering their close environment. Several hypotheses made for the mass calculation are then questionable. Most of these clusters are not spherical, and present either a preferential direction, or several substructures. The NFW profile used in Sect. 4.3 seems simplistic compared to these results, and it appears very difficult to find a mass profile that fits every cluster, when extending to radii higher than the cluster core.

Despite these very different behaviors, we try to classify our sample according to the smoothness of their WL contours and the presence of substructures or infalling groups:

(1) The only relaxed cluster of our sample is MACSJ1423. On small scales we see smooth symmetrical contours and no substructures. However, even for this cluster, we find that it might be embedded in at least one filamentary structure at larger scales.

(2) The second category gathers clusters which are highly asymmetrical but do not present any clear substructure or infalling group: LCDCS0829, RXJ1716, and MS2053. These clusters are probably recovering from old merger events, the direction of interaction of which only remains visible.

(3) The last category encompasses clusters with high levels of substructuring or apparent merging events. These clusters are recovering from a recent merging event or even are presently merging. Such behaviors are observed for MACSJ0454, A851, MS1621, OC02, NEP200, RXJ2328, CLJ0152, MACSJ0717, MACSJ1621, and CXOSEXSIJ2056.

Six clusters among this last list seem to be part of particularly intense extended filamentary structures: MACSJ0454, A851, MS1621, CLJ0152, MACSJ0717, and MACSJ1621. In addition, BMW1226 shows a large filament despite the fact that the cluster is not detected itself. However, fainter filamentary structures linking the different mass peaks can be seen in many cases, suggesting that every cluster lies in a large scale structure. These LSSs are often not clearly detected, as they are too diffuse compared to the mass peaks corresponding to either infalling groups, or small merger events. Finally, we note that most of our clusters are either past mergers ($\sim$ 21.5%) or recent or present mergers ($\sim$ 71.5%). This supports the standard hierarchical scenario in which clusters grow through the merging of smaller structures. In addition, it means that most massive clusters at $0.4 < z < 0.9$ are still evolving through this merging process. XDCS0329 is not discussed as it is only weakly detected. This classification is summarized in Table 4.

7. Conclusion

We accurately measured galaxy shears for eight CFHT/MegaCam and seven Subaru/Suprime-Cam images. We successfully estimated the mass of twelve clusters out of sixteen, by fitting their shear profiles with an NFW profile. Comparing with masses from X-ray data (*XMM*–Newton and *Chandra* observations), we found that our masses are generally higher than those from X-rays by about 22%, an expected result given that the X-ray masses rely on the hypothesis of hydrostatical equilibrium. However, our sample is small and we need higher statistics to compare both masses, and also to better compare to the WL literature.

We inverted the shear to obtain convergence maps, and overlaid the WL contours on images. We estimated the significance of each detected structure with a hundred realizations with a random ellipticity added to each galaxy. Comparing with X-ray contours and galaxy light density contours, we studied the environment of every cluster. We found that clusters are very different on large scales and doubt they can all be fitted with a simple NFW profile. We separated our sample between isolated relaxed clusters, asymmetrical clusters with no substructures and clusters which have a more complex environment. The second category corresponds to past mergers and the third one to recent or present mergers. Most of the sampled clusters are in the last two categories, providing strong observational support to the hierarchical growth scenario, and implying that clusters are still evolving through this process at $0.4 < z < 0.9$. Temperature maps from deep X-ray imaging could help characterize the different merging phases that we observe (see e.g. Durret et al. 2011, and references therein). Even in the isolated case, we found that clusters are embedded in complex large scale structures, often connecting to another group on megaparsec scales. We report possible filament detections in CLJ0152, MACSJ0454, MACSJ0717, A851, BMW1226, MS1621, and MACSJ1621, the first one also experiencing recent complex merger events. Finally, it is important to note that the distinction between a filament and an infalling group or small cluster is almost a semantic problem. However, groups and small clusters should contain more X-ray gas than filaments, and are more likely to possess a BCG, at least in the case of clusters. A more detailed study of each cluster with separate simulations is required to help distinguish between the two possibilities. We intend to study the galaxy populations of the proposed filaments in the framework of the DAFT/FADA survey, a work that will also help discriminating the nature of these structures.

Acknowledgements. We thank Raphael Gavazzi and Hugo Capelato for useful discussion, and Mathilde Jauzac for sharing her WL contours of MACSJ0717

Table 4. Results on environment. The first eight clusters are observed with CFHT/MegaCam and the last eight with Subaru/Suprime-Cam. The different columns correspond to #1: cluster ID, #2: cluster redshift, #3: structure ID, #4: significance of the WL peak in the 2D mass map in unit of σ_κ (see text for details), #5: percentage of re-detection above $3\sigma_\kappa$ over the hundred noise realizations, #6: detection of the structure in X-rays (Y for yes, N for no, ∼ when the detection is ambiguous, - for no data), #7: detection of the structure in galaxy density map (Y for yes, N for no, ∼ when the detection is ambiguous, - for no data), #8: derived status of the cluster from our analysis and possible presence of a large filament; numbers refer to the classification in the text.

Cluster	z	structure	σ_{2D}	detection percentage	X-ray	galaxies	Cluster status
XDCS0329	0.4122	1	2.8	44%	Y	Y	-
		2	5.6	96%	N	N	
		3	3.9	74%	N	∼	
MACSJ0454	0.5377	1	5.1	91%	Y	Y	recent or present merger (3) / filament
		2	4.2	76%	∼	∼	
		3	3.7	67%	N	∼	
		4	4.4	88%	N	Y	
		5	3.8	70%	N	N	
		6	4.2	82%	N	∼	
		7	4.0	78%	N	N	
		8	5.5	95%	N	N	
ABELL851	0.4069	1	7.6	100%	Y	Y	recent or present merger (3) / filament
		2	5.0	89%	∼	Y	
		3	4.3	81%	∼	∼	
		4	4.4	86%	N	N	
LCDCS0829	0.4510	1	5.5	98%	Y	Y	past merger (2)
		2	4.5	86%	-	Y	
		3	4.7	92%	-	Y	
MS1621	0.4260	1	8.3	100%	Y	Y	recent or present merger (3) / filament
		2	4.3	77%	∼	Y	
		3	3.5	67%	N	N	
		4	3.1	53%	N	N	
OC02	0.4530	1	4.7	88%	Y	Y	recent or present merger (3)
		2	5.8	98%	Y	N	foreground cluster (A2246)
		3	4.2	78%	N	∼	
NEP200	0.6909	1	5.1	93%	Y	∼	recent or present merger (3)
		2	4.6	84%	N	N	
RXJ2328	0.4970	1	5.5	93%	Y	Y	recent or present merger (3)
		2	3.9	73%	N	N	
CLJ0152	0.8310	1	8.3	100%	Y	Y	recent or present merger (3) / filament
		2	6.4	98%	Y	N	
		3	4.8	85%	Y	N	
		4	6.6	98%	Y	Y	
		5	4.7	89%	∼	N	
MACSJ0717	0.5458	1	10.9	100%	Y	Y	recent or present merger (3) / filament
		2	8.2	100%	∼	Y	
		3	5.7	98%	N	Y	
BMW1226	0.8900	0	-	-	Y	Y	- / filament
		1	5.6	97%	N	Y	
		2	2.9	46%	N	N	
MACSJ1423	0.5450	1	5.0	91%	Y	Y	Relaxed (1)
MACSJ1621	0.4650	1	6.8	97%	Y	Y	recent or present merger (3) / filament
		2	5.9	96%	N	Y	
RXJ1716	0.8130	1	7.3	98%	Y	Y	past merger (2)
		2	4.9	85%	N	N	
		3	5.4	86%	N	N	
MS2053*	0.5830	1	8.7	100%	Y	Y	past merger (2)
CXOSEXSI2056*	0.6002	2	4.4	84%	Y	N	recent or present merger (3)
		3	4.5	84%	N	N	
		4	3.2	55%	N	N	

*CXOSEXSI_J205617 and MS_2053.7-0449 are on the same image.

with us. We are grateful to the anonymous referee for his/her careful reading and comments that improved the quality of the manuscript. We thank Nick Kaiser for authorizing us to use the IMCAT software, Emmanuel Bertin for making his *astromatic* softwares publicly available, and Martin Kilbinger for his ATHENA software. DC acknowledges support from the National Science Foundation under Grant No. 1109576. FD acknowledges long-term support from CNES. IM acknowledges financial support from the Spanish Ministry of Economy and Competitiveness through the grant AYA2012-42227P.

References

Allen, S. W., Evrard, A. E., & Mantz, A. B. 2011, ARA&A, 49, 409
Applegate, D. E., von der Linden, A., Kelly, P. L., et al. 2014, MNRAS, 439, 48
Bahé, Y. M., McCarthy, I. G., & King, L. J. 2012, MNRAS, 421, 1073
Bartelmann, M. & Schneider, P. 2001, Phys. Rep., 340, 291
Battaglia, N., Bond, J. R., Pfrommer, C., & Sievers, J. L. 2013, ApJ, 777, 123
Becker, M. R. & Kravtsov, A. V. 2011, ApJ, 740, 25
Bertin, E. 2006, in Astronomical Society of the Pacific Conference Series, Vol.

3.3 Shear peaks

This section presents the results from Martinet et al. (2015, A&A in press): *Constraining cosmology with shear peak statistics: tomographic analysis*. The first subsection briefly summarizes the paper, its context, aims, methods, results, and conclusions. The detailed study can be read in the second subsection, where we display the article.

3.3.1 Summary

Context

Accurate shear measurements can be used to constrain the cosmological model of our Universe. Cosmic shear, i.e. the shear 2-point correlation function, is the standard cosmological probe for WL surveys. However, other statistical measures of shear maps incorporating higher order moments are possible, and they become increasingly attractive in light of the significant gain in signal-to-noise expected from the planned large WL surveys, such as *Euclid*. In particular the statistics of shear peaks, which trace the projected mass concentrations, is a promising cosmological probe. Dietrich & Hartlap (2010) showed that shear peaks contain complementary information than the standard cosmic shear.

The *Euclid* ESA space mission (Laureijs et al. 2011) is a weak lensing survey primarily designed to constrain the dark energy equation of state w. It will also reveal some important results about modified gravity, dark matter, and the initial density perturbations. The satellite will be launched in 2020, and will cover 15,000 square degrees of the sky in one visible and three infrared bands, with an expected average galaxy density of 30 galaxies per square arcmin.

Aims

We quantify the cosmological constraints attainable with shear peak statistics by a large-area survey similar to that expected from the *Euclid* mission, focusing on the density parameter, Ω_M, and on the power spectrum normalization, σ_8, for illustration.

Methods

We study peaks detected directly in shear maps, rather than convergence maps, an approach that has the advantage of working directly with the observable quantity, the galaxy ellipticity catalog. Using large numbers of numerical simulations to accurately predict the abundance of peaks and their covariance, we forecast the constraints attainable by the *Euclid* mission, on Ω_M and σ_8. This is done via a Fisher formalism where the observable is the distribution of peaks with respect to their detected signal-to-noise. Weak lensing maps are simulated with the SUNGLASS pipeline (Kiessling et al. 2011) for both the fiducial cosmology that allows to compute the covariance matrix, and the modified cosmologies used to calculate the derivative of the peak distribution with respect to cosmological parameters.

We also quantified the gain of a tomographic study over a simple 2D analysis, by slicing our galaxy sample in five redshift bins.

Results

We forecast conditional constraints of $(\delta_{\Omega_M}, \delta_{\sigma_8}) = (0.0012, 0.0018)$ without tomography, and $(0.0010, 0.0014)$ with tomography. This is in very good agreement with conditional constraints from other authors (Maturi et al. 2011; Hilbert et al. 2012; Marian et al. 2012, 2013).

In addition, our tomographic peak counting method improves the conditional (marginal) constraints by a factor 1.2 (2) over those from a two-dimensional (i.e., non-tomographic) peak-count analysis.

Finally, we find that peak statistics provide constraints comparable to those from cluster counts.

Conclusions

The peak counts, have the great advantage of not relying on any scaling relation that may prove difficult to establish to high accuracy. Together with the very good constraints found in the case of a *Euclid*-like survey, this makes shear peak statistics one of the best future cosmological probes. Even if the gain from a tomographic approach is weak for Ω_M and σ_8, it is worth investigating its effect on the measurement of the DE equation of state w.

3.3.2 Martinet et al. 2015b

A&A 581, A101 (2015)
DOI: 10.1051/0004-6361/201425164

Astronomy & Astrophysics

Constraining cosmology with shear peak statistics: tomographic analysis

Nicolas Martinet[1,3], James G. Bartlett[2,3], Alina Kiessling[3], and Barbara Sartoris[4,5]

[1] UPMC Universit Paris 06, UMR 7095, Institut d'Astrophysique de Paris, 98bis Bd Arago, 75014 Paris, France
e-mail: martinet@iap.fr
[2] APC, AstroParticule et Cosmologie, Universit Paris Diderot, CNRS/IN2P3, CEA/lrfu, Observatoire de Paris, Sorbonne Paris Cit , 10 rue Alice Domon et L onie Duquet, 75205 Paris Cedex 13, France
[3] Jet Propulsion Laboratory, California Institute of Technology, 4800 Oak Grove Drive, Pasadena, California, USA
[4] Dipartimento di Fisica, Sezione di Astronomia, Universit di Trieste, via Tiepolo 11, 34143 Trieste, Italy
[5] INAF/Osservatorio Astronomico di Trieste, via Tiepolo 11, 34143 Trieste, Italy

Received 16 October 2014 / Accepted 8 April 2015

ABSTRACT

The abundance of peaks in weak gravitational lensing maps is a potentially powerful cosmological tool, complementary to measurements of the shear power spectrum. We study peaks detected directly in shear maps, rather than convergence maps, an approach that has the advantage of working directly with the observable quantity, the galaxy ellipticity catalog. Using large numbers of numerical simulations to accurately predict the abundance of peaks and their covariance, we quantify the cosmological constraints attainable by a large-area survey similar to that expected from the *Euclid* mission, focusing on the density parameter, Ω_m, and on the power spectrum normalization, σ_8, for illustration. We present a tomographic peak counting method that improves the conditional (marginal) constraints by a factor of 1.2 (2) over those from a two-dimensional (i.e., non-tomographic) peak-count analysis. We find that peak statistics provide constraints an order of magnitude less accurate than those from the cluster sample in the ideal situation of a perfectly known observable-mass relation; however, when the scaling relation is not known a priori, the shear-peak constraints are twice as strong and orthogonal to the cluster constraints, highlighting the value of using both clusters and shear-peak statistics.

Key words. gravitational lensing: weak – cosmological parameters

1. Introduction

Weak gravitational lensing (WL) is a powerful probe of large-scale structure, dark matter, and dark energy (e.g., Bartelmann & Schneider 2001). In particular, cosmic shear surveys have demonstrated their ability to constrain cosmological parameters (e.g., Massey et al. 2007; Heymans et al. 2012), and the potential of large-area shear surveys covering thousands of square degrees to improve cosmological constraints to percent level accuracies is the prime motivation for ambitious programs like the ongoing Dark Energy Survey (DES)[1], and Stage IV experiments (Albrecht et al. 2006, 2009) like the Large Synoptic Survey Telescope[2] (LSST, LSST Science Collaboration et al. 2009), the Wide Field Infrared Survey Telescope (WFIRST)[3] (Spergel et al. 2013), and the *Euclid*[4] (Laureijs et al. 2011) missions.

The shear correlation function (equivalently, power spectrum), a measure of the second moment of the mass distribution, is the standard tool for analyzing WL surveys. Other statistical measures of shear maps incorporating higher order moments are possible, and they become increasingly attractive in light of the significant gain in signal-to-noise expected from the planned large WL surveys.

In this paper, we consider the statistics of peaks in a shear map (or shear catalog) as a cosmological probe. We define shear peaks by filtering the map with an aperture designed to detect localized projected mass concentrations, such as galaxy clusters. Indeed, WL surveys can be used to detect galaxy clusters, and the cluster counts then used as a cosmological probe (Kruse & Schneider 1999; Marian & Bernstein 2006). Projection effects, however, severely limit the purity of cluster samples defined through WL, despite attempts at constructing optimal filters, because many peaks result from the alignment of small systems along the line of sight (White et al. 2002; Hamana et al. 2004; Hennawi & Spergel 2005).

An alternative is to abandon the correspondence between shear peaks and clusters and simply use the statistics of peaks to characterize the projected mass distribution (Reblinsky et al. 1999). This is the approach we adopt in the present work. These general shear peaks do not necessarily have any meaning as physical objects, being a combination of real clusters and chance alignments. Their abundance, however, like clusters, is sensitive to the underlying cosmology (Jain & Van Waerbeke 2000; Wang et al. 2009; Dietrich & Hartlap 2010; Kratochvil et al. 2010).

One disadvantage of this approach is that we do not posses a simple analytic form for the abundance of peaks as a function of cosmological parameters. This is in contrast to the situation with clusters, where practical expressions do exist for the mass function that greatly facilitate the theoretical prediction of cluster abundance and exploration of parameter space

[1] http://www.darkenergysurvey.org
[2] http://www.lsst.org
[3] http://wfirst.gsfc.nasa.gov
[4] http://www.cosmos.esa.int/web/euclid

(Press & Schechter 1974; Jenkins et al. 2001; Tinker et al. 2008). We must instead resort to N-body simulations to predict WL peak abundance, and we require large suites of simulations to explore the parameter space.

Such studies have been undertaken by several authors in recent years (Dietrich & Hartlap 2010; Kratochvil et al. 2010; Yang et al. 2011; Hilbert et al. 2012; Marian et al. 2012, 2013). In this paper, we perform a Fisher analysis of the constraints from peak counts in the context of upcoming Stage IV dark energy surveys, comparing our results to constraints expected from cluster counts. We employ large suites of independent N-body simulations to mitigate what has been an important limitation of previous studies, and we work directly with shear measurements, rather than reconstructed convergence maps.

The SUNGLASS code (Kiessling et al. 2011) is a rapid simulation tool based on line-of-sight integration through N-body boxes to calculate the WL field. Its speed allows us to generate large numbers of simulated shear maps, and hence determine peak abundance as a function of cosmological parameters and its variance. In particular, we are able to accurately calculate the derivative of peak abundance with respect to the parameters needed for the Fisher matrix. It is important to note that while many previous works have employed N-body simulations for similar analyses, they have relied on statistically shifted maps generated from a limited number of simulations (e.g., Dietrich & Hartlap 2010; Kratochvil et al. 2010; Yang et al. 2011; Hilbert et al. 2012; Marian et al. 2012, 2013). By contrast, the maps in this work are truly independent, with each map generated from a separate N-body realization.

We work directly with ellipticity measurements, an unbiased estimator of the shear in the WL regime (e.g., Dietrich & Hartlap 2010; Maturi et al. 2011; Hamana et al. 2012; Hilbert et al. 2012), rather than convergence maps that have been used in several previous studies (e.g., Kratochvil et al. 2010; Yang et al. 2011; Marian et al. 2012, 2013). Convergence is not the direct observable, but must be reconstructed from shear measurements. Our approach avoids the complexity added by this inversion. In addition, the use of shear greatly simplifies the nature of map noise, which is non-trivial to estimate in the case of the reconstructed convergence.

Finally, we apply tomography to the peak statistics by dividing the lensed background galaxies into redshift bins. This offers a two-fold advantage; first it allows us to remove foreground galaxies ($z \leq 0.5$) that tend to dilute the shear signal, although the mass distribution below this redshift still contributes to the statistics measured using only the higher redshift galaxies. Second, we can detect shear peaks in different redshift planes and examine the statistics both within and between planes. As with the shear correlation function, the additional radial information significantly increases precision on cosmological constraints. Building on the work of Hennawi & Spergel (2005) and Dietrich & Hartlap (2010), we quantify the constraining power of tomographic shear peak statistics for Stage IV dark energy missions, such as *Euclid*.

We begin by describing our WL simulations in Sect. 2. The peak detection procedure and its application to the simulations are detailed in Sect. 3. In Sect. 4 we examine peak statistics and their use as a cosmological probe. Section 5 extends the approach to tomography. We conclude with a final discussion and comment on future directions in Sect. 6. Throughout the paper, for concreteness, we consider the specific case of a survey similar to that of the *Euclid* mission with a fiducial flat ΛCDM cosmology specified by $(\Omega_M, \Omega_\Lambda, \Omega_b, h, \sigma_8, n_S) = (0.272, 0.728, 0.0449, 0.71, 0.809, 1.000)$ (e.g., Hinshaw et al. 2013).

2. Weak lensing simulations

We employ the Fisher formalism to asses the cosmological constraints expected from peak counts in Stage IV dark energy experiments, taking as typical characteristics those of the *Euclid* (Laureijs et al. 2011) mission. *Euclid* will survey 15 000 deg^2 in three infrared bands (Y, J, and H) and a single, wide optical filter (combined riz bands), the latter with a point spread function (PSF) of 0.1 arcsec. The survey reaches a mean source galaxy density usable for lensing of 30 gals. arcmin^{-2} with a median redshift of $z = 0.8$, following the redshift distribution

$$P(z) = \frac{3}{2{z_0}^3} z^2 \mathrm{e}^{-\left(\frac{z}{z_0}\right)^{1.5}}, \quad (1)$$

with $z_0 = 0.7$.

Calculation of the Fisher matrix requires the derivative of the mean peak counts with respect to cosmological parameters, evaluated at the fiducial model. We also need the covariance of the peak counts about their mean in this model. Since we do not posses an analytical expression for the WL peak abundance, we must use simulations to calculate the expected peak counts. We need enough simulations to accurately determine the mean peak counts for each parameter variation and to determine their covariance in the fiducial model. This is non-trivial as much of the signal comes from non-linear scales in the mass distribution, which can only be properly modeled by N-body simulations.

Simulation speed is therefore essential. In our study we use the SUNGLASS pipeline developed by Kiessling et al. (2011). We give a brief description of the SUNGLASS pipeline here but for a full prescription of how the SUNGLASS WL shear and convergence catalogs are generated, see Kiessling et al. (2011). For a given set of parameters, SUNGLASS first generates an N-body realization with the GADGET-2 code Springel (2005). These simulations are performed with 512^3 paticles in a 512 h^{-1} Mpc box and the light cone is 100 square degrees and goes out to a redshift of $z = 2.0$. The convergence and shear of each mass point are calculated along the line of sight at multiple lensing source planes. This relies on the applicability of the Born approximation in the WL regime, i.e., that the mean path of the light bundle from a distant object remains adequately straight in the presence of lensing. The integration is much quicker than ray tracing through the simulation box, and allows the production of large suites of simulated WL observations. The shear and convergence is then interpolated on to the individual particles in the light cone, providing a highly sampled catalog of shear and convergence along the line of sight.

The speed of SUNGLASS enables us to produce many independent realizations, an improvement over previous studies that had to resort to shuffling the results from single realizations. The final WL catalogs are constructed by down-sampling the highly sampled SUNGLASS shear and convergence catalogs to 30 galaxies per square arc minute using the source galaxy redshift distribution of Eq. (1), and assuming that the galaxies trace the dark matter exactly. To model the shape noise arising from intrinsic galaxy ellipticity, we add a random ellipticity to each source galaxy in the simulated shear catalogs according to a Gaussian distribution with zero mean and standard deviation σ_ϵ. In practice, we use a Box-Muller Gaussian random number generator, drawing two uniform numbers (x, y) over the interval $(0, 1)$ to obtain two Gaussian random numbers (ϵ_1, ϵ_2)

that we add, respectively, to the shear components, γ_1 and γ_2:

$$\epsilon_1 = \frac{\sigma_\epsilon}{\sqrt{2}} \sqrt{-2\ln(x)} \cos(2\pi y) \quad (2)$$

$$\epsilon_2 = \frac{\sigma_\epsilon}{\sqrt{2}} \sqrt{-2\ln(x)} \sin(2\pi y). \quad (3)$$

Null values in the first step are replaced by arbitrarily chosen values.

This procedure corresponds to drawing a tangential ellipticity from a Gaussian of zero mean and dispersion σ_ϵ, which we take to be $\sigma_\epsilon = 0.3$ (e.g., Leauthaud et al. 2007). We note that the shear components, γ_1 and γ_2, are typically only a small percent of the noise, ϵ_1 and ϵ_2. Under the assumption that the noise is uncorrelated (i.e., in the absence of important intrinsic alignment effects), the mean ellipticity averaged over a number of source galaxies approaches the shear signal. We will discuss this fundamental hypothesis in Sect. 5.

3. Peak detection

3.1. Method

To identify peaks in a shear catalog, we employ aperture mass filtering (Schneider et al. 1998; Bartelmann & Schneider 2001) with an outer annulus to remove the integration constant, thereby resolving the finite space inversion problem. This technique does not return the true mass within the aperture, for example, when centered on a cluster; for that, one would have to know the true shape of the mass distribution as seen through the filter. By adopting a mass distribution, such as the NFW profile (Navarro et al. 1997), one can determine the true mass and also find clusters in WL surveys (e.g., Marian et al. 2012, 2013). Our goal, however, is not to measure the true mass of physical objects, but to compare the number of peaks expected in a WL survey for different cosmologies.

The aperture mass can be calculated either from the convergence field, κ, or the shear field, γ. In the former case, the aperture mass is calculated by integrating the convergence within the aperture centered at position $\boldsymbol{\theta}_0$ (a two-dimensional vector in the plane of the sky),

$$M_{\rm ap}(\boldsymbol{\theta}_0) = \int \mathrm{d}^2\theta\, U(|\boldsymbol{\theta} - \boldsymbol{\theta}_0|)\kappa(\boldsymbol{\theta}), \quad (4)$$

where U is a filter chosen to best fit the lens mass density profile.

In a WL survey, the observable is actually the source galaxy ellipticity, ϵ. It is related to the reduced shear, g, by

$$\langle\epsilon\rangle = g = \frac{\gamma}{1-\kappa} \approx \gamma, \quad (5)$$

which tends to the shear, γ, in the weak lensing regime where $(\kappa, \gamma) \ll (1, 1)$. The indicated average is over random orientations of intrinsic galaxy ellipticity. A WL survey thus directly measures shear, γ, rather than the convergence. Working directly with the observable quantity, γ, we avoid the non-trivial step of integrating the shear to obtain the convergence field, which is a derived quantity.

Shear and convergence are two mathematically distinct, although related, quantities, the first being a spinor of spin two and the second a scalar on the sphere. To adapt the expression for the aperture mass to the case of shear, we first define the scalar tangential shear, γ_t, for a galaxy image that accounts for both components of the shear (γ_1 and γ_2),

$$\gamma_{\rm t}(\boldsymbol{\theta}, \boldsymbol{\theta}_0) = -\left[\gamma_1(\boldsymbol{\theta})\cos 2\phi(\boldsymbol{\theta}, \boldsymbol{\theta}_0) + \gamma_2(\boldsymbol{\theta})\sin 2\phi(\boldsymbol{\theta}, \boldsymbol{\theta}_0)\right], \quad (6)$$

where ϕ is the angle giving the position of the galaxy image ($\boldsymbol{\theta}$) relative to an arbitrary fixed axis running through the center of the aperture, at position $\boldsymbol{\theta}_0$, in the image plane; this fixed axis defines a local cartesian coordinate system in the plane of the sky with origin positioned on the filter center. The aperture mass equation can then be rewritten in terms of the tangential shear and the new filter function Q:

$$Q(|\boldsymbol{\theta}|) = \frac{2}{\theta^2}\int_0^\theta \mathrm{d}^2\theta'\,\theta'\;U(|\boldsymbol{\theta}'|) - U(|\boldsymbol{\theta}|), \quad (7)$$

$$M_{\rm ap}(\boldsymbol{\theta}_0) = \int \mathrm{d}^2\theta\; Q(|\boldsymbol{\theta} - \boldsymbol{\theta_0}|)\gamma_{\rm t}(\boldsymbol{\theta}, \boldsymbol{\theta}_0). \quad (8)$$

The convergence has been used in several previous weak lensing peak studies (e.g., Kratochvil et al. 2010, Yang et al. 2011, Marian et al. 2012, 2013), although recent studies increasingly work directly with the shear (e.g., Dietrich & Hartlap 2010; Maturi et al. 2011; Hamana et al. 2012; Hilbert et al. 2012), which is also the approach adopted in this paper.

We use the following weight functions, U for convergence and Q for shear, appropriate for a circular aperture (see Bartelmann & Schneider 2001):

$$U(\theta) = \begin{cases} \frac{1}{\pi\theta_1^2} & \text{if } 0 < \theta < \theta_1 \\ \frac{1}{\pi(\theta_2^2-\theta_1^2)} & \text{if } \theta_1 < \theta < \theta_2 \\ 0 & \text{elsewhere} \end{cases} \quad (9)$$

$$Q(\theta) = \begin{cases} \frac{\theta_2^2}{\pi(\theta_2^2-\theta_1^2)\theta^2} & \text{if } \theta_1 < \theta < \theta_2 \\ 0 & \text{elsewhere.} \end{cases} \quad (10)$$

In practice, the integral over the aperture weight function becomes a sum weighted by the number density of galaxy images, n,

$$M_{\rm ap}(\boldsymbol{\theta}_0) = \frac{1}{n}\sum_i U(|\boldsymbol{\theta}_i - \boldsymbol{\theta}_0|)\kappa(\boldsymbol{\theta}_i) \quad (11)$$

$$M_{\rm ap}(\boldsymbol{\theta}_0) = \frac{1}{n}\sum_i Q(|\boldsymbol{\theta}_i - \boldsymbol{\theta}_0|)\gamma_{\rm t}(\boldsymbol{\theta}_i, \boldsymbol{\theta}_0), \quad (12)$$

where $\gamma_{\rm t}(\boldsymbol{\theta}_i, \boldsymbol{\theta}_0)$ and $\kappa(\boldsymbol{\theta}_i)$ are the tangential shear and the convergence of the image at $\boldsymbol{\theta}_i$ relative to the point θ_0.

By expressing the equations in terms of discrete sums, we explicitly account for the sampling inherent in the observations, i.e., we only measure the shear where there is a source galaxy. Moreover, we use the actual number density of galaxies in the aperture, rather than a fixed, average value. The link from simulations to observations is trivial, as it is sufficient to replace the tangential shear, $\gamma_{\rm t}$, in the last equation by the tangential component of the ellipticity, $\epsilon_{\rm t}$. This is the principal interest of using shear instead of convergence.

The aperture mass is convenient because in the case of the shear, it permits simple calculation of its variance due to the intrinsic ellipticity of the source galaxies, σ_ϵ:

$$\sigma(M_{\rm ap}) = \frac{\sigma_\epsilon}{\sqrt{2}n}\left(\sum_i Q^2(|\boldsymbol{\theta}_i - \boldsymbol{\theta}_0|)\right)^{1/2}. \quad (13)$$

This allows us to define a local noise level and peak detection threshold, which is another strong argument in favor of using shear peaks rather than convergence. We then define peak amplitude as

$$\Gamma(\boldsymbol{\theta}_0) = \frac{M_{\rm ap}}{\sigma(M_{\rm ap})} = \frac{\sum_i Q(|\boldsymbol{\theta}_i - \boldsymbol{\theta}_0|)\gamma_t(\boldsymbol{\theta}_i, \boldsymbol{\theta}_0)}{\frac{\sigma_\epsilon}{\sqrt{2}}(\sum_i Q^2(|\boldsymbol{\theta}_i - \boldsymbol{\theta}_0|))^{1/2}}. \quad (14)$$

The amplitude of a peak is independent of the normalization of the weight function, but does depend on the number of galaxies in the aperture through both the sums in numerator and denominator. Peak amplitude thus varies as the square root of the number of galaxies in the aperture. Intrinsic galaxy ellipticity also affects the signal-to-noise value, although it does not change the relative intensity of the peaks. As mentioned, we take $\sigma_\epsilon = 0.3$ (Leauthaud et al. 2007).

A critical point is the size and shape of the aperture. The chosen shape will preferentially select a specific form of structure, such as clusters or filaments, while the size will favor one cluster size over others. We must also adapt the aperture to include enough galaxies to optimize the signal-to-noise over the random shape noise (this point will be discussed in the section on tomography).

For simplicity, we adopt a radially symmetric aperture of fixed angular radius. The inner radius is set to $\theta_1 = 3.5'$, corresponding to the typical size of a cluster at redshift $z = 0.3$, where the contribution to shear peaks is the most important (Dietrich & Hartlap 2010), to exclude any contamination by cluster galaxies and the strong lensing regime, while the outer radius is set to $\theta_2 = 10'$, which is roughly the limit of the lensing effect at this redshift (see Hamana et al. 2012). In practice, we have found that the mass inside a given aperture strongly depends on the inner radius. In a future work, we plan to use a set of aperture sizes to extract information from different scales. One could also use an adaptive matched filter to preferentially select galaxy clusters (e.g., Marian et al. 2012). This is not our goal in this first study, and we leave the identification of an optimal filter to a future work. Finally, peaks are selected to be larger than all their neighbors in a radius equal to that of the aperture. Peaks situated at less than θ_2 from the map edges are discarded as they are not computed in the proper aperture.

4. Peak statistics

We first present our statistical methodology and results from a non-tomographic analysis of the peak counts. Section 5 then extends the analysis to tomographic peak counts.

4.1. Method

We implemented two statistical measures: a χ^2 test and the Fisher information matrix, both defined over bins of peak height. We chose our bins to include the same number of peaks based on the mean peak counts in our fiducial cosmology. This bin size is then maintained for the other cosmologies. Bin widths are given in Table 1, along with the number of peaks for one fiducial realization.

Let $N_{i,r}$ be the number of peaks in bin i of realization r for a given cosmology, and R be the total number of realizations of this cosmology. Defining $\langle N\rangle_i$ as the mean number of peaks in bin i, averaged over all R realizations, we calculate the covariance matrix of the binned peak counts as

$$C_{i,j} = \begin{cases} \frac{1}{R-2}\sum_r^R (N_{i,r} - \langle N\rangle_i)(N_{j,r} - \langle N\rangle_j) \text{ if } i \neq j \\ \frac{1}{R-1}\sum_r^R (N_{i,r} - \langle N\rangle_i)(N_{j,r} - \langle N\rangle_j) \text{ if } i = j, \end{cases} \quad (15)$$

using $R = 150$ independent realizations of the fiducial cosmology. Each of these realizations corresponds to a lightcone of 100 deg^2, and we subsequently normalize the covariance matrix to an area of 15 000 deg^2 (e.g., the useable extragalactic sky and *Euclid* target). Figure 1 shows the correlation matrix, i.e., the covariance matrix normalized to unity along the diagonal. We see that the correlation between bins is less than 20% except for the higher signal-to-noise bins where it can reach up to 40%. It seems reasonable that the stronger peaks would be more correlated between bins, with signal being dominated and seen by successive source planes, while the lower signal-to-noise peaks would be more affected by noise variations and projections between source planes. This agrees with the fact that high signal-to-noise peaks mostly correspond to galaxy clusters, while low signal-to-noise peaks are dominated by projections of large-scale structure and noise, as shown by Maturi et al. (2011).

Table 1. Bin widths and peak counts for one fiducial realization.

Bin number	Bin size	N
1	3.0	70
2	3.2	72
3	3.4	65
4	3.5	67
5	3.7	72
6	3.9	74
7	4.2	69
8	4.5	77
9	5.0	66
10	5.7	90

Notes. The second column gives the lower bound on the peak signal-to-noise for each bin and the third the total number of peaks in the bin; for example, the first line reads: in bin 1 there are 70 peaks with signal-to-noise between 3.0 and 3.2.

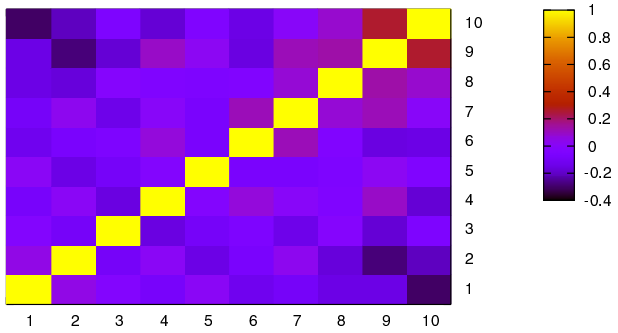

Fig. 1. Correlation matrix of the shear peak distribution for a 100 square-degree field, calculated by averaging over 150 realizations of the fiducial cosmology (see Eq. (15)). This is the covariance matrix normalized to unit diagonal. The x and y-axis values are the peak height bin numbers, defined in Table 1.

This covariance matrix is then used to compute either the χ^2 (Eq. (16)) or the Fisher matrix (Eq. (17)). The χ^2 is expressed as

$$\chi^2(r, f') = \sum_{i,j} (N^{f'}_{i,r} - \langle N^f\rangle_i)(C^f_{i,j})^{-1}(N^{f'}_{j,r} - \langle N^f\rangle_j), \quad (16)$$

where f represents the fiducial cosmology and f' a reference cosmology. We note that f' can be the same as f if we wish to compare one realization of a cosmology to all the other realizations of the same cosmology. This allows us, in particular, to test whether the χ^2 variable is actually distributed according to a χ^2-distribution. The Fisher matrix is given by

$$F_{p_\mathrm{a},p_\mathrm{b}} = \sum_{i,j} \frac{\partial\langle N\rangle_i}{\partial p_\mathrm{a}} \widehat{(C^f_{i,j})^{-1}} \frac{\partial\langle N\rangle_j}{\partial p_\mathrm{b}}, \quad (17)$$

where p_a and p_b are two cosmological parameters. We note that this expression is easily interpretable only in the case of

Gaussian distributed bin counts, i.e., as the number of peaks becomes large. Cosmological parameter constraints are then obtained by inverting the Fisher matrix,

$$C_{p_a,p_b} = (F)^{-1}_{p_a,p_b}. \quad (18)$$

Following Hartlap et al. (2007), we use the unbiased estimator, $\widehat{C^{-1}}$, for the inverse covariance matrix. Under the assumption of Gaussian errors and independent data vectors, it is related to the inverse of the estimated covariance matrix (Eq. (15)) through the number of realizations, R, and the number of degrees-of-freedom, D, as

$$\widehat{C^{-1}} = \frac{R-D-2}{R-1} C^{-1}, \quad (19)$$

where in our case D is the number of peak-height bins. This correction will thus be more important in our tomographic analysis where we build the covariance matrix through the assembled peak distributions of several redshift slices.

The derivative of the peak counts with respect to cosmological parameters averaged over all the realizations r is given by

$$\frac{\partial \langle N \rangle_i}{\partial p_a} = \frac{1}{R} \sum_{r=1}^{R} \frac{N_{i,r}(p_a + \Delta p_a) - N_{i,r}(p_a - \Delta p_a)}{2\Delta p_a}, \quad (20)$$

where Δp_a is the variation of the cosmological parameter p_a. This calculation requires a sufficient number, R, of numerical simulations of each cosmology to accurately determine the derivatives. For a single parameter variation, we used 250 cosmological simulations (150 for the fiducial cosmology and 50 for a variation of $+\Delta p_a$ and 50 for a variation of $-\Delta p_a$).

To determine if this is sufficient, we perform a convergence test on numbers of realizations by comparing the derivatives of the peak counts for increasing numbers of realizations of the modified cosmologies. In Fig. 2 we show the derivatives with respect to Ω_m and σ_8 when varying the number of realizations from 10 to 50 in increments of 10 realizations. We note that the derivatives do not significantly evolve beyond 30 realizations, justifying our choice of $R = 50$ for the modified cosmologies.

We use a larger number of realizations of the fiducial cosmology because the covariance matrix is computed for that model, while only the mean peak counts are required for the other cosmologies. Taylor & Joachimi (2014) calculated the accuracy of the covariance matrix given the number of realizations and of degrees of freedom of the data vectors. Following their Eq. (13), we estimate the precision of our covariance matrix to be better than ~13% with our 150 realizations. The additive factor of $2\nu^{-2}$, where ν is the desired accuracy, in the required number of realizations limits in practice the achievable accuracy on the covariance matrix; sub-percent accuracy, for instance, would demand at least 40 000 realizations. Our choice of 150 seems reasonable for the present test-study, but this issue calls for further attention and presents a crucial difficulty for many dark energy probes based on large-scale structure, such as cosmic shear.

4.2. Results

As an illustration of peak count statistics, we study achievable constraints on two cosmological parameters: the total matter density, Ω_m, and the present-day linear matter power spectrum normalization, σ_8. In the standard ΛCDM model, these are well constrained by cosmic microwave background (CMB) observations (Hinshaw et al. 2013; Planck Collaboration XVI 2014). Methods measuring their values at low redshifts, such as peak counts or other gravitational lensing observations, are useful to search for extensions of this simple model. The power spectrum normalization, σ_8, is a good example: differences between values obtained from the CMB and low redshift methods could indicate the need for a non-minimal neutrino mass (e.g., Planck Collaboration X 2014; Rozo et al. 2013; Battye & Moss 2014).

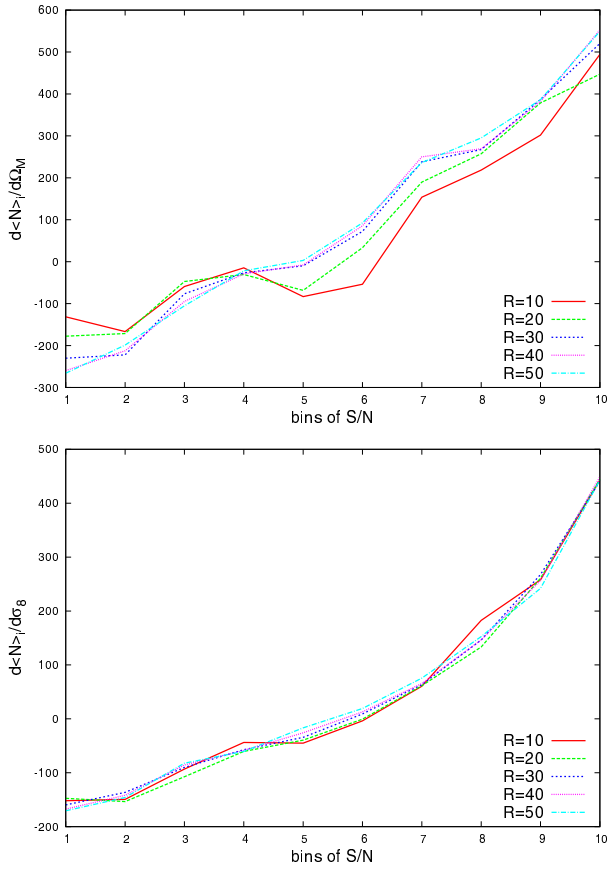

Fig. 2. Derivatives of the peak counts with respect to Ω_m (*top*) and σ_8 (*bottom*) as defined in Eq. (20) as a function of the number of realizations of the modified cosmologies. Results for $R = (10, 20, 30, 40, 50)$ correspond, respectively, to the red, green, blue, purple and cyan curves. There is little change beyond $R = 30$.

Each parameter was varied by 10% from its fiducial value given in Table 2 to define a reference cosmology. We generated 150 realizations of the fiducial cosmology and 50 realizations of each reference cosmology. When varying one parameter, the other remains at its fiducial value. However, when varying the matter density parameter, Ω_M, the dark energy density parameter, Ω_Λ, was also adjusted in order to maintain a flat Universe, $\Omega_M + \Omega_\Lambda = 1$.

4.2.1. Chi-squared distribution

We first examine the distribution of χ^2 values (Eq. (16)) in the fiducial cosmology, using the covariance matrix calculated over the 150 realizations and dividing the peak heights into 10 bins of equal numbers of peaks, on average. The top panel of Fig. 3 shows that the distribution observed in the simulations is reasonably well represented by a true χ^2 distribution with 10 degrees of

Table 2. Cosmological parameter values for the fiducial and reference cosmologies.

	Ω_M	σ_8	R
Fiducial	0.272	0.809	150
Low	0.245	0.728	50
High	0.299	0.890	50

Notes. The quantity R is the number of realizations of each cosmology. When varying one parameter, the other remains fixed at its fiducial value.

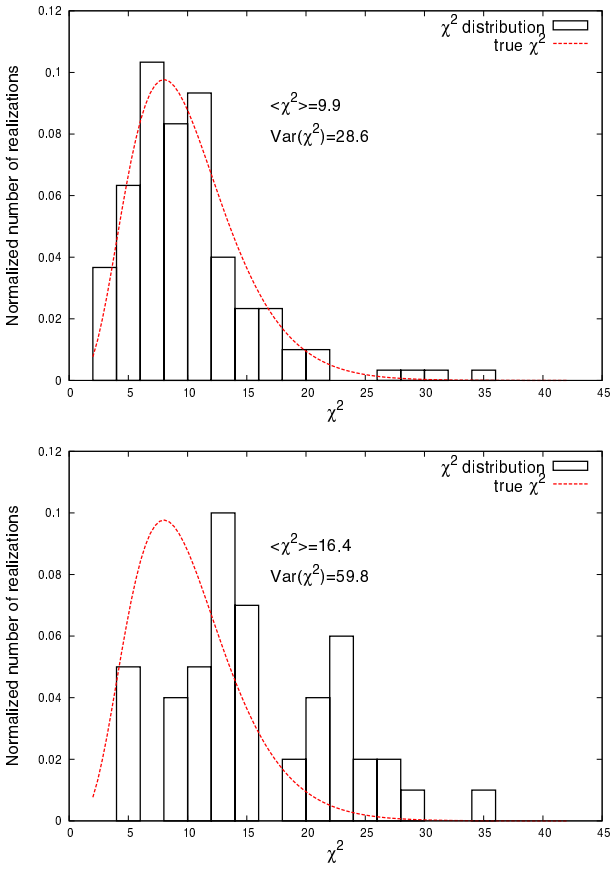

Fig. 3. Normalized χ^2 distribution based on the covariance matrix from the 150 realizations of the fiducial cosmology. We consider 10 bins in peak height with equal numbers of peaks in each bin (on average). Black histograms represent our data and red curve represents a theoretical χ^2 distribution with 10 degrees of freedom. The *top panel* shows the distribution for 150 fiducial realizations. The *bottom panel* is the distribution for 50 realizations with Ω_m increased by 10% from its fiducial value.

freedom, although with a slight deviation manifest by the somewhat larger variance.

When comparing a modified cosmology to the covariance matrix of the fiducial cosmology, we see that the χ^2 distribution strongly diverges from a true χ^2 law (lower panel of Fig. 3). This result illustrates the potential of this method to constrain cosmological parameters. The next step is to compute the constraints we would achieve with the *Euclid* survey using the Fisher formalism.

4.2.2. Fisher information

Following Eq. (17) we compute the Fisher matrix and invert it to obtain constraints on the cosmological parameters.

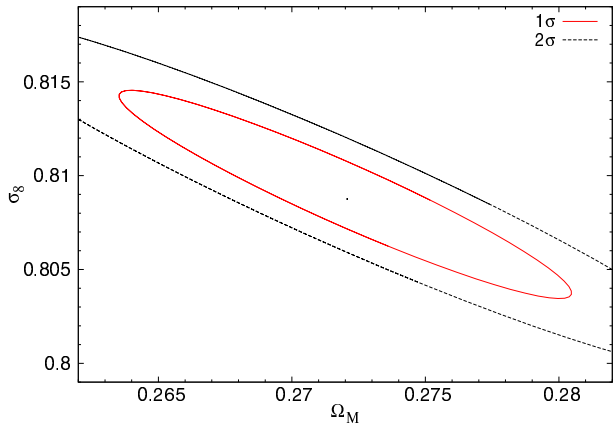

Fig. 4. Fisher joint conditional constraints on Ω_m and σ_8 with non-tomographic peak count statistics for a *Euclid*-like survey; the red and black contours delineate 1 and 2σ significance limits.

Two-dimensional constraints are plotted in Fig. 4 with 1σ and 2σ confidence contours. These constraints are summarized in Table 4.

5. Tomography

We develop a tomographic approach to peak count statistics with the aim of exploiting the radial information by dividing the source galaxies into redshift bins and detecting peaks to each source plane separately. We then perform a joint statistical analysis of the multi-plane peak counts. For example, with two redshift bins we would have a peak distribution consisting of 20 bins in which the first 10 bins represent the distribution of peaks detected to the first source plane, and the remaining 10 the distribution to the second source plane. Our analysis employs the full covariance of these 20 bins. We note that this approach differs from that employed by Dietrich & Hartlap (2010) in that we do not attempt to localize individual peaks in redshift space; the two approaches, however, access the same information. An important issue with tomography is to ensure that we have enough galaxies in each aperture for the average ellipticity noise to be negligible compared to the average tangential shear.

5.1. How to slice the redshift dimension

Adopting a Gaussian random distribution of intrinsic galaxy ellipticities with zero mean and dispersion σ_ϵ, the shape noise over an aperture is

$$\sigma_{\rm ap} \approx \frac{\sigma_\epsilon}{\sqrt{2N_{\rm ap}}}, \tag{21}$$

where $N_{\rm ap}$ is the average number of galaxies in the aperture. We denote y as the desired ratio between the average tangential shear, $\langle\gamma_t\rangle_{\rm ap}$, and the aperture shape noise. An estimate of the number of source galaxies required per aperture is then

$$N_{\rm ap} \approx \left(\frac{y\sigma_\epsilon}{\sqrt{2}\langle\gamma_t\rangle_{\rm ap}}\right)^2. \tag{22}$$

We take a shape-noise dispersion of $\sigma_\epsilon = 0.3$ and an average shear value of 0.04 (e.g., Jain & Taylor 2003; Jain & Seljak 1997). These values with $y = 7$ yield a required number of about 1400 source galaxies per aperture.

Table 3. Mean and one sigma variation of the number of peaks over the 150 realizations of the fiducial cosmology.

	$3 < \frac{S}{N} < 5$	$5 < \frac{S}{N} < 7$	$7 < \frac{S}{N} < 9$	$9 < \frac{S}{N}$	$3 < \frac{S}{N}$
All galaxies ($0.5 < z \leq 2$)	572 ± 19	104 ± 12	18 ± 5	7 ± 3	702 ± 20
$0.5 < z \leq 0.73$	344 ± 16	3 ± 2	0 ± 0	0 ± 0	347 ± 16
$0.73 < z \leq 0.93$	392 ± 16	7 ± 3	0 ± 1	0 ± 0	399 ± 16
$0.93 < z \leq 1.15$	445 ± 18	12± 4	1 ± 1	0 ± 0	458 ± 19
$1.15 < z \leq 1.43$	494 ± 19	17 ± 5	1 ± 1	0 ± 0	512 ± 20
$1.43 < z \leq 2$	553 ± 16	27 ± 6	2 ± 1	0 ± 0	583 ± 17

Working with fixed aperture size, the available number of galaxies per aperture depends on redshift. Using the distribution of redshifts in our simulations (Eq. (1)) normalized to the mean *Euclid* galaxy density of 30 galaxies per square arc-minute, we can estimate the number of galaxies per aperture for any slice of redshift. For the most distant redshift bin, the condition of having at least 1400 galaxies per aperture is satisfied for $1.43 < z \leq 2$. We adopt the same number of galaxies per redshift slice to avoid favoring any particular redshift bin. The condition on a minimal number of galaxies per aperture then directly translates into a condition on the maximum number of redshift bins. We also do not use the $z \leq 0.5$ redshift range to avoid diluting the signal. These conditions allow us to perform a tomographic analysis with up to five redshift slices between redshift 0.5 and 2. We note that relaxing the constraint on the shear to ellipticity ratio would allow more redshift slices. We also note that this approach is limited by the uncertainty on the photometric redshift information, which is on the order of $\sigma(z) = 0.05 \times (1 + z)$.

For a first tomographic study, we use the following five redshift slices with equal numbers of galaxies: $0.5 < z \leq 0.73$, $0.73 < z \leq 0.93$, $0.93 < z \leq 1.15$, $1.15 < z \leq 1.43$, and $1.43 < z \leq 2$. The mean density in each slice is about five galaxies per square arc-minute. This corresponds to about 1400 galaxies per aperture and a shear to ellipticity ratio of about seven.

5.2. Results

We use the same simulations and shape noise realizations as in Sect. 4 when studying the two-dimensional peak counts. The size of the peak-amplitude bins is determined to include the same number of peaks in each bin of a given redshift slice, based on the mean peak counts in our fiducial cosmology. Figure 5 shows the full correlation matrix across all bins and source redshift planes, with the first 10 bins corresponding to the lowest redshift source plane and followed in sequence out to the highest redshift plane.

Table 3 gives the mean and one sigma variation of the number of peaks over the 150 realizations of the fiducial cosmology. The mean number of peaks are also shown in Fig. 6.

As seen from Table 3 and Fig. 6, peaks detected toward a low redshift source plane tend to also be detected when using higher redshift planes. This correlates the peak counts between source planes, as indicated by the non-zero off-diagonal elements of the correlation matrix, especially in the higher signal-to-noise bins. The bins are not fully correlated, however, because new peaks are detected beyond the lower redshift source planes as we move outward. This tomographic view of the peak distribution contains valuable cosmological information that increases the constraining power of the peak counts.

This can be appreciated from the differences in the χ^2 distributions shown in Fig. 7. The black histogram in the upper panel gives the distribution in the simulations, compared to a

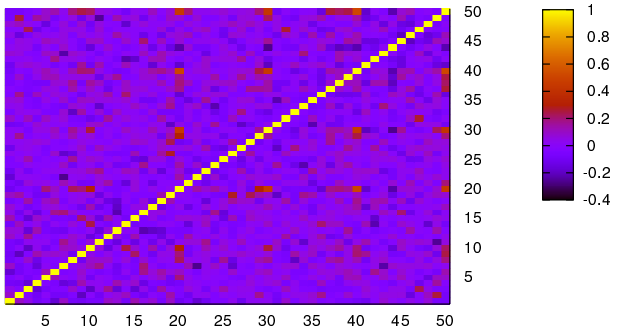

Fig. 5. Correlation matrix of the shear peak distribution for a 100 square-degree field with tomography, calculated by averaging over 150 realizations of the fiducial cosmology (see Eq. (15)). Each redshift slice is divided into ten bins of peak height. This is the covariance matrix normalized to unit diagonal. Correlations between bins are less than 20%, except at the highest signal-to-noise.

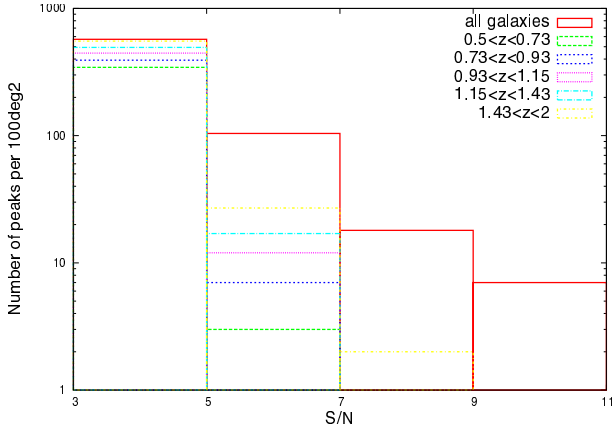

Fig. 6. Mean number of peaks over the 150 realizations of the fiducial cosmology. The red histogram corresponds to peaks detected in the 2D analysis while green, blue, pink, cyan, and yellow, respectively, correspond to peaks detected in the $0.5 < z \leq 0.73$, $0.73 < z \leq 0.93$, $0.93 < z \leq 1.15$, $1.15 < z \leq 1.43$, and $1.43 < z \leq 2$ redshift slices.

true χ^2 distribution with 50 degrees-of-freedom traced by the solid red line. The lower panel gives the distribution of our χ^2 variable for the same non-fiducial cosmology considered in the lower panel of Fig. 3. As before, the observed histogram strongly differs from the pure χ^2 distribution. The fact that the histograms differ even more than in the two-dimensional case illustrates our increased ability to distinguish these cosmological models.

We quantify this gain with a Fisher analysis of the same cosmological parameters considered in the two-dimensional case. The increase in the number of effective degrees-of-freedom in the peak distribution drops the precision on our estimated covariance matrix to 15%, calculated according to Taylor & Joachimi (2014). Doubling the number of realizations to $R = 300$ would

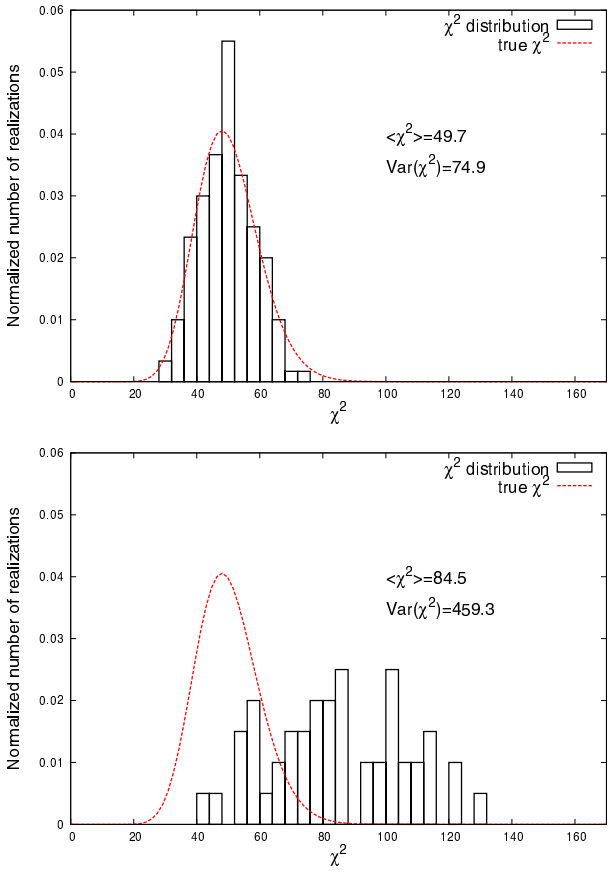

Fig. 7. Normalized χ^2 distributions with respect to the covariance matrix for 150 realizations of the fiducial cosmology with five source redshift planes. Each of the five source planes is associated with 10 signal-to-noise bins containing equal numbers of peaks. Black histograms trace the distribution observed in the simulations and the red curve represents a theoretical χ^2 distribution with 50 degrees-of-freedom. The *top panel* gives the distribution for the 150 realizations of the fiducial model. The *lower panel* gives the distribution for the 50 realizations of the alternate cosmology with Ω_m increased by 10% from its fiducial value.

Table 4. Predicted cosmological parameter constraints for a *Euclid*-like survey.

	δ_{Ω_m}	δ_{σ_8}
Unmarginalized		
All galaxies	0.0012 (0.43%)	0.0018 (0.22%)
Tomography	0.0010 (0.35%)	0.0014 (0.17%)
Marginalized		
All galaxies	0.0037 (1.34%)	0.0056 (0.69%)
Tomography	0.0018 (0.66%)	0.0026 (0.32%)

Notes. The numbers give 1σ uncertainties and the corresponding relative percentages of the fiducial parameter values $\Omega_m = 0.272$ and $\sigma_8 = 0.809$.

provide 10% precision, a small gain compared to the computational time required to generate twice as many realizations. We also verify that $R = 50$ realizations of the modified cosmologies is sufficient for calculation of the derivatives of the mean counts: as before, they are stable beyond 30 realizations. The constraints from our tomographic analysis are given in Fig. 8 and listed in Table 4, and they are compared to the two-dimensional case in Fig. 9.

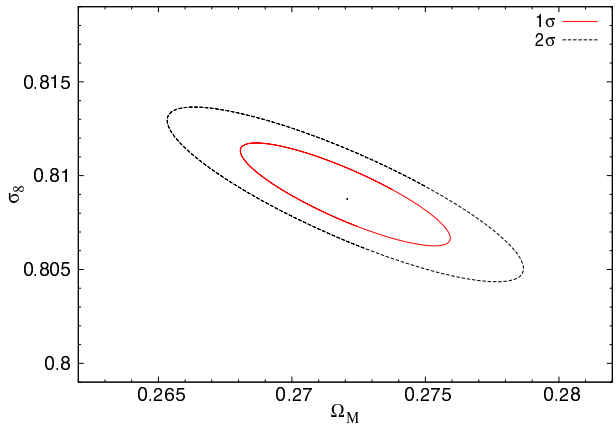

Fig. 8. Predicted joint conditional constraints on Ω_m and σ_8 for a *Euclid*-like survey using tomographic peak count statistics. Solid red and dashed black contours correspond to 1σ and 2σ confidence regions, respectively.

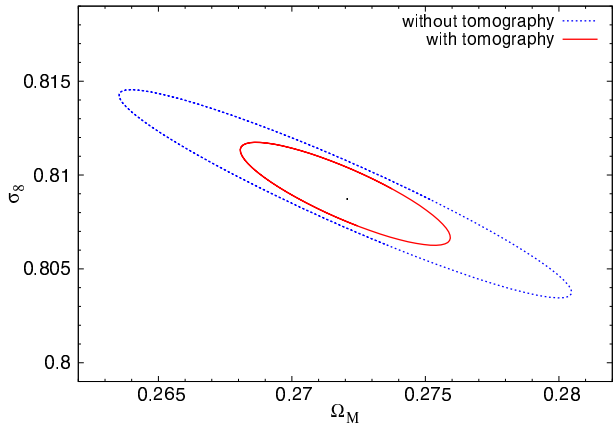

Fig. 9. Fisher ellipses (at 1σ) for Ω_m and σ_8 for a *Euclid*-like survey. The blue dashed curve shows the joint conditional constraints without tomography, while the solid red contour gives those when using tomography with five redshift bins, demonstrating the important gain.

6. Discussion

A number of authors have investigated the potential of lensing peak counts as a cosmological probe, although few have considered large Stage IV projects such as *Euclid* (Yang et al. 2011; Maturi et al. 2011; Hilbert et al. 2012; Marian et al. 2012, 2013). Kratochvil et al. (2010), for example, examined the difference in the χ^2 distributions from different cosmological models; however, it is difficult to make a direct comparison with our results since they varied a different set of cosmological parameters. In their pioneering study of tomographic peak counts, Dietrich & Hartlap (2010) considered a CFHTLS-like survey of about 180 deg^2.

In this work we focus on a typical Stage IV survey characterized by the redshift distribution of a *Euclid*-like survey, using a suite of independent numerical simulations to examine possible cosmological constraints. Figure 9 and Table 4 quantify gains in constraining power by using tomography. We improve the marginal constraints on Ω_m and σ_8 by more than a factor of two over the two-dimensional (non-tomographic) analysis. As to be expected, the conditional constraints are improved by smaller factors: about 1.2 for Ω_m and 1.3 for σ_8.

Among previous studies of peak-statistics, only Dietrich & Hartlap (2010) and Yang et al. (2011) have applied tomography,

the former maximizing the peak signal-to-noise given the redshift distribution of galaxies, and the latter placing source galaxies at either $z_s = 1$ or $z_s = 2$ and ray-tracing through simulations. Dietrich & Hartlap (2010) demonstrated the gain from tomographic peak counts for a survey of 180 deg^2. In their LSST-like survey of 20 000 deg^2, Yang et al. (2011) noted an improvement of the marginal constraints by factors of two to three when using tomography, in qualitative agreement with our results.

We also note that the impact of shape noise is effectively reduced with tomography, in particular for the peaks generated by structures at the higher redshifts. Binning the sources into redshift planes removes the shape noise contributed by foreground galaxies that do not carry any signal on the higher redshift peaks.

We compare our conditional constraints to those obtained by other authors. These vary over the range $0.0006 < \delta_{\Omega_m} < 0.0009$, according to Hilbert et al. (2012) and Marian et al. (2012, 2013), and $0.0013 < \delta_{\sigma_8} < 0.0016$, according to the same authors and Maturi et al. (2011). While these studies differ in a number of respects, the agreement on the conditional constraints among these authors and our results is very good. Indeed, we reach $(\delta_{\Omega_m}, \delta_{\sigma_8}) = (0.0012, 0.0018)$ without tomography, and $(0.0010, 0.0014)$ with tomography. The very small difference from the literature can be attributed to our use of a slightly lower survey area: 15 000 deg^2 compared to 18 000 to 20 000 deg^2 in these other studies.

Finally, we note that some authors have examined constraints on other cosmological parameters. In particular, it has been found that shear peaks have a good ability to constrain the dark energy equation-of-state w (e.g., Yang et al. 2011; Hilbert et al. 2012; Marian et al. 2012, 2013) and primordial non-Gaussianity f_{NL} (e.g., Maturi et al. 2011; Hilbert et al. 2012).

We also compare our forecasted constraints with those from other cosmological probes, in particular from cluster abundance studies. While some lensing peaks do arise from individual clusters, peak statistics represent a more general description of the matter distribution because many originate from projections along the line of sight. Figure 10 compares our predicted constraints from tomographic peak statistics with those from current galaxy cluster constraints as summarized by Allen et al. (2011). The peak counts yield much tighter constraints than those from the current cluster analyses, which is not surprising because we are comparing present day cluster constraints to future lensing counts.

A more pertinent comparison is between constraints predicted from cluster photometric sample for the *Euclid* survey and the peak count constraints. This is shown in Fig. 11. The cluster constraints have been evaluated by Sartoris et al. (2015) for a *Euclid* cluster catalog considering the information provided by cluster number counts. We note that, unlike what has been done in Sartoris et al. (2015), constraints from clusters have been performed by varying only the σ_8 and Ω_m cosmological parameters and the 4 parameters that describe the bias, the scatter of the observable mass relation, and their redshift evolution. This has been done to compare in a more appropriate way the constraints obtained from the clusters and those from the shear peaks. The reduction in the number of free cosmological parameters explains why the cluster constraints shown in Fig. 11 are smaller than those shown in Sartoris et al. (2015). We see that the constraints from tomographic peak counts are weaker than cluster counts by an order of magnitude when supposing that the observable-mass relation is fully known a priori (blue dotted ellipse). However, the shear-peak constraints are almost twice as strong when not making any assumption on the scaling relation parameters and their evolution (green dash dotted ellipse).

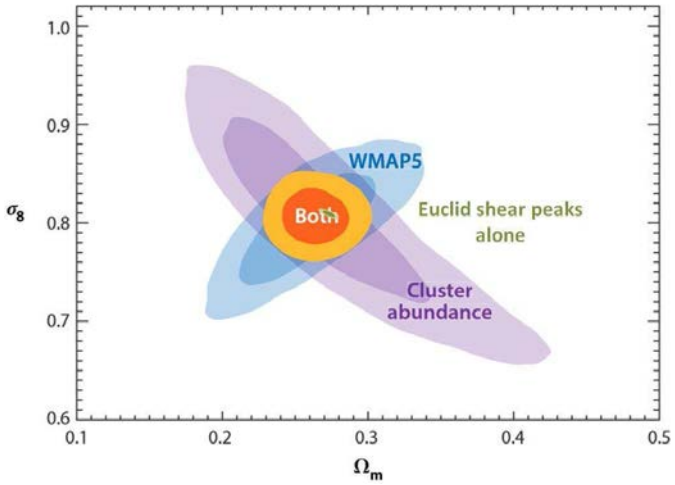

Fig. 10. Constraints from tomographic peak counts compared to current galaxy cluster constraints, with contours giving the 1 and 2σ confidence limits. The violet shading represents constraints from the maxBCG cluster catalog, blue those from WMAP-5, and the yellow their combination; they have been adapted from Allen et al. (2011). The green contours give the tomographic peak-count constraints for a *Euclid*-like survey covering 15 000 square degrees.

In addition, it is worth noting that the shear-peak contours are orthogonal to the clusters when the observable-mass relation is not known a priori. This essentially shows the value of using both clusters and shear-peak statistics. As it is difficult to predict how well we will be able to constrain the scaling relation, we show here two extreme cases for the cluster constraints, with the idea that the observational constraints should lie somewhere between the blue and green ellipses. In particular, the green contours are very conservative, as we could in principle already constrain the scaling relation at redshift $z = 0$, which would reduce the errors on the cosmological parameters.

We expect peak statistics to complement more standard two-point lensing statistics. In fact, the study by Dietrich & Hartlap (2010) suggests that peak statistics could yield tighter constraints than the classical 2-point correlation function, a result expected given that the peak statistics contain higher order correlations, and later confirmed by, e.g., Marian et al. (2012, 2013). Peak counts would also appear to be less affected by shape measurement systematics than the shear power spectrum in the sense that it is more difficult to reproduce the pattern necessary for peak identification than to affect the amplitude of two-point correlations. In similar vein, we expect that their respective sensitivities to photometric redshift uncertainties will not be the same. Overall, the two methods will not share the same systematics and therefore offer important complementarity.

7. Conclusion

We have found that shear peak statistics offer a potentially powerful cosmological probe, in agreement with previous studies. As an advance along these lines, our results clearly illustrate the gain of using tomography in the framework of Stage IV dark energy surveys, i.e., separating the source galaxies into redshift planes and counting peaks to each plane. With tomography, we improve the conditional (respectively, marginal) constraints by a factor of 1.2 (resp. 2) on Ω_m and σ_8.

For a large-area survey, typified here as that from a *Euclid*-like mission, we estimate that the peak-count constraints are an order of magnitude less powerful than those predicated from

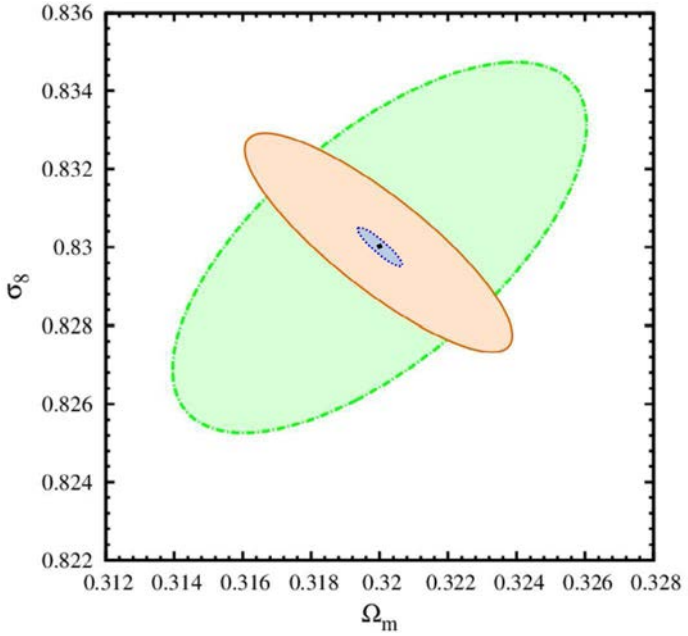

Fig. 11. Comparison of predicted constraints from *Euclid* clusters and peak counts for a *Euclid*-like survey (1σ confidence limits). The orange ellipse traces the tomographic peak-count results. The blue dotted ellipse reports the constraints obtained from cluster number counts with a 3σ selection function assuming a perfectly known observable-mass relation (see Sartoris et al. 2015). The green dash-dotted ellipse shows the same cluster constraints but leaving the 4 scaling relation parameters (bias, scatter, and their evolution) completely free to vary. We note the change of scale and shift of fiducial parameter values from Fig. 10.

galaxy cluster evolution when the observable-mass relation is fully known a priori, while they are twice as strong when not making any assumption on this relation. The peak counts, however, have the great advantage of not relying on such a scaling relation that may prove difficult to establish to high accuracy.

We have only explored the two parameters Ω_m and σ_8 in the present study, but plan to extend to other parameters, including the dark energy equation-of-state and primordial non-Gaussianity in future work. Further topics warranting exploration include the impact of various systematics, such as intrinsic alignments, photometric redshift errors, and shape measurement errors. These additional studies will quantify the extent to which peak counts are complementary to cosmic shear measurements.

The primary technical challenge in application of peak counts is the production of large suites of numerical simulations to calculate both the expected mean number of peaks and their covariance matrix over the cosmological parameter space. It is not, however, unique to the counts: all lensing studies face the same challenge because valuable signal, even in the two-point statistics of cosmic shear, originates in the non-linear regime. We therefore expect peak counts to accompany the more standard lensing measures in application to large lensing surveys.

Acknowledgements. We are grateful to the anonymous referee for his/her careful reading and helpful and constructive comments that improved the paper. N.M. thanks the cole Normale Sup rieure de Cachan and the Laboratoire AstroParticle et Cosmologie for financial support in the early stage of this work. B.S. acknowledges financial support from MIUR PRIN2010-2011 (J91J12000450001), from the PRIN-MIUR 201278X4FL grant, from a PRIN-INAF/2012 Grant, from the inDark INFN Grant and from the Consorzio per la Fisica di Trieste. A portion of the research described in this paper was carried out at the Jet Propulsion Laboratory, California Institute of Technology, under a contract with the National Aeronautics and Space Administration.

References

Albrecht, A., Bernstein, G., Cahn, R., et al. 2006, ArXiv e-prints [arXiv:astro-ph/0609591]
Albrecht, A., Amendola, L., Bernstein, G., et al. 2009, ArXiv e-prints [arXiv:0901.0721]
Allen, S. W., Evrard, A. E., & Mantz, A. B. 2011, ARA&A, 49, 409
Bartelmann, M., & Schneider, P. 2001, Phys. Rep., 340, 291
Battye, R. A., & Moss, A. 2014, Phys. Rev. Lett., 112, 051303
Dietrich, J. P., & Hartlap, J. 2010, MNRAS, 402, 1049
Hamana, T., Takada, M., & Yoshida, N. 2004, MNRAS, 350, 893
Hamana, T., Oguri, M., Shirasaki, M., & Sato, M. 2012, MNRAS, 425, 2287
Hartlap, J., Simon, P., & Schneider, P. 2007, A&A, 464, 399
Hennawi, J. F., & Spergel, D. N. 2005, ApJ, 624, 59
Heymans, C., Van Waerbeke, L., Miller, L., et al. 2012, MNRAS, 427, 146
Hilbert, S., Marian, L., Smith, R. E., & Desjacques, V. 2012, MNRAS, 426, 2870
Hinshaw, G., Larson, D., Komatsu, E., et al. 2013, ApJS, 208, 19
Jain, B., & Seljak, U. 1997, ApJ, 484, 560
Jain, B., & Taylor, A. 2003, Phys. Rev. Lett., 91, 141302
Jain, B., & Van Waerbeke, L. 2000, ApJ, 530, L1
Jenkins, A., Frenk, C. S., White, S. D. M., et al. 2001, MNRAS, 321, 372
Kiessling, A., Heavens, A. F., Taylor, A. N., & Joachimi, B. 2011, MNRAS, 414, 2235
Kratochvil, J. M., Haiman, Z., & May, M. 2010, Phys. Rev. D, 81, 043519
Kruse, G., & Schneider, P. 1999, MNRAS, 302, 821
Laureijs, R., Amiaux, J., Arduini, S., et al. 2011, ArXiv e-prints [arXiv:1110.3193]
Leauthaud, A., Massey, R., Kneib, J.-P., et al. 2007, ApJS, 172, 219
LSST Science Collaboration, Abell, P. A., Allison, J., et al. 2009, ArXiv e-prints [arXiv:0912.0201]
Marian, L., & Bernstein, G. M. 2006, Phys. Rev. D, 73, 123525
Marian, L., Smith, R. E., Hilbert, S., & Schneider, P. 2012, MNRAS, 423, 1711
Marian, L., Smith, R. E., Hilbert, S., & Schneider, P. 2013, MNRAS, 432, 1338
Massey, R., Rhodes, J., Leauthaud, A., et al. 2007, ApJS, 172, 239
Maturi, M., Fedeli, C., & Moscardini, L. 2011, MNRAS, 416, 2527
Navarro, J. F., Frenk, C. S., & White, S. D. M. 1997, ApJ, 490, 493
Planck Collaboration XVI. 2014, A&A, 571, A16
Planck Collaboration X. 2014, A&A, 571, A20
Press, W. H., & Schechter, P. 1974, ApJ, 187, 425
Reblinsky, K., Kruse, G., Jain, B., & Schneider, P. 1999, A&A, 351, 815
Rozo, E., Rykoff, E. S., Bartlett, J. G., & Evrard, A. E. 2013, ArXiv e-prints [arXiv:1302.5086]
Sartoris, B., Biviano, A., Fedeli, C., et al. 2015, MNRAS, submitted [arXiv:1505.02165]
Schneider, P., van Waerbeke, L., Jain, B., & Kruse, G. 1998, MNRAS, 296, 873
Spergel, D., Gehrels, N., Breckinridge, J., et al. 2013, ArXiv e-prints [arXiv:1305.5422]
Springel, V. 2005, MNRAS, 364, 1105
Taylor, A., & Joachimi, B. 2014, MNRAS, 442, 2728
Tinker, J., Kravtsov, A. V., Klypin, A., et al. 2008, ApJ, 688, 709
Wang, S., Haiman, Z., & May, M. 2009, ApJ, 691, 547
White, M., van Waerbeke, L., & Mackey, J. 2002, ApJ, 575, 640
Yang, X., Kratochvil, J. M., Wang, S., et al. 2011, Phys. Rev. D, 84, 043529

Chapter 4

Conclusions and Perspectives

In this 3-year thesis, I studied galaxy clusters and cosmology, based on two observables: galaxy magnitudes and galaxy shapes.

With galaxy magnitudes, we were able to compute photometric redshifts, and then galaxy luminosity functions. Investigating the behavior of GLFs for two galaxy populations within one of the largest cluster samples to date, we confirm in particular that the GLF faint end for blue galaxies does not evolve with redshift, while the faint end for red galaxies shows a drop at high redshift, which is more pronounced at higher redshifts. This result means that clusters still evolve between $z \sim 0.9$ and today, and that the faint blue galaxies are quenched into red passive ones.

Still using magnitudes, we computed the mass of the star component in groups and clusters of galaxies. We showed that in the case of groups, the star component cannot be neglected compared to the gas component, while it is often the case in clusters. Taking both the galaxy and gas fractions into account, we constrain the matter density parameter Ω_M.

Galaxy shapes enable us to calculate a weak lensing signal around massive objects. We computed cluster masses in the redshift range of the DAFT/FADA survey ($0.4 < z < 0.9$) from NFW fits to the shear profile of the background galaxies. Focusing on large field of view images, we estimate the fraction of recent merging events, and detect several filaments, observationally validating the hierarchical growth scenario for cluster formation, and determining that this process is still at work in this redshift range.

Finally, we dropped the classical approach of using cluster counts for cosmological studies, to focus on shear peaks, which correspond both to clusters and to chance alignments of multiple structures along the line of sight. Focusing on the case of the *Euclid* survey, we showed that this technique will provide cosmological constraints with similar sensitivity to the cluster counting experiments, but without necessitating any knowledge of the observable-mass relation. In addition, we quantified the gain of tomographic peak counts over a 2-dimensional method.

All these results naturally raised some new questions. In the next paragraphs, I review further developments that we either started, or plan to do in a near future.

Galaxy luminosity functions

In our study of cluster GLFs, we find that the faint end of the early type galaxies is decreasing when redshift increases. We interpret this result as the evolution of late type to early type galaxies, that enrich the red sequence from late to low redshifts.

However, we were not able to rule out the possible surface brightness selection effect observed in De Propris et al. (2013). The authors claim that the drop at the faint end of the high redshift early-type GLF could be due to the non detection of faint galaxies above the sky noise, in ground based images. Indeed, they use HST data in their study and therefore have a cleaner sky background and deeper observations. Artificially degrading the exposure time of their images resulted in the central surface brightness of galaxies being fainter, and then in a decrease of the number of galaxies observed at faint magnitudes. Note that galaxies are lost in the process, even when they are brighter than the completeness limit, because their central surface brightness is no longer above the detection threshold.

With the DAFT/FADA survey, we have the ability to verify this hypothesis. Indeed, we have both HST and ground based data for the same clusters. A comparison of the GLF of early type galaxies computed from the two different data sources will shed light on this issue. Having only two filters with HST, we won't be able to work with photometric redshifts and will rely on color magnitude diagrams to select cluster members. Finding a decreasing slope for the ground based GLF and a flat one for the space based GLF would confirm that surface brightness selection effects are responsible for the observed drop. On the other hand, finding a decreasing slope in both cases would rule out these effects.

Another subject worth investigating is the stellar mass function (SMF) of galaxy clusters. The SMF is similar to the GLF but represents the galaxy mass distribution instead of the galaxy luminosity distribution. Galaxy cluster and field SMFs have been extensively studied recently (e.g. Bell et al. 2003; Ilbert et al. 2010; Vulcani et al. 2013) because they compare better with theory and simulations than GLFs. However, one must suppose a proxy to the mass, either a conversion ratio from luminosity as tabulated in Kauffmann et al. (2003), or a value corresponding to the SED template if using photometric redshifts. This assumption usually makes SMFs less robust than GLFs.

We would like to study the SMFs for the same sample as in Martinet et al. (2015), and compare their behaviors with those of the GLFs. The masses of galaxies will be obtained in the template fitting with LePhare when estimating the galaxy photometric redshift. Finding the same trend for both functions would assess the robustness of both methods, while differences would highlight some problems in the conversion of luminosity to mass. A comparison with simulations will also be possible for the SMFs.

Fraction of baryons

In our study of the fraction of baryons, we found that low mass systems have a lower baryon fraction than high mass clusters. We first thought that it could be explained by a higher amount of intra cluster light (ICL) in groups. The ICL, also named diffuse light, corresponds to the stars that have been expelled from galaxies into the ICM, and are therefore not taken into account when measuring the magnitude of galaxies. As the ICL

is mainly due to baryon astrophysical processes, its amount is likely to be higher in groups than in clusters, as the gravitational potential well of groups is shallower. Evaluating the necessary contribution of ICL, we found that it cannot explain this difference. However, finding more ICL in groups could explain why the star fraction does not follow the same trend in groups than in clusters. Indeed, if groups were only low mass clusters, their stellar mass fraction should even be higher as seen in Fig. 1.2. The missing amount is compatible with the ICL amount found in compact groups, that can reach up to ∼50% of the stellar mass when considering the BCG envelope (e.g. Da Rocha et al. 2008; Arnaboldi et al. 2012).

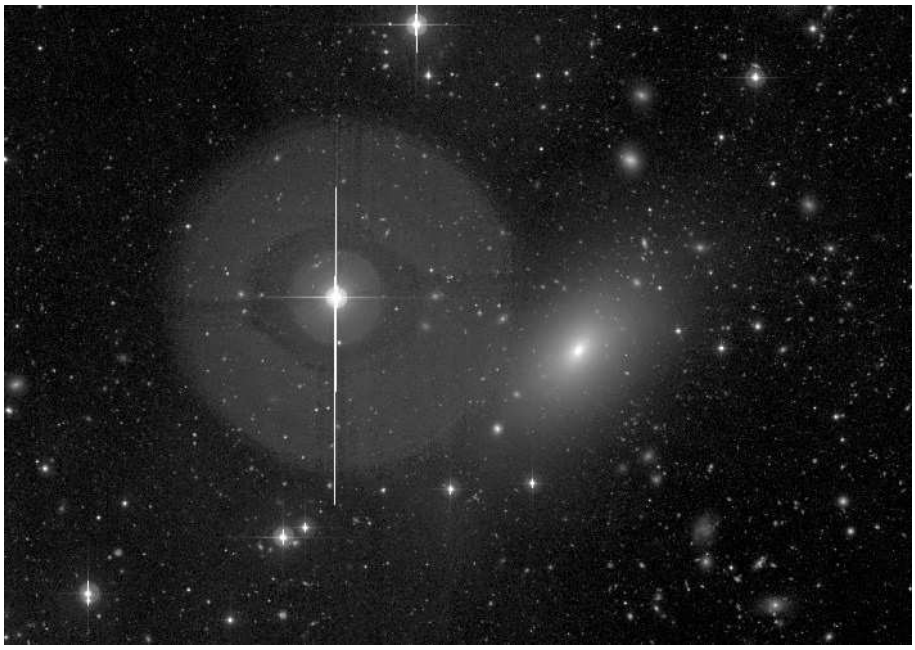

Figure 4.1: Effect of star halos on ICL detection, as seen on the r-band MegaCam image of NGC 1132, reduced with the Elixir-LSB pipeline.

To investigate the ICL in the studied groups we applied for telescope time at CFHT, and were granted imaging for our 9 groups. As the surface brightness of the expected ICL is very faint ($\mu > 26$ mag.arcsec^{-2}), we used the Elixir-LSB pipeline on MegaCam images. Elixir-LSB is a dithering pattern method that aims at properly estimating the sky background, allowing to reach surface brightness as low as 28 mag.arcsec^{-2}. This observational technique is described in Duc et al. (2011). Unfortunately, the ICL low surface brightness contribution is very close to the contribution of star halos due to the reflections on the secondary mirror. This is illustrated in Fig. 4.1, where a prominent star halo is found close to the group. Even when masking bright stars, fainter stars also have halos which will wrongly contribute to the ICL estimate. Careful modeling of the star halos would be needed in order to remove them from images. Another approach is the building of a new telescope optimized to detect ICL, which would have an off-axis design to avoid reflections on the secondary mirror. This is in particular the case of the MESSIER project. Finally we can note that the problem of stars is not very relevant at higher redshifts, where objects appear smaller and can be chosen far enough from dense star regions (Guennou et al. 2012; Burke et al. 2012).

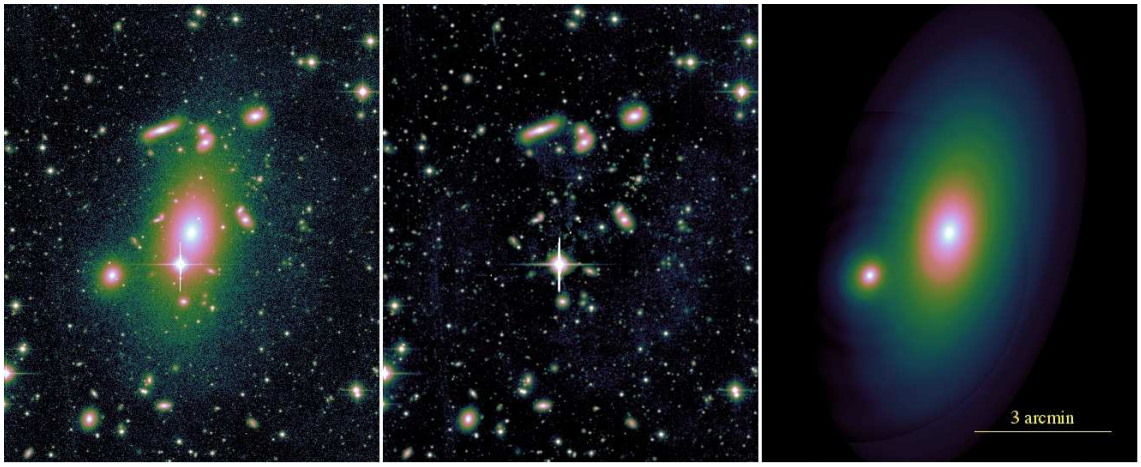

Figure 4.2: Fit to the BCG of AWM4, observed with MegaCam Elixir-LSB. *Left* corresponds to the observed image, *Right* to the modeled BCG with the second brightest galaxy using IRAF/ellipse, and *Middle* to the image with the model subtracted. Colors are chosen to better see the different levels of surface brightness.

In the case of our groups, we can thus only measure the ICL component found in the BCG envelope, which can be modeled, even with the presence of stars, as shown by our early results in Fig. 4.2. We use IRAF/ellipse to measure the surface brightness profile of the BCG and estimate the fraction of light which is lost when measuring the galaxy magnitude in a regular aperture. A detailed study of the BCGs in groups is currently in preparation.

Weak lensing

Having detected filaments in several fields, at redshifts between $0.4 < z < 0.9$, and having developed an algorithm to study galaxy luminosity functions, it would be interesting to combine these works, and compute the galaxy luminosity function inside filaments, to compare it with those of clusters and of the field. This will require deep imaging of the detected filaments, and also a study of closer filaments to measure their evolution with redshift. Finally, recent simulations found that galaxies embedded within filaments have their spin preferentialy aligned with the filaments for the low-mass galaxies and perpendicular for high masses (Dubois et al. 2014). Observationally verifying this hypothesis is important to evaluate the effect of this possible intrinsic alignment on cosmic shear studies as shown in e.g. Codis et al. (2015).

In addition, I started new collaborations to work more specifically on shear measurements, in the context of a post-doctoral position at the Argelander Institut für Astronomie with Peter Schneider and Tim Schrabback. In particular we intend to study the effects of color gradients and blending, two issues that have been neglected in previous shear measurement challenges.

As already mentioned in Sect. 3.1.2, Semboloni et al. (2013) showed that in principle it is possible to correct for color gradients to the *Euclid* required accuracy, using about 40,000 galaxies observed with HST in two filters. However, the analysis of Semboloni et al.

(2013) was simplistic in multiple aspects. Most importantly, it ignored the influence of noise in the HST data. Also, it is currently unknown, how accurate instrumental distortions in the HST data (e.g. the PSF and the impact of charge-transfer inefficiency) need to be removed in order not to bias the color gradient calibration. It will be the goal of this project to provide a more realistic color gradient analysis that accounts for the noise, and to derive requirements on the HST data analysis that ensure a sufficiently accurate color gradient calibration for Euclid. In addition to helping evaluate the required number of galaxies, this calibration will estimate potential problems not seen in the simulations. In particular, color gradients depend both on the galaxy sizes and redshifts, two parameters that can only be probed with deep observations.

The blending issue requires a different approach. Indeed, this phenomenon has not been studied in detail so far, and we usually resort to discarding galaxies that are too close to each other when performing shape measurements. Using the same HST archive images, one can quantify the effect of blending along with the proportion of blended objects. Simulations might be necessary to reproduce the HST data with realistic substructures. A technique to accurately measure the shape of blended objects would increase the number of galaxies usable for the cosmological probe, boosting their efficiency. Several methods can be tested, such as the fit of joint galaxy profiles.

Shear peak statistics

Our work on shear peaks can have several continuations, among which are the study of additional cosmological parameters, and the adaptation to observational data.

We have only explored the two parameters Ω_M and σ_8 in the present study, but plan to extend our analysis to other parameters. In particular, it has been found that shear peaks have a good ability to constrain the dark energy equation-of-state w (e.g., Yang et al. 2011; Hilbert et al. 2012; Marian et al. 2012, 2013) and primordial non-Gaussianity $f_{\rm NL}$ (e.g, Maturi et al. 2011; Hilbert et al. 2012). This adaptation mostly requires extra simulations, and a modification of the current SUNGLASS pipeline to include these parameters.

So far, shear peak statistics have only been investigated on simulations. Applying it to real data is a challenge that has to be taken before using it on larger data sets, such as *Euclid*. In the Fisher formalism, the cosmological constraints are computed from a comparison between the covariance matrix of the peak distribution calculated at the fiducial cosmology and the derivatives of the peak signal-to-noise distribution with respect to each cosmological parameter. Several strategies can be considered to apply the method we developed to observations. In this first attempt, we plan to measure the covariance matrix from the data, and to simulate the modified cosmologies, varying one cosmological parameter at a time. We showed that 30 independent realizations of each cosmology are required to have a reliable peak count derivative with respect to each cosmological parameter. Hence, a large number of simulations will be needed to explore the parameter space. To reduce this number, we plan to explore the cosmological parameter space with an adaptive mesh, focusing on areas where we have priors from e.g. Planck cosmological parameter values (Planck Collaboration et al. 2014), and then

interpolate the final cosmological constraints.

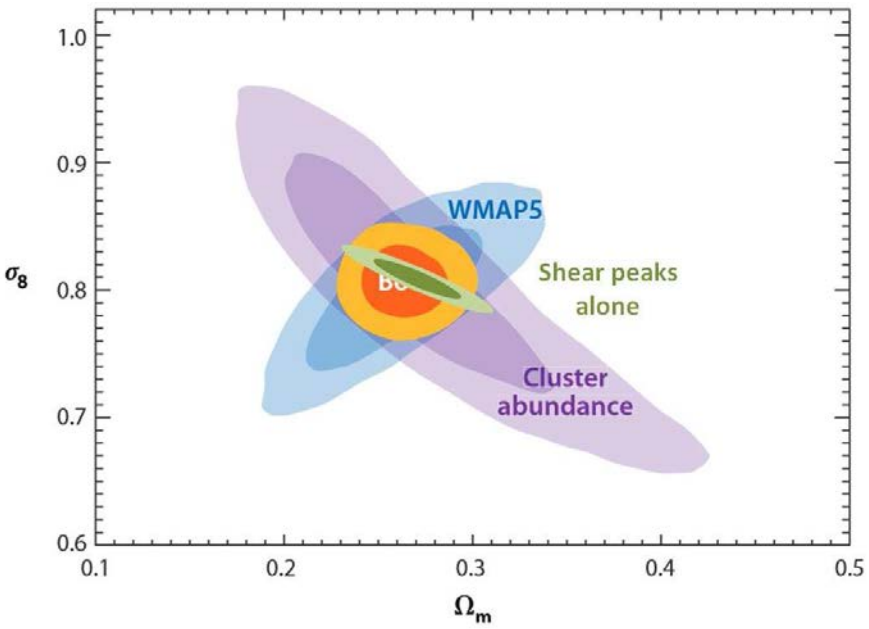

Figure 4.3: Constraints from 2-dimensional peak counts compared to current galaxy cluster constraints, with contours giving the 1- and 2-σ confidence limits. The violet shading represents constraints from the maxBCG cluster catalog, the blue those from WMAP-5, and the yellow their combination; they have been adapted from Allen et al. (2011). The green contours give the 2-dimensional peak-count constraints for the proposed combined set of data covering 2,000 square degrees.

I will use data coming from three different WL surveys: the Kilo Degree Survey (KiDS, http://kids.strw.leidenuniv.nl/), the Canada-France-Hawaii Lensing Survey (CFHTLenS, http://www.cfhtlens.org/public/canada-france-hawaii-lensing-survey), and the Red Cluster Sequence Lensing Survey (RCSLenS, http://www.rcslens.org/). This will allow to probe an area of about 2,000 square degrees. Reduced imaging and shear catalogs that I can use to detect the shear peaks are already available for these surveys. However, since the data are taken from three different analyses, work is needed to homogenize them. Indeed, the combination of data will require a normalization to the same magnitude depth, and an investigation of observational biases, that could demand accurate simulations of each data set. Note that masking should not be a tough problem as long as we apply the same observational masks to the simulations.

To show the relevance of this study, I already computed the expected constraints achievable with a 2-dimensional peak statistics survey of 2,000 deg^2. Note however, that this simulation is not optimal, as it is adapted from the Martinet et al. (2015, A&A in press) *Euclid* study, and re-scaled to the 2,000 deg^2 area. In particular, the galaxy density will be lower with ground based images, and this is why we prefer to show non-tomographic constraints. The constraints should not be too far from the forecasts presented in Fig. 4.3, which are compared with some of the best present observational constraints using cluster abundances. This figure exhibits the tremendous increase in precision that this work should achieve.

Bibliography[1]

Abell, G. O. 1958, ApJS, 3, 211

Adami, C., Cypriano, E. S., Durret, F., et al. 2015, A&A, 575, A69

Adami, C., Durret, F., Benoist, C., et al. 2010, A&A, 509, A81

Adami, C., Durret, F., Guennou, L., & Da Rocha, C. 2013, A&A, 551, A20

Adami, C. & Mazure, A. 1999, A&AS, 134, 393

Allen, S. W., Evrard, A. E., & Mantz, A. B. 2011, ARA&A, 49, 409

Allen, S. W., Mantz, A. B., Morris, R. G., et al. 2013, ArXiv: 1307.8152

Allen, S. W., Rapetti, D. A., Schmidt, R. W., et al. 2008, MNRAS, 383, 879

Allen, S. W., Schmidt, R. W., Ebeling, H., Fabian, A. C., & van Speybroeck, L. 2004, MNRAS, 353, 457

Arnaboldi, M., Ventimiglia, G., Iodice, E., Gerhard, O., & Coccato, L. 2012, A&A, 545, A37

Arnouts, S., Cristiani, S., Moscardini, L., et al. 1999, MNRAS, 310, 540

Balogh, M. L., Navarro, J. F., & Morris, S. L. 2000, ApJ, 540, 113

Barnes, J. E. & Hernquist, L. 1992, ARA&A, 30, 705

Barnes, J. E. & Hernquist, L. 1996, ApJ, 471, 115

Bartelmann, M. & Schneider, P. 2001, Phys. Rep., 340, 291

Bell, E. F., McIntosh, D. H., Katz, N., & Weinberg, M. D. 2003, ApJS, 149, 289

Bernstein, G. & Jain, B. 2004, ApJ, 600, 17

Bernstein, G. M. & Armstrong, R. 2014, MNRAS, 438, 1880

Bertin, E. 2011, in Astronomical Society of the Pacific Conference Series, Vol. 442, Astronomical Data Analysis Software and Systems XX, ed. I. N. Evans, A. Accomazzi, D. J. Mink, & A. H. Rots, 435

[1]References enclosed in published articles are listed in the corresponding paper, and are not necessarily listed in the thesis bibliography.

Bertin, E. & Arnouts, S. 1996, A&AS, 117, 393

Blandford, R. & Narayan, R. 1986, ApJ, 310, 568

Bocquet, S., Saro, A., Dolag, K., & Mohr, J. J. 2015, ArXiv: 1502.07357

Bridle, S., Balan, S. T., Bethge, M., et al. 2010, MNRAS, 405, 2044

Briel, U. G., Henry, J. P., & Boehringer, H. 1992, A&A, 259, L31

Brüggen, M. & Kaiser, C. R. 2002, Nature, 418, 301

Burke, C., Collins, C. A., Stott, J. P., & Hilton, M. 2012, MNRAS, 425, 2058

Churazov, E., Sunyaev, R., Forman, W., & Böhringer, H. 2002, MNRAS, 332, 729

Clowe, D., Bradač, M., Gonzalez, A. H., et al. 2006, ApJ, 648, L109

Codis, S., Gavazzi, R., Dubois, Y., et al. 2015, MNRAS, 448, 3391

Cowie, L. L. & Songaila, A. 1977, Nature, 266, 501

Cypriano, E. S., Amara, A., Voigt, L. M., et al. 2010, MNRAS, 405, 494

Da Rocha, C., Ziegler, B. L., & Mendes de Oliveira, C. 2008, MNRAS, 388, 1433

Davis, T. M., Mörtsell, E., Sollerman, J., et al. 2007, ApJ, 666, 716

De Propris, R., Phillipps, S., & Bremer, M. N. 2013, MNRAS, 434, 3469

de Vaucouleurs, G. 1948, Annales d'Astrophysique, 11, 247

Dietrich, J. P. & Hartlap, J. 2010, MNRAS, 402, 1049

Dodelson, S., Gates, E. I., & Turner, M. S. 1996, Science, 274, 69

Dressler, A. 1980, ApJ, 236, 351

Dubois, Y., Pichon, C., Welker, C., et al. 2014, MNRAS, 444, 1453

Duc, P.-A., Cuillandre, J.-C., Serra, P., et al. 2011, MNRAS, 417, 863

Dunkley, J., Komatsu, E., Nolta, M. R., et al. 2009, ApJS, 180, 306

Durret, F., Adami, C., Bertin, E., et al. 2015, ArXiv: 1504.00452

Einstein, A. 1916, Annalen der Physik, 354, 769

Evrard, A. E. 1997, MNRAS, 292, 289

Fassbender, R., Nastasi, A., Böhringer, H., et al. 2011, A&A, 527, L10

Friedmann, A. 1922, Zeitschrift fur Physik, 10, 377

Giodini, S., Pierini, D., Finoguenov, A., et al. 2009, ApJ, 703, 982

Gobat, R., Daddi, E., Onodera, M., et al. 2011, A&A, 526, A133

Gruen, D., Seitz, S., Koppenhoefer, J., & Riffeser, A. 2010, ApJ, 720, 639

Guennou, L., Adami, C., Da Rocha, C., et al. 2012, A&A, 537, A64

Guennou, L., Adami, C., Durret, F., et al. 2014a, A&A, 561, A112

Guennou, L., Adami, C., Ulmer, M. P., et al. 2010, A&A, 523, A21

Guennou, L., Biviano, A., Adami, C., et al. 2014b, A&A, 566, A149

Gunn, J. E. & Gott, III, J. R. 1972, ApJ, 176, 1

Haiman, Z., Mohr, J. J., & Holder, G. P. 2001, ApJ, 553, 545

Heymans, C., Van Waerbeke, L., Bacon, D., et al. 2006, MNRAS, 368, 1323

Hilbert, S., Marian, L., Smith, R. E., & Desjacques, V. 2012, MNRAS, 426, 2870

Hinshaw, G., Larson, D., Komatsu, E., et al. 2013, ApJS, 208, 19

Hirata, C. M., Mandelbaum, R., Ishak, M., et al. 2007, MNRAS, 381, 1197

Hoekstra, H., Herbonnet, R., Muzzin, A., et al. 2015, MNRAS, 449, 685

Hubble, E. P. 1926, ApJ, 64, 321

Ilbert, O., Arnouts, S., McCracken, H. J., et al. 2006, A&A, 457, 841

Ilbert, O., Capak, P., Salvato, M., et al. 2009, ApJ, 690, 1236

Ilbert, O., Salvato, M., Le Floc'h, E., et al. 2010, ApJ, 709, 644

Jain, B. & Taylor, A. 2003, Physical Review Letters, 91, 141302

Jarosik, N., Bennett, C. L., Dunkley, J., et al. 2011, ApJS, 192, 14

Jee, M. J., Tyson, J. A., Schneider, M. D., et al. 2013, ApJ, 765, 74

Kaiser, N. & Squires, G. 1993, ApJ, 404, 441

Kaiser, N., Squires, G., & Broadhurst, T. 1995, ApJ, 449, 460

Kauffmann, G., Heckman, T. M., White, S. D. M., et al. 2003, MNRAS, 341, 33

Kiessling, A., Heavens, A. F., Taylor, A. N., & Joachimi, B. 2011, MNRAS, 414, 2235

Kitching, T. D., Balan, S. T., Bridle, S., et al. 2012, MNRAS, 423, 3163

Laganá, T. F., Martinet, N., Durret, F., et al. 2013, A&A, 555, A66

Larson, R. B., Tinsley, B. M., & Caldwell, C. N. 1980, ApJ, 237, 692

Laureijs, R., Amiaux, J., Arduini, S., et al. 2011, ArXiv: 1110.3193

Lewis, A. 2009, MNRAS, 398, 471

Linder, E. V. 2003, Physical Review Letters, 90, 091301

LSST Science Collaboration, Abell, P. A., Allison, J., et al. 2009, ArXiv: 0912.0201

Mandelbaum, R., Rowe, B., Armstrong, R., et al. 2014, ArXiv: 1412.1825

Mantz, A., Allen, S. W., Rapetti, D., & Ebeling, H. 2010, MNRAS, 406, 1759

Mantz, A. B., Allen, S. W., Morris, R. G., et al. 2014, MNRAS, 440, 2077

Marian, L., Smith, R. E., Hilbert, S., & Schneider, P. 2012, MNRAS, 423, 1711

Marian, L., Smith, R. E., Hilbert, S., & Schneider, P. 2013, MNRAS, 432, 1338

Martinet, N., Bartlett, J. G., & Kiessling, A. 2015, A&A in press

Martinet, N., Clowe, D., Durret, F., & Adami, C. 2015, A&A submitted

Martinet, N., Durret, F., Guennou, L., et al. 2015, A&A, 575, A116

Massey, R., Heymans, C., Bergé, J., et al. 2007a, MNRAS, 376, 13

Massey, R. & Refregier, A. 2005, MNRAS, 363, 197

Massey, R., Rhodes, J., Ellis, R., et al. 2007b, Nature, 445, 286

Maturi, M., Fedeli, C., & Moscardini, L. 2011, MNRAS, 416, 2527

Mihos, J. C. & Hernquist, L. 1996, ApJ, 464, 641

Milgrom, M. 1983, ApJ, 270, 365

Miller, L., Kitching, T. D., Heymans, C., Heavens, A. F., & van Waerbeke, L. 2007, MNRAS, 382, 315

Mohr, J. J., Mathiesen, B., & Evrard, A. E. 1999, ApJ, 517, 627

Moore, B., Katz, N., Lake, G., Dressler, A., & Oemler, A. 1996, Nature, 379, 613

Moore, B., Lake, G., & Katz, N. 1998, ApJ, 495, 139

Mulchaey, J. S. 2000, ARA&A, 38, 289

Murphy, K. J., Schrabback, T., Clowe, D., et al. 2014, A&A

Negroponte, J. & White, S. D. M. 1983, MNRAS, 205, 1009

Okabe, N., Takada, M., Umetsu, K., Futamase, T., & Smith, G. P. 2010, PASJ, 62, 811

Ostriker, J. P. & Tremaine, S. D. 1975, ApJ, 202, L113

Peng, Y.-j., Lilly, S. J., Kovač, K., et al. 2010, ApJ, 721, 193

Planck Collaboration, Ade, P. A. R., Aghanim, N., et al. 2014, A&A, 571, A16

Ponman, T. J., Sanderson, A. J. R., & Finoguenov, A. 2003, MNRAS, 343, 331

Press, W. H. & Schechter, P. 1974, ApJ, 187, 425

Quilis, V., Moore, B., & Bower, R. 2000, Science, 288, 1617

Rozo, E., Wechsler, R. H., Rykoff, E. S., et al. 2010, ApJ, 708, 645

Rudnick, G., von der Linden, A., Pelló, R., et al. 2009, ApJ, 700, 1559

Schechter, P. 1976, ApJ, 203, 297

Schneider, P., Ehlers, J., & Falco, E. E. 1992, Gravitational Lenses

Seitz, C. & Schneider, P. 1995, A&A, 297, 287

Semboloni, E., Hoekstra, H., Huang, Z., et al. 2013, MNRAS, 432, 2385

Serna, A. & Gerbal, D. 1996, A&A, 309, 65

Sérsic, J. L. 1963, Boletin de la Asociacion Argentina de Astronomia La Plata Argentina, 6, 41

Sijacki, D. & Springel, V. 2006, MNRAS, 366, 397

Smith, G. P., Treu, T., Ellis, R. S., Moran, S. M., & Dressler, A. 2005, ApJ, 620, 78

Spergel, D., Gehrels, N., Breckinridge, J., et al. 2013, ArXiv: 1305.5422

Spergel, D. N., Bean, R., Doré, O., et al. 2007, ApJS, 170, 377

Spitzer, Jr., L. & Baade, W. 1951, ApJ, 113, 413

Springel, V., White, S. D. M., Jenkins, A., et al. 2005, Nature, 435, 629

Tegmark, M., Blanton, M. R., Strauss, M. A., et al. 2004, ApJ, 606, 702

Tewes, M., Cantale, N., Courbin, F., Kitching, T., & Meylan, G. 2012, A&A, 544, A8

Tinker, J., Kravtsov, A. V., Klypin, A., et al. 2008, ApJ, 688, 709

Ulmer, M. P., Adami, C., Lima Neto, G. B., et al. 2009, A&A, 503, 399

van Waerbeke, L. 2000, MNRAS, 313, 524

Voit, G. M. 2005, Reviews of Modern Physics, 77, 207

von der Linden, A., Allen, M. T., Applegate, D. E., et al. 2014, MNRAS, 439, 2

Vulcani, B., Poggianti, B. M., Oemler, A., et al. 2013, A&A, 550, A58

Wang, L. & Steinhardt, P. J. 1998, ApJ, 508, 483

White, S. D. M., Navarro, J. F., Evrard, A. E., & Frenk, C. S. 1993, Nature, 366, 429

Yang, X., Kratochvil, J. M., Wang, S., et al. 2011, Phys. Rev. D, 84, 043529

Zucca, E., Ilbert, O., Bardelli, S., et al. 2006, A&A, 455, 879

Zwicky, F. 1933, Helvetica Physica Acta, 6, 110

List of Figures[2]

List of Tables[3]

[2]Figures enclosed in published articles are not listed in the thesis list of figures.
[3]Tables enclosed in published articles are not listed in the thesis list of tables.

Appendix A

Contribution to other papers

In this appendix, I review my contribution to the following papers:

1) Durret et al. (2015): **Galaxy clusters in the SDSS Stripe 82 based on photometric redshifts** (Sect. A.1),

2) Adami et al. (2015): **Two spectroscopically confirmed galaxy structures at z = 0.61 and 0.74 in the CFHTLS Deep 3 field** (Sect. A.2),

3) Guennou et al. (2014a): **Structure and substructure analysis of DAFT/FADA galaxy clusters in the [0.4-0.9] redshift range** (Sect. A.3).

These contributions allowed me to work with different researchers, to apply and test some of the algorithms I developped to other data sets, and to obtain a better understanding of the galaxy cluster field.

A.1 Article 1: Durret et al. 2015

In this section, I review my contribution to the Durret et al. (2015) paper: **Galaxy clusters in the SDSS Stripe 82 based on photometric redshifts**.

In this study, we detect galaxy clusters in the Stripe 82 region of the SDSS, and analyze optical properties of these clusters. The detection is based on isolating over-densities in photometric redshift slices, using the Adami & Mazure Cluster Finder (Adami & Mazure 1999), and then separating structures through a minimal spanning tree. Stacking the detected galaxy clusters, we compute composite galaxy luminosity functions, and estimate the disk-to-spheroid flux ratio, both in different redshift slices from $z = 0.15$ to 0.70. Applying the same detection algorithm to the Millennium simulation, we find that these clusters are of masses between $\sim 10^{13}$ and a few $10^{14} M_{\odot}$. The GLFs are typical of those of clusters at these redshifts, but with a possible contamination from field galaxies, that could be due to false detections. The morphological study shows an increase of the early-type fraction from high redshift until today.

My main contribution to this paper is the computation of the GLFs, following the method described in Martinet et al. (2015). Cluster members are selected according to their photometric redshifts. Field galaxies measured in regions where no cluster is

detected are subtracted. The completeness limit is estimated using the SDSS apparent magnitude limit converted into an absolute magnitude limit, correcting from the k-correction at each studied redshift. Stacked GLFs are fitted with Schechter functions, the parameters of which are discussed. The Stripe 82 being less deep than the DAFT/FADA images, the high redshift faint end is difficult to discuss, while in the lower redshift bins the faint end shows a decrease. This drop of faint early-type galaxies is a bit too strong at these redshifts compared to the GLFs from Martinet et al. (2015), and a contamination from field galaxies, which show a more decreasing faint end slope (Zucca et al. 2006), is probable.

Astronomy & Astrophysics manuscript no. Durret
April 14, 2015

Galaxy clusters in the SDSS Stripe 82 based on galaxy photometric redshifts ⋆

F. Durret[1], C. Adami[2], E. Bertin[1], J. Hao[3], I. Márquez[4], N. Martinet[1], S. Maurogordato[5], T. Sauvaget[1,6,7], N. Scepi[1,8], A. Takey[9], and M.P. Ulmer[7]

[1] UPMC-CNRS, UMR7095, Institut d'Astrophysique de Paris, 98bis Bd Arago, F-75014, Paris, France
[2] LAM, OAMP, Pôle de l'Etoile Site Château-Gombert, 38 rue Frédéric Juliot-Curie, 13388 Marseille Cedex 13, France
[3] Center for Particle Astrophysics, Fermi National Accelerator Laboratory, Batavia, IL 60510, USA
[4] Instituto de Astrofísica de Andalucía, CSIC, Glorieta de la Astronomía s/n, 18008, Granada, Spain
[5] OCA, Cassiopée, Boulevard de l'Observatoire, B.P. 4229, F-06304 NICE Cedex 4, France
[6] Observatoire de Paris-Meudon, GEPI, 92195 Meudon cedex, France
[7] Department of Physics & Astronomy, CIREA, Northwestern University, Evanston, IL 60208-2900, USA
[8] ENS-Cachan, 61, avenue du président Wilson, F-94235 Cachan cedex, France
[9] National Research Institute of Astronomy and Geophysics (NRIAG), 11421 Helwan, Cairo, Egypt

Accepted . Received ; Draft printed: April 14, 2015

ABSTRACT

Context. The discovery of new galaxy clusters is important for two reasons. First, clusters are interesting *per se*, since their detailed analysis allows us to understand how galaxies form and evolve in various environments and second, they play an important part in cosmology because their number as a function of redshift gives constraints on cosmological parameters.
Aims. We have searched for galaxy clusters in the Stripe 82 region of the Sloan Digital Sky Survey, and analysed various properties of the cluster galaxies.
Methods. Based on a recent photometric redshift (hereafter photo−z) galaxy catalogue, we built a cluster catalogue by applying the Adami & MAzure Cluster FInder (AMACFI). Extensive tests were made to fine-tune the AMACFI parameters and make the cluster detection as reliable as possible. The same method was applied to the Millennium simulation to estimate our detection efficiency and the approximate masses of the detected clusters. Considering all the cluster galaxies (i.e. within a 1 Mpc radius of the cluster to which they belong and with a photo−z differing by less than ±0.05 from that of the cluster), we stacked clusters in various redshift bins to derive colour–magnitude diagrams and galaxy luminosity functions (GLFs). For each galaxy brighter than $M_r < -19.0$, we computed the disk and spheroid components by applying SExtractor, and by stacking clusters we determined how the disk-to-spheroid flux ratio varies with cluster redshift and mass.
Results. We detected 3663 clusters in the redshift range $0.15 \leq z \leq 0.70$, with estimated mean masses between $\sim 10^{13}$ and a few 10^{14} $M_\odot$. We cross-matched our catalogue of candidate clusters with various catalogues extracted from optical and/or X-ray data. The percentages of redetected clusters are at most 40% because in all cases we detect relatively massive clusters, while other authors detect less massive structures. By stacking the cluster galaxies in various redshift bins, we find a clear red sequence in the $(g' - r')$ versus r' colour-magnitude diagrams, and the GLFs are typical of clusters, though with a possible contamination from field galaxies. The morphological analysis of the cluster galaxies shows that the fraction of late-type to early-type galaxies shows an increase with redshift (particularly in 9σ clusters) and a decrease with detection level, i.e. cluster mass.
Conclusions. From the properties of the cluster galaxies, the majority of the candidate clusters detected here seem to be real clusters with typical cluster properties.

Key words. Surveys ; Galaxies: clusters: general; Cosmology: large-scale structure of Universe.

1. Introduction

The cluster count technique (e.g. Gioia et al. 1990, Allen et al. 2011) is used to constrain cosmological parameters, and requires catalogues with large numbers of clusters at various redshifts, including high redshifts (z≥1), and in extended fields of view (several tens of square degrees). This is why, with the advent of large cameras on 4m class telescopes, cluster searches at optical wavelengths have increased in number and redshift depth over these last ten years (see e.g. Durret et al. 2011b and references therein).

Several techniques have been applied to search for clusters, among which we particularly want to mention the ORCA (Overdense Red-sequence Cluster Algorithm) method, developed for the Panoramic Survey Telescope and Rapid Response System (Pan-STARRS) described in detail by Murphy et al. (2012) and applied by Geach et al. (2011, hereafter GMB; see below) to the same Stripe 82 region used in the present paper.

Other cluster searches were based on the red sequence in the colour magnitude diagram (Erben et al. 2009, Thanjavur et al. 2009). Among other techniques used to search for clusters in large imaging surveys, a matched filter detection algorithm was applied to the Canada France Hawaii Telescope Legacy Survey (CFHTLS) Deep fields (Olsen et al. 2007, 2008, Grove et al. 2009, Milkeraitis et al. 2010). The combination of optical and infrared imaging surveys has recently led to the discovery of many high redshift ($z > 1.1$) groups and clusters (Bielby et al. 2010). Lensing techniques were employed to detect massive

Send offprint requests to: F. Durret e-mail: durret@iap.fr

structures (i.e. with masses larger than 10^{13} $M_\odot$) in the CFHTLS (e.g. Cabanac et al. 2007, Gavazzi & Soucail 2007, Bergé et al. 2008, Limousin et al. 2009). More recently, weak lensing mass measurements were made for clusters in part of the CFHTLS Wide survey (Shan et al. 2012). A Bayesian cluster finder has been applied to detect galaxy clusters in the CFHTLS by Ascaso et al. (2012) and in the Deep Lens Survey by Ascaso et al. (2014). Van Breukelen & Clewley (2009) developed yet another algorithm, named 2TecX, to search for high redshift clusters in optical/infrared imaging surveys. This method is based on photometric redshifts (hereafter photo−zs) estimated from the full redshift probability function and on the identification of cluster candidates by cross-checking two different selection techniques (adaptations of the Voronoi tessellations and of the friends-of-friends method). The most recent technique, redMapper, has been developed by Rykoff et al. (2014) and applied to the SDSS DR8.

Geach et al. (2011) have searched for clusters in Stripe 82, a region of the Sloan Digital Sky Survey (SDSS) covering a surface of 270 deg^2 across the celestial equator in the Southern Galactic Cap ($-50° < \alpha < 59°$, $|\delta| \leq 1.25°$). They found 4098 clusters up to redshift $z \sim 0.6$ with a median redshift z=0.32. To do this, they applied an algorithm that searches for statistically significant overdensities of galaxies in a Voronoi tessellation of the projected sky. They define a cluster as having at least five galaxy members, so we expect them to detect a higher number of clusters than that obtained with our method. Geach et al. (2011) published a full cluster catalogue, allowing us to compare our results directly to theirs.

We have developed a method to search for clusters in large multiband imaging surveys: AMACFI (Adami & MAzure Cluster FInder, Adami & Mazure 1999). We have applied it to the CFHTLS Deep and Wide fields (Mazure et al. 2007, Adami et al. 2010, Durret et al. 2011b, hereafter M07, A10, and D11, respectively). We have recently confirmed spectroscopically two clusters at $z = 0.61$ and $z = 0.74$ detected in the CFHTLS Deep 3 field (Adami et al. 2015a), and a third one at $z = 0.53$ (Adami et al. 2015b), and this gives us yet more confidence in our method. We have also applied AMACFI to the Stripe 82 data and present our results below.

We must keep in mind that all these cluster searches produce lists of cluster *candidates*. It is therefore important to see whether different methods lead to the same cluster detections, and we will therefore compare our list of cluster candidates with other available cluster catalogues.

The paper is organized as follows. The data and method used to search for clusters is briefly summarized in Section 2. Results on cluster candidates are described in Section 3: catalogue and redshift distribution. In Section 4 we compare our cluster candidates to those found with other detection algorithms. By stacking clusters in redshift bins of 0.1, we obtained colour-magnitude diagrams and galaxy luminosity functions, and discuss these results in Section 5. We then compute in Section 6 the fraction of early- to late-type galaxies in stacked clusters as a function of redshift and of cluster mass. A brief discussion and conclusions are given in Section 7.

In this paper we assume $H_0 = 70$ km s^{-1} Mpc^{-1}, Ω_m=0.3, Ω_Λ=0.7.

2. Data and method

The SDSS has obtained many scans in the so-called Stripe 82 (hereafter S82) field, defined by right ascension approximately in the range 310° − 59° and declination $|\delta| \leq 1.25°$ (J2000). Five photometric bands are available: u', g', r', i', and z'. These repeated observations have been averaged to produce deeper and more accurate photometry than the nominal 2% single-scan photometric accuracy (Ivezić et al. 2004).

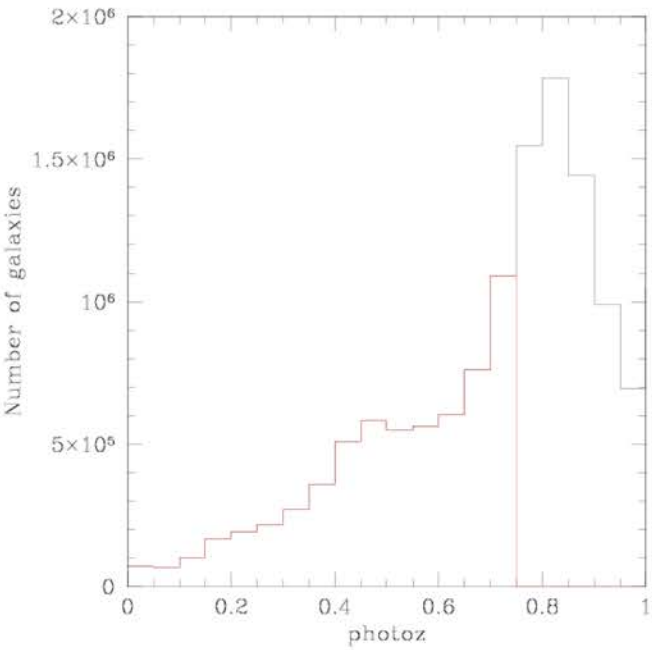

Fig. 1. Photometric redshift histogram for the initial sample of 13,621,717 objects (black) and for the selected sample of 6,110,921 objects with $z_{phot} \leq 0.75$ (red).

2.1. Stripe 82 catalogues

We started with the Msplit catalogue of 13,621,717 objects available in the SDSS database. For each object this catalogue contains the SDSS identification (19 digit number), right ascension, declination, photo−z, and error on the photo−z made by Reis et al. (2012), and is limited in magnitude to $r' < 24.5$. The photo−z histogram of these 13,621,717 objects is shown in Fig. 1. To avoid incompleteness (which becomes apparent in Fig. 1 for $z_{phot} \sim 0.8$), we cut this catalogue at $z_{phot} \leq 0.75$ and were then left with 6,110,921 objects. This photo−z catalogue was used to detect cluster candidates.

As a check to the quality of the Reis photo−z catalogue, we cross-correlated it with the SDSS spectroscopic catalogue, *SpecObj* table of the recent data release DR12. The result is shown in Fig. 2 for 105,613 galaxies. For the difference $|z_{p,\mathrm{Reis}} - z_s|$ between the Reis photo−zs $z_{p,\mathrm{Reis}}$ and the spectroscopic redshifts z_s, the mean value is 0.027, the median is 0.016, and the standard deviation is 0.047. As a comparison, we made the same correlation between the DR12 photo−zs extracted from the *Photoz* table and the spectroscopic redshifts $|z_{p,\mathrm{DR12}} - z_s|$ and found a mean value of 0.038, a median of 0.023, and a standard deviation of 0.053. This confirms that the Reis photo−z catalogue is better than the general *Photoz* DR12 catalogue, and we will therefore use the Reis catalogue for our analysis. The fact that there are very few spectroscopic redshifts above $z \sim 0.8$ to calibrate the photo−zs justifies our cut at $z_{phot} = 0.75$.

We also retrieved the dereddened magnitude catalogue of 8,485,885 objects (Annis et al. 2014) which we later cross-correlated with the photo−z catalogue to obtain a complete cata-

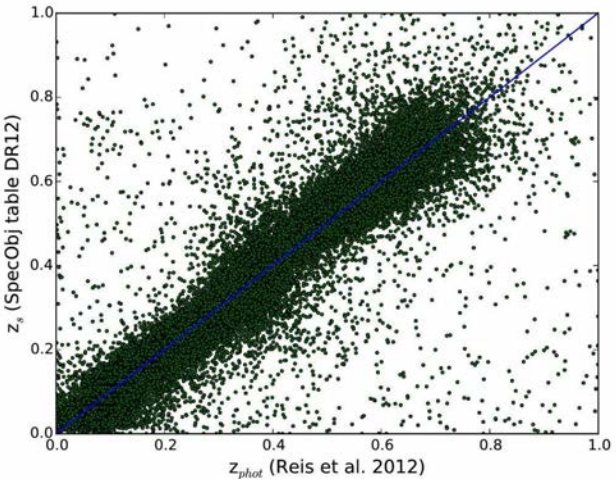

Fig. 2. Spectroscopic redshifts in the S82 region taken from SDSS DR12 versus photometric redshifts from Reis et al. (2012) for 105,613 galaxies. The blue line shows the diagonal of the square.

logue of 4,999,968 galaxies that was fed into the Le Phare software (Arnouts et al. 1999, Ilbert et al. 2006) to compute the absolute magnitudes that we will exploit further in the paper.

We first considered the curves shown in Fig. 8 of Annis et al. (2014) to estimate the 90% completeness limit of our magnitude catalogue. These give the following approximate values: u'_{lim}=23.1, g'_{lim}=22.8, r'_{lim}=22.4, i'_{lim}=22.1, and z'_{lim}=20.4. However, when drawing the magnitude histograms in the five photometric bands (see Fig. A.1) and superimposing these limits (marked as dotted vertical lines), we found that although in the u' and g' bands the Annis limits seemed acceptable (i.e. brighter than the magnitude when incompleteness becomes obvious), in the r' and i' bands these limits were obviously too faint while in the z' band the limit was too bright. We therefore take the following (rather conservative) 90% completeness limits: u'_{lim}=23.0, g'_{lim}=22.8, r'_{lim}=22.1, i'_{lim}=21.5, and z'_{lim}=21.2 (marked as full vertical lines in Fig.A.1).

2.2. Method for cluster detection

2.2.1. Overall description of the method

We applied to this photo−z catalogue the same treatment as in M07, A10, and D11, where a full description is given. This method has also been applied by A10 to the Millennium simulation (Springel et al. 2005) to assess the quality of the detections and to obtain a rough estimate of the relation between the cluster masses and the significance level at which clusters were detected. We have done the same for the S82 data, as described below.

We first divided the photo−z catalogue in slices of 0.1 in redshift, each slice overlapping the previous one by 0.05 (i.e. the first slice covers redshifts 0.1 to 0.2, the second 0.15 to 0.25, etc. and the last slice is 0.65–0.75). As discussed by A10, the 0.1 redshift width of the studied slices is the best compromise between the redshift resolution and the possible dilution of the density signal due to typical photometric redshift uncertainties. Then, to make the data manageable (in ram-active CPU memory), each subcatalogue was then divided into slices of 1.1 deg in right ascension, with an overlap of 0.1 deg between slices. No cut was made in declination.

We built galaxy density maps for each redshift slice, based on the adaptative kernel technique described in M07, with a pixel size (originally taken to be 1 arcmin) that will be discussed below and 100 bootstrap resamplings of the maps to estimate the background level correctly.

We then detected structures in these density maps with the SExtractor software (Bertin & Arnouts 1996) in the different redshift bins at various significance levels: 3σ, 4σ, 5σ, 6σ, and 9σ (as defined by SExtractor).

The structures were then assembled in larger structures (called *detections* in the following) using a minimal spanning tree friends-of-friends algorithm (see Adami & Mazure 1999). Two *detections* with centres distant by less than 2 arcmin (twice the pixel size defined originally) were merged into a single one which was assigned the redshift of the *detection* having the highest S/N. We did not merge *detections* within 2 arcmin into a single one if their photometric redshifts differed by more than 0.09 to avoid losing clusters that could be almost aligned along the line of sight but located at very different redshifts. With this separation limit (hereafter called the separation parameter), the typical uncertainty on cluster positions is therefore about 2 arcmin. This respectively corresponds to 310 kpc and 860 kpc at $z = 0.15$, the lowest redshift, and $z = 0.7$, the highest redshift in our cluster sample. We also briefly discuss below the influence of the choice of this separation limit on the final cluster catalogue.

2.2.2. Choice of pixel size for the density maps and of the separation parameter

We initially built galaxy density maps for each redshift slice, with a pixel size of 1.002×1.002 arcmin^2. With this pixel size we obtained a cluster catalogue containing 956 clusters in the redshift range of 0.15–0.7. Since S82 covers an area of 270 deg^2, the spatial density of this catalogue is 956/270 = 3.54 clusters deg^{-2}, while if we consider the clusters detected in the CFHTLS–Wide 1, Wide 2, Wide 3, and Wide 4 (D11) in the same redshift range ($0.15 \leq z \leq 0.70$), we find respective densities of 17.0, 15.9, 14.8, and 16.6 clusters deg^{-2}, using a pixel size of 0.54 arcmin and a separation parameter of 3 arcmin. When the search for clusters in the CFHTLS was made, the separation parameter was still an angle, while in the minimal spanning tree code we now implement a separation in Mpc, which is more physical. So our detection level in S82 was smaller than that of the CFHTLS–Wide by a factor between 4.2 and 4.8. A first explanation could be that the S82 catalogue is shallower than that of the CFHTLS, and does not reach similar redshifts and/or magnitudes. However, if we compare the galaxy photo−z histogram of the S82 to that of the CFHTLS Wide survey (Fig. 2 in D11, black line), we can see that the S82 histogram starts decreasing for z>0.85, while the CFHTLS–Wide starts decreasing for z>0.90, so the photo−z completeness limit of S82 is lower than that of the CFHTLS–Wide only by $\sim$ 0.05. If we compare the magnitude completeness limits of the two surveys, the S82 90% completeness limit is reached for r$\sim$ 22.1 according to Annis et al. (2014). In the CFHTLS–Wide, incompleteness begins to show for $i' \sim 23.5$, which corresponds to r' between 22.5 and 23 (for an elliptical galaxy at redshift 0.2 or 0.5, respectively), showing that the S82 catalogue is shallower that the CFHTLS–Wide only by approximately half a magnitude. So the discrepancy by a factor of 4 between the density of clusters detected with AMACFI in the two surveys seems too large to be explained only by their difference in depth. This led us to question our method and to

make several tests, first on the pixel size chosen to compute the density maps on which our cluster detection is based, and second on the separation parameter.

Since the CPU time necessary to compute density maps increases dramatically as the pixel size decreases (and hence the number of pixels increases), we made the following tests on a subregion of S82 covering 1 <RA< 10 deg, with the full declination range $|\delta| \leq 1.25°$. We considered pixel sizes of 30×30 arcsec^2, 15×15 arcsec^2, and 10×10 arcsec^2. As the pixel size decreases, the number of structures detected increases, so the completeness of the cluster catalogue increases. However, we must be careful not to start detecting very small structures that cannot be clusters, because in this case the purity of the cluster catalogue will decrease.

As mentioned above, we took a separation parameter of 2 Mpc. Since the separation parameter could have an influence on the number of candidate clusters detected, we made tests with separation parameters of 1 Mpc, 2 Mpc, and 3 Mpc, and the results are given below.

We also tested how the quality of the photo−zs could influence the numbers of candidate clusters detected by applying two different selections. First, we considered only the galaxies with an error $\delta_{zp} \leq 0.1$ on their photo−z. Such a cut reduces the number of galaxies with photo−$z \leq 0.75$ from 6,110,921 to 2,458,235, and therefore excludes 59.8% of the galaxies. Second, we considered only the galaxies with a relative error smaller than 50%: $\delta_{zp}/z_p \leq 0.5$. In this case, the total number of galaxies drops from 6,110,921 to 4,469,271, and thus we exclude 26.9% of the galaxies.

In order to have an objective criterium for the choice of the cluster detection parameters, we considered the plots showing the cumulative number of clusters hotter than 2 keV expected in a region of 800 deg^2 for different cosmologies as a function of redshift, taken from Romer et al. (2001), Fig. 5b. The mass-temperature relation of Xu et al. (2001) implies that kT>2 keV corresponds to clusters of masses $M_{r200} > (1.2-1.6) \times 10^{14}$ M$_\odot$. As a first test, we overplotted on these curves the densities of clusters detected by D11 in the four CFHTLS Wide fields. We found a very good agreement between our cluster densities and the Romer curves for $\Omega_0 = 0.3$ when considering the clusters detected at 4σ and above, as illustrated in Fig. 3 (top). We then overplotted on the same curves the densities of clusters detected at a 4σ level in a subregion of S82 defined by 1 <RA< 10 deg and $|\delta| \leq 1.25°$ for the nine cases summarized in Table 1.

In Table 1, for each case we give the pixel size chosen to compute the density maps and the "separation", that is the minimum value above which two detected structures are considered to be different if they differ by more than 0.09 in redshift. In some cases we have also applied a cut based on the error on the photo−z.

We now compare the numbers of clusters detected at a 4σ level and higher in Stripe 82 to the Romer et al. (2001) curves, as shown in Fig. 3 (bottom). First, we can see that our original choice of parameters (case 1) leads to a number of clusters that is much too small. Pixel sizes of 30×30 arcsec^2 (case 2) and 15×15 arcsec^2 (case 5) also lead to too few clusters. If we take a separation equal to 1 Mpc or 3 Mpc (cases 4 and 7, respectively), the numbers of clusters fall clearly above and below the Romer curve, so we decided to keep a separation of 2 Mpc. The number of clusters detected in case 8 is also much too small. The best match with the Romer et al. curves is obtained for cases 3, 6, and 9. In order to keep our sample as similar as possible to the cluster sample extracted in the CFHTLS-W, we chose to make the cluster detection on the full catalogue (limited to $z_p \leq 0.75$, but with no condition on the photo−z error) with a pixel size of 10×10 arcsec^2 and a separation of 2 Mpc (case 3).

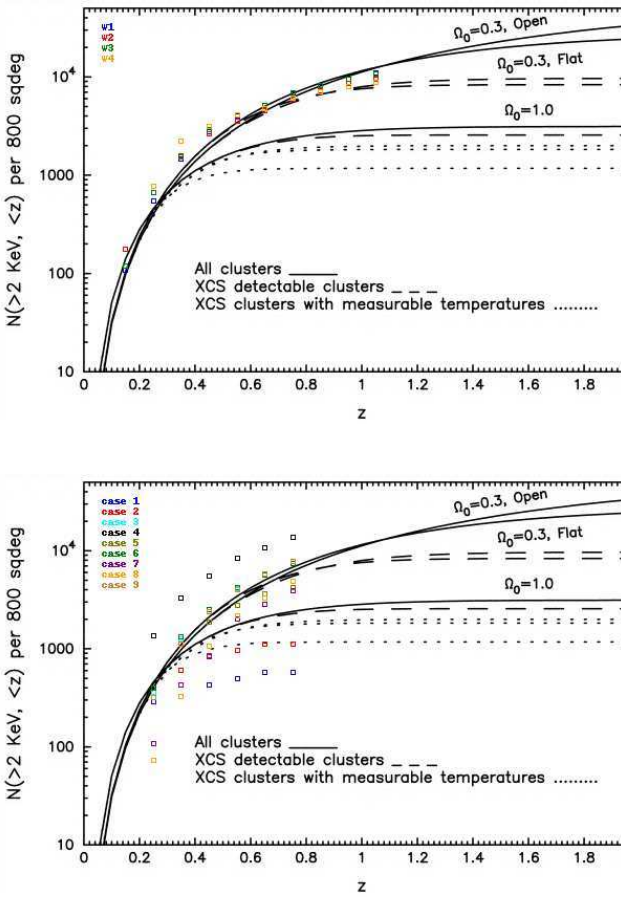

Fig. 3. Cumulative number of clusters hotter than 2 keV expected in a region of 800 deg^2 for different cosmologies as a function of redshift, taken from Romer et al. (2001), Fig. 5. The numbers of clusters in the four CFHTLS–Wide fields are shown in the top figure, and the numbers detected in Stripe 82 for the various cases described in Table 1 (see text) are plotted in the bottom figure. Only clusters detected at a 4σ level and above are taken into account.

In this way we obtained a final catalogue of 3663 candidate clusters detected at a significance level from 3σ to 9σ. This catalogue– including for each cluster the coordinates, photo−z, detection level and number of cluster galaxies– will be available at the VizieR interface of the Simbad database[1].

3. Cluster catalogue

3.1. Significance level and spatial distribution of the candidate clusters

In the catalogue of 3663 cluster candidates, the numbers of clusters detected at the various significance levels of 3σ, 4σ, 5σ, 6σ, and 9σ are: 1133, 792, 623, 820, and 295, respectively. In Sections 5 and 6 we concentrate on the properties of the 2530 clusters detected at 4σ and above to limit our analysis to the objects that are the most likely to be real clusters.

[1] http://vizier.u-strasbg.fr/viz-bin/VizieR

Table 1. Cases considered in the various tests on cluster detection parameters. The columns are: (1) running number of test; (2) pixel size chosen to compute the density maps; (3) separation, that is the minimum value above which two detected structures are considered to be different if they differ by more than 0.09 in redshift; (4) cut depending on the photometric redshift uncertainty when applicable.

Case	pixel size (arcsec× arcsec)	separation (Mpc)	cut on z_p
1	60×60	2	–
2	30×30	2	–
3	10×10	2	–
4	10×10	1	–
5	15×15	2	–
6	10×10	2	$\Delta z_p/z_p \leq 0.5$
7	10×10	3	$\Delta z_p/z_p \leq 0.5$
8	10×10	3	$\Delta z_p \leq 0.1$
9	10×10	3	–

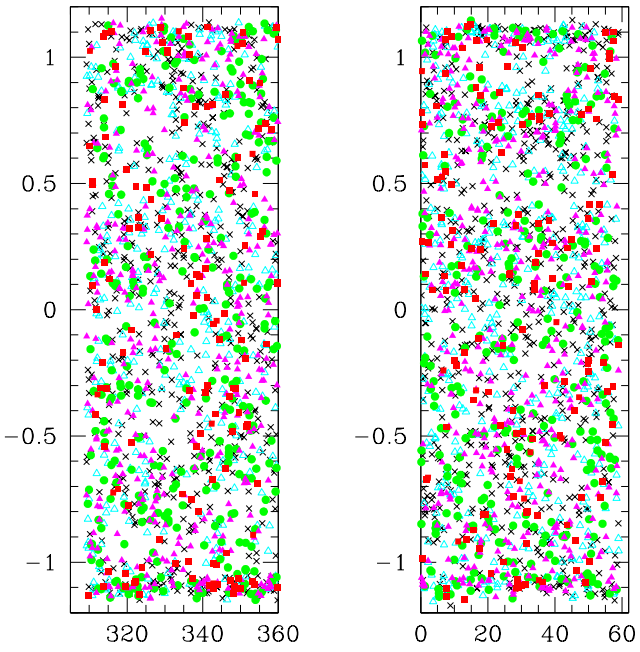

Fig. 4. Projected spatial distribution of the 3663 candidate clusters, colour coded as follows: red squares: S/N=9σ, magenta filled triangles:S/N= 6σ, green filled circles: S/N= 5σ, cyan empty triangles: S/N= 4σ, black crosses: S/N= 3σ.

The projected spatial distribution of all the detected clusters is shown in Fig. 4 with different symbols for the various significance levels. We can see concentrations of candidate clusters at the edges in declination, for $|\delta| \sim 1.1 - 1.2$, which are most probably spurious detections. We keep these objects in our final catalogue for the sake of completeness, but we note this shortcoming.

3.2. Redshift distribution of the candidate clusters

The photometric redshift distribution of the 3663 candidate clusters detected in S82 in the redshift range 0.15–0.7 (divided by 270 deg^2 to obtain a surface density directly comparable to those found in the literature) is shown in Fig. 5. This photo−z distribution has a mean value of 0.51 and a median of 0.53, with dispersions of 0.15 around these values. The median redshift of our clusters is notably higher than the median redshift z=0.32 found by Geach et al. (2011) for their sample of 4098 clusters, and the comparison between both samples will be made in Section 4.

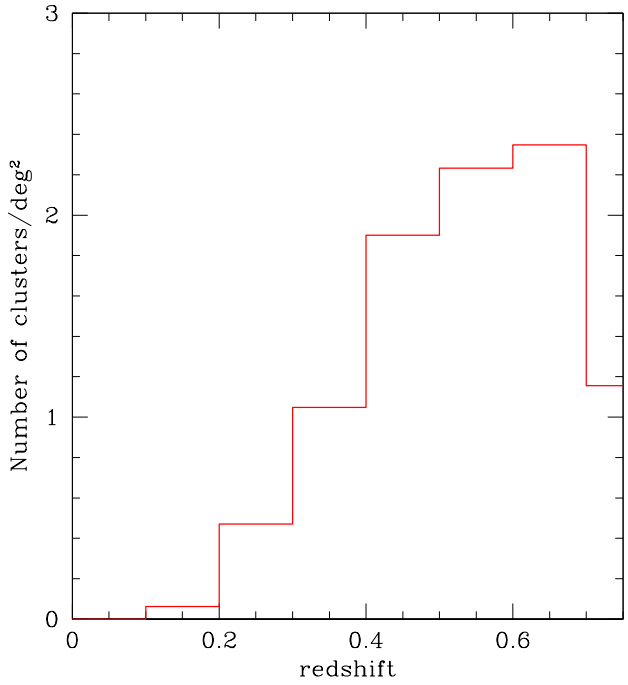

Fig. 5. Histogram of the surface density of cluster candidates in S82 as a function of photometric redshift.

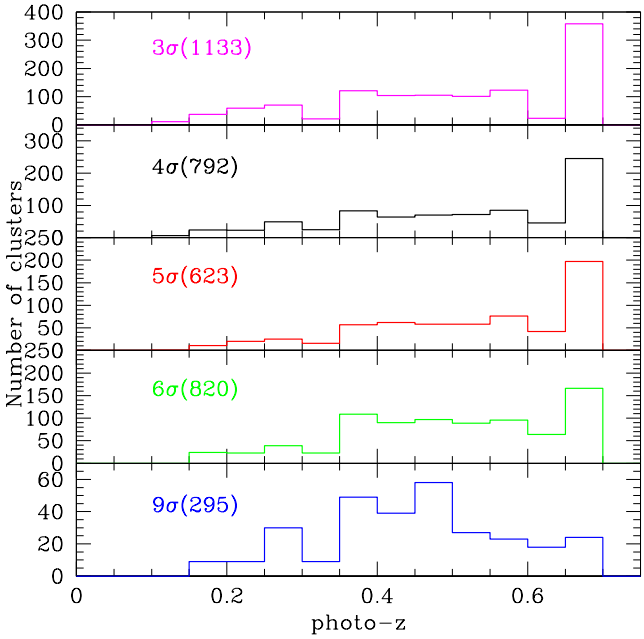

Fig. 6. Photometric redshift histograms of the 3663 candidate clusters detected in S82 for various detection significance levels (indicated in each plot, together with the corresponding number of clusters in parentheses). For clarity, the scale of the y-axis is not the same for each plot.

The photo−z histograms for clusters detected at different significance levels are shown in Fig. 6.

Table 2. Percentages of Millennium haloes detected with our method as a function of lower mass cutoff. The columns are: (1) halo mass in units of 10^{12} $M_\odot$; (2)–(7) percentages of redetected haloes in the following redshift intervals: $z1 : z \leq 0.2$, $z2 : 0.2 < z \leq 0.3$, $z3 : 0.3 < z \leq 0.4$, $z4 : 0.4 < z \leq 0.5$, $z5 : 0.5 < z \leq 0.6$, and $z6 : 0.6 < z \leq 0.8$.

M_{halo}	$z1$	$z2$	$z3$	$z4$	$z5$	$z6$
250	-	100	66	33	20	0
65	66	68	54	10	5	0
20	75	68	59	2	1	0
7.5	76	63	67	2	1	0
3.0	67	64	59	1	1	0

3.3. Cluster masses

By applying the same detection method to the Millennium simulation, we have shown (see A10, Table 2) that there is a rough correspondence between the cluster detection level and its mass. We have redone the same exercise, selecting data from the Millennium simulation and adapting them to the conditions of the S82 data analysed here, in terms of photometric redshift precision and photometric catalogue depth.

We ran AMACFI on this catalogue, exactly in the same way as for the S82 galaxy catalogue, and detected 30 structures. The percentages of detected haloes are given in Table 2 for five classes with masses ranging from 3.0×10^{12} $M_\odot$ to 2.5×10^{14} $M_\odot$ in six redshift bins: $z \leq 0.2$, $0.2 < z \leq 0.3$, $0.3 < z \leq 0.4$, $0.4 < z \leq 0.5$, $0.5 < z \leq 0.6$, and $0.6 < z \leq 0.8$.

We can see that for all the haloes the percentage of detections is larger than about 60% up to $z \sim 0.4$. In the next redshift bin, this percentage drops to 33% and 10% for the two most massive haloes and becomes extremely low for the three least massive haloes. The corresponding orders of magnitude for the masses are that clusters detected at 3σ and 4σ have masses in the approximate range $[10^{13} - 10^{14}$ $M_\odot]$, while clusters detected at 6σ have masses larger than 10^{14} $M_\odot$. As in A10, because the Millennium simulation only covers an area corresponding to 1 deg^2, it includes no cluster corresponding to a 9σ detection in our study, so we cannot estimate the typical mass of the clusters detected at a 9σ level; all we can say is that these clusters must have masses larger than 10^{14} $M_\odot$.

By varying the detection parameters used in SExtractor, we estimate that the errors on these halo masses are of the order of 5%.

3.4. Cluster spatial density

We found 3663 clusters in a region of about 270 deg^2 in the redshift range 0.15–0.70, which gives a detection rate of about 13.6 clusters per square degree. Geach et al. (2011) detected 3896 clusters in the same redshift range, corresponding to about 14.4 clusters per square degree, a detection rate 1.06 times higher than ours. This small difference is most probably due to the fact that they call "a cluster" any structure with five galaxies or more. The application of our cluster detection method to the Millennium simulation shows that the minimum mass of a 3σ detected cluster is $\sim 10^{13}$ $M_\odot$, and we therefore do not detect less massive structures.

We can also compare the cluster density that we find in S82 with that found in the four CFHTLS Wide fields. In these fields, we have detected 4061 candidate clusters at 3σ and above, corresponding to between 21 and 28 clusters per square degree (depending on the field considered), reaching redshift 1.15 (see D11). The corresponding cluster densities for $0.15 \leq z \leq 0.7$ are between 14.8 and 17.0 clusters per square degree. The cluster density detected in S82 is therefore of the same order of magnitude as in the CFHTLS, as seen from the comparison of Fig. 5 in the present paper with Fig. 7 (bottom) in D11.

Table 3. Common systems in our cluster catalogue and in other optically and X-ray selected cluster catalogues within a search radius of 2 Mpc. The percentages of recovered systems in the published catalogues are given in parentheses.

Catalogue	z_{phot} range	N_{ClG}	$N_{ClG,match}$ $\Delta z < 0.05$	$N_{ClG,match}$ $\Delta z < 0.1$
GMB	$0.15 \leq z_p \leq 0.70$	3896	472 (12%)	838 (22%)
WHL12	$0.15 \leq z_p \leq 0.70$	2901	538 (19%)	838 (29%)
RedMaPPer	$0.15 \leq z_p \leq 0.55$	665	188 (28%)	268 (40%)
XCS-DR1	$0.15 \leq z_p \leq 0.70$	28	5 (18%)	7 (25%)
XMM/SDSS	$0.15 \leq z_p \leq 0.68$	30	5 (17%)	6 (20%)

3.5. Number and magnitude distributions of the cluster galaxies

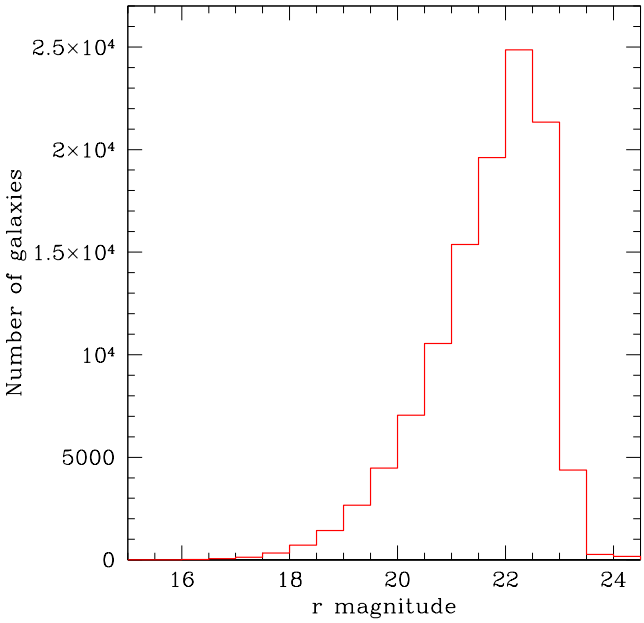

Fig. 7. Magnitude histogram of the cluster galaxies in the r band.

We define cluster galaxies as the galaxies located within a circle of 1 Mpc radius around each cluster and within ±0.05 of the redshift of the cluster to which they belong. The magnitude histogram of the 113,411 cluster galaxies in the r band is shown in Fig. 7.

4. Comparison with optically and X-ray detected clusters in S82

We have cross-correlated our catalogue of candidate clusters with several catalogues extracted from optical and/or X-ray data: GMB, WHL12 (Wen et al. 2012), RedMaPPer (Rykoff et al. 2014), XCS-DR1 (Mehrtens et al. 2012), and XMM/SDSS (Takey et al. 2013, 2014). The matching criteria were a linear

separation smaller than 2 Mpc and a redshift difference smaller than 0.05 or 0.1 (see e.g. Hao et al. 2010). The numbers of clusters in common are given in Table 3.

Geach et al. (2011) detected 4098 clusters in the S82 region, but with a different definition, since they consider that a cluster begins with five galaxies. The number of recovered clusters from the GMB catalogue is 22%, a rather low number. This can be explained by the fact that 73% of the GMB clusters have less than ten members, while the clusters in our sample with the lowest richness have several tens of galaxies.

The rather low number of recovered clusters from the WHL12 catalogue (29%) can be explained in the same way: 30% of the clusters in WHL12 have 10 members or fewer (in the r'_{200} radius), and 86% have 20 members or fewer, so WHL12 detect clusters that are mostly less massive than ours.

In the RedMaPPer catalogue, Ryckoff et al. (2014) give two parameters (Λ and S) that can be used to determine the number of cluster galaxies $N = \Lambda/S$, where N is in the range 20–203. About 64% of their clusters have $N < 30$ and their cluster masses are $M_{r200} \geq 10^{14}$ $M_\odot$. We recover 40% of their clusters.

Since the detection of our candidate clusters as diffuse X-ray sources would be an obvious way to confirm that they are real clusters, we also correlate our detections with the XCS-DR1 catalogue (Mehrtens et al. 2012). This X-ray catalogue has 41 clusters in the S82 region (as defined in Section 1), among which 28 are in the same redshift range as ours. Our matching percentage is 25%.

A similar survey to the XCS is the 2XMMi/SDSS galaxy cluster survey (Takey et al. 2011, 2013, 2014) that provided 35 clusters in the S82 region. Of these, 30 clusters are almost in the same redshift range [0.15–0.68] as our S82 cluster candidates. About 70% of these clusters have masses $M_{500} < 10^{14}$ $M_\odot$. With our cross-matching criteria, we have recovered 20% of the 2XMMi/SDSS clusters that are in the S82 region and in the redshift range 0.15–0.68.

Other observational biases can, however, be present. X-ray serendipitous surveys such as the XCS and 2XMMi/SDSS make use of existing XMM observations for which the main targets are most of the time not the detected clusters. For example, bright stars or large nearby galaxies can have been targeted, and this would obviously result in a large masking percentage of the S82 optical data, potentially preventing us from detecting the X-ray extended structure as a galaxy concentration. In addition, these serendipitous surveys of clusters avoided the clusters (usually the massive ones) that were targets of pointed XMM-Newton observations. All these observational biases reduce the recovered fraction of the X-ray selected clusters. It is worth performing a detailed comparison of X-ray clusters and our S82 clusters similar to the X-CLASS-redMaPPer galaxy cluster comparison (Sadibekova et al. 2014). We therefore plan in the near future to make this detailed comparison.

5. Properties of stacked clusters

In this section we will limit our analysis to the 1738 clusters detected at 5σ and above, and to galaxies within a radius of 1 Mpc of a cluster and with a photo$-z$ within ± 0.05 of that of the corresponding cluster for two reasons: first, to avoid having too much contamination by galaxies that do not belong to the clusters, and second to derive galaxy luminosity functions (GLFs) in redshift bins of width 0.1 that do not overlap.

5.1. Colour-magnitude diagrams

We first derive colour-magnitude diagrams by stacking galaxies in photometric redshift bins. The red sequence is apparent in all colour-magnitude diagrams, but the $(g - r)$ versus r' colour-magnitude diagram is the one that shows the smallest dispersion, and so we use it to select cluster galaxies and build GLFs. We show these diagrams in five redshift bins in Figs. 8 and 9, respectively, before and after background correction (see Section 5.2.2 for explanations on the method used to subtract the background contribution).

The fact that we detect a red sequence shows that we have selected galaxies with similar star formation histories that belong to well-assembled structures, and therefore that our candidate clusters are mostly old galaxy structures. As seen in these figures, the red sequence defined by the cluster galaxies is in good agreement with the predictions of the Bruzual & Charlot (2003) model.

5.2. Galaxy luminosity functions

5.2.1. Computing absolute magnitudes and 90% completeness limits

In order to be able to stack the cluster GLFs it was necessary to compute absolute magnitudes for all the galaxies. For this, we applied the Le Phare software as described in Section 2.1, with photo$-z$s fixed to the SDSS values.

Since the GLF parameters can strongly vary with the magnitude interval in which they are computed (as discussed e.g. by Martinet et al. 2015 and references therein), it is necessary to estimate the absolute magnitudes for which the completeness is better than 90%. For this, our starting point is the 90% completeness limits given in Section 2.1: $u' \sim 23.0$, $g' \sim 22.8$, $r' \sim 22.1$, $i' \sim 21.5$, and $z' \sim 21.2$. We computed the corresponding 90% completeness limits in absolute magnitudes with two independent methods.

First, we translated these apparent magnitude completeness limits to absolute magnitude completeness limits by applying in each redshift bin the k-correction and distance modulus. Le Phare uses galaxy SED model libraries to estimate the theoretical k-corrections that depend on galaxy types and redshifts. For early-type galaxies, we measure the mean and the dispersion of the k-correction over galaxy templates in a redshift range of ± 0.05 around the cluster redshift. We set our corrective factors to the mean values plus 2σ to be representative of 95% of our galaxy population. This step is illustrated in Eq. 1 where C_X and C_x are the completeness limits in absolute and apparent magnitude in the x band, $DM(z)$ is the distance modulus, and $k_x(z)$ the k-correction in the x band at redshift z:

$$C_X = C_x - DM(z) - (< k_x(z) > + 2\sigma_{k_x(z)}). \quad (1)$$

With this method we obtained the 90% completeness limits in absolute magnitude for each filter and each redshift bin. These values are given in the last column of Table 4.

As a check, we also performed simulations for 112 clusters. For this, we first selected in each cluster the galaxies with a photo$-z$ within ± 0.05 of that of the cluster (i.e. galaxies for which the distance modulus and k-corrections are known) and with no nearby neighbour (i.e. no galaxy within 3 times their size) to avoid crowding effects. We extracted the image of each of these galaxies, subtracted the background computed around each galaxy at a distance larger than 3 times the galaxy size

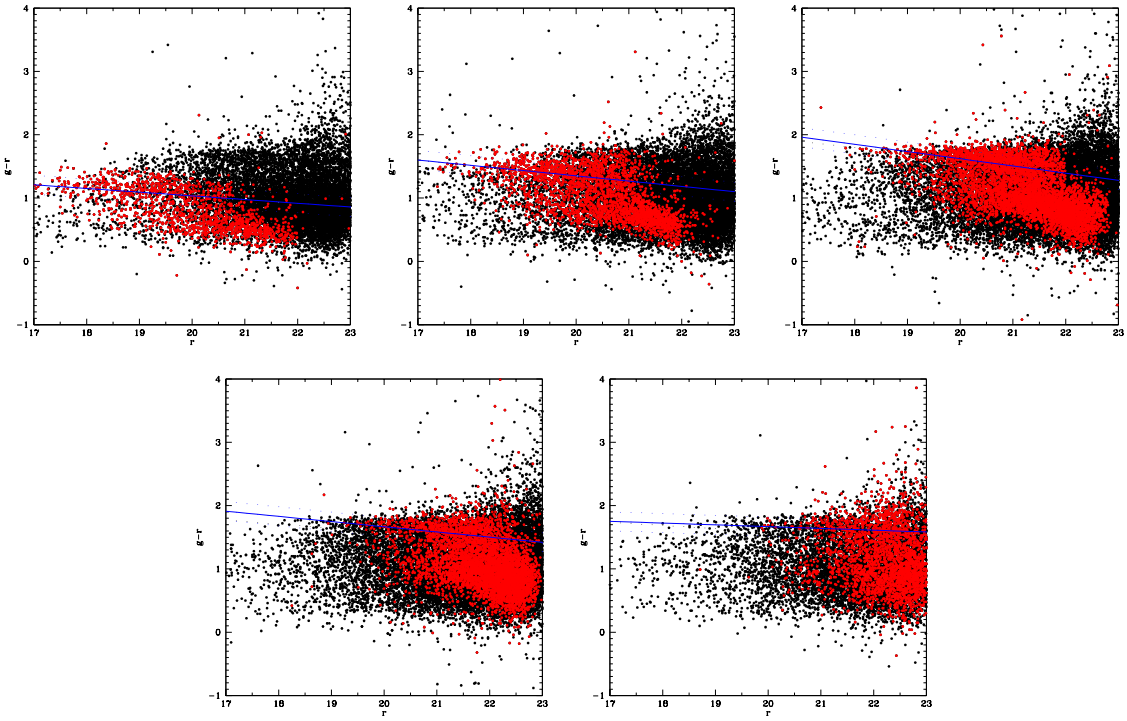

Fig. 8. Colour-magnitude diagrams ($(g-r)$ versus r') stacked in the five redshift bins (from left to right: $0.15 < z < 0.25$, $0.25 < z < 0.35$, $0.35 < z < 0.45$, $0.45 < z < 0.55$, $0.55 < z < 0.65$) before background subtraction (see text). The black points show all the galaxies within a radius of 1 Mpc of a cluster, and the red points correspond to the galaxies with a photometric redshift within ±0.05 of that of the cluster to which they belong. The solid blue line shows the best fit.

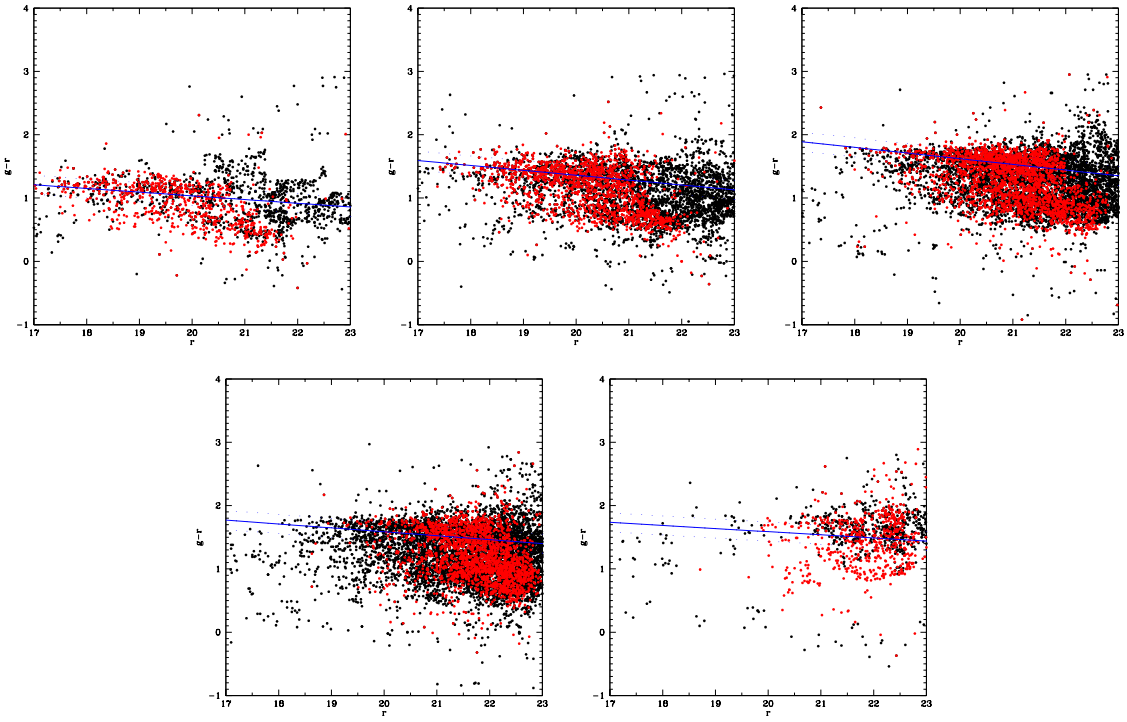

Fig. 9. Same as Fig. 8 after background subtraction.

(as measured by SExtractor), and added this background subtracted image 100 times at uniformly distributed random locations within a square of 2000 × 2000 pixels^2 centred on the cluster centre. We then redetected the galaxy on the image with SExtractor and noted how many times it was redetected. This allowed us to estimate the number of times we could redetect a galaxy with the absolute magnitude of the considered galaxy. By applying this treatment to all the cluster galaxies, we thus recon-

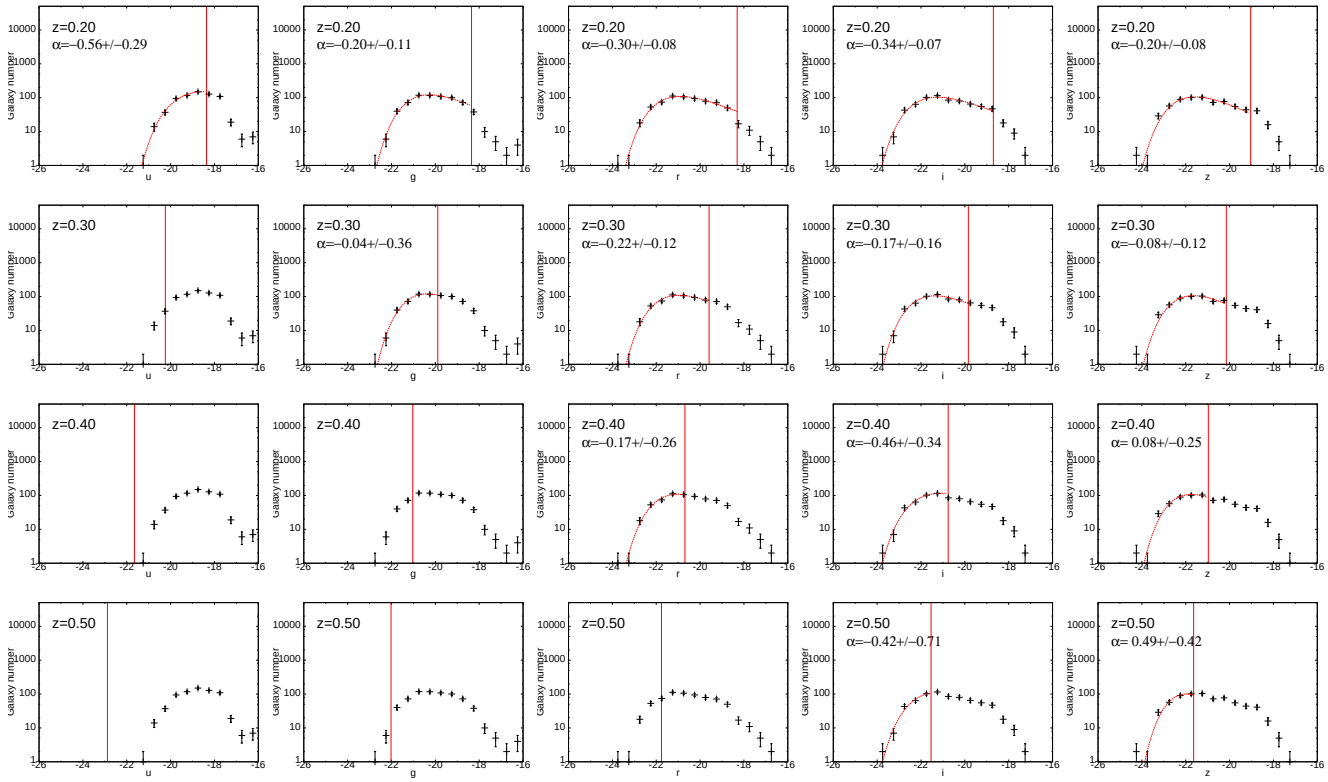

Fig. 10. GLFs in the u, g, r, i and z bands (from left to right). Black crosses are the stacked GLFs with no surface normalization. The red curves are the best Schechter fits corresponding to the black crosses. The vertical red lines indicate the 90% completeness limits. Only galaxies brighter than the 90% completeness limit are taken into account for the fits. The plots for which no Schechter parameters are given in Table 4 are only shown for completeness, but will not be taken into account in the discussion.

structed a completeness curve as a function of absolute magnitude. Since such a computation is only valid for a small magnitude range, we repeated it for galaxies 10 times brighter (with magnitudes smaller by 2.5) and 10 times fainter (with magnitudes larger by 2.5), and obtained curves such as those shown in Fig. B.1 for the i' band. This method has obvious limitations, but it gives 90% completeness limits very close to those estimated with our first method, in most cases within one 0.5 magnitude bin, thus giving us confidence in our completeness level estimates. Hereafter, we will limit our GLF fits to the 90% completeness absolute magnitude limits derived with the first method.

5.2.2. Background subtraction

As stated above, we extracted a catalogue containing all the galaxies located within a 1 Mpc radius around each cluster and with a photo$-z$ within ± 0.05 of that of the corresponding cluster. The composite $(g'-r')$ versus r' colour magnitude diagrams have been corrected for contamination from background/foreground galaxies in a statistical way. For this purpose, the field colour-magnitude diagram has been estimated from the whole S82 distribution, excluding galaxies in a given physical radius (in our case 1 h^{-1} Mpc) around the position of detected clusters. The statistical correction has been performed following the method described in Pimbblet et al. (2002). Counts in the "cluster + field" and "field" populations are estimated in a grid in the colour-magnitude diagram, and the probability of a galaxy in a colour-magnitude bin of being a field galaxy is derived and used to statistically subtract the field population. This method has been applied to the composite clusters stacked in photo$-z$ bins. In the case of subsamples of the stacks where galaxies are selected in a photometric redshift window around the cluster mean redshift, a grid in the colour-magnitude-photometric redshift space is used. More details will be provided in Maurogordato et al. (in preparation).

After this statistical background subtraction was applied, for each redshift bin we extracted the galaxies located in the red sequence of the $(g'-r')$ versus r' colour magnitude diagrams and thus obtained the GLFs that we fit with a Schechter function:

$$N(M) = 0.4\ log_{10}\phi^*[10^{0.4(M^*-M)}]^{\alpha+1} exp\ (-10^{0.4(M^*-M)}). \qquad (2)$$

5.2.3. Results

We stacked the 1738 clusters detected at 5σ and above, limiting our analysis to the galaxies within a radius of 1 Mpc of a cluster and with a photo$-z$ within ± 0.05 of that of the corresponding cluster and subtracting the background as explained above. This allowed us to obtain stacked GLFs in the same five redshift bins as for the colour-magnitude diagrams.

The GLFs in the u', g', r', i', and z' bands are shown in Fig. 10 and the parameters of the best fit Schechter functions are given in Table 4. No values were given in Table 4 when the fits did not converge. This happened mostly when the number of points brighter than the 90% completeness limit became too

Table 4. Parameters of the best fit Schechter functions for the galaxy luminosity functions in the five bands and in the five redshift bins.

redshift/ filter	α	M*	ϕ*	90% completeness
z=0.20				
u'	−0.56 ± 0.29	−19.2 ± 0.2	368± 50	−18.4
g'	−0.20 ± 0.11	−20.5 ± 0.1	352± 23	−18.4
r'	−0.30 ± 0.08	−21.3 ± 0.1	306± 21	−18.3
i'	−0.34 ± 0.07	−21.7 ± 0.1	285± 22	−18.7
z'	−0.20 ± 0.08	−21.8 ± 0.1	304± 19	−19.0
z=0.30				
u'	–	–	–	−20.2
g'	−0.04± 0.36	−20.4± 0.2	353± 24	−19.9
r'	−0.22± 0.12	−21.2± 0.1	314± 22	−19.6
i'	−0.17± 0.16	−21.6± 0.1	307± 23	−19.8
z'	−0.08± 0.12	−21.7± 0.1	314± 18	−20.1
z=0.40				
u'	–	–	–	−21.6
g'	–	–	–	−21.0
r'	−0.17± 0.26	−21.2± 0.2	315± 21	−20.7
i'	−0.46± 0.34	−21.7± 0.2	302± 41	−20.8
z'	0.08± 0.25	−21.7± 0.1	315± 19	−21.0
z=0.50				
u'	–	–	–	−22.9
g'	–	–	–	−22.0
r'	–	–	–	−21.8
i'	−0.42± 0.71	−21.7± 0.4	303± 39	−21.5
z'	0.49± 0.42	−21.5± 0.2	267± 54	−21.6

small for a three-parameter fit. In some cases, the fits converged, but gave values with large error bars. We chose to show these values in Table 4 to keep the information as complete as possible, but they should be considered with caution.

In Fig. 10 it can be seen that in some cases there is an excess of very bright galaxies over the Schechter function, mostly in the z' band. This feature is rather common, particularly in merging clusters (see e.g. Durret et al. 2011a and references therein). We checked the possibility that this excess could be due to bright stars misclassified as galaxies in one cluster. For this we detected all the objects with SExtractor in the i' band image and plotted the maximum surface brightness as a function of magnitude ($\mu_{\rm max,i} - i$ diagram). The bright objects from our initial galaxy catalogue that could account for the excess of bright galaxies in the GLF are all very clearly located in the galaxy zone in the $\mu_{\rm max,i} - i$ diagram, so it seems likely that the excess of very bright galaxies detected in some cases is real, and not due to bright stars misclassified as galaxies.

If we now consider the faint end slope of the GLF, we can see that α is above −1, traducing a decrease in the faint galaxy population, and this drop becomes more significant with increasing redshift, at least in the bands where the fit converges in the highest redshift bins. As expected from the relative shallowness of the images in the u' band, the GLFs can only be computed in the first redshift bin.

At low redshifts there are fewer faint galaxies than expected (α is notably larger than the expected value of ~ -1), probably in part due to background contamination. The α parameter of early-type field GLFs is about −0.16 in U and −0.31 in the V, R and I bands in the redshift range $0.4 < z < 0.9$, and is found to depend only weakly on redshift (Zucca et al. 2006).

6. Morphological properties of cluster galaxies

6.1. Early- to late-type galaxy fraction

Based on the catalogue of clusters that we have detected in a homogeneous way, we now analyse statistically the morphological properties of the galaxies belonging to these clusters (or at least having a high probability of being in these clusters, since this study is based on photometric redshifts). With the large number of cluster galaxies available, this allows us to estimate the variations of the late- to early-type number ratio as a function of redshift and of detection level. Because the positions of the cluster centres are not well defined, we will not attempt to search for variations of the elliptical-to-spiral number ratio as a function of clustercentric radius. We consider here the cluster galaxies, with the definition given in Section 5.

To estimate the morphological properties of the galaxies, we extracted images around each cluster, covering an area of 1×1 Mpc^2 at the cluster redshift, with a pixel scale of 0.396 arcsec/pixel, in the r' band. We applied a tool developed in SExtractor that calculates the respective fluxes in the bulge (spheroid) and disk for each galaxy. This new experimental SExtractor feature fits to each galaxy a two-dimensional model comprised of a de Vaucouleurs spheroid (the bulge) and an exponential disk. Briefly, the fitting process is very similar to that of the GalFit package (Peng et al. 2002) and is based on a modified Levenberg-Marquardt minimization algorithm. The model is convolved with a supersampled model of the local point spread function (PSF), and downsampled to the final image resolution. The PSF model used in the fit was derived with the PSFEx software (Bertin 2011) from a selection of point source images. The PSF variations were fit using a six–degree polynomial of x and y image coordinates. The model fitting was carried out in the r' band.

We used this tool to look for differences in galaxy morphologies as a function of redshift and of significance level (which is related to cluster mass) by computing the flux in the disk f_{disk} and that in the spheroid $f_{spheroid}$ for each galaxy. We classified a galaxy as early-type if $f_{spheroid}/(f_{disk} + f_{spheroid}) \geq 0.35$ and as late-type if $f_{spheroid}/(f_{disk} + f_{spheroid}) < 0.35$, as in Simard et al. (2009). SExtractor also computes the 1σ uncertainties on these fluxes and on the $f_{spheroid}/(f_{disk} + f_{spheroid})$ flux ratio. We must note that the distribution of the estimated uncertainties can be highly asymmetric and that the limiting value of 0.35 for the $f_{spheroid}/(f_{disk} + f_{spheroid})$ ratio to distinguish early and late types is somewhat arbitrary (see e.g. Simard et al. 2009 and references therein).

Before stacking clusters and searching for variations of galaxy morphologies with redshift, it is necessary to make a cut in absolute magnitude in order to have comparable samples in all the redshift bins. We make the choice of the limiting magnitude by considering the redshift range that imposes the strongest constraints on the relative uncertainty on the spheroid-to-total ratio: $0.4 \leq z < 0.75$. A plot of this uncertainty as a function of absolute magnitude for all the cluster galaxies in the redshift range $0.4 \leq z < 0.75$ is shown in Fig. 11. We choose to limit the relative uncertainty on the spheroid to total flux ratio to 20% and to cut the sample at $M_r \leq -19.0$ (which roughly corresponds to M^*+3). Out of the initial sample of 1,574,505 galaxies, there are 1,128,389 galaxies with $M_r \leq -19.0$, of which 522,605 have an uncertainty $err_{fluxratio}$ on the spheroid-to-total flux ratio smaller than or equal to 20%. So for $M_r \leq -19.0$ we can consider that about 50% of the galaxies have $err_{fluxratio} \leq 20\%$. Hereafter we will take into account only the galaxies with an absolute magnitude brighter than $M_r < -19.0$.

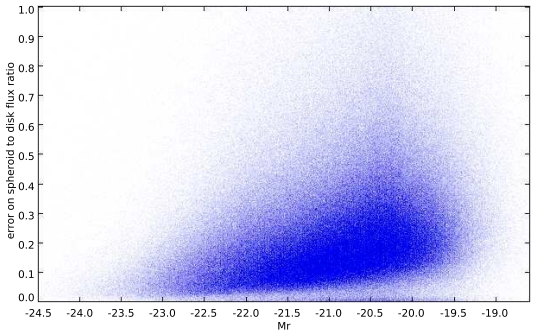

Fig. 11. Relative error on the spheroid to total flux ratio as a function of magnitude for all the galaxies in a 1 Mpc radius within clusters at redshift $0.4 \leq z < 0.75$.

In the following analysis, we will limit our analysis to the 2530 clusters detected at a 4σ level and above to have a sample of clusters that is as reliable as possible. We stacked clusters in six redshift bins: $z \leq 0.15$, $0.15 < z \leq 0.25$, $0.25 < z \leq 0.35$, $0.35 < z \leq 0.45$, $0.45 < z \leq 0.55$, and $z > 0.55$ and computed the percentages of late-type galaxies. If we assume that there is no observational bias due to the loss of spatial resolution for galaxies when redshift increases, we find that the percentage of late-type galaxies tends to decrease with redshift, opposite to what is expected. We also stacked clusters in four bins of detection level: 4σ, 5σ, 6σ, and 9σ, which roughly correspond to cluster mass bins. Here too, we tend to find that the percentage of late-type galaxies somewhat increases with significance level, the opposite of what is expected (more massive clusters are expected to host more early-type galaxies). We therefore performed simulations to test the hypothesis that these unexpected results could be due to an observational bias.

6.2. Influence of the redshift on the morphological classification

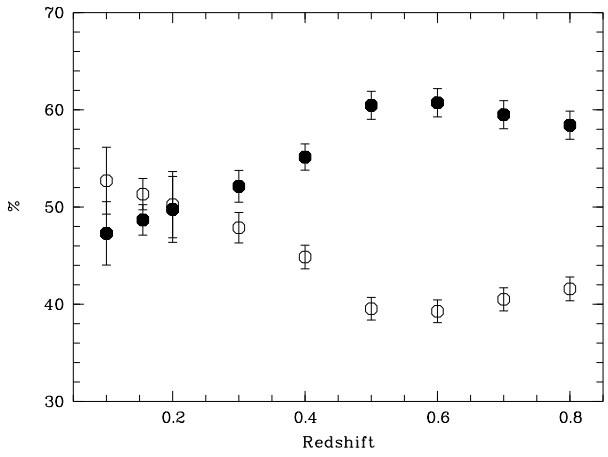

Fig. 12. Percentage of early-type galaxies (filled black circles) and late-type galaxies (empty black circles) as a function of redshift obtained by stacking 103 clusters artificially degraded to mimic the influence of increasing redshift (see Section 6.2).

Table 5. Percentage of late-type galaxies as a function of redshift obtained by degrading the images to mimic the effect of increasing redshift, as explained in the text.

Redshift	% of late types	number of galaxies
0.1	52.7	4005
0.155	51.3	17824
0.2	50.2	3893
0.3	47.9	17543
0.4	44.9	27283
0.5	39.5	26191
0.6	39.3	25895
0.7	40.5	25652
0.8	41.6	25003

In order to test how the image degradation due to increasing redshift could influence the value of the $f_{spheroid}/(f_{disk}+f_{spheroid})$ flux ratio on which our late- and early-type galaxy percentages are based, we selected 103 clusters with redshift $z \leq 0.20$ and detected at least at the 4σ level. Starting from the original images, we artificially degraded the images by rebinning them to larger pixel sizes to mimic the effect of increasing redshift. In this way images were computed to simulate the clusters as if they were located at redshifts between 0.2 and 0.8, in bins of 0.1 in redshift. The rebinned images were then treated with SExtractor as above to compute the $f_{spheroid}/(f_{disk} + f_{spheroid})$ flux ratios of all the cluster galaxies.

The percentages of late- and early-type galaxies were then stacked in redshift bins, and the results are shown in Fig. 12. This figure clearly shows that, as a bias due to redshift, the percentage of late-type galaxies tends to decrease with redshift and that of early types to increase. Therefore, when estimating the early-to-late-type ratio, a correcting factor must be applied to correct for this bias. The number of late-type galaxies for various redshifts is given in Table 5. We note that we only consider here cluster galaxies, for which the computed absolute magnitudes take into account the k-corrections and luminosity distance corrections.

6.3. Results

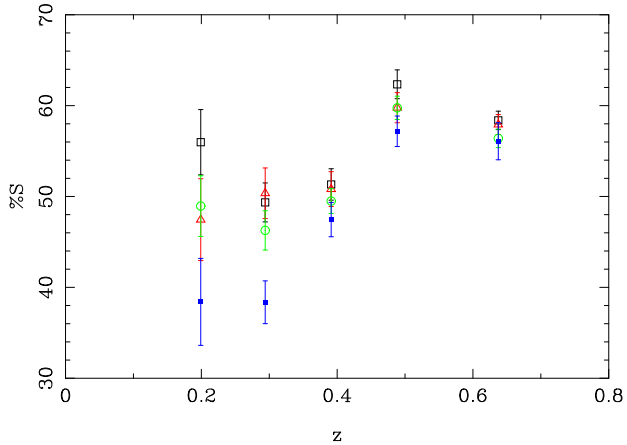

Fig. 13. Percentage of late-type galaxies as a function of redshift, based on the bulge to disk decomposition in the r' band. The data points are colour–coded as a function of detection level: black circles for 4σ, red triangles for 5σ, green circles for 6σ, and blue squares for 9σ. The correction factors explained in the text have been applied.

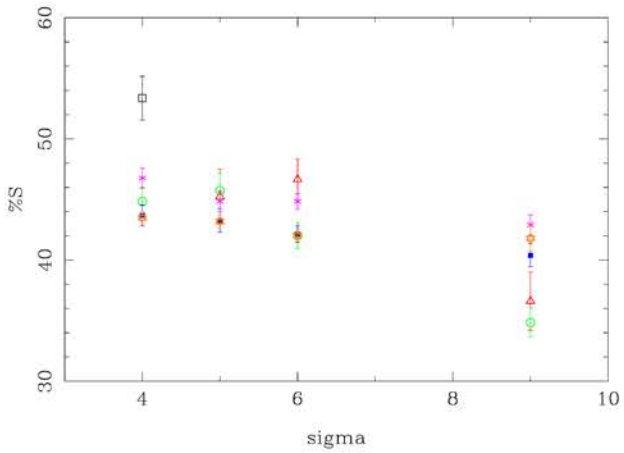

Fig. 14. Percentage of late-type galaxies as a function of detection level, based on the bulge to disk decomposition in the r' band. The data points are colour–coded in bins of redshift: black squares for $z \leq 0.2$, red triangles for $0.2 < z \leq 0.27$, green circles for $0.27 < z \leq 0.37$, blue squares for $0.37 < z \leq 0.47$, magenta crosses for $0.47 < z \leq 0.57$, and orange stars for $z > 0.57$. The correction factors explained in the text have been applied.

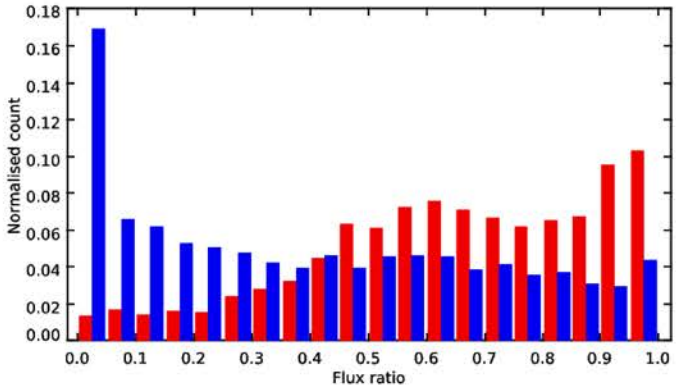

Fig. 15. Histograms of the normalized counts of late-type (in blue) and early-type (in red) galaxies as classified by Le Phare, as a function of spheroid-to-disk flux ratio.

If we apply the correction factors derived from Table 5 to the percentages of late-type and early-type cluster galaxies found above, we obtain the results displayed in Figs. 13 and 14. In these two figures, the error bars were taken to be Poissonian: $\sqrt{N}/N$, where N is the number of early-type galaxies corresponding to each point.

We can see that the percentages of late-type galaxies increase with redshift. This is particularly visible for 9σ clusters, where the percentage of late types increases from 20% to almost 60% between redshifts z=0.2 and z=0.5.

The percentages of late-type galaxies show a trend of decreasing with detection level (i.e. with cluster mass). We note that the percentages of late-type galaxies that we find are notably higher than those of Postman et al. (2005) or Smith et al. (2005) perhaps because our classification of late- and early-type galaxies is not the same, and/or because our cluster galaxies are probably at least partly contaminated by field galaxies.

6.4. Comparison of the galaxy type classifications by SExtractor and Le Phare

Since we had to run the Le Phare software to compute the absolute magnitudes of the cluster galaxies in order to calculate GLFs, as a by-product we obtained a Le Phare galaxy type classification (the same one as that used in the COSMOS survey). Le Phare assigns each galaxy a type coded as a number between 1 and 31, with early-type galaxies between 1 and 7, late-type galaxies between 8 and 19, and AGN between 20 and 31. These types correspond to the best spectral template allowing a fit to the photometric data.

The early- and late-type classifications that we made with SExtractor based on pure morphological properties are not expected to match exactly those derived with Le Phare. However, we believe it is interesting to compare them on a large statistical basis.

If we take into account all the cluster galaxies (77,162 galaxies), we find that 70% of the early-type and 53% of the late-type galaxies have the same classification with the two methods, after eliminating the AGN and starburst types from Le Phare (which add noise to the final morphological classification).

We cross-identified the cluster galaxies with the spectroscopic catalogue described in Section 2.1. The sample is then reduced to only 8,105 galaxies. For this sample, we find that 74% of the early-type galaxies are well classified by both methods, 61% of the late types and 68% if we add late types and AGN.

As a test, we also considered 73,970 galaxies in the Stripe 82 region having a spectroscopic redshift available, independent of whether they were cluster galaxies or not. We ran Le Phare on those galaxies, fixing their photo$-z$ to be equal to their spectroscopic redshift to obtain the best possible Le Phare type. We find that 69% of the early-type and 58% of the late-type galaxies have the same classification with Le Phare and SExtractor. This percentage becomes 63% if we add late types and AGN.

As an illustration, we show in Fig. 15 the histograms of the normalized counts of late- and early-type galaxies as classified by Le Phare as a function of spheroid-to-disk flux ratio computed by SExtractor.

Since these two ways of classifying galaxies are very different from one another (one being purely morphological while the other is purely spectral), and since morphological and spectral evolutions can also be quite different, it is rather satisfying to see that they agree between 58% and 74% of the cases.

6.5. Eye-test of the morphological classification

In order to test the morphological classification obtained with SExtractor, six high school students (see their names in the acknowledgements) selected about 1000 galaxies in the redshift range $0.15 < z < 0.25$ classified as early-type or late-type and examined them visually with ds9 one by one. They found that the SExtractor and eye classifications agreed for 80±10% of the galaxies.

7. Summary and conclusions

Based on the galaxy photometric redshift catalogue of Reis et al. (2012), we have searched for galaxy clusters in the Stripe 82 region of the Sloan Digital Sky Survey by applying the AMACFI cluster finder (Adami & Mazure 1999). After making nine tests with different AMACFI parameters that have a strong influence on the cluster detection rate, we detected 3663 candidate clusters

at a 3σ level and above, in the redshift range $0.1 \leq z \leq 0.7$, with estimated mean masses between $\sim 10^{13}$ and a few 10^{14} $M_\odot$. We cross-correlated our catalogue of candidate clusters with various catalogues extracted from optical and/or X-ray data. The percentages of redetected clusters are at most 40%, but in all cases this can be explained by the fact that we detect relatively massive clusters, while other authors detect less massive structures.

The colour-magnitude diagrams and galaxy luminosity functions of the clusters detected at 5σ and above and stacked in redshift bins of width 0.1 are typically those of *bona fide* clusters. This confirms that the clusters we have detected have a high probability of being real clusters.

The morphological analysis of the cluster galaxies shows that the fraction of late-type to early-type galaxies shows an increase with redshift and a decrease with significance level, i.e. cluster mass. This result is obtained after correcting for a bias due to the effect of increasing redshift that we quantified through simulations.

Although the 3663 candidate clusters detected here seem mostly to be real clusters, spectroscopic confirmation would of course be necessary. We are in the process of improving the positions and redshifts of our clusters by searching for the brightest cluster galaxies, and retrieving spectroscopic redshifts in the SDSS data base. As yet another confirmation to the reality of the clusters detected in S82, we are also identifying our candidate clusters with diffuse X-ray sources detected by XMM-Newton when available. These results will be published in a forthcoming paper.

Counting the number of clusters per unit volume and the growth of clusters with redshift are methods for delimiting cosmological model parameters such as w, dw/dz, and σ_8 (Allen et al. 2011). This motivated the present search for clusters in the Stripe 82 region of the SDSS, as well as our previous searches for clusters in the CFHTLS. In the near future, the Dark Energy Survey expects to find approximately 170,000 clusters with masses $\geq 5 \times 10^{13}$ $M_\odot$ (http://en.wikipedia.org/wiki/The_Dark_Energy_Survey), and LSST more than 100,000 clusters with masses $\geq 2 \times 10^{14}$ $M_\odot$ (Tyson et al. 2003).

Based on our experience here, we conclude that is it very important not to depend on using just one cluster detection algorithm. Therefore, for future surveys we suggest the following approach to derive cosmological parameters from optical/near IR cluster surveys: 1) take a $\sim 6\sigma$ cut and a $\sim 4\sigma$ cut; and 2) estimate the completeness of the survey by comparing two or more different cluster finding techniques. The derived cosmological parameters based on two (or more) different σ cuts and techniques can then be used to determine the underlying systematic limits to the values of these cosmological parameters.

Acknowledgements. F.D. acknowledges long-term support from CNES. I.M. acknowledges financial support from the Spanish grants AYA2010-15169 and AYA2013-42227-P and from the Junta de Andalucia through TIC-114 and the Excellence Project P08-TIC-03531. A.T. acknowledges the support and the hospitality of IAP/CNRS for two one–month visits.

We are grateful to Andrea Biviano for giving us his IDL program to fit GLFs with a Schechter function and to Alberto Cappi for discussions. We thank the six high school students M.A. García Valverde, B. Hernández Ramos, J. Leon Lovell, L. Martínez Sánchez de Lara, J. Rodríguez Zamorano and L. Vallecillos Azor for their careful eye classification of about 1000 galaxies.

Funding for SDSS-III has been provided by the Alfred P. Sloan Foundation, the Participating Institutions, the National Science Foundation, and the U.S. Department of Energy Office of Science. The SDSS-III web site is `http://www.sdss3.org/`.

SDSS-III is managed by the Astrophysical Research Consortium for the Participating Institutions of the SDSS-III Collaboration including the University of Arizona, the Brazilian Participation Group, Brookhaven National Laboratory, Carnegie Mellon University, University of Florida, the French Participation Group, the German Participation Group, Harvard University, the Instituto de Astrofisica de Canarias, the Michigan State/Notre Dame/JINA Participation Group, Johns Hopkins University, Lawrence Berkeley National Laboratory, Max Planck Institute for Astrophysics, Max Planck Institute for Extraterrestrial Physics, New Mexico State University, New York University, Ohio State University, Pennsylvania State University, University of Portsmouth, Princeton University, the Spanish Participation Group, University of Tokyo, University of Utah, Vanderbilt University, University of Virginia, University of Washington, and Yale University.

References

Adami C. & Mazure A. 1999, A&AS 134, 393
Adami C., Durret F., Benoist C. et al. 2010, A&A 509, 81 (A10)
Adami C., Cypriano E., Durret F. et al. 2015a, A&A 575, 69
Adami C., Pompei E., Sadibekova T. et al. 2015b, A&A submitted
Allen S.W., Evrard A.E., Mantz A.B. 2011, ARA&A 49, 409
Annis J., Soares-Santos M., Lupton R.H. et al. 2014, ApJ 794, 120
Arnouts S., Cristiani S., Moscardini L. et al. 1999, MNRAS 310, 540
Ascaso B., Wittman D., Benítez N. et al. 2012, MNRAS 420, 1167
Ascaso B., Wittman D., Dawson W. 2014, MNRAS 439, 1980
Bergé J., Pacaud F., Réfrégier A., et al. 2008, MNRAS 385, 695
Bertin E., Arnouts S. 1996, A&AS 117, 393
Bertin E. 2011, ASPC 442, 435
Bielby R.M., Finoguenov A., Tanaka M. et al. 2010, A&A 523, 66
Bruzual G. & Charlot S. 2003, MNRAS 344, 1000
Cabanac R.A., Alard C., Dantel-Fort M. et al. 2007, A&A 461, 813
Durret F., Laganá T.F., Haider M. 2011a, A&A 529, 38
Durret F., Adami C., Cappi A. et al. 2011b, A&A 535, 65 (D11)
Erben T., Hildebrandt H., Lerchster M. et al. 2009, A&A 493, 1197
Fukugita M., Shimasaku K., Ichikawa T. 1995, PASP 107, 945
Gavazzi R., Soucail G. 2007, A&A 462, 459
Geach J.E., Murphy D.N.A., Bower R.G. 2011, MNRAS 413, 3059 (GMB)
Gioia I.M., Henry J.P., Maccacaro T. et al. 1990, ApJ 356, L35
Grove L.F., Benoist C, Martel F. 2009, A&A 494, 845
Hao J., McKay T.A., Koester B.P. et al. 2010, ApJS 191, 254
Ilbert O., Arnouts S., McCracken H.J. et al. 2006, A&A, 457, 841
Ivezić Z., Lupton R.H., Schlegel D. et al. 2004, Astron. Nachr., 325, 583
Limousin M., Cabanac R., Gavazzi R., et al., 2009, A&A 502, 445
Martinet N., Durret F., Guennou L. et al. 2014, A&A 575, 116
Mazure A., Adami C., Pierre M. et al. 2007, A&A 467, 49 (M07)
Mehrtens N., Romer A.K., Hilton M. et al. 2012, MNRAS 423, 1024
Milkeraitis M., Van Waerbeke L., Heymans C. et al. 2010, MNRAS 406, 673
Murphy D.N.A., Geach J.E. & Bower R.G. 2012, MNRAS 420, 1861
Olsen L.F., Benoist C., Cappi A. et al. 2007, A&A 461, 81
Olsen L.F., Benoist C., Cappi A. et al. 2008, A&A 478, 93
Peng C.Y., Ho L.C., Impey C.D., Rix H.W. 2002, AJ 124, 266
Pimbblet K.A., Smail I., Kodama T. et al. 2002, MNRAS 331, 333
Postman M., Franx M., Cross N.J.G. et al. 2005, ApJ 623, 721
Reis R.R.R., Soares-Santos M., Annis J. et al. 2012, ApJ 747, 59
Romer A.K., Viana P.T.P., Liddle A.R., Mann R.G. 2001, ApJ 547, 594
Rykoff E.S., Rozo E., Busha M.T. et al. 2014, ApJ 785, 104
Sadibekova T., Pierre M., Clerc N. et al. 2014, A&A 571, 87S
Shan H., Kneib J.-P., Tao C. et al. 2012, ApJ 748, 56
Simard L., Clowe D., Desai V. et al. 2009, A&A 508, 1141
Smith G.P., Treu T., Ellis R.S., Moran S., Dressler A. 2005, ApJ 620, 78
Springel V., White S.D.M., Jenkins A. et al. 2005, Nature 435, 629
Takey A., Schwope A., Lamer G. 2011, A&A 534, 120
Takey A., Schwope A., Lamer G. 2013, A&A 558, 75
Takey A., Schwope A., Lamer G. 2014, A&A 564, 54
Thanjavur K., Willis J., Crampton D. 2009, ApJ 706, 571
Tyson J. A., Wittman D. M. , Hennawi J. K., Spergel D. A. 2003, Nuclear Physics B (Proc. Suppl.) 124, 21
van Breukelen C. & Clewley L. 2009, MNRAS 395, 1845
Wen Z.L., Han J.L., Liu F.S. 2012, ApJS 199, 34W
Xu H., Jin G., Wu X.-P. 2001, ApJ 553, 78
Zucca E., Ilbert O., Bardelli S. et al. 2006, A&A 455, 879

Appendix A: Magnitude histograms

The magnitude histograms in the five bands of the 4,999,968 galaxies of the initial magnitude catalogue used to compute absolute magnitudes are shown in Fig. A.1.

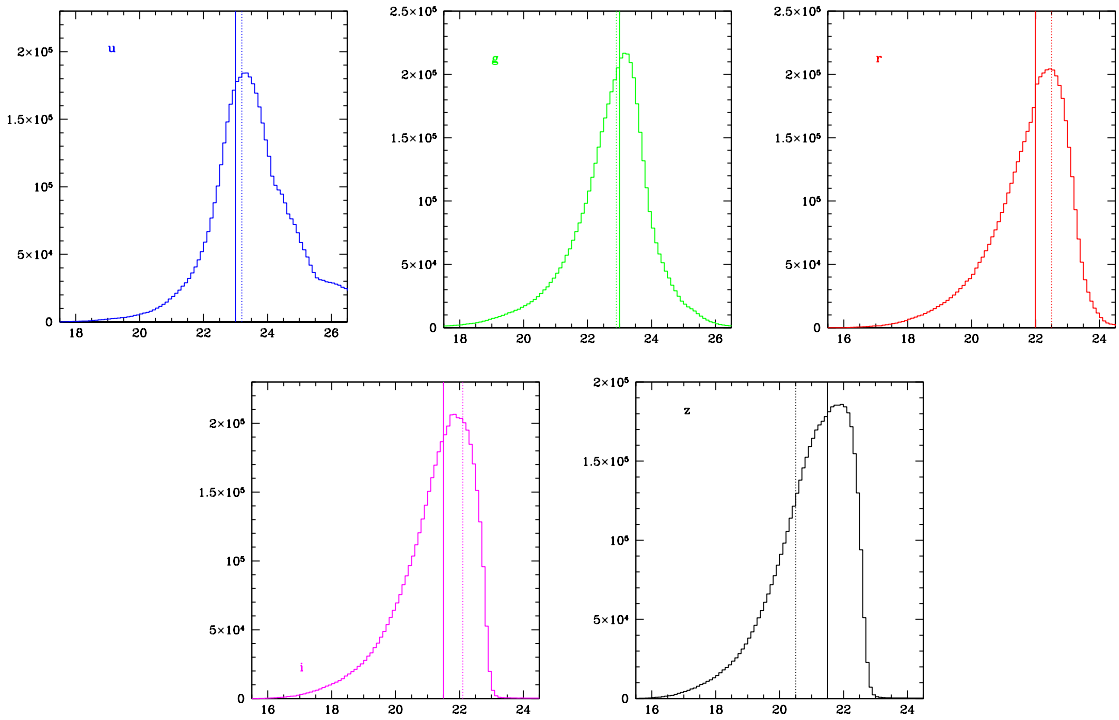

Fig. A.1. Magnitude histograms in the five bands of the 4,999,968 galaxies of the initial magnitude catalogue used to compute absolute magnitudes. The full vertical lines show the 90% completeness limits beyond which the galaxy counts will not be considered as fitting the GLFs. These limits are: u'_{lim}=23.0, g'_{lim}=22.8, r'_{lim}=22.1, i'_{lim}=21.5, and z'_{lim}=21.2. The dotted vertical lines show the 90% completeness limits derived from Fig. 8 in Annis et al. (2014) for comparison.

Appendix B: Completeness simulations

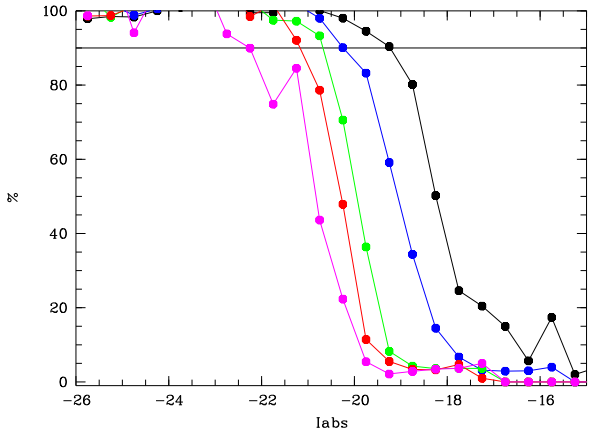

Fig. B.1. Percentage of redetected galaxies as a function of absolute magnitude in the i' band derived from our simulations in five magnitude bins: z=0.2 in black, z=0.3 in blue, z=0.4 in green, z=0.5 in red, and z=0.6 in magenta (see Section 5.2.1).

We show in Fig. B.1 the percentages of redetected galaxies as a function of absolute magnitude in the i' band derived from our simulations in five magnitude bins: z=0.2 in black, z=0.3 in blue, z=0.4 in green, z=0.5 in red, and z=0.6 in magenta (see Section 5.2.1). Simulations in the other bands give comparable curves and are not shown here to save space.

A.2 Article 2: Adami et al. 2015

In this section, I review my contribution to the Adami et al. (2015) paper: **Two spectroscopically confirmed galaxy structures at z = 0.61 and 0.74 in the CFHTLS Deep 3 field**.

This paper is a study of two galaxy cluster candidates at redshift $z > 0.5$ detected by applying the Adami & Mazure Cluster Finder (Adami & Mazure 1999) to the CFHTLS in Adami et al. (2010). Using new spectroscopy from Gemini, we measure the cluster galaxy redshifts, and perform a dynamical study. We also compute their GLFs, and measure a weak lensing signal, based on the CFHT/MegaCam images. Finally, we compare the lensing detection to the X-ray detection from *Chandra*. We found that the two candidates correspond to real clusters at redshifts $z = 0.607$ and $z = 0.739$. The first one of low mass is probably a small group, not detected in WL, while the second seems to be a merging of two groups, which is weakly detected through WL ($\sim 3\ \sigma$), but not in X-rays. These detections validate the potential of the cluster finder that was used.

I took care of the WL reduction for these two clusters on sub-images of MegaCam fields. The shear measurement is similar to that of Martinet et al. (2015, A&A submitted). The background galaxies are selected according to their photometric redshifts. The convergence map is produced by applying the Kaiser & Squires (1993) method but not refining it in the cluster region through the iterative Seitz & Schneider (1995) procedure as in the mentioned paper. This should not cause a too large bias, as the clusters studied here are probably of very low masses. The detection level is estimated from the noise threshold corresponding to the shape noise with a Gaussian smoothing (see van Waerbeke 2000). One cluster is not detected at all and the other one is weakly detected ($\sim 3\ \sigma$). From the lensing, at least the second candidate is a true small cluster. Note however, that these clusters are at high redshifts, and that the number of background galaxies usable for lensing is therefore low.

A&A 575, A69 (2015)
DOI: 10.1051/0004-6361/201425159

Astronomy & Astrophysics

Two spectroscopically confirmed galaxy structures at $z = 0.61$ and 0.74 in the CFHTLS Deep 3 field⋆

C. Adami[1], E. S. Cypriano[2], F. Durret[3], V. Le Brun[1], G. B. Lima Neto[2], N. Martinet[3], F. Perez[1], B. Rouze[1], and L. Sodr Jr.[2]

[1] Aix-Marseille Universit , CNRS, LAM (Laboratoire d'Astrophysique de Marseille) UMR 7326, 13388 Marseille, France
e-mail: christophe.adami@lam.fr
[2] IAG, USP, R. do Mat o 1226, 05508-090 S o Paulo, SP, Brazil
[3] UPMC-CNRS, UMR 7095, Institut d'Astrophysique de Paris, 75014 Paris, France

Received 15 October 2014 / Accepted 16 December 2014

ABSTRACT

Context. Galaxy evolution is known to depend on environment since it differs in clusters and in the field, but studies are sometimes limited to the relatively nearby Universe ($z < 0.5$). It is still necessary to increase our knowledge of cluster galaxy properties above $z = 0.5$.
Aims. In a previous paper we have detected several cluster candidates at $z > 0.5$ as part of a systematic search for clusters in the Canada France Hawaii Telescope Legacy Survey by applying the Adami & MAzure Cluster FInder (AMACFI), based on photometric redshifts. We focus here on two of them, located in the Deep 3 (hereafter D3) field: D3-6 and D3-43.
Methods. We have obtained spectroscopy with Gemini/GMOS instrument and measured redshifts for 23 and 14 galaxies in the two structures. These redshifts were combined with those available in the literature. A dynamical and a weak lensing analysis were also performed, together with the study of X-ray *Chandra* archive data.
Results. Cluster D3-6 is found to be a single structure of eight spectroscopically confirmed members at an average redshift $z = 0.607$, with a velocity dispersion of 423 km s^{-1}. It appears to be a relatively low-mass cluster. D3-43-S3 has 46 spectroscopically confirmed members at an average redshift $z = 0.739$. The cluster can be decomposed into two main substructures, having a velocity dispersion of about 600 and 350 km s^{-1}. An explanation of the fact that D3-43-S3 is detected through weak lensing (only marginally, at the $\sim 3\sigma$ level) but not in X-rays could be that the two substructures are just beginning to merge more or less along the line of sight. We also show that D3-6 and D3-43-S3 have similar global galaxy luminosity functions, stellar mass functions, and star formation rate (SFR) distributions. The only differences are that D3-6 exhibits a lack of faint early-type galaxies, a deficit of extremely high stellar mass galaxies compared to D3-43-S3, and an excess of very high SFR galaxies.
Conclusions. This study shows the power of techniques based on photometric redshifts to detect low to moderately massive structures, even at $z \sim 0.75$. Combined-approach cluster surveys such as EUCLID are crucial to find and study these clusters at these relatively high redshifts. Finally, we show that photometric redshift techniques are also well suited to study the galaxy content and properties of the clusters (galaxy types, SFRs, etc.).

Key words. galaxies: clusters: general

1. Introduction

Galaxy evolution is still a major topic in cosmology because of the complexity of the processes involved. The current theoretical framework (e.g. White & Frenk 1991) assumes that galaxies are formed by accretion of baryonic matter onto dark matter haloes and evolve through mergers and other interactions with other galaxies and the intergalactic medium (IGM). The study of evolution in clusters is particularly interesting because some extreme conditions (e.g. high galaxy density, large amounts of hot gas in the IGM) are found in these structures and, consequently, galaxy evolution is affected by many environmentally-driven processes, as evidenced by the evolution of the morphological mix of their galaxies (e.g. Boselli et al. 2014). Naturally, in this scenario the evolution of galaxies is not independent from the evolution of cluster structures. According e.g. to Mateus et al. (2007), galaxy evolution is accelerated in denser environments. All this makes clusters ideal laboratories to investigate galaxy evolution.

Most of our current knowledge about processes affecting galaxies in clusters comes primarily from studies in the nearby ($z < 0.5$) Universe. At higher redshifts, several studies have focussed on the evolution of morphological type fractions (e.g. Holden et al. 2007; van der Wel et al. 2007; Simard et al. 2009), on their clustering properties (e.g. Poggianti et al. 2010; Ross et al. 2010), or on the evolution of specific galaxy types (such as red galaxies: S nchez-Bl zquez et al. 2009).

The question we want to answer is how do cluster galaxies evolve in the redshift interval $0.5 < z < 1$. We propose adding our contribution to this problem through spectroscopy and photometry of candidate cluster galaxies observed with GEMINI/GMOS and primarily detected from CFHTLS survey photometric redshift catalogues. In this framework, Adami et al. (2010) have published a catalogue of ~1200 cluster candidates from public photometric redshifts (obtained following Ilbert et al. 2006; also see Coupon et al. 2009) of the CFHTLS data release T0004 in the D2, D3, D4, W1, W3, and W4 regions. This catalogue contains several cluster candidates at redshift larger than 0.5, detected with high confidence (signal-to-noise ratio equal to or larger than 4) and also detected by other methods

⋆ Appendices are available in electronic form at http://www.aanda.org

(Olsen et al. 2007; Thanjavur et al. 2009). We choose to focus on two of them.

We describe the optical identification of our candidate clusters in Sect. 2. The mass characterisation of the two structures is discussed in Sect. 3. In Sect. 4 we present some properties of the galaxy populations in the clusters, and in Sect. 5 we summarise our results.

We adopted, where necessary, the Dunkley et al. (2009) ΛCDM concordance cosmological model (H_0 = 71.9 km s^{-1} Mpc^{-1}, $\Omega_\Lambda = 0.742$, $\Omega_M = 0.258$).

2. Optical identification of our candidate clusters

2.1. CFHTLS imaging

The two clusters studied here were discovered as part of a systematic search for clusters in the Canada France Hawaii Telescope Legacy Survey (Adami et al. 2010). They were found in the Deep 3 field, which covers 1 deg^2 and is centred at coordinates 14:19:27.00, +52:40:56 (J2000.0). This field is among the deepest optical images available from the ground, corresponding to a total exposure time of the order of 90 h.

To identify clusters in this field we applied the Adami & MAzure cluster FInder (AMACFI, Mazure et al. 2007), based on photometric redshifts (hereafter photo-zs). After the photo-z catalogue is cut in photometric redshift slices, galaxy density maps are drawn with an adaptive kernel technique, and overdensities are detected at a chosen significance level with SExtractor. Detections are then sorted with a minimal spanning tree method, leading to a catalogue of candidate clusters.

The two candidate clusters studied here were detected at a 4σ significance level. Their identifications in the Adami et al. (2010) catalogue are D3-6 and D3-43.

2.2. Gemini GMOS spectroscopy

We were awarded 8.5 h of GEMINI/GMOS time (program GN-2011A-Q46, PI: L. Sodr) to observe these two cluster candidates spectroscopically. We initially used the R400 grism and one arcsec slits. Final 1D spectra were rebinned to have ∼7 per pixel.

We were able to fit 27 and 16 slits in the D3-6 and D3-43 fields respectively. Reduction was made in the IRAF environment with the GMOS dedicated tools. We applied the EZ redshift measurement code (Garilli et al. 2010) on the final 1D spectra, allowing an additional smoothing from 3 to 9 pixels to find the redshift value more easily. The redshift measurements were done in the same way as for the VIPERS survey (e.g. Guzzo et al. 2014). Independent measurers provided two first estimates of the redshifts (Le Brun & Adami). The two values were then reconciled and a quality flag was assigned between 1 and 4. Flag 1 means that we have a 50% chance to have the correct redshift estimate, flag 2 means that we have a 75% chance, flag 3 means that we have a 95% chance, and flag 4 means that we have more than 99% chance. We only considered the objects with flags 2, 3, and 4 to be successful measurements. We obtained an excellent success rate: 15 of the 16 D3-43 spectra and 26 of the 27 D3-6 spectra provided successful redshift measurements. Only four spectra turned out to be of stellar origin, while we obtained galaxy redshifts for 23 and 14 galaxies in the fields of D3-6 and D3-43, respectively.

Coordinates and successfully measured redshifts for this sample are given in Tables 1 and 2. We show four examples of spectra corresponding to flags 4, 3, and 2 in Figs. B.1 and B.2.

Table 1. Running number, coordinates (J2000), redshifts, and spectral flags for the objects observed with GEMINI/GMOS in the D3-43 field of view.

#	RA	Dec	Redshift	Flag
1	14:20:51.079	53:03:38.76	0.8264	3
2	14:20:56.214	53:02:21.28	0.8950	3
3	14:20:56.472	53:02:35.13	0.7111	4
4	14:20:58.824	53:01:11.63	0.7497	4
5	14:20:59.161	53:01:36.41	0.7404	4
6	14:21:00.276	53:04:29.72	0.7737	4
7	14:21:02.344	53:05:03.26	0.6723	4
8	14:21:02.572	53:01:22.74	0.3347	4
9	14:21:05.073	53:02:06.92	0.7393	4
10	14:21:10.762	53:02:49.93	0.7350	4
11	14:21:11.665	53:04:44.20	0.8217	3
12	14:21:15.013	53:00:57.71	0.	4
13	14:21:18.394	53:03:28.41	0.9748	4
14	14:21:18.842	53:00:32.05	0.7395	4
15	14:21:21.818	53:01:55.12	0.7321	4

Table 2. Running number, coordinates (J2000), redshifts, and spectral flags for the objects observed with GEMINI/GMOS in the D3-6 field of view.

#	RA	Dec	Redshift	Flag
1	14:16:36.004	53:04:31.73	0.7163	3
2	14:16:37.152	53:04:32.32	0.5268	3
3	14:16:38.064	53:03:44.66	0.7441	2
4	14:16:39.084	53:05:44.23	0.6083	4
5	14:16:40.173	53:05:01.37	0.	4
6	14:16:41.339	53:04:54.53	0.6474	3
7	14:16:46.077	53:01:47.67	0.5758	4
8	14:16:46.824	53:04:38.55	0.6090	4
9	14:16:47.833	53:03:04.95	0.6046	4
10	14:16:49.100	53:05:55.98	0.6067	3
11	14:16:50.122	53:05:10.06	0.6077	3
12	14:16:51.068	53:02:17.15	0.6007	2
13	14:16:53.373	53:05:51.77	0.	4
14	14:16:55.542	53:05:16.50	0.6064	4
15	14:16:56.983	53:02:43.27	0.9006	3
16	14:16:57.645	53:04:29.12	0.6074	2
17	14:16:58.438	53:03:47.13	0.5888	2
18	14:16:59.666	53:02:26.51	0.6064	4
19	14:17:00.703	53:05:15.49	0.9670	4
20	14:17:01.736	53:03:19.29	0.6441	3
21	14:17:03.493	53:00:50.72	0.5255	2
22	14:17:04.775	53:03:15.64	0.7748	4
23	14:17:05.915	53:05:58.64	0.5255	3
24	14:17:06.757	53:05:55.87	0.5270	4
25	14:17:08.225	53:00:47.94	0.6478	4
26	14:17:09.578	53:03:34.14	0.	4

2.3. Publicly available spectroscopy

One of the two studied candidate clusters (D3-43) was also covered by the KECK/DEIMOS DEEP2 spectroscopic survey (Newman et al. 2013). This provided 336 redshifts in a 5 arcmin radius circle around the cluster centre, in addition to the GEMINI/GMOS redshifts. Ten of these GEMINI/GMOS redshifts were also measured by the KECK/DEIMOS DEEP2 survey, and this allowed us to assess our own redshift measurements, as shown in Fig. A.1. We do not detect any noticeable difference. Even the two galaxies with the most different redshift values in the two surveys do not exhibit a redshift difference larger than 0.015. This typically corresponds to the 3σ uncertainty according to the smoothing we applied to

Table 3. Structures detected along the line of sight to the two candidate clusters.

Name	#	N_{gal}	z	Vel. disp. (km s^{-1})	SG substructures
D3-6	1	8	0.607	423	1
D3-43	S1	17	0.201	489	/
	S2	11	0.378	250	/
	S3	46	0.739	1152	2
	S4	18	0.975	575	/

Notes. The columns are: (1) cluster name; (2) number of the structure; (3) number of galaxies in the structure; (4) mean redshift of the structure; (5) Rostat velocity dispersion; (6) number of substructures when analysed by the Serna & Gerbal (1996) method.

GEMINI/GMOS spectra before redshift measurements (dashed lines in Fig. A.1). If we consider only redshifts lower than 0.8, the typical uncertainty between the two redshift measurements is 0.0005.

The other candidate cluster (D3-6) has only three additional objects with known spectroscopic redshifts available through the NED and Simbad databases (Howell et al. 2005; Hsieh et al. 2005; Walker et al. 2011). None are in common with our GEMINI/GMOS catalogue.

2.4. The main structures along the two lines of sight

We first merged our own redshift catalogue with those of the literature and eliminated the galaxies observed twice, as well as the stars. We then computed redshift histograms along the two lines of sight, and searched for empty gaps wider than 0.001 in the redshift distribution. This is a classical method to detect galaxy structure candidates (e.g. Katgert et al. 1996). We only retained galaxy concentrations between two such gaps of more than five objects. This provided four potential structures along the D3-43 line of sight and only one along the D3-6 line of sight (see Table 3 and Fig. 1).

The D3-6 line of sight only shows one structure at $z = 0.607$ (see Fig. 2) sampled with eight galaxies with spectroscopic redshifts. The $(r' - z')$ values of these galaxies are relatively similar and of the order of 1.4 and 1, also in good agreement with the colours of $z = 0.5$ early-type and spiral galaxies respectively (e.g. Fukugita et al. 1995). The mean redshift of the only detected structure along the D3-6 line of sight ($z = 0.607$) also being close to the candidate cluster photometric redshift value ($z = 0.6$), we decided to associate it with the D3-6 candidate cluster of Adami et al. (2010).

Figure 3 displays the colour–magnitude relations of the potential structures along the D3-43 line of sight in the $(r' - z')$ versus r' space. We clearly see a red sequence (showing an old galaxy population) around $(r' - z') \sim 1.8$ and a bluer cloud around $(r' - z') \sim 1$ for structure S3. These colours are consistent with $z = 0.8$ early and late-type galaxies (e.g. Fukugita et al. 1995). Other structures of the D3-43 line of sight are less prominent and do not show the same dichotomy between an early-type and a late-type galaxy population. The structure S3 is also by far the most populated: it has more confirmed galaxies than the three others taken together. The structure S3 is clearly the closest to the 3σ peak of the weak lensing detection (see below and Fig. 6). The brightest galaxy of S3 is at ~600 kpc of the peak, while the brightest galaxies of S1, S2, and S4 are located at ~850 kpc, ~2300 kpc, and ~1300 kpc (at the structure redshift). The structure S3 is the only structure for which the galaxy dispersion on the sky is larger than the distance between the structure centre and the 3σ peak of the weak lensing detection (1.2 × larger). The ratio is 0.4 for S1, 0.3 for S2, and 0.9 for S4. Finally, the spectroscopic redshift of S3 is remarkably close to the photometric redshift of D3-43 in Adami et al. (2010): 0.75. We therefore decided to choose S3 as the main structure along the D3-43 line of sight, to associate it with the weak lensing detection (see below), and with the D3-43 candidate cluster of Adami et al. (2010).

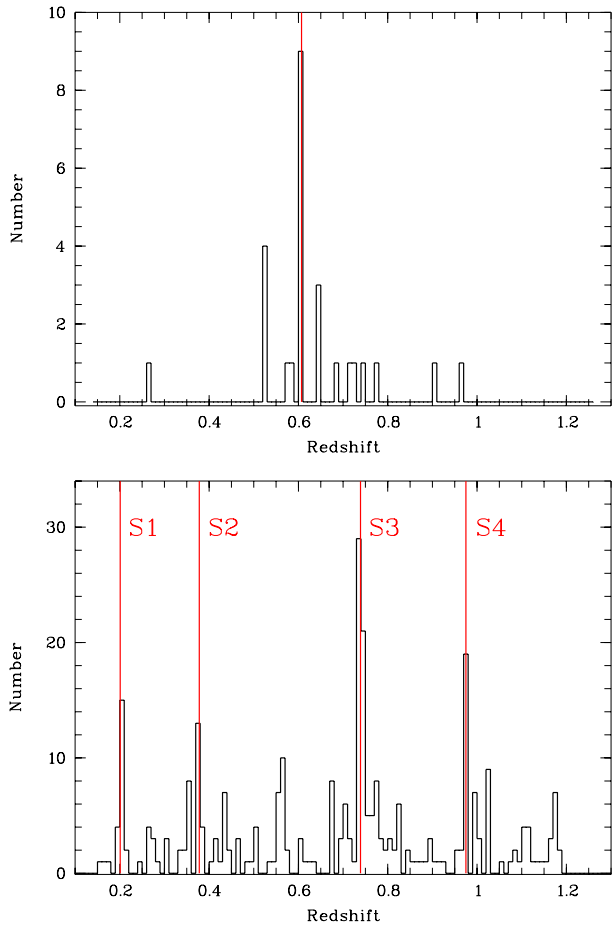

Fig. 1. Distribution of the Gemini/GMOS and DEEP2 galaxies with known spectroscopic redshifts along the D3-6 (*top*), and D3-43 (*bottom*) lines of sight. Detected structures from Table 3 are shown as red vertical lines.

This leads us to conclude that we probably have detected at least two real structures along the D3-6 and D3-43 lines of sight at $z = 0.607$ (D3-6 in the following) and $z = 0.739$ (D3-43-S3 in the following) respectively. The redshift distributions of the galaxies with known spectroscopic redshifts inside these structures are displayed in Fig. 4.

2.5. Internal structure of D3-6 and D3-43-S3

We investigated the internal structures of D3-6 and D3-43-S3 by applying the Serna-Gerbal technique (hereafter SG, 1996 release, Serna & Gerbal 1996). This hierarchical code based on spectroscopic redshifts and optical magnitudes, is designed to detect substructures in the optical. A number of other methods are available to search for substructures at optical wavelengths, such as the Δ-test (Dressler & Schechtman 1988). However, the SG method has proven to be quite powerful detecting evidence for substructuring in nearby (see Abell 496: Durret et al. 2000; Coma: Adami et al. 2005, 2009; Abell 780: Durret et al. 2009; Abell 85: Bou et al. 2008), moderate redshift

Table 4. Main characteristics of the two confirmed structures.

Name	RA(D3) deg	Dec(D3) deg	z(D3)	RA(spec) deg	Dec(spec) deg	z(spec)	Vel. disp. km s^{-1}	SG mass $M_\odot$	X-ray mass $M_\odot$
D3-6	214.2207	53.0568	0.60	214.2314	53.0879	0.607	423	2.2×10^{14}	2.5×10^{14}
D3-43-S3	215.271	53.0353	0.75	215.2710	53.0353	0.739	1152 (611 + 357)	$3.6 \times 10^{14} + 8.8 \times 10^{13}$	$\leq 8 \times 10^{13}$

Notes. The columns are: (1) name; (2) + (3) coordinates in the D3 CFHTLS cluster catalogue; (4) photometric redshift in the D3 CFHTLS cluster catalogue; (5) and (6) central coordinates of the spectroscopic catalogue defined as the coordinates of the brightest galaxy member; (7) mean spectroscopic redshift; (8) velocity dispersion from Rostat estimates (Beers et al. 1991; values are also given for the two substructures of D3-43-S3); (9) mass estimate from the Serna-Gerbal analysis (values are also given for the two substructures of D3-43-S3); (10) mass estimate from the X-ray analysis (within r_{500}).

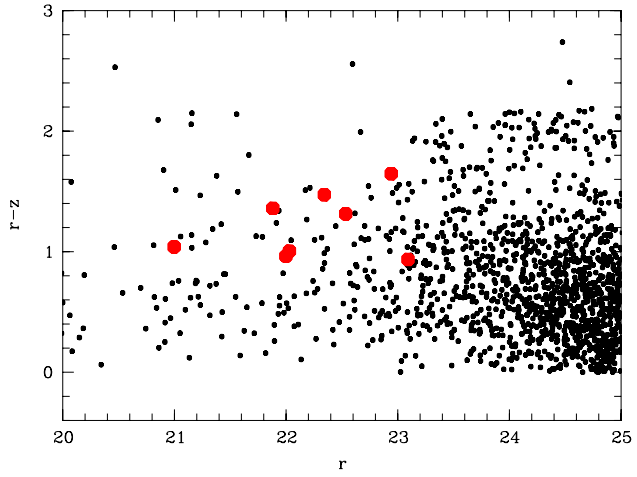

Fig. 2. Colour–magnitude relation along the D3-6 cluster line of sight. Small black dots are the CFHTLS galaxies, red disks are the spectroscopically confirmed cluster members.

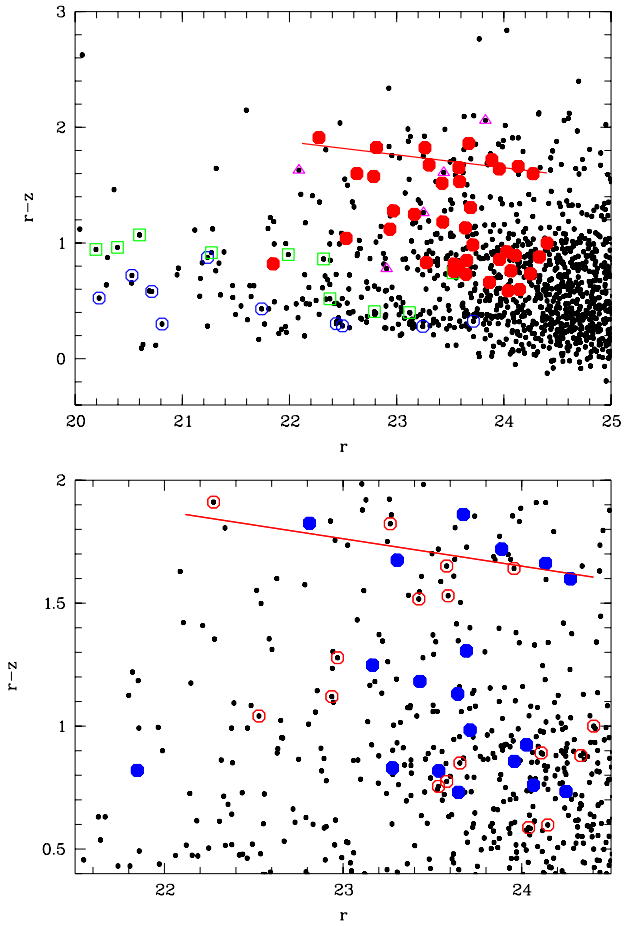

Fig. 3. Colour–magnitude relations along the D3-43 candidate cluster line of sight. Small black dots are the CFHTLS galaxies. *Upper figure*: red disks are the spectroscopically confirmed members of S3, blue circles are the S1 members, green squares are the S2 members, pink triangles are the S4 members. The inclined red line is the tentative red sequence for structure S3 early-type galaxies. *Lower figure*: red circles are the S3 substructure #1 members, blue disks are the S3 substructure #2 members (see text for details). The inclined red line is the tentative red sequence for S3 early-type galaxies.

(Abell 222/223: Durret et al. 2010), and high redshift clusters (RX J1257.2+4738: Ulmer et al. 2009). Recently, it was also successfully applied and compared with X-ray detections on a larger sample (the DAFT/FADAS sample: Guennou et al. 2014). Assuming a value of the mass to luminosity ratio (here taken to be 100 in the r' band, to be homogeneous with the Guennou et al. 2014 simulations), the SG method allows us to estimate the masses of the substructures that it detects. Guennou et al. (2014) have shown that although the absolute masses are not accurate (typical uncertainties are clearly larger than 10^{14} $M_\odot$), the mass ratios of the various substructures were well determined. The SG method has also been extensively tested on simulations by Guennou (2012), in particular concerning the effect of undersampling on mass determinations. We stress that this method requires a very good precision in the galaxy distance determinations, and therefore spectroscopic redshifts are essential, while photometric redshifts are inappropriate.

The level of refinement in the substructure detection obviously depends on the spectroscopic sampling, as already shown by the previously quoted articles. We first processed the D3-6 structure. Since it is only sampled by eight galaxies with known spectroscopic redshifts, the SG code would only be able to detect large substructures that would be present in cluster-cluster merging, and this is not the case, showing that D3-6 is probably not undergoing a major merger.

The D3-43-S3 structure is much better sampled spectroscopically. The SG method detects two relatively massive substructures (see Table 4) and several other more dynamically isolated galaxies. Substructure #1 includes the dominant galaxy of D3-43-S3 and has an estimated dynamical mass of 3.6×10^{14} $M_\odot$. The estimated mass of substructure #2 is lower, of the order of 8.8×10^{13} $M_\odot$. D3-43-S3 is therefore probably about to undergo an important merger between at least two comparable galaxy structures (see also Sect. 5). To confirm this statement, we also show in Fig. 3 (bottom part) the colour-magnitude relation of the two substructures in the D3-43-S3 region. This shows that the two substructures have both red and blue galaxies. We are

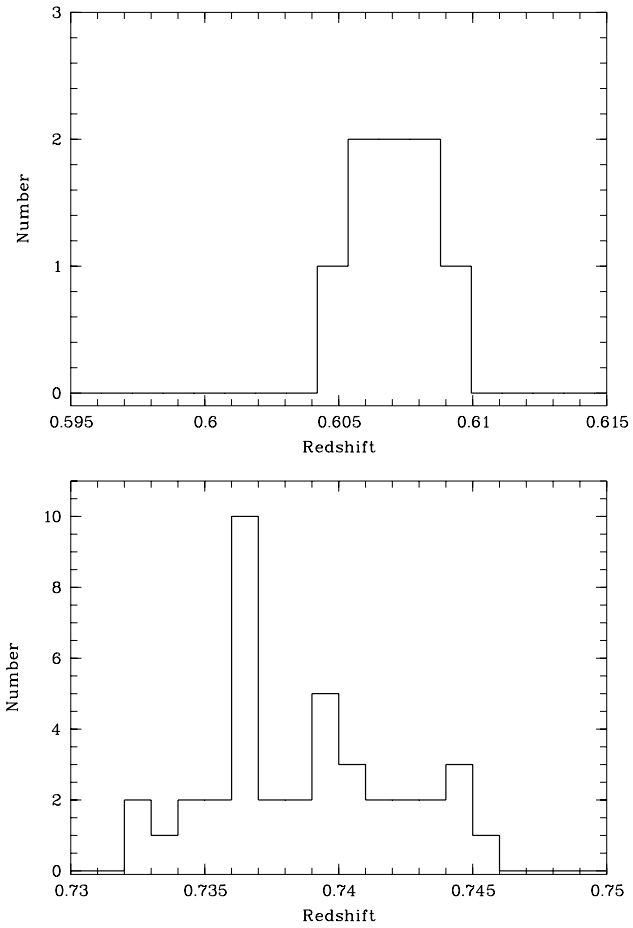

Fig. 4. Redshift distribution of the Gemini/GMOS galaxies with known spectroscopic redshifts in the D3-6 (*top*), and D3-43-S3 (*bottom*) structures.

therefore not dealing with a structure populated by young galaxies merging with an older galaxy structure. The apparently high velocity dispersion of D3-43-S3 (when not considering the detected substructures) is also consistent with this scenario.

3. Mass characterisation of the D3-6 and D3-43-S3 structures

At this stage, we have secured the detection of the D3-6 and D3-43-S3 structures, confirmed that they are populated by both red and blue galaxies, shown that D3-6 is not undergoing a major merger, and that D3-43-S3 is probably about to undergo such a merger. However, we do not yet have robust estimates of the masses of these two structures (the SG test does not give reliable absolute mass values, as already stated).

3.1. Publicly available X-ray data

Both fields D3-6 and D3-43-S3 were observed by the *Chandra* X-ray telescope. Even if the collecting area of *Chandra* is not favourable to the characterisation of such distant structures, the exposure times were long enough to at least give an estimate of the X-ray luminosities of these structures.

There are four pointings at the D3-43 region with the ACIS-I detector (obs_id 5845, 5846, 56214, 6215, PI K. Nandra, taken in 2005). Following the "Science Threads" from the *Chandra* X-ray Center (CXC), using 4.6[1], we have reprocessed these observations and merged them together producing a single broad-band (0.5–7.0 keV) exposure-map corrected surface brightness image with a pixel scale of 1.968 arcsec ($14/h_{70}$ kpc assuming $z = 0.739$). The total effective exposure time for this image is 193.6 ks. There is apparently no visible large scale extended X-ray emission coinciding with the position of D3-43-S3 (e.g. not detected in Erfanianfar et al. 2013). We only see a collection of three compact sources. In a circular region of radius $R = 2$ arcmin, we estimate that an extended source with count rate above 4.2×10^{-4} cnt/s (about 85 counts) would be detected. Thus, assuming a plasma thermal emission, we can put an upper limit of $f_X < 4.3 \times 10^{-15}$ erg s^{-1} cm^{-2}. This corresponds to an upper limit for the X-ray luminosity $L_X < 1.5 \times 10^{43}$ erg s^{-1} if the source is at $z = 0.739$. This could be typical of a massive structure of galaxies, but at this stage this is not enough to reach a conclusion about the massive nature of D3-43-S3.

The D3-6 region was observed in April 2002 with ACIS-I (obs_id 3239, P.I. E. Ellingson) with an exposure time of 62.82 ks. We followed the same reduction procedure, producing a flat (exposure-corrected) image in the 0.5–7.0 keV band with a pixel scale of 1.968 arcsec ($13/h_{70}$ kpc assuming $z = 0.607$). A faint, extended source is visible at 14:17:01.7, +53:05:13 (J2000). To produce an image showing only the diffuse component, we have detected all point sources with the task , following Science Threads[2], which is based on the wavelet image decomposition technique. Then, the regions containing the detected point sources were replaced with a Poissonian noise, using the task, with the same mean value sampled from an elliptical annulus around the source. Finally, for display purposes, we have smoothed the diffuse emission image with a Gaussian kernel of 12 pixels (23.6″). Within 2 arcmin, we estimate a net count rate (background subtracted) of $(5.56 \pm 0.97) \times 10^{-3}$ cnt/s. This corresponds to a flux $f_X = (5.44 \pm 0.92) \times 10^{-14}$ erg s^{-1} cm^{-2} and, assuming a redshift $z = 0.607$, a bolometric luminosity $L_X = (1.12 \pm 0.19) \times 10^{44}$ erg s^{-1}, typical of a low-mass cluster of galaxies. The derived X-ray luminosity corresponds to a velocity dispersion $\sigma_v \approx 500$ km s^{-1}, using the scaling relation by Lopes et al. (2009). This estimate is very close to our Serna-Gerbal value (see Table 4). We show in Fig. 5 the *Chandra* contours and the galaxies with known spectroscopic redshifts in the D3-6 cluster overlaid onto the CFHTLS i' band image. Five of the galaxies with known spectroscopic redshifts are at less than 1 Mpc from the cluster X-ray centre, and this is probably enough to secure the association between the X-ray emission and the galaxy redshift concentration (see e.g. Adami et al. 2011, for the XMM-LSS survey). This association would need to be definitively confirmed by measuring the redshift of the X-ray central galaxy, however.

If we convert the X-ray luminosities to masses by applying the scaling relation of Lopes et al. (2009), we find a mass of 2.5×10^{14} $M_\odot$ for D3-6, and an upper limit of 8×10^{13} $M_\odot$ for D3-43 (calculated within r_{500}).

3.2. Weak lensing characterisation of D3-43-S3

To check if we can investigate the mass distribution around D3-43-S3 in an independent way, we took advantage of the CFHTLS D3 images in the i' band for which a special release is available with a seeing of 0.64 arcsec. Even with such a good

[1] asc.harvard.edu/ciao/
[2] http://cxc.harvard.edu/ciao/threads/

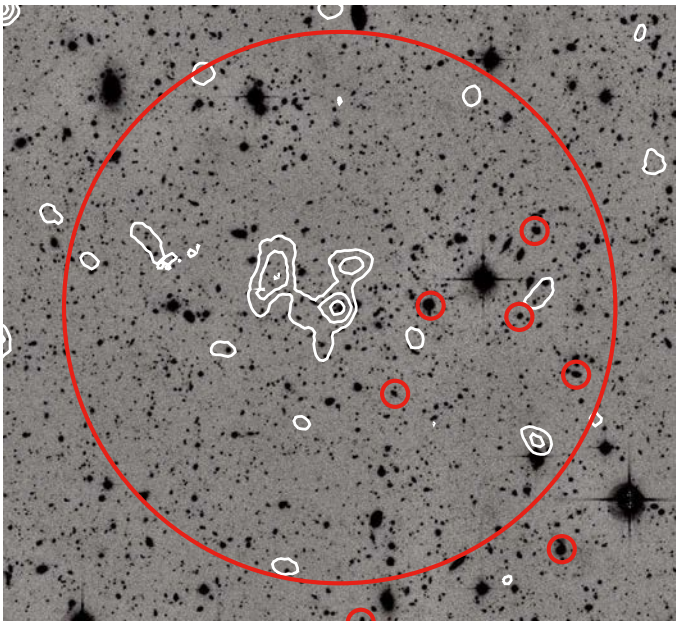

Fig. 5. CFHTLS i' band image of D3-6 overlaid with *Chandra* contours in white (see text). Small red circles show the galaxies with known spectroscopic redshifts inside the $z = 0.607$ D3-6 structure. The large red circle represents a 1 Mpc radius area.

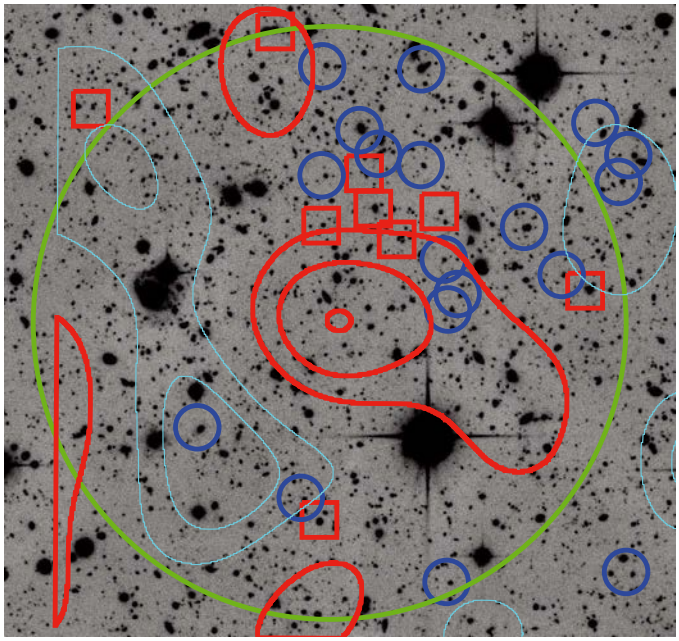

Fig. 6. CFHTLS i' band image of D3-43 overlaid with weak lensing contours (see text). Red squares and blue circles are the galaxies with known spectroscopic redshifts inside the $z = 0.739$ D3-43-S3 substructures #1 and #2, respectively. The green circle has a radius of 1 Mpc. We show the positive sources as thick red contours and the negative sources as thin cyan contours. The contours are given in numbers of sigma corresponding to the noise in the convergence map reconstruction, starting with 1σ.

ground-based seeing, it is still a difficult task to try to detect modest mass concentrations at $z \sim 0.74$, but we have no other possibility with the data available to tell if D3-43-S3 has a significant mass or not.

We cut a subimage centred on our structure with a field of view of $6.3' \times 6.3'$ (corresponding to 2.74×2.74 Mpc^2). This is roughly the size of VLT/FORS2 images, which are well suited for cluster weak lensing studies at this redshift (e.g. Clowe et al. 2006). We measure object positions using SExtractor (Bertin & Arnouts 1996) and shapes using the latest *imcat* software tools (Kaiser 2011). We then apply the standard KSB+ methodology for PSF correction (Kaiser et al. 1995; Luppino & Kaiser 1997). The full detail of the method applied will be found in Martinet et al. (in prep.). The general idea is to measure the PSF distortion on the stars in the image to subtract it from the galaxy shape measurements. In practice, this information is retained in the fourth moment of object surface brightness distributions. Stars are discriminated from galaxies in a half-light radius versus magnitude plot. A visual inspection of both stars and galaxies in the field is mandatory to eliminate false detections, objects that are blended or near saturated stars and artefacts. We also apply a correction factor that represents the bias of our method and was calibrated on STEP2 simulations (Massey et al. 2007). We eliminate cluster and foreground galaxies to avoid diluting the signal, by considering photometric redshifts computed on the basis of u^*, g', r', i', z', J, H, Ks (CFHTLS and WIRDS release, see Bielby et al. 2012) magnitudes. Given the precision of these photometric redshifts, we remove all objects at redshifts lower than the structure redshift plus 0.1, keeping only distant galaxies, the only ones potentially sensitive to the D3-43-S3 mass concentration. Finally, the shear catalogue is converted into a binned shear map, which is then inverted into a convergence map following Kaiser & Squires (1993). We then apply a Gaussian smoothing that allows us to estimate the noise level in the map (van Waerbeke 2000). The density of background galaxies is ~18 galaxies per square arcmin. The contours are given in numbers of sigma corresponding to the noise in the convergence map reconstruction. The result is that D3-43-S3 is barely detected at a 3σ level (see Fig. 6). We note that given the quite low detection level, we did not try to calibrate the weak lensing countours in terms of mass.

We show in Fig. 6 the weak lensing contours and the galaxies with known spectroscopic redshifts in D3-43-S3 overlaid on the CFHTLS i' band image. Twentytwo of the galaxies with known spectroscopic redshifts are at less than 1 Mpc from the cluster weak lensing centre. We will not discuss the weak lensing analysis of D3-6 since its detection level is smaller than 3σ.

4. Properties of the galaxy populations in the two structures

Publicly available photometric redshifts in the CFHTLS D3 field are among the best available from ground-based data (computed with LePhare, e.g. Coupon et al. 2009). Following Coupon et al. (2009), we chose to limit our photometric redshift samples to $i' \leq 24$ ($g' \leq 25$ with Fukugita et al. 1995).

We also verified that for the spectroscopic member galaxies of D3-43-S3, the statistical uncertainty of the photometric redshifts was of the order of 0.037. To keep as many structure galaxies as possible in our samples, we then chose to select a slice of $\pm 3 \times 0.037$ around the two clusters. The price to pay is the likely inclusion of field galaxies satisfying this criterium. This contribution is quite easy to remove statistically however, using for example a comparison field (CF) taken in the CFHTLS D3 field (with the same angular size as the considered cluster), empty from any known candidate cluster and with galaxies selected in the same photometric redshift range.

The remaining uncertainty in the cluster galaxy counts comes from the catastrophic errors present in the photometric redshifts. To take this uncertainty into account, we considered

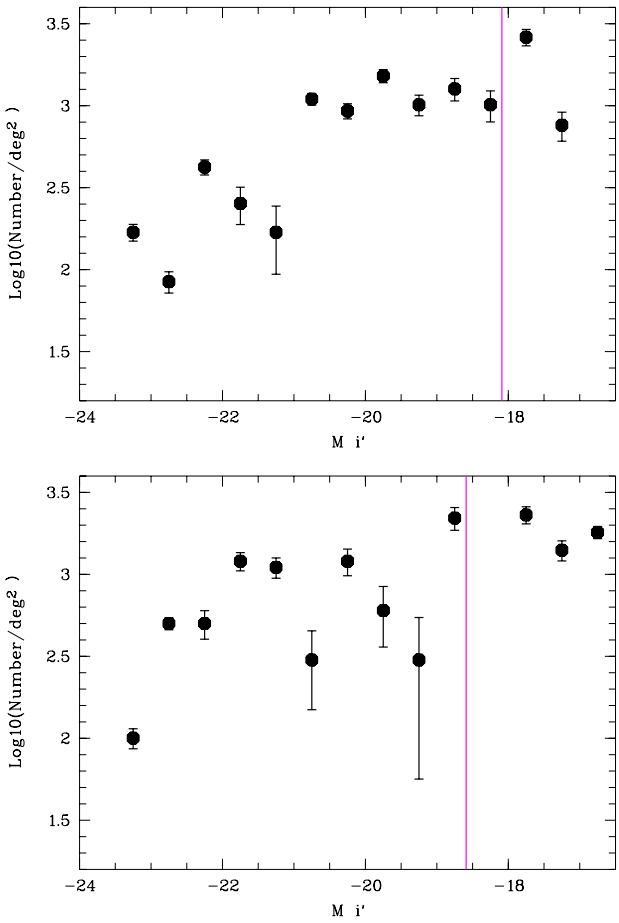

Fig. 7. Luminosity functions for the whole galaxy population of D3-6 (*top*) and D3-43-S3 (*bottom*) per bin of 0.5 mag normalised to 1 deg^2. The vertical lines show the limits in absolute magnitude computed from the $i' = 2490\%$ completeness limit, applying the distance modulus and the mean K-correction in the D3-6 and D3-43-S3 fields.

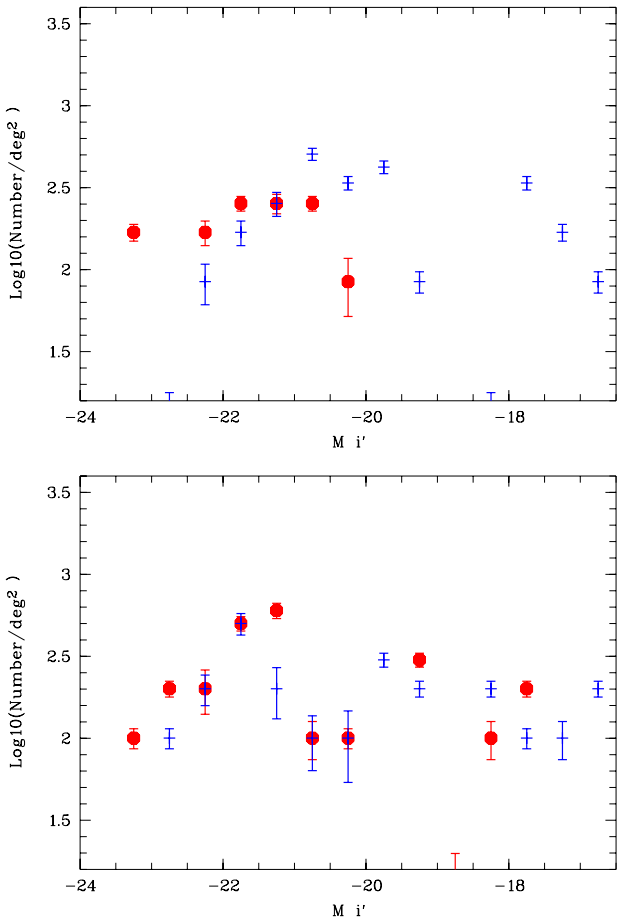

Fig. 8. Luminosity functions for the galaxies with morphological types classified as later (blue crosses) and earlier (red disks) than Sb. *Upper panel*: D3-6; *lower panel*: D3-43-S3.

the percentage of such catastrophic errors in the CFHTLS deep fields computed in Coupon et al. (2009): 4%. This was added to the Poissonian error bars estimated for each magnitude bin in what follows.

We then re-ran the LePhare code with both the Cosmos-survey SEDs (e.g. Ilbert et al. 2010) and the Bruzual & Charlot (2003) SEDs, fixing the redshifts of the selected samples to the spectroscopic redshifts of the two structures. We only considered galaxies for which all the bands were available. This gave us rest-frame absolute magnitudes, stellar masses, and star formation rates (SFRs).

4.1. Galaxy luminosity functions

Galaxy luminosity functions were computed by counting the galaxies along the D3-6 and D3-43-S3 lines of sight and statistically subtracting the empty field counts.

We then compared the rest-frame absolute i' magnitude band galaxy luminosity functions (in a 1.5 Mpc radius) of the two clusters (Fig. 7). We note that K-corrections are already taken into account in the absolute magnitudes and this allows us to compare the luminosity functions of the two main structures. To compare the two luminosity functions, first we had to increase (0.07 towards the high values along the y-axis) the D3-6 values by 18% to take the fact that the two structures are at different redshifts into account. We limited the luminosity functions to absolute magnitudes brighter than −18.5 (see Fig. 7). We then performed 10 000 realisations of the two luminosity functions within the error bars and performed a Kolmogorov-Smirnov test each time. The probability for the two luminosity functions to originate from the same parent distribution was then found to be higher than 99% for 47% of the realisations, and higher than 75% for 97% of the realisations. This clearly shows that the D3-6 and D3-43 luminosity functions are not significantly different.

The next step is to consider the luminosity functions per morphological type. This can be done by considering the modelled types available in the photometric redshift catalogues. These types go from 1 (elliptical galaxies) to 31 (starburst galaxies). We divided our galaxy sample into types earlier and later than Sb to generate Fig. 8.

We performed the same Kolmogorov-Smirnov tests and found that for the D3-6 cluster, the probability for the early and late-type galaxy luminosity functions to originate from the same parent distribution was higher than 99% for 0% of the realisations, and higher than 75% for only 63% of the realisations. In this case, we can conclude that the early and late-type galaxy luminosity functions in D3-6 are probably different, and that this cluster clearly has more late-type galaxies than early-type galaxies in the faint magnitude regime (this is quite obvious in Fig. 8).

The same exercise yields different results for the D3-43-S3 cluster. The probability that the early and late-type galaxy luminosity functions originate from the same parent distribution

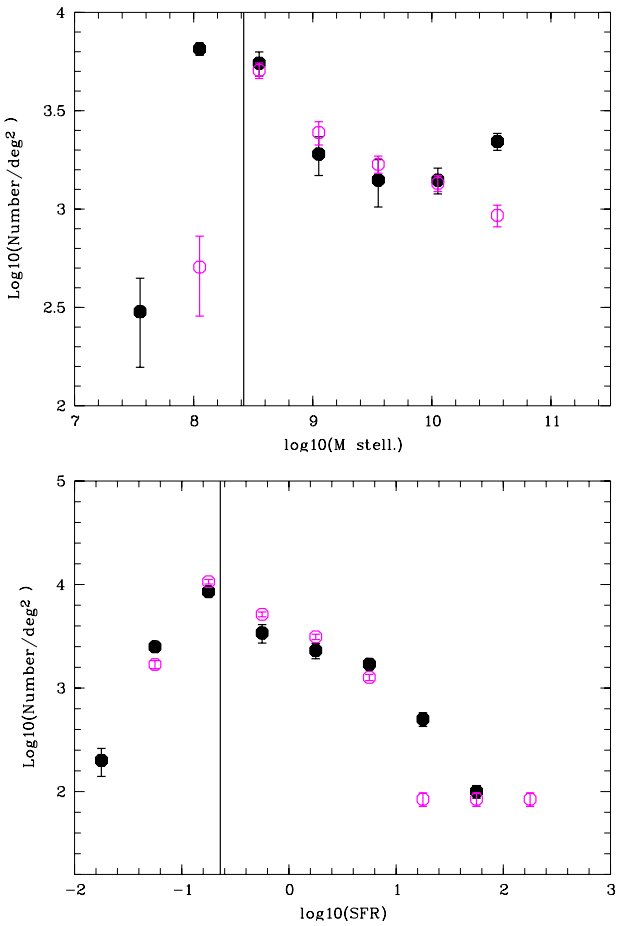

Fig. 9. *Upper panel*: stellar mass functions for the galaxy populations of D3-6 (pink circles) and D3-43-S3 (black disks). *Lower panel*: SFR functions for the galaxy populations of D3-6 (pink circles) and D3-43-S3 (black disks), in units of $M_\odot$/yr. In both plots, the vertical lines show the values corresponding to the most stringent i' band absolute magnitude 90% completeness level.

is higher than 99% for 42% of the realisations, and higher than 75% for 100% of the realisations. In this case, we have similar luminosity functions for early and late-type galaxies (as seen in Fig. 8).

4.2. Star formation history in D3-6 and D3-43-S3

To investigate the stellar formation history in the galaxies of the considered clusters more precisely, we first computed galaxy stellar mass functions in D3-6 and D3-43-S3 (after statistical subtraction of the empty field values). These are displayed in Fig. 9. The two clusters exhibit very similar stellar mass functions. Even if D3-43-S3 is richer than D3-6 for the highest stellar mass bin, a Kolmogorov-Smirnov test shows that the two global distributions (in the domain where the data are 90% complete) are the same.

We also considered the SFRs of the galaxies in D3-6 and D3-43-S3 (see Fig. 9). A Kolmogorov-Smirnov test shows that the SFRs are very similar for both structures: probability greater than 99% for 49% of the realisations, and higher than 75% for 100% of the realisations. Considering each bin of Fig. 9 separately, the only significant differences occur towards high values of the SFR, with D3-43-S3 having more galaxies with SFR of ~16 $M_\odot$/yr (these galaxies could have their SFR boosted by the ongoing merger taking place in D3-43-S3), and D3-6 having more galaxies with intense SFR (~150 $M_\odot$/yr).

We estimated the SFR and stellar mass completeness levels in the following way: we selected the galaxies with a magnitude differing by less than 0.1 from the i' magnitudes at the 90% completeness limit. We then computed the mean SFRs and stellar masses for these galaxies and considered that these values represented the SFR and stellar mass completeness levels.

5. Conclusions

With data obtained with GEMINI/GMOS and data taken from the literature and NED, we spectroscopically confirmed two structures initially detected with the AMACFI photometric redshift based cluster finder in the CFHTLS D3 field.

The first structure, D3-43-S3, can be decomposed into two substructures, each with a velocity dispersion of ~350 and ~600 km s^{-1}, which could be in the process of collapsing into a large structure more or less along the line of sight. Since no X-ray emission is detected, the interaction is probably not strong yet, explaining the fact that we (barely) detect it in weak lensing (where we are probably seeing the addition of the two structure masses along the line of sight) but not in X-rays.

The D3-6 structure is found to be a single structure at an average redshift $z = 0.607$, with a velocity dispersion of 423 km s^{-1}. It appears to be a relatively low-mass cluster.

We also show that D3-6 and D3-43-S3 have similar global galaxy luminosity functions, stellar mass functions, and SFR distributions. The only differences are that D3-6 exhibits a lack of faint early-type galaxies, a deficit of extremely high stellar mass galaxies compared to D3-43-S3, and an excess of very high SFR galaxies.

Besides the fact that this work adds two compact galaxy structures to the strategical and still relatively poorly cluster-populated $0.5 < z < 1$ redshift range, it also shows the power of photometric redshift based techniques to detect and study distant clusters (galaxy types, SFR, etc.), provided that a large spectral coverage in the optical and near infrared is available. Combined-approach cluster surveys (e.g. photometric redshifts to detect them and X-rays or weak lensing to characterise them in terms of mass) are also crucial. EUCLID is the perfect example of such a mission for clusters, since it will combine weak lensing and cluster detections based on photometric redshifts.

Acknowledgements. Based on observations obtained at the Gemini Observatory, which is operated by the Association of Universities for Research in Astronomy, Inc., under a cooperative agreement with the NSF on behalf of the Gemini partnership: the National Science Foundation (United States), the Science and Technology Facilities Council (United Kingdom), the National Research Council (Canada), CONICYT (Chile), the Australian Research Council (Australia), Minist rio da Ci ncia, Tecnologia e Inova o (Brazil) and Ministerio de Ciencia, Tecnolog a e Inovaci n Productiva (Argentina). This research has made use of the VizieR catalogue access tool at CDS, Strasbourg, France. This research has also made use of the NASA/IPAC Extragalactic Database (NED), which is operated by the Jet Propulsion Laboratory, California Institute of Technology, under contract with the National Aeronautics and Space Administration. Finally, this paper is based on observations obtained with MegaPrime/MegaCam, a joint project of CFHT and CEA/IRFU, at the Canada-France-Hawaii Telescope (CFHT), which is operated by the National Research Council (NRC) of Canada, the Institut National des Sciences de l'Univers of the Centre National de la Recherche Scientifique (CNRS) of France, and the University of Hawaii. This work is based in part on data products produced at Terapix available at the Canadian Astronomy Data Centre as part of the Canada-France-Hawaii Telescope Legacy Survey, a collaborative project of NRC and CNRS. We would like to dedicate this paper to Alain Mazure, deceased in 2013, and who was part of this work in its early stages. We gratefully acknowledge financial support from the Centre National d'Etudes Spatiales during many years. This work was also supported by the Brazilian agencies FAPESP and CNPq and benefited

from the CAPES-COFECUB agreement number 711/11. We thank the referee for interesting comments.

References

Adami, C., Biviano, A., Durret, F., & Mazure, A. 2005, A&A, 443, 17
Adami, C., Le Brun, V., Biviano, A. et al. 2009, A&A, 507, 1225
Adami, C., Durret, F., Benoist, C., et al. 2010, A&A, 509, A81
Adami, C., Mazure, A., Pierre, M., et al. 2011, A&A, 526, A18
Beers, T. C., Gebhardt, K., Forman, W., Huchra, J. P., & Jones, C. 1991, AJ, 102, 1581
Bertin, E., & Arnouts, S. 1996, A&AS, 117, 393
Bielby, R., Hudelot, P., McCracken, H. J., et al. 2012, A&A, 545, A23
Bou , G., Durret, F., Adami, C., et al. 2008, A&A, 489, 11
Boselli, A., Voyer, E., Boissier, S., et al. 2014, A&A, 570, A69
Bruzual, G., & Charlot, S. 2003, MNRAS, 344, 1000
Clowe, D., Schneider, P., Arag n-Salamanca, A., et al. 2006, A&A, 451, 395
Coupon, J., Ilbert, O., Kilbinger, M., et al. 2009, A&A, 500, 981
Dressler, A., & Schechtman, S. A. 1988, AJ, 95, 985
Dunkley, J., Komatsu, E., Nolta, M. R., et al. 2009, ApJS, 180, 306
Durret, F., Adami, C., Gerbal, D., & Pislar, V. 2000, A&A, 356, 815
Durret, F., Slezak, E., & Adami, C. 2009, A&A, 506, 637
Durret, F., Lagan , T. F., Adami, C., & Bertin, E. 2010, A&A, 517, A94
Erfanianfar, G., Finoguenov, A., Tanaka, M., et al. 2013, ApJ, 765, 117
Fukugita, M., Shimasaku, K., & Ichikawa, T. 1995, PASP, 107, 945
Garilli, B., Fumana, M., Franzetti, P., et al. 2010, PASP, 122, 827
Guennou, L. 2012, Ph.D., Universit de Marseille-Provence
Guennou, L., Adami, C., Durret, F., et al. 2014, A&A, 561, A112
Guzzo, L., Scodeggio, M., Garilli, B., et al. 2014, A&A, 566, A108
Holden, B. P., Illingworth, G. D., Franx, M., et al. 2007, ApJ, 670, 190
Howell, D. A., Sullivan, M., Perrett, K., et al. 2005, ApJ, 634, 1190
Hsieh, B. C., Yee, H. K. C., Lin, H., & Gladders, M. D. 2005, ApJS, 158, 161
Ilbert, O., Arnouts, S., McCracken, H. J., et al. 2006, A&A, 457, 841
Ilbert, O., Salvato, M., Le Floc'h, E., et al. 2010, ApJ, 709, 644
Kaiser, N., & Squires, G. 1993, ApJ, 404, 441
Kaiser, N., Squires, G., & Broadhurst, T. 1995, ApJ, 449, 460
Kaiser, N. 2011 [record ascl:1108.001]
Katgert, P., Mazure, A., Perea, J., et al. 1996, A&A, 310, 8
Lopes, P. A. A., de Carvalho, R. R., Kohl-Moreira, J. L., & Jones, C. 2009, MNRAS, 399, 2201
Luppino, G. A., & Kaiser, N. 1997, ApJ, 475, 20
Massey, R., Heymans, C., Berg , J., et al. 2007, MNRAS, 376, 13
Mateus, A., Sodr , L., Cid Fernandes, R., & Stasińska, G. 2007, MNRAS, 374, 1457
Mazure, A., Adami, C., Pierre, M., et al. 2007, A&A, 467, 49
Newman, J. A., Cooper, M. C., Davis, M., et al. 2013, ApJS, 208, 5
Olsen, L. F., Benoist, C., Cappi, A., et al. 2007, A&A, 461, 81
Poggianti, B. M., De Lucia, G., Varela, J., et al. 2010, MNRAS, 405, 995
Ross, A. J., Percival, W. J., & Brunner, R. J. 2010, MNRAS, 407, 420
S nchez-Bl zquez, P., Jablonka, P., Noll, S., et al. 2009, A&A, 499, 47
Serna, A., & Gerbal, D. 1996, A&A, 309, 65
Simard, L., Clowe, D., Desai, V., et al. 2009, A&A, 508, 1141
Thanjavur, K., Willis, J., & Crampton, D. 2009, ApJ, 706, 571
Ulmer, M. P., Adami, C., Lima Neto, G. B., et al. 2009, A&A, 503, 399
van der Wel, A., Holden, B. P., Franx, M., et al. 2007, ApJ, 670, 206
van Waerbeke, L. 2000, MNRAS, 313, 524
Walker, E. S., Hook, I. M., Sullivan, M., et al. 2011, MNRAS, 410, 1262
White, S. D. M., & Frenk, C. 1991, ApJ, 379, 52

Appendix A: DEIMOS/GMOS redshift comparison

We show in Fig. A.1 the difference between the GEMINI/GMOS redshifts and the KECK/DEIMOS DEEP2 redshifts as a function of redshift.

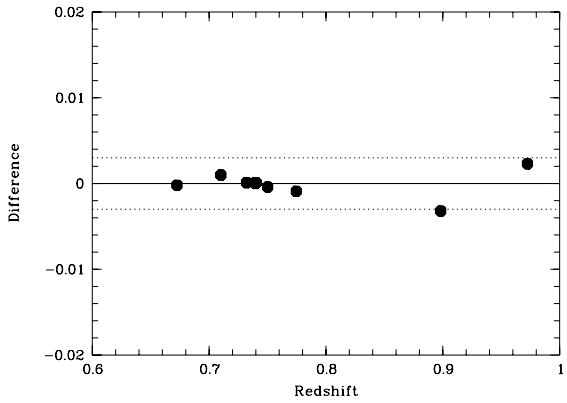

Fig. A.1. Comparison of Deep2 Keck/DEIMOS and GMOS/Gemini redshifts. The solid horizontal line symbolises the perfect agreement. The two dashed lines represent the 3σ maximum uncertainty between the two redshift measurements taking the resolution of the GMOS grism and the smoothing of the spectra into account.

Appendix B: Examples of spectra

Below are four examples of spectra corresponding to flags 4, 3, and 2 in Figs. B.1 and B.2.

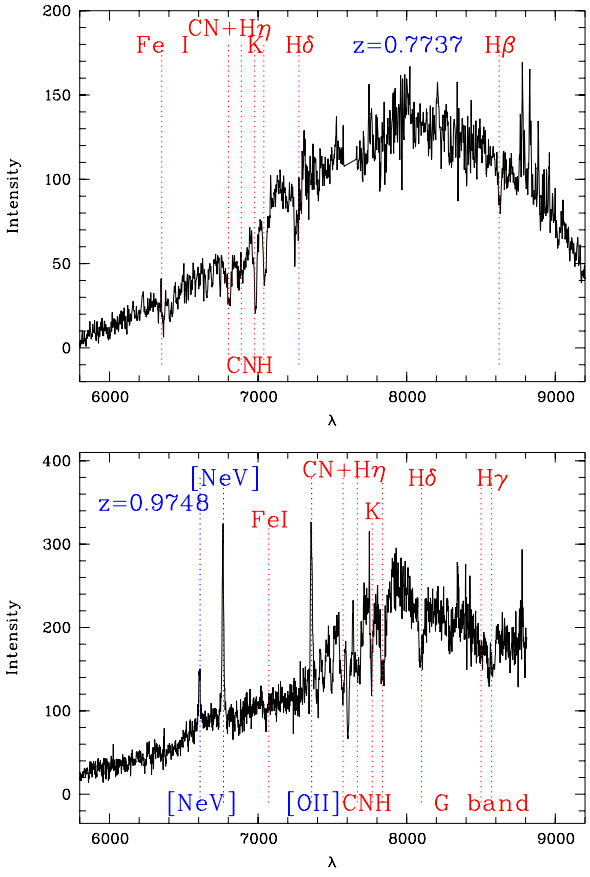

Fig. B.1. Two examples of Gemini/GMOS spectra with flags 4. Red labelled lines show absorption lines and blue labelled lines show emission lines.

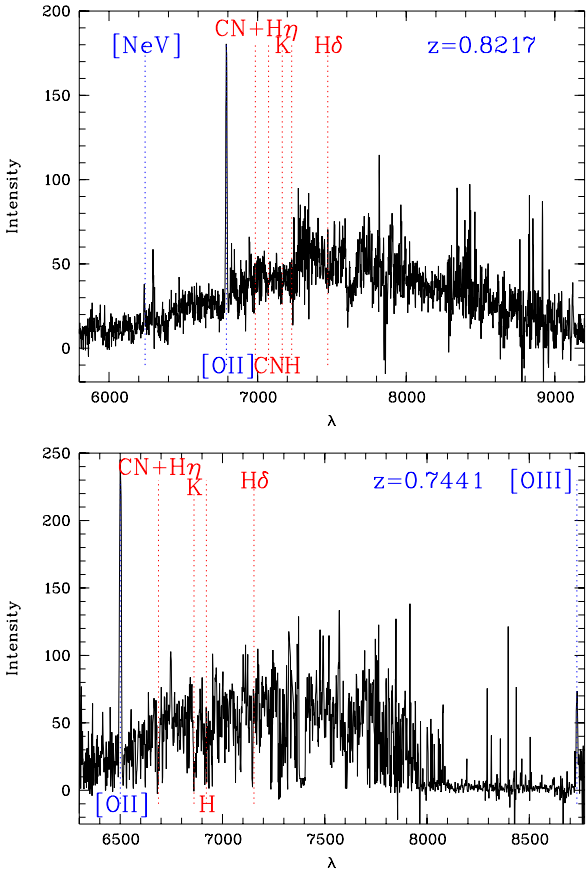

Fig. B.2. Two examples of Gemini/GMOS spectra with flags 3 and 2. Red labelled lines show absorption lines and blue labelled lines show emission lines. *From top to bottom*: one spectrum with flag 3 and one spectrum with flag 2.

A.3 Article 3: Guennou et al. 2014a

In this section, I review my contribution to the Guennou et al. (2014a) paper: **Structure and substructure analysis of DAFT/FADA galaxy clusters in the [0.4-0.9] redshift range**.

We study the structures of galaxy clusters for a subsample of 32 DAFT/FADA clusters, using X-ray and spectroscopic data, with the aim of detecting substructures and mergers. We model the X-ray emission of clusters and subtract it to *XMM*–Newton images to identify residuals. Point sources are removed using *Chandra* observations or AGN catalogs, to avoid considering them as residuals. For clusters with at least 15 spectroscopic redshifts, we apply a Serna & Gerbal (Serna & Gerbal 1996) analysis, which hierarchically classifies galaxies according to their redshift and position. We estimate the masses of detected substructures using a scaling relation to the galaxy luminosities. We find that the percentage of mass included in substructures is about 5-15% and is roughly constant with redshift, in agreement both with the general CDM framework and with the results of numerical simulations.

My contribution to the paper is the computation of the masses of the substructures. In the Serna & Gerbal method, a rough estimate of the mass of the substructure is computed using a total mass-to-light ratio of 100. I refined this estimation, using a stellar mass-to-light ratio for each galaxy from Kauffmann et al. (2003), and then a scaling relation of the stellar mass with respect to the total mass. This scaling relation is calculated from groups of galaxies studied in Giodini et al. (2009), as substructures have masses closer to those of groups than of clusters. Both mass estimates agree for small substructures ($< 10\%$ in mass) but they differ for some larger structures.

Due to their length, Annexes are not displayed but can be consulted on the online version of the paper. They present the X-ray and/or spectroscopic study of each individual cluster.

A&A 561, A112 (2014)
DOI: 10.1051/0004-6361/201321208

Astronomy & Astrophysics

Structure and substructure analysis of DAFT/FADA galaxy clusters in the [0.4–0.9] redshift range⋆

L. Guennou[1,2], C. Adami[1], F. Durret[3], G. B. Lima Neto[4], M. P. Ulmer[5], D. Clowe[6], V. LeBrun[1], N. Martinet[3], S. Allam[7,8], J. Annis[7], S. Basa[1], C. Benoist[9], A. Biviano[3,10], A. Cappi[9,11], E. S. Cypriano[4], R. Gavazzi[3], C. Halliday[12], O. Ilbert[1], E. Jullo[1], D. Just[13,14], M. Limousin[1], I. Márquez[15], A. Mazure[1], K. J. Murphy[6], H. Plana[16], F. Rostagni[9], D. Russeil[1], M. Schirmer[17,18], E. Slezak[9], D. Tucker[7], D. Zaritsky[13], and B. Ziegler[19]

(Affiliations can be found after the references)

Received 31 January 2013 / Accepted 25 October 2013

ABSTRACT

Context. The DAFT/FADA survey is based on the study of ∼90 rich (masses found in the literature $>2 \times 10^{14}\ M_{\odot}$) and moderately distant clusters (redshifts $0.4 < z < 0.9$), all with HST imaging data available. This survey has two main objectives: to constrain dark energy (DE) using weak lensing tomography on galaxy clusters and to build a database (deep multi-band imaging allowing photometric redshift estimates, spectroscopic data, X-ray data) of rich distant clusters to study their properties.

Aims. We analyse the structures of all the clusters in the DAFT/FADA survey for which *XMM-Newton* and/or a sufficient number of galaxy redshifts in the cluster range are available, with the aim of detecting substructures and evidence for merging events. These properties are discussed in the framework of standard cold dark matter (ΛCDM) cosmology.

Methods. In X-rays, we analysed the *XMM-Newton* data available, fit a β-model, and subtracted it to identify residuals. We used *Chandra* data, when available, to identify point sources. In the optical, we applied a Serna & Gerbal (SG) analysis to clusters with at least 15 spectroscopic galaxy redshifts available in the cluster range. We discuss the substructure detection efficiencies of both methods.

Results. *XMM-Newton* data were available for 32 clusters, for which we derive the X-ray luminosity and a global X-ray temperature for 25 of them. For 23 clusters we were able to fit the X-ray emissivity with a β-model and subtract it to detect substructures in the X-ray gas. A dynamical analysis based on the SG method was applied to the clusters having at least 15 spectroscopic galaxy redshifts in the cluster range: 18 X-ray clusters and 11 clusters with no X-ray data. The choice of a minimum number of 15 redshifts implies that only major substructures will be detected. Ten substructures were detected both in X-rays and by the SG method. Most of the substructures detected both in X-rays and with the SG method are probably at their first cluster pericentre approach and are relatively recent infalls. We also find hints of a decreasing X-ray gas density profile core radius with redshift.

Conclusions. The percentage of mass included in substructures was found to be roughly constant with redshift values of 5–15%, in agreement both with the general CDM framework and with the results of numerical simulations. Galaxies in substructures show the same general behaviour as regular cluster galaxies; however, in substructures, there is a deficiency of both late type and old stellar population galaxies. Late type galaxies with recent bursts of star formation seem to be missing in the substructures close to the bottom of the host cluster potential well. However, our sample would need to be increased to allow a more robust analysis.

Key words. galaxies: clusters: general

1. Introduction

The DAFT/FADA survey[1] is based on the study of ∼90 rich (masses found in the literature $>2 \times 10^{14}\ M_{\odot}$) and moderately distant ($0.4 < z < 0.9$) galaxy clusters, all with HST imaging data available. This survey has two main objectives. The first one is to constrain dark energy (DE) using weak lensing tomography on galaxy clusters. The second one is to build a database of rich distant clusters to study their properties. The requirement of obtaining photometric redshifts for the DAFT/FADA survey fields has indeed allowed us to build a rich multi-band imaging database for these clusters. For a number of them, we have also obtained spectroscopic data for several tens of galaxies in the cluster redshift range, either from our own observations, or from public databases.

DAFT/FADA is a nice complement to other cluster surveys such as for example the Local Cluster Substructure Survey (LoCuSS, X-ray selected, around $z \sim 0.2$, Smith et al. 2010), the MAssive Cluster Survey (MACS, X-ray selected, $z > 0.3$, but with only 12 clusters above $z = 0.5$, Ebeling et al. 2001a, 2007, 2010), or the Cluster Lensing And Supernova survey with *Hubble* (CLASH, Postman et al. 2012) which analyses the high mass end of the cluster population, with only 14 clusters in the redshift range of our survey.

The redshift range chosen for the DAFT/FADA survey is an important one in terms of studying cluster evolution. First, because clusters have achieved nearly full growth in terms of mass by redshift of about 1 (see review by Kravtsov & Borgani 2012, hereafter KB12, and references therein) and the DE density becomes the dominant form of energy density just below redshift 0.4 (under the standard cold dark matter, hereafter ΛCDM, cosmology). Second, clusters have acquired a hot and

⋆ Tables 1, 2, 4 and Appendices A–C are available in electronic form at http://www.aanda.org

[1] PIs: M. Ulmer, C. Adami, and D. Clowe, see Guennou et al. (2010) and http://cencos.oamp.fr/DAFT/ for a full description of the project.

dense enough intracluster medium (ICM) to become detectable at $z < 2$, and yet, clusters continue to evolve, with infalling substructures present to current day, such as the Coma cluster and the NGC 4839 subgroup (Neumann et al. 2003). The [0.4, 0.9] redshift range is also interesting because it spans a time frame of about 3 Gyr, giving substructures time to infall, and thus allowing comparison of the younger systems with the older ones on a meaningful time scale. With a typical infall speed of 1000 km s^{-1}, substructures have enough time to cross the cluster about three times between z of 0.9 (age of universe 6.3 Gyr) and 0.4 (9.4 Gyr). Understanding how the three major components (the ICM, the galaxies, and the dark matter concentrations that are the seeds of clusters) form to grow into massive clusters is still a work in progress though (KB12).

The cluster formation simulations all involve an assumption about initial density perturbations and must include interplay between (at least) non-interacting cold dark matter (CDM) and the evolution of the baryon content in the cluster, including the ICM and galaxies.

While on the galactic scale there is a possible disagreement between the number of subhaloes found and predicted (e.g. Strigari et al. 2010), there have not been enough observations yet at the cluster and substructure scales to require any adjustments or re-examination of the ΛCDM paradigm.

Tonnesen & Bryan (2008) offer a useful review of cluster substructure observations. Among the numerous papers dealing with the observations of cluster substructures, we can also quote for X-rays Böhringer et al. (1994), Dupke & Bregman (2001), Furusho et al. (2001), Shibata et al. (2001), Churazov et al. (2003), Böhringer et al. (2010), and Weissmann et al. (2013). And in the optical: Adami et al. (2005), Ulmer et al. (2009), Einasto et al. (2012), and Wen & Han (2013). However, there has been little coupling of X-ray and optical data, especially in the redshift range [0.4, 0.9] of the DAFT/FADA sample. Over this time frame of about 3 Gyr, some galaxy groups are infalling for the first or second time (e.g. Poole et al. 2007 and the present paper). As noted above, clusters have already accreted enough material to become detectable by $z \sim 1$, and the time scale from $z = 0.9$ to 0.4 is just sufficient for a substructure to move in and out of a cluster.

Thus, we can compare our work with the predictions of simulations such as those by Poole et al. (2007) and the observations of subgroups that are in the field. Further work done by Tonnesen & Bryan (2008) also shows that the existence and properties of subclusters affect the evolution of ram pressure stripping of galaxies due to the local relative velocities between the substructures and the cluster galaxies. In related work on the ICM in subgroups, Takizawa (2005), for example, has shown that subclusters do not lose all their mass via ram pressure stripping, say, in the first passage, which agrees with the simulations of Poole et al. (2007). Thus, one would expect to see (as is observed) substructure in some of the cluster X-ray emission images over all redshift ranges below about 1. In complementary work by Gao et al. (2012: the Phoenix project), they and others (e.g. Springel et al. 2008a,b; Navarro et al. 2010, the Aquarius Project) predict the fraction of mass clusters made up of subclusters (at $z = 0$, however), and we can compare our results (albeit at higher redshift) with those simulations as a first step in linking these cluster formation codes with our observations.

Our data could therefore lead to improvements in the simulations to describe the substructure mass fraction growth and evolution over the $z = 1$–0 time frame in a more quantitative way than results obtained, for example, by simulation movies (e.g. Diemand[2] and Hydro-ski[3]) or images (e.g. Borgani & Kravtsov (2009). Perhaps the present paper and future observational papers will encourage more quantitative simulations and their analysis.

From an observational point of view, the substructure forming groups that clusters continue to accrete at later epochs than $z \simeq 1$ have smaller scales than do the clusters themselves or those of larger groups accreted above about $z \simeq 2$ (e.g. Adami et al. 2012; Connelly et al. 2012). The existence of such groups of galaxies has been confirmed up to $z \sim 1.3$ (e.g. Gerke et al. 2007 or Lilly et al. 2009) and groups are very common at lower redshifts (e.g. Carlberg et al. 2001). This also implies different mechanisms in the group accretion (e.g. simulated in Poole et al. 2007, see also KB12) than during the initial cluster formation and should have direct consequences on the cluster dynamical state, which can be probed by detecting substructures. The search for substructures in the [0.4, 0.9] redshift range thus allows us to search for traces of this accretion mechanism inside galaxy clusters. This search can be made either in the galaxy distribution or in the ICM through X-ray data.

We primarily used data from the *XMM-Newton* archive to detect substructures in all the clusters of the DAFT/FADA survey for which such data were available (about half of the sample) and then we carried out follow-up *Chandra* analysis. A review of methods available to search for substructures in X-rays can be found in Andrade-Santos et al. (2012). In the optical, we used the Serna & Gerbal (1996, hereafter SG) hierarchical code (based on spectroscopic redshifts and optical magnitudes) to detect optical substructures. A number of better-known methods are available to search for substructures in the optical, such as the Δ-test (Dressler & Schechtman 1988), which searches for deviations in the local mean velocity and velocity dispersion from the overall values. However, the SG method is quite powerful for showing evidence of substructuring, as illustrated by the results for a number of different clusters, at low redshift (Abell 496: Durret et al. 2000; Coma: Adami et al. 2005, 2009; Abell 780: Durret et al. 2009; Abell 85: Boué et al. 2008), moderate redshift (Abell 222/223: Durret et al. 2010), and high redshift (RX J1257.2+4738: Ulmer et al. 2009). The SG method has also been extensively tested on simulations by Guennou (2012), in particular on the effect of undersampling on mass determinations.

Our aim in this paper is to investigate the structure of the DAFT/FADA clusters for which X-ray and/or optical spectroscopic+imaging data are available. This will improve our knowledge of clusters (analysed in a homogeneous way) in the [0.4, 0.9] redshift range.

As we show below, at least in a general way, there is agreement between theory (simulations) and our observations of substructure in rich clusters, but further work is needed on both fronts to determine if the standard ΛCDM model of the Universe needs any modification with regards to the effects of the CDM on the growth of large scale-structures in the Universe.

The paper is presented in the following way. In Sect. 2, we present the X-ray data, analyses, and results. Section 3 is dedicated to optical data and SG analyses. Our results are presented in Sect. 4 and summarized in Sect. 5. The majority of the figures (X-ray images and X-ray residuals over an azimuthally averaged β-model, spectroscopic redshift histograms), except for a few illustrative ones, are grouped in the Appendices (available in electronic form).

[2] http://krone.physik.unizh.ch/~diemand/clusters/
[3] http://astro-staff.uibk.ac.at/~hydroskiteam/

We adopted the Dunkley et al. (2009) concordance cosmological model ($H_0 = 71.9$ km s^{-1} Mpc^{-1}, $\Omega_\Lambda = 0.742$, $\Omega_M = 0.258$).

2. X-ray data and data analysis

We retrieved *XMM-Newton* data from the public archive and only kept the clusters with data of sufficient quality and depth (typically those for which the relative error on the MOS1 count rate, hence the X-ray luminosity, is less than 20%). The *XMM-Newton* data obtained with the EPIC-MOS (Metal Oxide Semi-conductor) instruments were reduced using the SAS (Science Analysis System developed by the *XMM-Newton* team) tool from the Heasarc package. After this we applied the code created by Andy Read to remove flares, using a 3σ clipping technique, and we calibrated the images.

2.1. Basic parameters

We analysed the *XMM-Newton* data available for 42 clusters to derive their X-ray temperatures and luminosities and search for substructures. A spatial analysis was possible for 32 of these clusters, but only 23 had deep enough X-ray data for a really robust spatial analysis (i.e. the β-model ftting process converged for those 23 clusters).

The information on the 32 clusters in our sample that have usable *XMM-Newton* data is given in Table 1. X-ray luminosities in the [0.5, 8.0] keV interval were computed for all of them, but in seven cases the X-ray emission was not sufficient to estimate the temperature of the X-ray gas. For 17 clusters that we have in common with Baldi et al. (2012), we compared our X-ray gas temperatures and find good agreement (mean difference of −0.27 keV with a dispersion of 1.34 keV).

Though the main aim of this paper is to study the substructures in the DAFT/FADA survey, we computed the gas masses and total masses for the 25 clusters with measurable X-ray temperatures, and these masses can give interesting information on cluster properties. We estimated the X-ray gas masses and total masses in the r_{500} radius for the clusters with reliable X-ray temperatures using the proxy calculated by Kravtsov et al. (2006), based on simulations with cosmological parameters close to ours. The parameters of the proxy determined by Kravtsov et al. (2006) are given for relaxed and unrelaxed clusters, and for $z = 0$ and $z = 0.6$, with small differences from one category to another. Because our X-ray clusters cover a redshift range between 0.4 and 0.9, and some are relaxed and some are not (and in a number of cases we cannot classify our clusters as relaxed or unrelaxed), we took average values in the Kravtsov et al. (2006) Table 2 ($\log_{10}C = 14.4$ and $\alpha = 1.500$) to obtain the following formulae (which give the gas and total masses in solar masses as a function of the X-ray gas temperature kT in keV):

$$M_{\rm gas,500} = \frac{2.5 \times 10^{14}}{11.2} \left(\frac{kT_{\rm keV}}{3}\right)^{1.5} M_\odot. \quad (1)$$

To compute the total mass, we decided to take one of the best determinants, also given by Kravtsov et al. (2006):

$$Y_x = kT \times M_{\rm gas,500}. \quad (2)$$

Using the average values of the parameters (for all redshifts and all clusters: $\log_{10}C = 14.27$ and $\alpha = 0.581$), we computed the total mass with the relation:

$$M_{\rm tot,500} = 10^{14.27} \times \left(\frac{Y_x}{4.0 \times 10^{13}}\right)^{0.581} M_\odot. \quad (3)$$

Total masses may be slightly underestimated here, since the stellar contribution (stars in galaxies and intracluster light) has not been taken into account (though it has been shown not to be negligible, see e.g. Gonzalez et al. 2007). The corresponding masses are given in Table 1. In the case of unrelaxed clusters, we may expect the total masses derived from X-rays to be overestimated (e.g. Mamon 2000; Chon et al. 2012, and references therein).

2.2. Model subtraction to search for substructures

The X-ray images, with a pixel size of 3.2×3.2 arcsec^2, were then fit with an azimuthally symmetric elliptical β-model (as given by Sherpa[4]):

$$\Sigma(r) = \Sigma_0 \left[1 + \left(\frac{r}{r_c}\right)^2\right]^{-3\beta+0.5} + b$$

where $\Sigma(r)$ is the surface brightness as a function of radius r, Σ_0 is the central surface brightness, r_c the core radius, β the shape parameter, and b accounts for the background, which is assumed to be constant throughout the image.

To analyse the best quality data possible to search for substructures, we had to make a compromise between having a high number of photons to improve our detections and avoiding artifacts due in particular to the superposition of images obtained with different detectors (and thus summing up their defects). In this context, to limit the number of artefacts, we ignored the observations that were contaminated by bad pixels and/or had CCD gaps passing through the cluster image, mainly the PN and sometimes the MOS-2 data.

We opted to model our clusters with a simple beta-model rather than with more complex ones, such as the "modified β-model" (e.g. Vikhlinin et al. 2006) or double β-model (e.g. Eckmiller et al. 2011). The reason is that many of our clusters are very faint and have a small angular size, and their cores are hardly resolved by XMM. This makes it very difficult to give meaningful constraints for models with 12 or more free parameters (remembering that we are also fitting the ellipticity, position angle, and coordinates of the centre). Therefore, to compare all clusters uniformly we used the standard 2D β-model described above.

This model represents a relaxed cluster with a homogeneous gravitational potential, simulated with the Sherpa tool[5] from CIAO[6]. The residuals were computed as the difference between the image and the fit, allowing us to bring out any perturbation from a homogeneous gravitational potential due to the substructures that are not completely merged with the cluster yet. This is a classical technique used, for example, to study the Coma cluster with *XMM-Newton* (Neumann et al. 2003).

Results for each cluster are shown in the Appendix and a summary of the properties of the X-ray detected substructures is given in Table 2, together with other quantities described in Sect. 4.3. We only give the SG-estimated velocity dispersions for substructures also detected in X-rays.

2.3. Assessing substructure detections with simulations

To test our method of identifying substructures in X-rays, we have generated a series of synthetic X-ray images. These images

[4] http://cxc.cfa.harvard.edu/sherpa4.4/ahelp/beta2d.html

[5] http://cxc.harvard.edu/sherpa4.4/index.html

[6] *Chandra* Interactive Analysis of Observations, see http://asc.harvard.edu/ciao

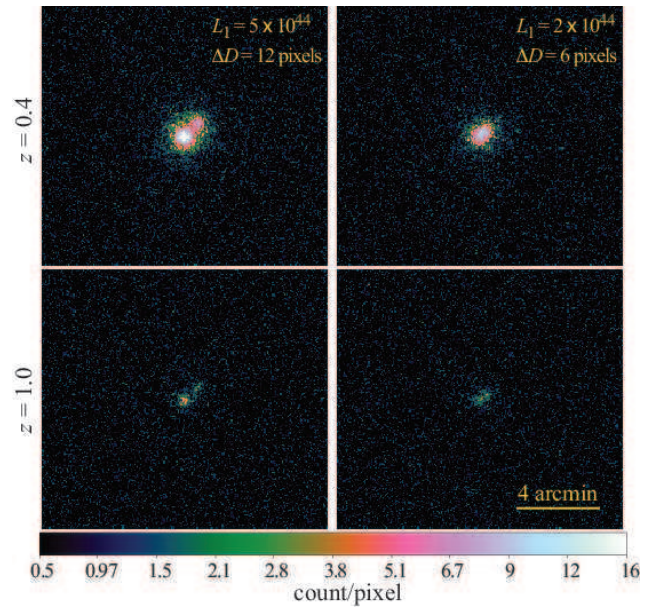

Fig. 1. A few examples of simulated images showing the situation where the subcluster can be easily detected (low redshift, well separated) and the case where the subcluster is hardly seen (high redshift, small separation). See text for more details.

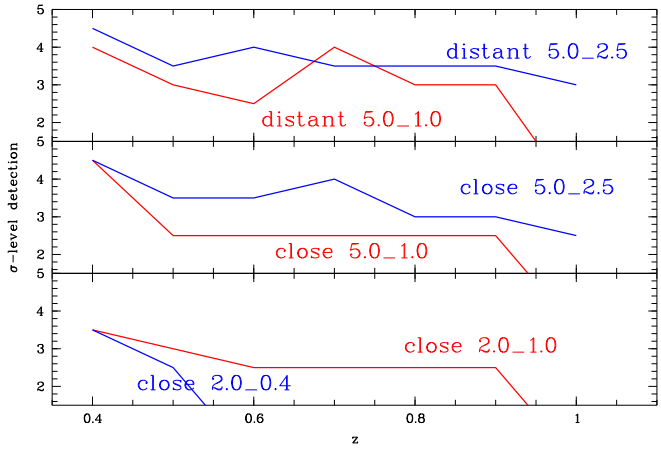

Fig. 2. Detection level (in σ units) of the X-ray simulated substructures (50 ks exposures) versus redshift. *Lower panel*: 2.0×10^{44} erg/s cluster + 0.4×10^{44} erg/s subcluster (close 2.0_0.4) and 2.0×10^{44} erg/s cluster + 1.0×10^{44} erg/s subcluster (close 2.0_1.0). Separated by 6 px in both cases. *Middle panel*: 5.0×10^{44} erg/s cluster + 1.0×10^{44} erg/s subcluster (close 5.0_1.0) and 5.0×10^{44} erg/s cluster + 2.5×10^{44} erg/s subcluster (close 5.0_2.5). Separated by 6 px in both cases. *Upper panel*: 5.0×10^{44} erg/s cluster + 1.0×10^{44} erg/s subcluster (distant 5.0_1.0) and 5.0×10^{44} erg/s cluster + 2.5×10^{44} erg/s subcluster (distant 5.0_2.5). Separated by 12 px in both cases. When the line stops, it means that the subcluster is no longer detected. The close 2.0_0.4 configuration, for example, provides detections of the subcluster only up to $z = 0.5$ at the 2.5σ level.

consist of a primary luminous cluster and a fainter subcluster, both represented by a projected β-model, with $\beta = 0.6$ (a typical value, see e.g. Jones & Forman 1984). The surface brightness per pixel is converted in counts/s taking the MOS response, the cluster temperature, and the K-correction, which is important given the redshift range we are covering ($0.4 \leq z \leq 1.0$) into account. The simulated cluster temperature is fixed using an $L_X - T_X$ scaling relation (Xue & Wu 2000). The cluster images are then generated assuming a Poisson distribution for each pixel.

We assumed the equivalent of 50 ks, 25 ks, and 10 ks exposures. This optimally covers our range of exposure durations (see Table 1). The synthetic images have a scale of 3.2 arcsec/pixel, corresponding to the binning we used. We added a flat Poissonian background with a count rate of 6.6×10^{-7} counts s^{-1} arcsec^{-2}, corresponding to the typical on-axis MOS background in the [0.3–8.0] keV band observed in our (real) images.

We generated synthetic images in a coarse grid (see Fig. 1) where the cluster and subcluster were separated by either 6 or 12 pixels (19.2 arcsec and 38.4 arcsec, or ~140 and 280 kpc at $z = 0.7$). For both separations, we fixed the luminosity ratio at 1/5 and 1/2, with the luminosity of the primary cluster fixed to be either $L_X = 5 \times 10^{44}$ or 2×10^{44} erg s^{-1}. Images were generated between redshifts 0.4 and 1.0 in steps of 0.1. In this way, we generated 42 simulated images per exposure time (126 in total), to which we can apply our X-ray substructure detection procedure. The analysis of these simulations is given in Fig. 2 for 50 ks exposures (small bumps in the curves are due to hot pixels coinciding with a substructure, which artificially increase the S/N).

We also show in Fig. 3 the detection limits of the 50 ks, 25 ks, and 10 ks runs overlaid on our cluster distributions in a plot of useful *XMM-Newton* exposure time as a function of redshift. The results can be summarized as follows. There are indeed no clusters without detected substructures in Fig. 3 located inside the area where we theoretically cannot detect substructures. The detection of a substructure strongly depends on its X-ray luminosity (more than on the ratio of the luminosity of the substructure to that of the main structure). The more luminous the substructure, the better it is detected at high redshift. The distance between the substructure and the cluster centre does not change the maximum redshift of the detection, but has an influence on the significance level of the detection. It is easier to detect a substructure far from the cluster centre.

To be more quantitative, simulations predict the detection of substructures brighter than 1.0×10^{44} erg/s in our redshift interval, while fainter substructures should be detected only for $z < 0.5$. This is consistent with our results: all the substructures that we detect are brighter than 10^{44} erg/s except three (Abell 851, RXC J1206, and LCDCS 0504), out of which the first two clusters are at $z < 0.45$. In three quarters of the cases, we also detect residuals of the cluster itself at a 2.5σ level. Therefore, potential substructures detected very close to the cluster centre are probably only residuals from the cluster itself, and not real substructures.

The results of these simulations allow us to indicate in Table 1 whether a substructure was detected or not. If it was not detected, these simulations allow confirming that there is indeed no substructure above the solid lines in Fig. 3, or if substructures, if any, are below our detection limit (the solid lines in Fig. 3). Open symbols touching the solid lines were flagged 0/–1 in Table 1.

2.4. Contamination by point sources

In some of the residual images it was difficult to distinguish substructures from point sources owing to the limited spatial resolution of *XMM-Newton*. To check this point, we considered *Chandra* images when available. Thanks to their very good angular resolution, these data allowed us to locate bright point sources, which were usually bright enough not to be plagued by the relatively poor *Chandra* collecting power.

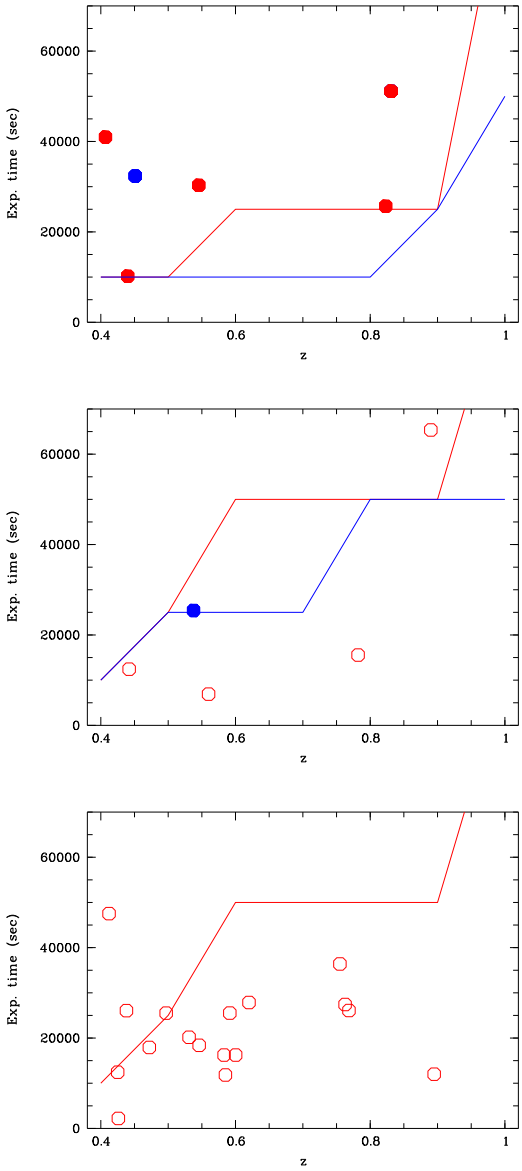

Fig. 3. Clusters in our sample in diagrams of useful *XMM-Newton* exposure time versus redshift. Filled symbols are clusters with one or more detected substructures, and open symbols clusters without any detected substructures. Solid lines are susbstructure detection limits below which it is not possible to detect a substructure. *Upper panel*: red symbols are clusters brighter than 5.0×10^{44} erg/s with detected substructures fainter than 2.5×10^{44} erg/s and more distant than 7 pixels from the cluster centre (or no detected substructures). Blue symbols are clusters brighter than 5.0×10^{44} erg/s with detected substructures brighter than 2.5×10^{44} erg/s and more distant than 7 pixels from the cluster centre. *Middle panel*: red symbols are clusters brighter than 5.0×10^{44} erg/s with detected substructures fainter than 2.5×10^{44} erg/s and less distant than 7 pixels from the cluster centre (or no detected substructures). Blue symbols are clusters brighter than 5.0×10^{44} erg/s with detected substructures brighter than 2.5×10^{44} erg/s and less distant than 7 pixels from the cluster centre. *Lower panel*: red symbols are clusters fainter than 5.0×10^{44} erg/s with detected substructures fainter than 0.4×10^{44} erg/s and less distant than 7 pixels from the cluster centre (or no detected substructures).

Second, we also searched for all X-ray point sources known as AGN and QSOs in the fields covered by *XMM-Newton* but not by *Chandra*. This was done via the NED and Vizier databases, as well as with our own spectroscopic observations (see below).

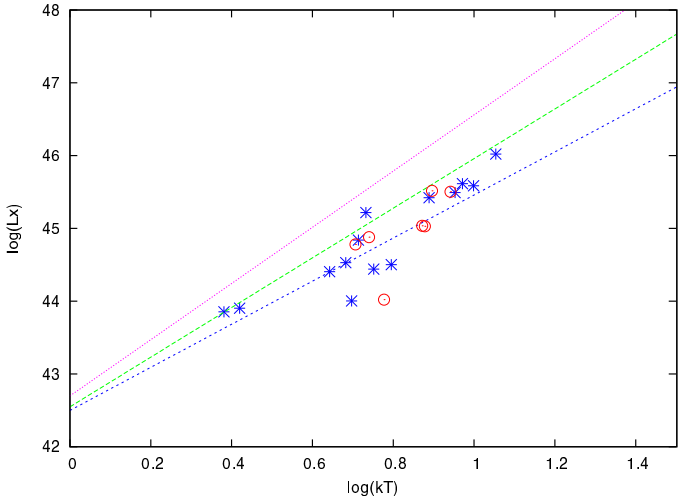

Fig. 4. X-ray luminosity as a function of X-ray temperature for our clusters on a logarithmic scale. The blue crosses and red circles represent clusters with redshifts respectively lower and higher than 0.6. The central green dashed line represents the L_X–T_X relation found by Takey et al. (2011), and the blue and pink dashed lines indicate the uncertainty on this relation.

Most of the time, public databases referred to the work by Gilmour et al. (2009).

2.5. Validation of X-ray luminosities and temperatures

Even though this was not one of the primary goals of the present study, it was important to validate our X-ray measurements. We plot the X-ray luminosities as a function of the X-ray temperatures in Fig. 4, with different symbols for the clusters at redshifts lower and higher than 0.6 (the redshift limit of Takey et al. 2011), and we plot on the same figure the Takey et al. (2011) relation. We can see that our X-ray data agree reasonably well with the Takey et al. (2011) L_X–T_X relation. If we try to separate clusters with and without substructures, we find no obvious dependence in the relation between L_X and T_X and the level of substructuring, perhaps because of the relatively small size of our sample.

3. Optical data and Serna & Gerbal analysis

3.1. Optical imaging and spectroscopic data

Our survey was initiated for clusters with HST images available, generally at least in the F814W band. We obtained deep optical imaging for most of the clusters in several bands, with various telescopes (Blanco, Calar Alto, CFHT, Gemini, GTC, SOAR, TNG, VLT, WIYN, WHT). Part of the images were also taken from observatory archives (e.g. CFHT, Subaru, ESO). We are also presently in the process of acquiring infrared *J* band images to have better constraints on the photometric redshifts of distant galaxies (for weak lensing tomography)[7].

The galaxy magnitudes used here were measured in the *V* photometric band images, calibrated and extinction-corrected in the usual way (see Guennou et al. 2010). Some archive images were observed in other bands, and in this case they were converted into the *V* band following Fukugita et al. (1995).

We retrieved all the galaxy spectroscopic redshifts available in NED, VizieR, and in the literature in a region of radius

[7] http://cencos.oamp.fr/DAFT/

Table 3. Clusters with no usable X-ray data but with more than 15 galaxy redshifts in the cluster range.

Name	RA	Dec	z	Nz
Cl J0023+0423B	5.96587	4.37797	0.8453	23
CXOMP J 002650.2+171935	6.70917	17.32658	0.4907	29
CXOMP J 091126.6+055012	137.86083	5.83681	0.7682	18
LCDCS 0110	159.46917	–12.72889	0.5789	18
LCDCS 0130	160.17333	–11.93083	0.7043	30
LCDCS 0172	163.60083	–11.77167	0.6972	48
LCDCS 0173	163.68125	–12.76389	0.7498	37
CL J1103.7-1245a	165.89542	–12.77944	0.6300	19
CXOMP J 111726.1+074335	169.35875	7.72639	0.4770	36
LCDCS 0340	174.54292	–11.56639	0.4798	51
LCDCS 0531	186.97458	–11.63889	0.6355	24
LCDCS 0541	188.12708	–12.84250	0.5414	80
ClG J1236+6215	189.16500	62.26500	0.8500	40
XDCS mf J 131001.9+322110	197.50792	32.35278	0.4370	19
NSCS J 132336+302223	200.91500	30.37600	0.461	19
MJM98 034	203.80742	37.81564	0.383	16
3C 295 Cluster	212.83396	52.20251	0.4600	66
GHO 1601+4253	240.80762	42.76005	0.5391	50
RX J1716.4+6708	259.20667	67.14167	0.809	37

Notes. (1) Name (as in NED), (2) right ascension in degrees (J2000.0), (3) declination in degrees (J2000.0), (4) redshift, (5) number of galaxies with redshifts in the cluster range.

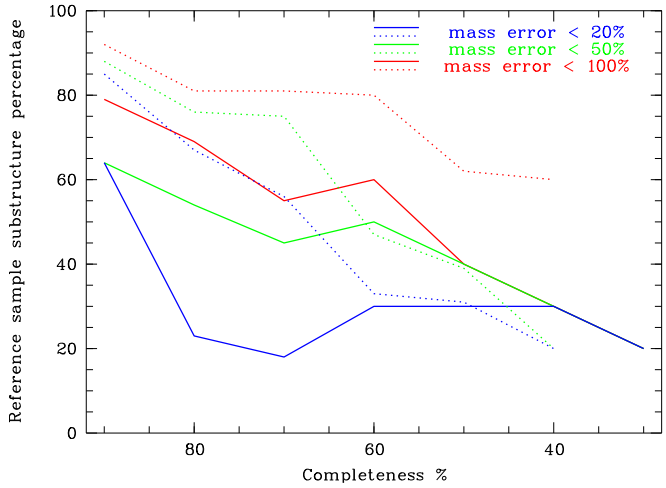

Fig. 5. Effects of the undersampling of the input spectroscopic catalogue on the results of the SG method. The figure shows the percentages of substructures in the total reference cluster sample (versus the spectroscopic catalogue completeness percentage) for which the mass estimates are plagued by an error of less than X% (compared with the 100% complete spectroscopic catalogue). Blue lines are for X = 20%, green lines for X = 50%, and red lines for X = 100%. Continuous and dashed lines respectively correspond to substructures that merged and that did not merge with other substructures during the spectroscopic catalogue resampling process.

5 arcmin around each cluster centre. Such a zone corresponds to a radius of 1.59 Mpc at z = 0.4 and 2.24 Mpc at z = 0.8, and therefore covers the entire cluster. We also added redshifts that we obtained during several observing runs with 8 m telescopes (42 redshifts obtained with GMOS on the Gemini telescope and 60 obtained with FORS2 on the VLT). Typical errors on the velocities measured with FORS2 are ±180 km s^{-1} (see Guennou et al., in prep.). For redshifts taken from NED, the uncertainties are not given, so we assume them to be comparable to those of our FORS2 data.

Gemini/GMOS spectroscopy has a resolution of 7 Å/px (see Guennou et al. 2013 for details). The targeted objects were brighter than $I_{AB} \sim 24$, and the reduction was made with the IRAF package and the Gemini/Gmos environment.

VLT/FORS2 spectroscopy was obtained during ESO period 85 (programme: 085.A-0016) with a resolution of 3 Å/px. The targeted objects were brighter than $I_{AB} \sim 23$. We applied the standard ESO reduction since it proved to be good enough to measure redshifts for most of our targets.

In order not to eliminate a priori galaxies that could be close to the clusters on the line of sight, we applied the SG method (see below) to all the galaxies with measured redshifts. For each cluster, the number of galaxies in the cluster redshift range is given in Tables 1 and 3. The cluster redshift range is defined as the range within ±0.025 of the mean cluster redshift (which corresponds to ±3 times the maximum velocity dispersion observed in clusters: ~1500 km s^{-1}).

Galaxy spectroscopic redshift histograms are given in the Appendix. In most cases we only show a zoom around the mean cluster redshift. When necessary, a full redshift histogram is also given (e.g. when several structures are detected along the line of sight and/or when the cluster redshift given in NED could be wrong).

3.2. Searching for substructures by applying a Serna & Gerbal analysis: the method

For each cluster, the catalogue of galaxies for which positions, spectroscopic redshifts and magnitudes were available was analysed with the SG method, in a region comparable to the X-ray image (when available). We limited our sample to the clusters having at least 15 spectroscopic galaxy redshifts in the cluster range. Assuming a mean number of three SG detected substructures per cluster, this allows us to have statistically about 5 galaxies per substructure, close to the number required to avoid being too affected by incompleteness (see below).

The SG hierarchical method calculates the potential binding energy between pairs of galaxies and detects substructures taking positions and redshifts into account. The output is a file containing lists of galaxies distributed in a hierarchical way. For example, structure 1 will be the cluster and structure 2 will be galaxies outside the cluster. Structure 1 will then be divided into 11 and 12, etc.

Assuming a value of 100 (in solar units) for the total mass-to-stellar luminosity ratio (but results do not strongly depend on this quantity, e.g. Adami et al. 2005), galaxy magnitudes can be transformed into masses, and approximate values can be estimated for the total masses of the various substructures detected by the SG method. The comparison with other mass estimates (see Sects. 3.4 and 4.2) strongly suggests that the absolute values of the optical masses estimated by the SG method cannot be considered as fully reliable. However, mass ratios (i.e. when trying to determine if a substructure is more massive than another one) can be considered as robust, keeping in mind, however, that assuming a constant M/L for all galaxies is probably an oversimplification. Figure 5 allows us to estimate the typical uncertainties on these mass ratios. Considering

only completeness levels lower than 80% (we never reach higher completeness levels in spectroscopy), the typical dispersion in mass estimates is of the order of 18%. The mass ratios of two such masses therefore must have uncertainties of the order of 25% (the quadratic sum of the relative uncertainties on cluster and substructure masses, both taken to be 18%). By 25%, we mean that if a mass ratio is 40%, the uncertainty on this value will be $0.25 \times 40\% = 10\%$. Typical uncertainties on the mass ratios computed with the scaling law method (see below) are estimated to be of the same order, however we neglect here the uncertainty on the M/L ratio assumed for the galaxies. This, by the way, makes any comparison between the stellar and total masses of the substructures difficult, in particular because by assuming the same M/L ratio for all galaxies, mass ratios are in fact just optical luminosity ratios. Given the typical uncertainties estimated above, we chose not to give the actual values of the mass ratios in Tables 2 and 4, but rather to give estimates of these values in 10% wide intervals.

3.3. Results of the Serna & Gerbal analysis

A summary of the substructures (if any) found by the SG method for each cluster is given in Table 2.

3.4. Influence of the undersampling of redshift catalogues

An important question concerning the application of the SG method is that of estimating how the undersampling in the optical spectroscopy of galaxies can affect our results. To estimate the importance of this effect, we considered six reference clusters from the literature that have more than one hundred spectroscopic redshifts in the cluster redshift range and in various dynamical states (relaxed, with minor, or with major ongoing mergers). We observed the changes in the results depending on the completeness of the input catalogue. The clusters that were considered (and total numbers of galaxy redshifts in parentheses) were Abell 85 (815), Abell 168 (695), Abell 496 (499), Abell 851 (211), Abell 2744 (131), and Coma (595).

To estimate the effects of undersampling, we considered between 100% and 10% of the complete catalogue for each of the six clusters. At each step we randomly took out 10% of the galaxies, reapplied the SG, and checked the results to detect differences with growing incompleteness. This is what we call in the following the resampling process of the spectroscopic catalogue. In this way, we can observe the impact of the undersampling on substructure detection and its effects on the results (numbers of substructures found and corresponding masses) depending on the richness of the substructures.

As expected, substructures with many members tend to be detected down to lower completeness levels, while substructures with few members disappear faster when the undersampling increases. Typically, substructures detected with more than six members in the original spectroscopic catalogues will remain detected by the SG analysis down to completenesses of ~50% to 30%.

The precision on the mass of the substructures detected by the SG analysis varies with completeness level, as seen in Fig. 5. We distinguished two cases: (1) a given substructure is artificially merging with another one during the spectroscopic catalogue resampling process (this process will naturally tend to overestimate the substructure masses) and (2) a given substructure is not polluted by other substructures during the spectroscopic catalogue resampling process. Figure 5 shows that the SG precision on the mass remains better than 50% for about half of the sample down to incompletenesses of about 60%, while the SG analysis is not able to estimate the mass of most of the substructures precisely for completeness levels lower than ~50%.

As a further test of the influence of undersampling on our results, we also applied the SG method to a halo from the Millennium simulation (halo #51 037 100 000 000). This halo has a theoretical mass of $4.4 \times 10^{14}\ M_{\odot}$ and is at a redshift $z = 0.37$. It has 23 subhaloes with more than three galaxies.

Considering the mass resolution of the Millennium simulation, if we use the same semi-analytical models as those applied to the CFHTLS clusters (Adami et al. 2010) we estimate that the completeness limit in this halo corresponds to an absolute magnitude $M_I \sim -17.5$, which roughly corresponds to the completeness limit of the DAFT/FADA survey. In this simulated cluster, if we consider 100% of the galaxies, the SG method detects the five most massive substructures (numbered from #1 to #5), the mass of the least massive one (#5) being $3.5 \times 10^{12}\ M_{\odot}$. Two smaller structures are also detected with masses of $7.9 \times 10^{11}\ M_{\odot}$ and $5.2 \times 10^{11}\ M_{\odot}$.

If we now randomly remove 10% of the galaxies from the initial simulated galaxy catalogue, then 20%, etc., we start to lose some of the initially detected substructures. The percentage of undersampling inducing the loss of a given substructure is the result of a complex interplay between the intrinsic richness of the substructure (a poor substructure will obviously be easier to lose when undersampling the catalogue) and the galaxy mass distribution in the substructure (a cD-dominated substructure will be easier to lose if the cD is removed). For example, because substructure #1 is both very rich (451 galaxies) and not strongly cD-dominated (only 19% of the total mass of the substructure is associated with the cD), we are able to detect it down to a sampling rate of only 10%. The other substructures disappear between sampling rates 90% and 10%, but as a general statement we can say that we are able to detect some of the most massive substructures down to about 30% of the original sampling. The mass estimate remains within a factor of 2 down to 40% sampling.

We also see below that in most cases massive substructures are detected both in X-rays and with the SG analysis, when both types of data are available. However, since the SG mass estimate is sometimes inaccurate, we describe in the next section an alternative way to estimate the mass of a substructure based on optical data.

3.5. Alternative determination of the masses of the substructures detected by the Serna & Gerbal method

As mentioned above, the SG algorithm allows the total structure masses to be estimated in a rather crude way, since the mass-to-luminosity ratio (set to $M/L = 100$) is assumed to be the same for all the galaxies. However, the exact value of M/L does not strongly affect the substructure content since it mainly relies on the spectroscopic redshifts of galaxies, as shown for example by Adami et al. (2005). We have then developed a new method to estimate masses of the substructures detected with the SG algorithm based on more physical arguments. It is well known that the stellar-to-luminosity ratio of a galaxy depends on its spectrum, hence on its magnitude (e.g. Bell et al. 2003; Tremonti et al. 2004; Cappellari et al. 2006). Following this, we propose to apply a different stellar mass-to-light ratio to each galaxy, depending on its luminosity, and then to convert the stellar mass of the substructure to its total mass (i.e. including X-ray gas and

dark matter) using the cluster scaling relation between those two quantities.

We first compute absolute magnitudes by calculating the distance modulus for each galaxy. This is made possible by our only using galaxies with an accurate spectroscopic redshift. We then convert our V-band magnitudes to the g-band, applying a colour correction of $g - V = 0.28$, as found in Fukugita et al. (1995). This allows the stellar mass-to-light ratio to be estimated, as measured for SDSS data for an "average type" galaxy by Kauffmann et al. (2003, see their Fig. 14). Each galaxy is assigned its own stellar mass-to-light ratio and luminosity, taking an absolute magnitude of 5.11 for the Sun in the g-band. Summing the stellar masses of the galaxies belonging to the substructure provides us with the estimated stellar mass of the substructure.

The last step is to convert stellar masses to total masses using the following scaling relation defined by Giodini et al. (2009) for clusters within r_{500}:

$$\frac{M_{\rm star}}{M_{\rm tot}} = (5.0 \pm 0.1) \times 10^{-2} \left(\frac{M_{\rm tot}}{5 \times 10^{13}\, M_{\odot}} \right)^{-0.37 \pm 0.04}. \quad (4)$$

One must note that the ±0.04 uncertainty on the exponent in the previous equation results in large error bars on the total substructure mass (about 85%).

We calculated substructure masses following this method and compared them to those calculated with the SG method for the 18 clusters with optical substructures and X-ray data (e.g. Table 2) and we have a rough overall agreement. We are aware that none of these methods gives the exact mass of substructures, so we present both to cross check our mass ratios. When the results obtained with both methods agree, we have a good chance of having a reasonable estimate.

We also calculated substructure masses for the clusters to which we applied the SG method but for which no X-ray analysis was possible, and give results in Table 4.

4. X-ray gas distribution

The results for the invidual clusters with X-rays and/or a SG analysis are described in the Appendix. In Appendix A, we give a full X-ray (and optical when enough galaxy redshifts are available) analysis for the clusters with usable *XMM-Newton* data. In Appendix B, we present the SG analysis for the clusters with no usable X-ray data but with at least 15 galaxy redshifts in the cluster range. In Appendix C we give brief notes on the clusters for which we have little spatial information, but which are worth mentioning in particular because several of them seem to have redshifts differing from those given by NED.

4.1. Cluster core radius versus redshift

We first investigate the possible variations in the cluster X-ray gas distribution (modelled by a β-model) versus redshift. There is no significant correlation between the redshift and the β-model slope. We may, however, detect a tendency between the β-model core radius and the redshift (see Fig. 6). To produce this figure, we first only selected clusters for which the β-model fitting provides a converging solution (true for ~80% of the clusters). Then, we eliminated double clusters as CL J0152.7-1357. Figure 6 shows that clusters at redshifts lower than 0.65 tend to have larger core radii.

If we now eliminate the clusters with X-ray-detected substructures for which the core radius may be biased the tendency

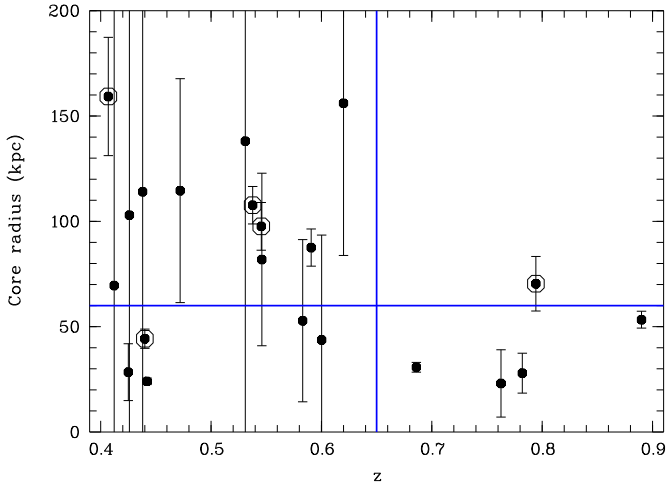

Fig. 6. β-model core radius as a function of redshift for the considered clusters (see text). The circled disks are the clusters with detected X-ray substructures. The two lines symbolize the $z = 0.65$ limit and the maximal value of the core radii for $z \geq 0.65$ not significantly substructured clusters (from an X-ray point of view).

is even more pronounced. The respective mean core radii are 76 ± 42 kpc, 93 ± 45 kpc, and 34 ± 13 kpc for the clusters in the redshift bins [0.4; 0.5], [0.5; 0.65], and [0.65; 0.9]. Even though our sample is limited (only 16 clusters in total after all the selections), it suggests that the highest redshift clusters are younger structures that have not yet accreted large amounts of matter and therefore have smaller core radii. However, this could be due to several selection effects, since our cluster sample is not homogeneous in terms of numbers of detected clusters versus redshift: it is a collection of clusters known in the literature to which we applied simple criteria on mass and available data (see Sect. 1).

The first question is to know if the *XMM-Newton* data we have in hand are able to measure large core radii at $z \geq 0.65$. The collected *XMM-Newton* data are of two types: (1) pointed observations for which the cluster was the main target or (2) observations made for other purposes and where clusters were observed by chance.

We can hope that type (1) *XMM-Newton* pointings will not be too affected by the inability to measure core radii, because exposure times have been selected by the original PIs to specifically study the clusters and modelling a gas distribution is one of the most basic tasks. To test this point, we computed that ~80% of core radius measurements in the type (1) pointings were successful. The calculation of the core radius with Sherpa converged for 80% of the clusters. Among the ~20% unsuccessful measurements, half were at $z \geq 0.65$ and half at $z \leq 0.65$. Type (1) observations therefore do not seem to be affected by a variable (with redshift) ability to measure core radii. Similarly, we also checked that $z \geq 0.65$ and $z \leq 0.65$ did not provide X-ray photon count rates that are too different (the basic parameter for modelling the gas distribution). Clusters at $z \leq 0.65$ are sometimes very bright, but if these bright objects are excluded, we have somewhat lower count rates at low redshifts than at high reshifts. Almost 40% of the $z \leq 0.65$ clusters have count rates that are higher than 0.04 counts/s, while 50% of the $z \geq 0.65$ clusters have count rates higher than 0.04 counts/s. We therefore do not find a strong variation in the cluster count rates with redshift in our sample.

Type (2) observations could present a variable core radius measurement efficiency because their exposure times were not specifically selected to study the clusters. However, these

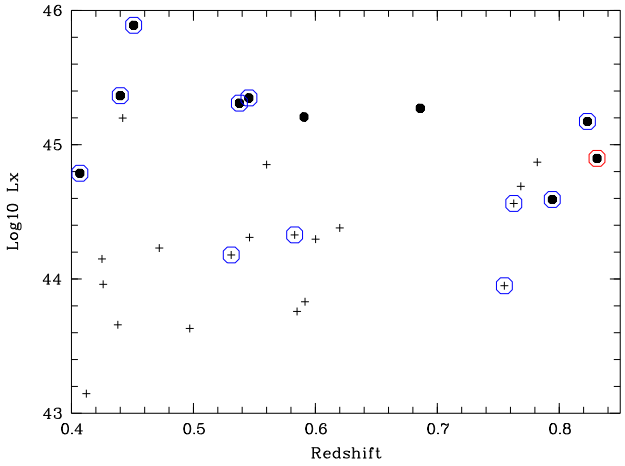

Fig. 7. Cluster total X-ray luminosity as a function of redshift. Filled disks are clusters for which substructures were detected with the X-ray method. Crosses indicate clusters with no X-ray detected substructures. The blue and red circles correspond to clusters for which substructures representing less and more respectively than 15% of the total cluster mass (estimated with the SG method) were detected with the SG method.

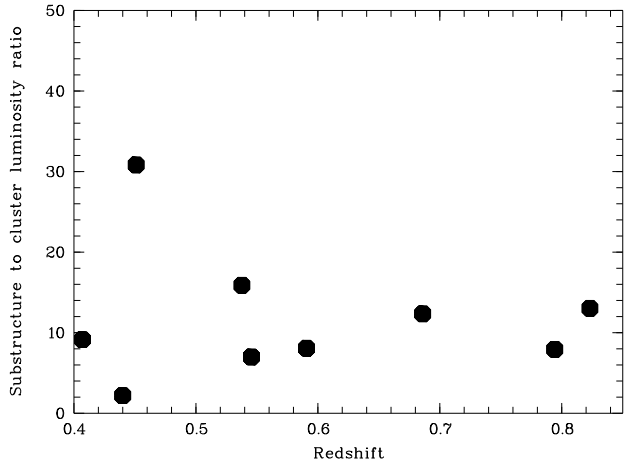

Fig. 8. Substructure to cluster luminosity ratios from the X-ray analysis (in %) versus redshift.

observations represent only 17% of the sample, and only one third of them corresponds to $z \geq 0.65$ clusters. The effect is therefore limited.

A second bias could be due to the fact that X-ray clusters of galaxies often exhibit relations between size, luminosity, and temperature (the well known fundamental plane of galaxy clusters, e.g. Adami et al. 1998). Since distant clusters in the literature are more easily detected when they are luminous (and therefore have high luminosity or temperature), we may imagine a tendency to select clusters with small core radii due to the selection of high-luminosity or high-temperature clusters. To test this point, we checked that relations between the core radius and the luminosity or temperature were visible in our sample. We did not detect any clear correlations, so even a luminosity or temperature selection effect in our sample would not induce a core radius effect, such as the one seen in Fig. 6.

However, that the high redshift clusters could systematically have smaller core radii will have to be confirmed on larger samples in the coming years. We detect no correlation between the core radius and the X-ray temperature (and therefore the X-ray mass), and we detect no clear relation between the velocity dispersion and the X-ray luminosity either.

4.2. X-ray versus SG substructures

Figure 7 shows that substructures were detected with the X-ray method at all redshifts. However, it is mainly the most X-ray luminous clusters ($\geq 4 \times 10^{44}$ erg/s) that provided such detections. To check that these are instrumental effects (only luminous clusters could provide substructure detections due to their higher S/N), we put the substructure information coming from the SG analysis on the same figure. We see that we detected substructures with the SG method even for clusters with undetected X-ray substructures, and even for clusters with low X-ray luminosities. Therefore, X-ray selection effects must indeed be at work. However, nearly all the substructures undetected in X-rays but detected by the SG method seem to be minor (less than 15% of the total cluster mass). It is therefore tempting to conclude that all the major substructures (or at least a large percentage of these) were effectively detected with the X-ray data in hand.

We can now examine the variations in the X-ray luminosity ratio (substructure versus cluster) as a function of redshift. We find that this percentage remains more or less constant with redshift in a 5–15% interval (see Fig. 8). Even if such percentages are probably an underestimate of the mass fraction of clusters that is in the form of substructures (because we do not detect them all, see Sect. 2.3), they are in good agreement with the Millennium simulation (see Appendix of Adami et al. 2013 or Gao et al. 2012) predicting that clusters below $z \sim 1$ primarily undergo minor mergers.

4.3. X-ray substructure merging stages

We concentrate in this part on substructures detected both in X-rays and with the SG method. We consider the X-ray substructures that we detected as relics of more or less recently infalling groups of galaxies. We were able to measure physical parameters for these groups based on their X-ray gas phase and on their galaxy phase. Gas and galaxies have different time-scales in galaxy structures in response to gravitational perturbations such as mergers. We are therefore theoretically in the position of deducing the merging stage of the considered infalling groups with the corresponding clusters.

More precisely, we know the position of isolated groups in L_X versus galaxy velocity dispersion diagrams (e.g. Connelly et al. 2012). We compared the substructures that we have detected in the present paper to these isolated groups. This was done after applying a 1.73 correction factor to translate the Connelly et al. (2012) X-ray luminosities (measured in the 0.1−2.4 keV energy range (see their Sect. 3.1 for details) to our 0.5−8 keV energy range.

Four of our substructures exhibit velocity dispersions over 500 km s^{-1}. This may appear large for dynamically relaxed groups. For SG1 in CL J0152.7-1357, it is not surprising because this cluster is undergoing a major merger, so SG1 is already a pretty massive structure. It is more difficult to explain the high values for Abell 851 (SG3), MS 1054-03 (SG1), and RXC J1206.2-0848 (SG4) if they are relaxed. We may then deal with highly unrelaxed groups in an already quite advanced fusion stage.

We clearly see in Fig. 9 that most of our substructures have higher X-ray luminosities than the isolated groups of Connelly

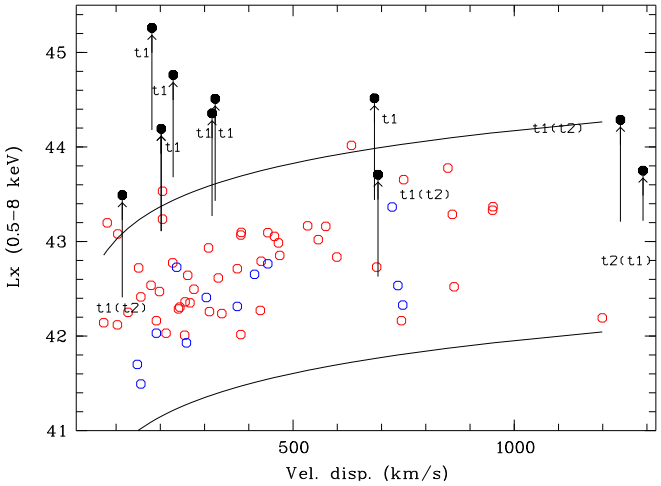

Fig. 9. X-ray luminosity as a function of galaxy velocity dispersion. Open circles are from Connelly et al. (2012), red: X-ray selected groups, blue: optically selected groups. The two black curves show the 3σ envelope of the Connelly et al. (2012) X-ray selected sample. The black filled circles correspond to our detected substructures. The lower extremities of the vertical lines show the places of the infalling structures prior to their dynamical capture assuming the epoch written next to the lines. Other epochs written in parentheses are also possible to place the infalling structures inside the Connelly et al. (2012) envelope.

et al. (2012). This shows that, as expected, our substructures are not classical isolated groups but have already undergone some transformations when falling into the clusters.

Merging simulations (e.g. Poole et al. 2007) show that these transformations include, among others, several increases in the main cluster X-ray luminosity during the merging process at well-defined epochs. More precisely, there is a first increase of the X-ray luminosity at the epoch that we will call $t0$ in the present paper (first virial encounter of the infalling structure with the impacted cluster), then a more significant one at $t1$ (first pericentre approach of the infalling structure), and a third and a fourth smaller increases at epochs $t2$ (second pericentre approach) and $t3$ (relaxation of the impacted structure).

That we still detect X-ray substructures in our clusters naturally excludes the $t3$ epoch. Given the depth of our X-ray data, we never detect the cluster X-ray contributions up to the virial radius, and this prevents us from detecting substructures at the $t0$ stage. Our clusters are therefore somewhere between the $t1$ and $t2$ epochs.

The simulations of Poole et al. (2007) quantified the increase in the X-ray luminosity with time. By applying their predicted increasing factors for major mergers (which the infalling groups experience when merging with a larger cluster) and considering the $t1$ and $t2$ epochs, we were able to estimate the original X-ray luminosities of our infalling groups prior to their gravitational capture. We then selected the possible epochs ($t1$ and/or $t2$), allowing the infalling groups to have been optimally located in the L_X versus velocity dispersion diagram for isolated groups (from Connelly et al. 2012) before gravitational capture. These epochs are listed in Table 2. The increasing factors that we applied are applicable to clusters merging with another cluster of comparable mass. This is not the case here, but it is the best estimation at our disposal of the increase in X-ray luminosity caused by a merger. Poole et al. (2007) did not simulate what happens for merging ratios greater than 1. The X-ray luminosity shifts in Fig. 9 could therefore be greater. We see that most of the X-ray detected substructures are probably at the $t1$ epoch (first pericentre approach) and therefore are relatively recent in the clusters.

5. Galaxy content in substructures

As already mentioned, we collected ground-based imaging and spectroscopy at visible and near-infrared wavelengths. Our ultimate goal is to gather at least five bands in the visible domain (typically B, V, R, I, z') and one in the near-infrared domain (J or Ks) to compute photometric redshifts with the LePhare tool (see Guennou et al. 2010). We are in the process of completing this data collection for our ~90 lines of sight, but for now all clusters of Table 2 with detected substructures (except MS 1621.5+2640) have the full dataset available. This allowed us to compute photometric redshifts for these clusters, and we are therefore now ready to investigate the galaxy content of these structures and of their detected substructures.

The LePhare tool, as for other photometric redshift tools, can be used to compute photometric redshifts, as well as to characterize the considered galaxies in terms of type or stellar population age (e.g. Adami et al. 2009). If we can fix the redshift at its true value (considering only spectroscopic catalogues), then we limit the number of free parameters and we have even better constraints on the type and stellar population ages. This is the approach we have presently chosen, with the spectroscopic catalogues at our disposal. We selected galaxies with a known spectroscopic redshift and chose Bruzual & Charlot (2003) spectral templates in LePhare, fixed the redshift to its value, and estimated the stellar population ages and photometric types. These photometric types are arbitrarily coded between 10 (early galaxies) and 31 (late starbursts). We then investigated the galaxy distribution in an age versus type space. We assume that the age can be considered as driven by the epoch of the last burst of star formation.

5.1. Cluster versus field galaxies

The first thing to check is the general behaviour of cluster versus field galaxies. In order to limit the contamination of the cluster sample by field galaxies as much as possible, we defined the cluster sample as all galaxies with a redshift differing by less than 0.01 from the lower redshift and higher redshift substructures in Table 2. This corresponds to three times the typical velocity dispersion of a massive cluster. The field sample was defined as all galaxies with a redshift differing by more than 0.02 from the lower redshift and higher redshift subtructures in Table 2. This corresponds to six times the typical velocity dispersion of a massive cluster. We are aware that this eliminates galaxies between three and six times the typical cluster velocity dispersion, but these galaxies are potentially in an intermediate state, and they would have made our results noisier.

Figure 10 shows the expected behaviour in both the field and cluster samples, with a population of earlier type galaxies more prominent in the cluster sample. We see a clear dichotomy between early and late types happening around type 17 for both the cluster and the field samples, the gap being less populated in the cluster sample.

Performing a two-dimensional Kolmogorov-Smirnov test gives a probability greater than 99.9% to have populations (cluster and field galaxies) coming from different parent samples. This behaviour has been reported before, but it confirms that our approach to compute age and type is valid.

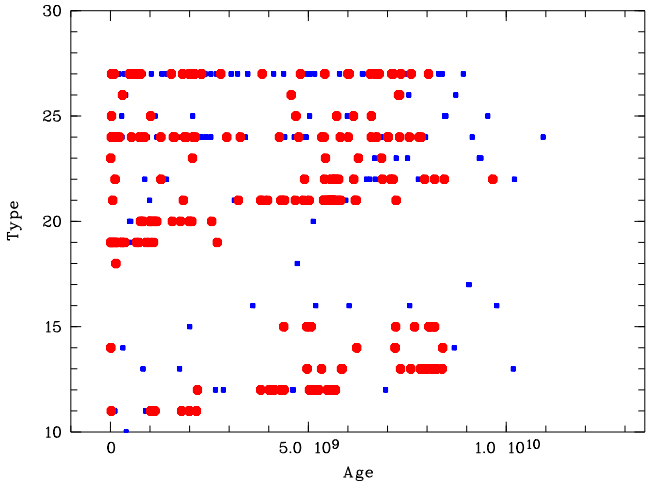

Fig. 10. Cluster (large red circles) and field (small blue squares) galaxies in an age versus type plot.

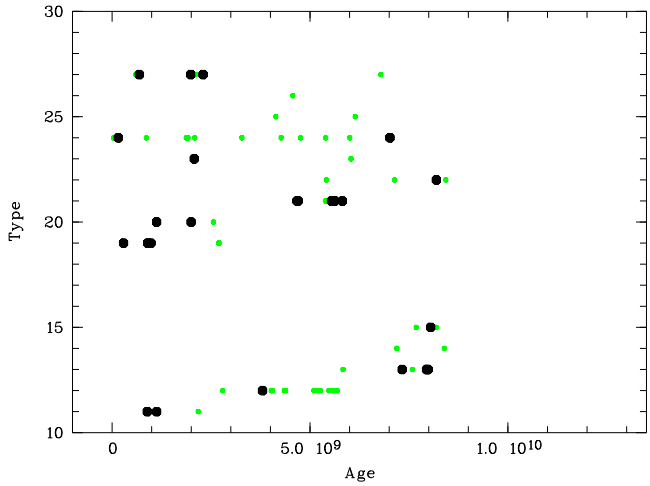

Fig. 11. Galaxies in SG detected (small green disks) and SG+X-rays detected (large black disks) substructures in a plot of galaxy type versus age.

5.2. General position of galaxies in substructures

We first note that galaxies members of substructures are very different from field galaxies. A Kolmogorov-Smirnov test gives a probability over 99.9% to have populations (galaxies in substructures and field galaxies) coming from different parent samples. Figure 11 shows that there is perhaps a lack of both late-type and old stellar population galaxies in substructures detectable in X-rays. This could be explained if galaxies in X-ray detected substructures had undergone recent bursts of star formation induced by shocks in the hot medium. However, this has to be confirmed on larger samples.

5.3. Galaxies in substructures as a function of substructure characteristics

Given the modest size of the galaxy samples in substructures detected both by the SG and X-ray methods, we concentrate here on the substructures detected at least by the SG method in order to maximize our sample.

We chose to characterize the substructures by their velocity difference with the mean cluster velocity. This gives an idea of the importance of the cluster influence on the substructure.

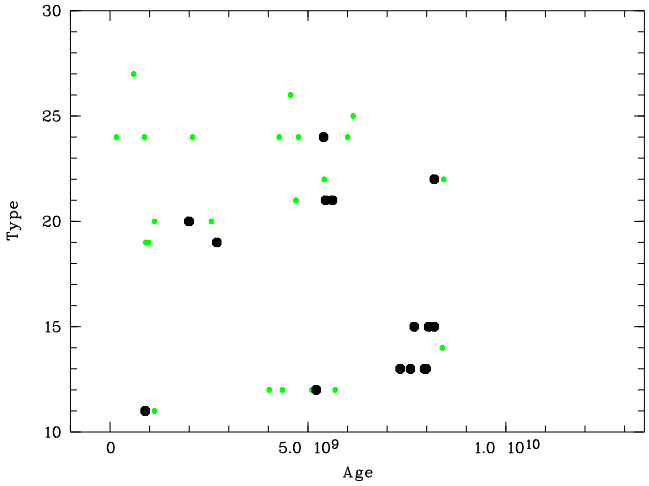

Fig. 12. Galaxies in SG detected substructures at less than 900 km s^{-1} (small green disks) and at less than 300 km s^{-1} (large black disks) from the mean cluster velocity in a plot of galaxy type versus age.

For example, the difference between the substructure members closer than 300 km s^{-1} and 900 km s^{-1} from the cluster mean velocity appears in Fig. 12 to be due to the lack of late type galaxies with recent bursts of star formation in the substructures closest to the cluster mean velocity. This may indicate that substructures close to the bottom of the cluster potential well have consumed a large part of their gas and are therefore less able to form new generations of stars.

5.4. Summary

In conclusion to this section, we can say that galaxy populations in substructures have the same general behaviour as regular cluster galaxies, but with several noticeable differences:

- a possible lack of both late type and old stellar population galaxies in substructures detectable in X-rays and in SG substructures contributing the most to the cluster mass,
- a possible lack of late type galaxies with recent bursts of star formation in the closest substructures to the cluster mean velocity.

These tendencies can be explained by classical expected behaviours in clusters where galaxies close to the bottom of the cluster potential have probably consumed a large part of their gas and are therefore less able to form new generations of stars, and where galaxies in important substructures would have undergone recent bursts of star formation initiated by shocks induced in the hot medium and energy transfer from the surrounding cluster.

6. Discussion

We studied a sample of 32 clusters of galaxies with usable X-ray data and of 19 clusters of galaxies without X-ray data but with more than 15 available spectroscopic redshifts in the cluster range. Ten substructures were detected both in X-rays and by the SG method at optical wavelengths.

We eliminated point source contamination by using *Chandra* data when available and with public catalogues of active galactic nuclei or radio sources. We detected substructures based on X-ray analysis via the statistically significant detection of residuals based on a surface-brightness β-model subtraction, or

optically via an application of the SG dynamical method to our spectroscopic redshift catalogues.

From this work we derived a new set of substructures in rich clusters of galaxies in the redshift range [0.4, 0.9]. We have verified that these are dynamically bound systems by combining the detection in X-rays with a dynamical analysis based on spectroscopic redshifts. We now discuss these results in the context of cluster evolution, as well as in comparison with previous work, where appropriate. A major goal in understanding cluster formation is to be able to use clusters as a tool for studying cosmology, we begin with a brief summary of the relationship between clusters and cosmology.

Because astrophysicists have come to realize there is a direct link between (1) clusters, (2) how large scale structure formed, (3) dark matter, and (4) dark energy, clusters of galaxies are being used more and more as cosmological tools (see for example Allen et al. 2011 and Kravtsov & Borgani 2012). Those works (and references therein) show how cluster counts and cluster-cluster correlations may shed light on the Gaussianity or non-Gaussianity of the initial primordial fluctuations in the early Universe. Furthermore, these papers and others have shown that studies of clusters can also be used to delimit the value of w, if w is variable with redshift, or if there are deviations from General Relativity that are causing the apparent acceleration of the Universe (e.g. Vikhlinin et al. 2009; Allen et al. 2011; Kravtsov & Borgani 2012). On the finest cosmological scale of galaxies, work is going on to determine if there is indeed a missing sub-halo problem or not, but so far there is no consensus (see for example Strigari et al. 2010).

On the in-between scales of groups of galaxies that are continually falling into galaxy clusters, the hierarchical build up of clusters with groups has been described both in published works, such as Poole et al. (2007), Gao et al. (2012, and references therein, too many to list them all), and the Millennium project (Springel et al. 2005), but also in simulations posted on the web.

The Poole et al. (2007) results are in partial agreement with our data, as are those of Gao et al. (2012), in that (a) we find that the X-ray detected groups are in the luminous stage as if they were "lit up" by infall to the cluster as predicted by Poole et al. (2007); (b) Gao et al. (2012) found that at redshift $z = 0$, the total masses in substructures relative to the total cluster masses in their simulations were about 5–15%. This 5–15% value is about the same as the one we found for clusters in our sample, but what is uncertain is how this percentage should change (if at all) with redshift between 0.4 and 0.9. For example, a cluster initially without substructure could grow in such a way that at higher redshifts its initial mass is relatively low, so that added sub-clumps are a relatively high percentage of the total cluster mass. Conversely, it could be that as clusters grow, many of the substructures are not dissipated enough to disappear, and the total mass in substructures actually grows over time. That our mass percentage in substructures at $z = 0.4$–0.9 is about equal to what is predicted by Poole et al. (2007) at $z = 0$ argues that most likely events conspire to keep the detectable mass in substructures in clusters approximately constant from $z = 0.9$ to the current day. This would also be in good agreement with the quite constant level of diffuse light present in clusters between $z = 0.4$ and 0.9 (see Guennou et al. 2012).

The work of Mann & Ebeling (2012) states that the fraction of "disturbed" clusters increases with increasing redshift, implying a higher substructure mass with higher redshift, in apparent contradiction to our work. To be consistent with their work, we would expect the mass in substructures to be higher at higher redshift, if we could add more clusters to our sample and divide them into several bins within the $z = 0.4$–0.9 range.

In comparison, Baldi et al. (2012) find no change in the temperature profile, over the redshift range that they broke their sample into (above and below 0.4), implying that there is little change in shape over this redshift range, in apparent contradiction (in terms of a trend) to what we found. However, Baldi et al. (2012) did not have enough data points to subdivide their $z = 0.4$–0.9 cluster results into smaller redshift bins for a direct comparison to our observations. Also, as by-product of fitting the X-ray data with a simple beta model, we found an increase in the physical extent (i.e. a larger core radius) of the X-ray surface brightness with decreasing redshift. We judge that this effect is *not* due to an inability to detect more extended emission at higher redshift, based on the analysis presented in Sect. 4.1.

Our findings are consistent in a general way with the hierarchical cluster growth scenario in that the extent of clusters apparently grows with decreasing redshift. However, if cluster temperature is a valid measure of the cluster mass (independent of redshift), then the fact that we found no relationship between cluster extent and temperature would argue for the mass not having grown significantly over the redshift range from 0.9 to 0.4, as also indicated by our finding no correlation between the total mass estimated from the X-ray temperature (given in the last column of Table 1) and the redshift. This is plausible if (a) the number of groups infalling over this time period of about 3.6 Gyr is relatively small, and (b) at the same time, the infalling subgroups have caused the ICM to become more extended but not hotter or significantly more massive.

7. Summary and conclusions

By the means of a comparison with Takey et al. (2011), we showed that our X-ray luminosities and temperatures were consistant with literature studies. We estimated the substructure detection efficiency with simulations for the X-ray and SG methods. The X-ray detections proved to be efficient up to $z \sim 0.9$ for substructures brighter than 1.0×10^{44} erg/s and up to $z \sim 0.5$ for substructures only brighter than 0.4×10^{44} erg/s.

The SG detection efficiency was tested by considering six reference clusters outside of our sample, all very well sampled spectroscopically. Substructures with more than six members in the original spectroscopic catalogues remained detected by the SG analysis down to completenesses of 50% to 30%. We showed that the SG precision on the mass estimate remained better than 50% for about half of the sample down to incompletenesses of about 60%, while the SG analysis was not able to precisely estimate the mass of most of the substructures for completeness levels lower than 50%. SG masses were also compared to an optically based cluster mass determination, and we found qualitative agreement. We emphasize, however, that only *relative* SG masses should be considered as reliable.

We found that the core radius of the X-ray gas density profile may decrease with redshift, but this needs to be confirmed with a larger sample of clusters. Ten substructures were detected by both methods (X-rays and SG). These were systematically the SG most massive substructures in each cluster. For a given cluster, the percentage of mass included in substructures was roughly constant with redshift at values of ~5–15%. We also showed that most of our substructures detected both in X-rays and with the SG method were probably at their first cluster pericentre approach and therefore corresponded to relatively recent infalls.

Finally, compared to regular cluster galaxies, galaxy populations in substructures exhibit a possible lack of both late type and old stellar population galaxies, and a possible lack of late type galaxies with recent bursts of star formation in the substructures closest to the mean cluster velocity. In general, our results are consistent with the picture of CDM hierarchical structure formation in that substructure exists. The approximate X-ray properties and masses of the substructures relative to the entire clusters are in the range predicted by theory: 5–15%, see Gao et al. (2012) for the fraction found at $z = 0$, and by the Millennium simulation, which predicts that clusters below $z \sim 1$ only undergo minor mergers. On the simulation front, the percentage of the substructure mass relative to the total mass of the cluster would be interesting to compare with the data we have presented here, as well as with future increased samples produced by our DAFT/FADA collaboration and others.

Acknowledgements. We thank the referee for useful comments. We gratefully acknowledge financial support from the Centre National d'Etudes Spatiales for many years. This project has benefitted from CAPES/COFECUB (programme 711/11). IM has been partially funded by projects AYA2010-15169 from the Spanish Ministerio de Ciencia e Innovación and TIC 114 and PO08-TIC-3531 from Junta de Andalucía. We thank Calar Alto Observatory for allocation of director's discretionary time to this programme. Based on *XMM-Newton* archive data and on data retrieved from the NASA/IPAC Extragalactic Database (NED), which is operated by the Jet Propulsion Laboratory, California Institute of Technology, under contract with the National Aeronautics and Space Administration. The scientific results reported in this article are also based in part on data obtained from the *Chandra* Data Archive. Based on observations made with the FORS2 multi-object spectrograph mounted on the Antu VLT telescope at ESO-Paranal Observatory (programmes 085.A-0016, 191.A-0268; PI: C. Adami). Also based on observations obtained at the Gemini Observatory, which is operated by the Association of Universities for Research in Astronomy, Inc., under a cooperative agreement with the NSF on behalf of the Gemini partnership: the National Science Foundation (United States), the Science and Technology Facilities Council (United Kingdom), the National Research Council (Canada), CONICYT (Chile), the Australian Research Council (Australia), Ministério da Ciência, Tecnologia e Inovação (Brazil), and Ministerio de Ciencia, Tecnología e Innovación Productiva (Argentina). Also based on observations made with the Italian Telescopio Nazionale *Galileo* (TNG) operated on the island of La Palma by the Fundación Galileo Galilei of the INAF (Istituto Nazionale di Astrofisica) at the Spanish Observatorio del Roque de los Muchachos of the Instituto de Astrofísica de Canarias. Also based on service observations made with the WHT operated on the island of La Palma by the Isaac Newton Group in the Spanish Observatorio del Roque de los Muchachos of the Instituto de Astrofísica de Canarias. Also based on observations collected at the German-Spanish Astronomical Center, Calar Alto, jointly operated by the Max-Planck-Institut fur Astronomie Heidelberg and the Instituto de Astrofísica de Andalucía (CSIC). Based on observations obtained with MegaPrime/MegaCam, a joint project of CFHT and CEA/IRFU, at the Canada-France-Hawaii Telescope (CFHT) which is operated by the National Research Council (NRC) of Canada, the Institut National des Sciences de l'Univers of the Centre National de la Recherche Scientifique (CNRS) of France, and the University of Hawaii. This work is based in part on data products produced at Terapix available at the Canadian Astronomy Data Centre as part of the Canada-France-Hawaii Telescope Legacy Survey, a collaborative project of NRC and CNRS. Also based on observations obtained at the WIYN telescope (KNPO). The WIYN Observatory is a joint facility of the University of Wisconsin-Madison, Indiana University, Yale University, and the National Optical Astronomy Observatory. Kitt Peak National Observatory, National Optical Astronomy Observatory, is operated by the Association of Universities for Research in Astronomy (AURA) under cooperative agreement with the National Science Foundation. Also based on observations obtained at the MDM observatory (2.4 m telescope). MDM consortium partners are Columbia University Department of Astronomy and Astrophysics, Dartmouth College Department of Physics and Astronomy, University of Michigan Astronomy Department, The Ohio State University Astronomy Department, Ohio University Dept. of Physics and Astronomy. Also based on observations obtained at the Southern Astrophysical Research (SOAR) Telescope, which is a joint project of the Ministério da Ciência, Tecnologia, e Inovação (MCTI) da República Federativa do Brasil, the US National Optical Astronomy Observatory (NOAO), the University of North Carolina at Chapel Hill (UNC), and Michigan State University (MSU). Also based on observations obtained at the Cerro Tololo Inter-American Observatory, National Optical Astronomy Observatory, which are operated by the Association of Universities for Research in Astronomy, under contract with the National Science Foundation. Finally, this research has made use of the VizieR catalogue access tool, CDS, Strasbourg, France.

References

Abell, G. O., Corwin, H. G. Jr, & Olowin, R. P. 1989, ApJS, 70, 1
Adami, C., Mazure, A., Biviano, A., Katgert, P., & Rhee, G. 1998, A&A, 331, 493
Adami, C., Biviano, A., Durret, F., & Mazure, A. 2005, A&A, 443, 17
Adami, C., Pellò, R., Ulmer, M. P., et al. 2009a, A&A, 495, 407
Adami, C., Le Brun, V., Biviano, A., et al. 2009b, A&A, 507, 1225
Adami, C., Durret, F., Benoist, C., et al. 2010, A&A, 509, A81
Adami, C., Jouvel, S., Guennou, L., et al. 2012, A&A, 540, A105
Adami, C., Durret, F., Guennou, L., & Da Rocha, C. 2013, A&A, 551, A20
Allen, S. W., Evrard, A. E., & Mantz, A. B. 2011, ARA&A, 49, 409
Andrade-Santos, F., Lima Neto, G. B., & Laganá, T. F. 2012, ApJ, 746, 139
Baldi, A., Ettori, S., Molendi, S., & Gastaldello, F. 2012, A&A, 545, A41
Barkhouse, W. A., Green, P. J., Vikhlinin, A., et al. 2006, ApJ, 645, 955
Bell, E. F., McIntosh, D. H., Katz, N., & Weinberg, M. D. 2003, ApJS, 149, 289
Böhringer, H., Briel, U. G., Schwarz, R. A., et al. 1994, Nature, 368, 828
Böhringer, H., Pratt, G. W., Arnaud, M., et al. 2010, A&A, 514, A32
Borgani, S., & Kravtsov, A. 2011, Adv. Sci. Lett., 4, 204
Boué, G. Durret, F., Adami, C., et al. 2008, A&A, 489, 11
Bruzual, G., & Charlot, S. 2003, MNRAS, 344, 1000
Cappellari, M., Bacon, R., Bureau, M., et al. 2006, MNRAS, 366, 1126
Carlberg, R. G., Yee, H. K. C., Morris, S. L., et al. 2001, ApJ, 552, 427
Chon, G., Böhringer, H., & Smith, G. P. 2012, A&A, 548, A59
Clowe, D. I., Luppino, G. A., Kaiser, N., Henry, J. P., & Gioia, I. M. 1998, ApJ, 497, L61
Clowe, D., Schneider, P., Aragón-Salamanca, A., et al. 2006, A&A, 451, 395
Connelly, J. L., Wilman, D. J., Finoguenov, A., et al. 2012, ApJ, 756, 139
Churazov, E., Forman, W., Jones, C., & Böhringer, H. 2003, ApJ, 590, 225
Dawson, S., Stern, D., Bunker, A. J., Spinrad, H., & Dey, A. 2001, AJ, 122, 598
De Filippis, E., Schindler, S., & Castillo-Morales, A. 2003, A&A, 404, 63
Dressler, A., & Schechtman, S. A. 1988, AJ, 95, 985
Dunkley, J., Komatsu, E., Nolta, M. R., et al. 2009, ApJS, 180, 306
Dupke, R. A., & Bregman, J. N. 2001, ApJ, 547, 705
Durret, F., Adami, C., Gerbal, D., & Pislar, V. 2000, A&A, 356, 815
Durret, F., Slezak, E., & Adami, C. 2009, A&A, 506, 637
Durret, F., Laganá, T. F., Adami, C., & Bertin, E. 2010, A&A, 517, A94
Ebeling, H., Edge, A. C., & Henry, J. P. 2001a, ApJ, 553, 668
Ebeling, H., Jones, L. R., Fairley, B. W., et al. 2001b, ApJ, 548, L23
Ebeling, H., Barrett, E., Donovan, D., et al. 2007, ApJ, 661, L33
Ebeling, H., Edge, A. C., Mantz, A., et al. 2010, MNRAS, 407, 83
Eckmiller, H. J., Hudson, D. S., & Reiprich, T. H. 2011, A&A, 535, A105
Einasto, M., Vennik, J., Nurmi, P., et al. 2012, A&A, 540, A123
Fukugita, M., Shimasaku, K., & Ichikawa, T. 1995, PASP, 107, 945
Furusho, T., Yamasaki, N. Y., Ohashi, T., Shibata, R., & Ezawa, H. 2001, ApJ, 561, L165
Gal, R. R., & Lubin, L. M. 2004, ApJ, 607, L1
Gal, R. R., Lubin, L. M., & Squires, G. K. 2005, AJ, 129, 1827
Gal, R. R., Lemaux, B. C., Lubin, L. M., Kocevski, D., & Squires, G. K. 2008, ApJ, 684, 933
Gao, L., Navarro, J. F., Frenk, C. S., et al. 2012, MNRAS, 425, 2169
Gerke, B. F., Newman, J. A., Faber, S. M., et al. 2007, MNRAS, 376, 1425
Gilmour, R., Best, P., & Almaini, O. 2009, MNRAS, 392, 1509
Giodini, S., Pierini, D., Finoguenov, A., et al. 2009, ApJ, 703, 982
Gioia, I. M., Maccacaro, T., Schild, R. E., et al. 1990, ApJS, 72, 567
Gioia, I. M., Henry, J. P., Mullis, C. R., Ebeling, H., & Wolter, A. 1999, AJ, 117, 2608
Gioia, I. M., Braito, V., Branchesi, M., et al. 2004, A&A, 419, 517
Girardi, M., Demarco, R., Rosati, P., & Borgani, S. 2005, A&A, 442, 29
Gladders, M. D., & Yee, H. K. C. 2005, ApJS, 157, 1
Gonzalez, A. H., Zaritsky, D., Dalcanton, J. J., & Nelson, A. 2001, ApJS, 137, 117
Gonzalez, A. H., Zaritsky, D., & Zabludoff, A. I. 2007, ApJ, 666, 147
Green, P. J., Infante, L., Lopez, S., Aldcroft, T. L., & Winn, J. N. 2005, ApJ, 630, 142
Guennou, L. 2012, Ph.D. Thesis, Université de Marseille-Provence, France
Guennou, L., Adami, C., Ulmer, M. P., et al. 2010, A&A, 523, A21
Guennou, L., Biviano, A., Adami, C., et al. 2013, A&A, submitted
Gunn, J. E., Hoessel, J. G., & Oke, J. B. 1986, ApJ, 306, 30
Halliday, C., Milvang-Jensen, B., Poirier, S., et al. 2004, A&A, 427, 397
Harrison, F. A., Eckart, M. E., Mao, P. H., Helfand, D. J., & Stern, D. 2003, ApJ, 596, 944

Henry, J. P., Gioia, I. M., & Mullis, C. R. 1997, AJ, 114, 1293
Holden, B. P., Stanford, S. A., Rosati, P., et al. 2001, AJ, 122, 629
Jee, M. J., & Tyson, J. A. 2009, ApJ, 691, 1337
Jones, C., & Forman, W. 1984, ApJ, 276, 38
Kauffmann, G., Heckman, T. M., White, S. D. M., et al. 2003, MNRAS, 341, 33
Kolokotronis, V. Georgakakis, A., Basilakos, S., et al. 2006, MNRAS, 366, 163
Komatsu, E., Matsuo, H., Kitayama, T., et al. 2001, PASJ, 53, 57
Korngut, P. M., Dicker, S. R., Reese, E. D., et al. 2011, ApJ, 734, 10
Kravtsov, A. V., & Borgani, S. 2012, ARA&A, 50, 353
Kravtsov, A., Vikhlinin, A., & Nagai, D. 2006, ApJ, 650, 128
Lilly, S. J., LeBrun, V., Maier, C., et al. 2009, ApJS, 184, 218
Lopes, P. A. A., de Carvalho, R. R., Capelato, H. V., et al. 2006, ApJ, 648, 209
Mamon, G. A. 2000, ASPC, 197, 377
Mann, A. W., & Ebeling, H. 2012, MNRAS, 420, 2120
Mathur, S., & Williams, R. J. 2003, ApJ, 589, L1
Maughan, B. J., Jones, C., Jones, L.R.., & Van Speybroeck, L. 2007, ApJ, 659, 1125
Maughan, B. J., Jones, C., Forman, W., & Van Speybroeck, L. 2008, ApJS, 174, 117
McHardy, I. M., Jones, L. R., Merrifield, M. R., et al. 1998, MNRAS, 295, 641
Milvang-Jensen, B., Noll, S., Halliday, C., et al. 2008, A&A, 482, 419
Moran, S. M., Ellis, R. S., Treu, T., et al. 2007, ApJ, 671, 1503
Mulchaey, J. S., Lubin, L. M., Fassnacht, C., Rosati, P., & Jeltema, T. E. 2006, ApJ, 646, 133
Navarro, J. F., Ludlow, A., Springel, V., et al. 2010, MNRAS, 402, 21
Neumann, D. M., Lumb, D. H., Pratt, G. W., & Briel, U. G. 2003, A&A, 400, 811
Perlman, E. S., Horner, D. J., Jones, L. R., et al. 2002, ApJS, 140, 265
Poole, G. B., Babul, A., McCarthy, I. G., et al. 2007, MNRAS, 380, 437
Postman, M., Coe, D., Benítez, N., et al. 2012, ApJS, 199, 25
Schindler, S., Guzzo, L., Ebeling, H., et al. 1995, A&A, 299, L9
Schirmer, M., Suyu, S., Schrabback, T., et al. 2010, A&A, 514, A60
Serna, A., & Gerbal, D. 1996, A&A, 309, 65
Shibata, R., Matsushita, K., Yamasaki, N. Y., et al. 2001, ApJ, 549, 228
Smith, G. P., Khosroshahi, H. G., Dariush, A., et al. 2010, MNRAS, 409, 169
Springel, V., White, S. D. M., Jenkins, A., et al. 2005, Nature, 435, 629
Springel, V., White, S. D. M., Frenk, C. S., et al. 2008a, Nature, 456, 73
Springel, V., Wang, J., Vogelsberger, M., et al. 2008b, MNRAS, 391, 1685
Strigari, L. E., Frenk, C. S., & White, S. D. M. 2010, MNRAS, 408, 2364
Takey, A., Schwope, A., & Lamer, G. 2011, A&A, 534, A120
Takizawa, M. 2005, ApJ, 629, 791
Tonnesen, S., & Bryan, G. L. 2008, ApJ, 684, L9
Tremonti, C. A., Heckman, T. M., Kauffmann, G., et al. 2004, ApJ, 613, 898
Ulmer, M. P., Adami, C., Covone, G., et al. 2005, ApJ, 624, 124
Ulmer, M. P., Adami, C., Lima Neto, G. B., et al. 2009, A&A, 503, 399
Vikhlinin, A., McNamara, B. R., Forman, W., et al. 1998, ApJ, 502, 558
Vikhlinin, A., Kravtsov, A., Forman, W., et al. 2006, ApJ, 640, 691
Vikhlinin, A., Murray, S., Gilli, R., et al. 2009, Astro2010: The Astronomy and Astrophysics Decadal Survey (Science White Papers), 305 [arXiv:0903.5320]
Voges, W., Aschenbach, B., Boller, T., et al. 1999, A&A, 349, 389
Weissmann, A., Böhringer, H., & Chon, G. 2013, A&A, 555, A147
Wen, Z. L., & Han, J. L. 2013, MNRAS, 436, 275
Xue, Y. J., & Wu, X. P. 2000, ApJ, 538, 65

[1] Aix-Marseille Université, CNRS, LAM (Laboratoire d'Astrophysique de Marseille) UMR 7326, 13388 Marseille, France
e-mail: guennou@ukzn.ac.za
[2] Astrophysics and Cosmology Research Unit, University of KwaZulu-Natal, 4041 Durban, South Africa
[3] UPMC-CNRS, UMR7095, Institut d'Astrophysique de Paris, 75014 Paris, France
[4] Departamento de Astronomia, Instituto de Astronomia, Geofísica e Ciências Atmosféricas, Universidade de São Paulo, Rua do Matão 1226, 05508-900 São Paulo, Brazil
[5] Dept of Physics and Astronomy & Center for Interdisciplinary Exploration and Research in Astrophysics (CIERA), Evanston IL 60208-2900, USA
[6] Department of Physics and Astronomy, Ohio University, 251B Clippinger Lab, Athens OH 45701, USA
[7] Fermi National Accelerator Laboratory, PO Box 500, Batavia IL 60510, USA
[8] CSC/STScI, 3700 San Martin Dr., Baltimore MD 21218, USA
[9] OCA, Cassiopée, Boulevard de l'Observatoire, BP 4229, 06304 Nice Cedex 4, France
[10] INAF/Osservatorio Astronomico di Trieste, via Tiepolo 11, 34143 Trieste, Italy
[11] INAF – Osservatorio Astronomico di Bologna, via Ranzani 1, 40127 Bologna, Italy
[12] 23 rue d'Yerres, 91230 Montgeron, France
[13] Steward Observatory, University of Arizona, 933 N. Cherry Ave., Tucson AZ 85721, USA
[14] Department of Astronomy & Astrophysics, University of Toronto, 50 St George Street, Toronto M5S 3H4, Canada
[15] Instituto de Astrofísica de Andalucía, CSIC, Glorieta de la Astronomía s/n, 18008 Granada, Spain
[16] Laboratório de Astrofísica Teórica e Observacional, Universidade Estadual de Santa Cruz, 45662-000 Ilhéus, Brazil
[17] Gemini Observatory, 603 Casilla, La Serena, Chile
[18] Argelander-Institut für Astronomie, Universität Bonn, auf dem Hügel 71, 53121 Bonn, Germany
[19] University of Vienna, Department of Astronomy, Türkenschanzstrasse 17, 1180 Vienna, Austria

Pages 15 to 60 are available in the electronic edition of the journal at http://www.aanda.org

Table 1. Data for the clusters with usable *XMM-Newton* data.

Name	RA	Dec	z	Nz	Δt (s)	kT (keV)	L_X (erg s^{-1})	$M_{gas,r500}$ ($M_\odot$)	$M_{tot,r500}$ ($M_\odot$)	Substructure
CL 0016+1609	4.63888	16.44329	0.5455	173	30320	8.97 ± 0.40	2.23 ± 0.06e+45	1.17 ± 0.03e+14	1.24 ± 0.04e+15	1
CL J0152.7-1357	28.17083	–13.96250	0.8310	115	51150	7.55 ± 0.65	7.91 ± 0.74e+44	7.72 ± 0.28e+13	8.83 ± 0.38e+14	1
MS 0302.5+1717	46.32911	17.47729	0.4250	1	12440	6.23 ± 1.13	1.41 ± 0.35e+44	6.02 ± 0.72e+13	6.84 ± 0.67e+14	0/–1
XDCS cm J032903.1+025640	52.26175	2.94033	0.4122	13	47520	3.26 ± 0.38	1.40 ± 0.89e+43	2.60 ± 0.30e+13	2.88 ± 0.40e+14	–1
RX J0337.6-2522	54.43812	–25.37669	0.5850	5	11820	2.40 ± 0.78	5.73 ± 4.98e+43	1.65 ± 0.25e+13	1.85 ± 0.36e+14	0
MACS J0454.1-0300	73.54552	–3.01865	0.5377	194	25420	9.97 ± 0.59	2.04 ± 0.06e+45	1.29 ± 0.04e+14	1.39 ± 0.04e+15	1
BMW-HRI J052215.8-362452	80.55917	–36.41778	0.4720	1	17920	5.64 ± 0.66	1.70 ± 0.27e+44	4.99 ± 0.32e+13	5.78 ± 0.41e+14	0/–1
MACS J0647.7+7015	101.94125	70.25083	0.5907	1	32030	7.74 ± 0.35	1.61 ± 0.07e+45	9.76 ± 0.32e+13	1.02 ± 0.04e+15	1
MACS J0744.9+3927	116.21583	39.45917	0.6860	2	71260	7.87 ± 0.28	1.87 ± 0.06e+45	8.96 ± 0.19e+13	9.86 ± 0.30e+14	1
RX J0847.1+3449	131.79708	34.82111	0.5600	1	6908		7.11 ± 0.49e+44			0
MACS J0913.7+4056	138.40277	40.94315	0.4420	2	12430	5.39 ± 0.19	1.58 ± 0.06e+45	5.29 ± 0.09e+13	5.83 ± 0.20e+14	0
Abell 851	145.73601	46.98942	0.4069	213	40970	5.17 ± 0.16	6.13 ± 0.20e+44	5.04 ± 0.10e+13	5.53 ± 0.21e+14	1
MS 1054-03	164.25093	–3.62428	0.8231	326	25680	8.64 ± 0.66	1.49 ± 0.13e+45			1
UM 425 Cluster	170.83542	1.62944	0.7685	8	26090	14.5 ± 4.2	4.90 ± 0.34e+44	1.17 ± 0.06e+14	1.64 ± 0.06e+15	0
MS 1137.5+6624	175.09696	66.14485	0.7820	17	15560	7.43 ± 0.90	7.41 ± 1.05e+44	8.49 ± 0.58e+13	9.25 ± 0.59e+14	0
CLG J1205+4429	181.46410	44.48600	0.5915	10	25520		6.77 ± 3.32e+43			0
RXC J1206.2-0848	181.54991	–8.80001	0.4400	53	10200	9.36 ± 0.59	2.32 ± 0.08e+45	1.23 ± 0.05e+14	1.31 ± 0.05e+15	1
LCDCS 0504[a]	184.18845 (184.18792)	–12.02147 (–12.02139)	0.7943	65	23460	5.49 ± 0.64	3.91 ± 0.50e+44	9.00 ± 0.93e+13	8.02 ± 0.77e+14	1
BMW-HRI J122657.3+333253	186.74167	33.54836	0.8900	35	65350	8.74 ± 0.42	2.02 ± 0.10e+45	1.16 ± 0.03e+14	1.21 ± 0.04e+15	–1
GHO 1322+3027	201.20091	30.19276	0.7550	38	36390	5.98 ± 1.33	8.91 ± 3.64e+43	5.17 ± 0.63e+13	6.11 ± 0.62e+14	0
ZwCl 1332.8+5043	203.58333	50.51506	0.6200	1	27860	5.08 ± 0.59	2.40 ± 0.51e+44	4.39 ± 0.33e+13	5.05 ± 0.42e+14	0
LCDCS 0829	206.88333	–11.76167	0.4510	50	32370	11.31 ± 0.24	7.75 ± 0.06e+45	1.58 ± 0.02e+14	1.69 ± 0.03e+15	1
LCDCS 0853	208.53958	–12.51639	0.7627	18	27420		3.65 ± 0.38e+44			0
RX J1354.2-0221	208.57042	–2.36306	0.5460	2	18390	2.18 ± 0.98	2.04 ± 0.62e+44	1.38 ± 0.29e+13	1.58 ± 0.29e+14	0
MACS J1423.8+2404[b]	215.95125	24.07972	0.5450	9	113400	5.3 ± 0.1	1.71 ± 0.05e+45	5.24 ± 0.10e+13	5.74 ± 0.10e+14	1 (*Chandra*)
GHO 1602+4312	241.10483	43.08131	0.8950	26	12000		8.96 ± 8.39e+43			0
MS 1621.5+2640	245.89863	26.56378	0.4260	104	2210		9.13 ± 3.46e+43			0
CXOU J205617.1-044155	314.07150	–4.69864	0.6002	1	16240	2.46 ± 1.02	1.98 ± 0.42e+44	5.02 ± 0.71e+13	3.59 ± 0.66e+14	0
MS 2053.7-0449	314.09321	–4.62873	0.5830	30	16240	4.81 ± 1.17	2.13 ± 0.56e+44	4.42 ± 0.63e+13	4.91 ± 0.62e+14	0
GHO 2143+0408	326.52000	4.38861	0.5310	1	20170	4.39 ± 0.43	1.51 ± 0.30e+44	4.60 ± 0.29e+13	4.77 ± 0.39e+14	0
RX J2202.7-1902	330.68708	–19.03611	0.4380	8	26060	4.97 ± 1.34	4.56 ± 2.07e+43	4.41 ± 0.57e+13	5.00 ± 0.58e+14	–1
RX J2328.8+1453	352.20792	14.88667	0.4970	1	25510	2.63 ± 0.53	4.28 ± 1.78e+43	2.03 ± 0.26e+13	2.20 ± 0.37e+14	0/–1

Notes. (1) Name given by NED (LCDCS clusters come from Gonzalez et al. 2001), (2) right ascension in degrees (J2000.0), (3) declination in degrees (J2000.0), (4) redshift, (5) number of galaxies with redshifts in the cluster range, (6) useful *XMM-Newton* exposure time (in seconds), (7) temperature of the X-ray gas, (8) X-ray luminosity in the [0.5, 8.0] keV band, (9) X-ray gas mass in the r_{500} radius, (10) total mass in the r_{500} radius, (11) subtructure inside the cluster (1 means yes, –1 means no, 0 means not detectable with data in hand). [(a)] The position given for LCDCS 504 comes from Guennou et al. (2013) where we determined the centre as the position of the cD, whereas the position given in parentheses was obtained from NED. [(b)] Cluster MACS J1423.8+2404 did not have any *XMM-Newton* public data, but we collected *Chandra* data with enough depth to be able to subtract a β-model and search for substructures.

Table 2. Detected substructures.

Name	#	N_{gal}	z	$(M_{SS}/M_{tot})_{SG}$ (%)	$(M_{SS}/M_{tot})_{sc}$ (%)	Vel. disp. (km s^{-1})	L_X (erg/s)	Merging stage
CL 0016+1609	1	64	0.5418	[10;20]	[10;20]			
	2	17	0.5505	[0;10]	[0;10]			
	3	13	0.5530	[0;10]	[0;10]			
	4	24	0.5597	[0;10]	[0;10]	200	1.56×10^{44}	t1
CL J0152.7-1357	1	49	0.8382	[20;30]	[40;50]	680	3.28×10^{44}	t1
	2	17	0.8323	[0;10]	[0;10]			
	3	29	0.8279	[0;10]	[0;10]			
	4	34	0.8458	[20;30]	[0;10]	320	2.27×10^{44}	t1
XDCS cm J032903.1+025640	1	7	0.4115	[0;10]	[50;60]			
	2	4	0.4095	[0;10]	[0;10]			
MACS J0454.1-0300	1	31	0.5365	[10;20]	[0;10]			
	2	5	0.5407	[0;10]	[0;10]			
	3	18	0.5434	[0;10]	[0;10]	320	3.24×10^{44}	t1
	4	6	0.5376	[0;10]	[0;10]			
	5	3	0.5320	[0;10]	[0;10]			
	6	12	0.5309	[0;10]	[0;10]			
	7	3	0.5390	[0;10]	[0;10]			
	8	4	0.5457	[0;10]	[0;10]			
	9	4	0.5287	[0;10]	[0;10]			
Abell 851	1	6	0.4070	[0;10]	[0;10]			
	2	3	0.4100	[0;10]	[0;10]			
	3	4	0.4036	[0;10]	[0;10]	1300	5.63×10^{43}	t0 (t1 or t2)
	4	3	0.4059	[0;10]	[0;10]			
	5	4	0.4100	[0;10]	[0;10]			
	6	8	0.4142	[0;10]	[0;10]			
	7	3	0.4100	[0;10]	[0;10]			
	8	3	0.4163	[0;10]	[0;10]			
MS 1054-03	1	7	0.8218	[0;10]	[0;10]	1250	1.94×10^{44}	t1 (t0 or t2)
	2	26	0.8261	[0;10]	[0;10]			
	3	5	0.8267	[0;10]	[0;10]			
	4	5	0.8270	[0;10]	[0;10]			
CLG J1205+4429	1	11	0.5948	[90;100]*	[90;100]			
BMW-HRI J122657.3+333253	1	10	0.8816	[20;30]	[0;10]			
	2	4	0.8910	[0;10]	[0;10]			
	3	5	0.8920	[0;10]	[0;10]			
	4	5	0.8930	[0;10]	[0;10]			
	5	4	0.8960	[0;10]	[0;10]			
	6	4	0.8970	[0;10]	[0;10]			
RXC J1206.2-0848	1	5	0.4255	[0;10]	[0;10]			
	2	3	0.4336	[0;10]	[0;10]			
	3	6	0.4409	[0;10]	[0;10]			
	4	4	0.4373	[0;10]	[0;10]	690	5.10×10^{43}	t1 (t0 or t2)
LCDCS 0504	1	7	0.8036	[0;10]	[0;10]	110	3.10×10^{43}	t1 (t0 or t2)
	2	10	0.7996	[0;10]	[0;10]			
	3	17	0.7858	[0;10]	[0;10]			
	4	5	0.7913	[0;10]	[0;10]			
	5	6	0.7966	[0;10]	[0;10]			
	6	7	0.7953	[0;10]	[0;10]			
	7	6	0.7940	[0;10]	[0;10]			
GHO 1322+3027	1	44	0.7562	[90;100]*	[90;100]			
LCDCS 0829	1	22	0.4503	[0;10]	[40;50]	230	5.79×10^{44}	t1
	2	14	0.4529	[0;10]	[20;30]			
	3	15	0.4465	[0;10]	[0;10]			
	4	12	0.4553	[0;10]	[0;10]	180	1.82×10^{45}	t1
LCDCS 0853	1	3	0.7648	[90;100]*	[20;30]			
MACS J1423.8+2404	1	3	0.5445	[90;100]*	[30;40]			
GHO 1602+4312	1	29	0.8941	[90;100]*	[90;100]			
MS 1621.5+2640	1	24	0.4245	[0;10]	[10;20]			
	2	19	0.4264	[0;10]	[0;10]			
	3	43	0.4307	[10;20]	[20;30]			
	4	20	0.4211	[0;10]	[0;10]			
MS 2053.7-0449	1	28	0.5837	[90;100]*	[90;100]			
GHO 2143+0408	1	4	0.5205	[90;100]*	[80;90]			

Notes. (1) Cluster name, (2) substructure number, (3) substructure number of galaxies, (4) substructure mean redshift, (5) substructure to total cluster mass ratio estimated with the SG method and given in 10% wide intervals (the asterisk means that we only detected the main structure), (6) substructure to total cluster mass ratio estimated with the method based on a scaling relation described in Sect. 3.5 and given in 10% wide intervals, (7) substructure velocity dispersion estimated with SG for the substructures also detected in X-rays, (8) substructure X-ray luminosity, (9) merging stage (see text).

Table 4. Optical structures found in the clusters with no X-ray data.

Name	#	N_{gal}	z	$(M_{SS}/M_{tot})_{SG}$ (%)	$(M_{SS}/M_{tot})_{sc}$ (%)
CXOMP J091126.6+055012	1	11	0.7687	[20;30]	[30;40]
	2	7	0.7623	[0;10]	[10;20]
	3	6	0.7748	[0;10]	[0;10]
LCDCS 0110	1	4	0.5807	[0;10]	[10;20]
	2	9	0.5777	[0;10]	[40;50]
LCDCS 0130	1	7	0.7041	[0;10]	[0;10]
	2	5	0.7028	[0;10]	[0;10]
	3	8	0.7059	[0;10]	[0;10]
LCDCS 0172	1	24	0.6977	[0;10]	[30;40]
	2	6	0.6979	[0;10]	[0;10]
	3	7	0.6944	[0;10]	[0;10]
LCDCS 0173	1	12	0.7498	[0;10]	[10;20]
	2	11	0.7477	[0;10]	[10;20]
	3	8	0.7523	[0;10]	[0;10]
	4	5	0.7573	[10;20]	[0;10]
CXOMP J111726.1+074335	1	22	0.4833	[0;10]	[30;40]
	2	16	0.4790	[0;10]	[10;20]
LCDCS 340	1	9	0.4852	[0;10]	[0;10]
	2	5	0.4765	[0;10]	[0;10]
	3	5	0.4818	[0;10]	[0;10]
	4	4	0.4801	[0;10]	[0;10]
	5	4	0.4787	[0;10]	[0;10]
	6	5	0.4796	[0;10]	[0;10]
LCDCS 0541	1	9	0.5420	[0;10]	[0;10]
	2	11	0.5447	[0;10]	[0;10]
	3	10	0.5395	[0;10]	[0;10]
	4	13	0.5347	[20;30]	[0;10]
	5	7	0.5432	[0;10]	[0;10]
	6	9	0.5408	[0;10]	[0;10]
	7	4	0.5379	[0;10]	[0;10]
	8	12	0.5492	[0;10]	[0;10]
ClG J1236+6215	1	23	0.8521	[0;10]	[30;40]
	2	17	0.8494	[0;10]	[0;10]
	3	13	0.8495	[0;10]	[0;10]
	4	16	0.8462	[10;20]	[10;20]
3C 295 Cluster	1	10	0.4560	[0;10]	[10;20]
	2	17	0.4618	[0;10]	[20;30]
GHO 1601+4253	1	37	0.5392	[0;10]	[50;60]
	2	14	0.5439	[0;10]	[0;10]

Notes. (1) Cluster name, (2) number of the substructure, (3) number of galaxies with redshift in the substructure, (4) mean redshift of the substructure, (5) substructure to total cluster mass ratio estimated with the SG method and given in 10% wide intervals, (6) substructure to total cluster mass ratio estimated with the method based on a scaling relation described in Sect. 3.5 and given in 10% wide intervals.